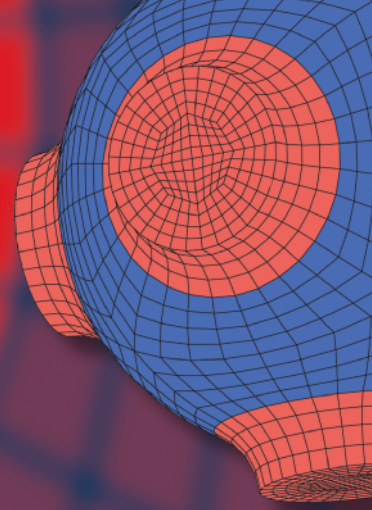Hans Irschik
Michael Krommer
Valerii P. Matveenko
Alexander K. Belyaev   *Editors*

Dynamics and Control of Advanced Structures and Machines

Contributions from the 4th International Workshop, Linz, Austria

Springer

Advanced Structured Materials

Volume 156

Series Editors

Andreas Öchsner, Faculty of Mechanical Engineering, Esslingen University of Applied Sciences, Esslingen, Germany

Lucas F. M. da Silva, Department of Mechanical Engineering, Faculty of Engineering, University of Porto, Porto, Portugal

Holm Altenbach , Faculty of Mechanical Engineering, Otto von Guericke University Magdeburg, Magdeburg, Sachsen-Anhalt, Germany

Common engineering materials reach in many applications their limits and new developments are required to fulfil increasing demands on engineering materials. The performance of materials can be increased by combining different materials to achieve better properties than a single constituent or by shaping the material or constituents in a specific structure. The interaction between material and structure may arise on different length scales, such as micro-, meso- or macroscale, and offers possible applications in quite diverse fields.

This book series addresses the fundamental relationship between materials and their structure on the overall properties (e.g. mechanical, thermal, chemical or magnetic etc.) and applications.

The topics of *Advanced Structured Materials* include but are not limited to

- classical fibre-reinforced composites (e.g. glass, carbon or Aramid reinforced plastics)
- metal matrix composites (MMCs)
- micro porous composites
- micro channel materials
- multilayered materials
- cellular materials (e.g., metallic or polymer foams, sponges, hollow sphere structures)
- porous materials
- truss structures
- nanocomposite materials
- biomaterials
- nanoporous metals
- concrete
- coated materials
- smart materials

Advanced Structured Materials is indexed in Google Scholar and Scopus.

More information about this series at http://www.springer.com/series/8611

Hans Irschik · Michael Krommer ·
Valerii P. Matveenko · Alexander K. Belyaev
Editors

Dynamics and Control of Advanced Structures and Machines

Contributions from the 4th International
Workshop, Linz, Austria

Editors
Hans Irschik
Institute of Technical Mechanics
Johannes Kepler University of Linz
Linz, Oberösterreich, Austria

Michael Krommer
Institute of Technical Mechanics
Johannes Kepler University of Linz
Linz, Oberösterreich, Austria

Valerii P. Matveenko
UB RAS
Institute of Continuous Media Mechanics
Perm, Russia

Alexander K. Belyaev 🔘
Institute for Problems in Mechanical
Engineering
Russian Academy of Sciences
St. Petersburg, Russia

Preface

This present book presents a collection of 23 contributions presented during the *4th International Workshop on Advanced Dynamics and Model Based Control of Structures and Machines*, which was held in September 2019 at the *Institute of Technical Mechanics* of the Johannes Kepler University Linz, Austria. 13 contributions are from Austria, 5 from Russia, 3 from Taiwan and 1 each from Germany and France.

The workshop continued a series of international workshops—the *Japan–Austria Joint Workshop on Mechanics and Model Based Control of Smart Materials and Structures*, the *Russia–Austria Joint Workshop on Advanced Dynamics and Model Based Control of Structures and Machines* and the first three editions of the *International Workshop on Advanced Dynamics and Model Based Control of Structures and Machines*. The previous workshops took place in Austria in 2008 (Linz), 2010 (Linz) and 2015 (Vienna) and in Russia in 2012 (St. Petersburg) and 2017 (Perm).

The general goal of these workshops has been to present and discuss the frontiers in the mechanics of controlled machines and structures with the intention

- to enable the interchange of ideas from advanced mechanics of materials and structures and control theory,
- to clarify the expectations of researchers in the field of mechanics from advanced control theory and vice versa,
- to develop ideas for and to initiate future bilateral research proposals
- and to encourage collaborations among industry and universities across the borders of the participating countries.

To meet the last objective, a special session on R&D in industry was organized by the *Linz Center of Mechatronics (LCM)*, which in the COMET-K2 center *Symbiotic Mechatronics* conducts applied basic research projects together with company partners. These projects exhibit a high scientific share and a high implementation risk with a possibly high gain. Four presentations sharing the latest cooperative research with company partners were given by senior researchers of LCM and the corresponding papers are part of this book.

The participation of a total of 31 scientists from Austria, Russia, Taiwan, Germany, France and the U.S.A. led to fruitful scientific discussions among the participants, further deepening of long-lasting cooperations and friendships, and to the publication of this book.

Linz, Austria   Hans Irschik
Linz, Austria   Michael Krommer
Perm, Russia   Valerii P. Matveenko
St. Petersburg, Russia   Alexander K. Belyaev
December 2020

Acknowledgements

Contents

Contributors

Christoph Adam University of Innsbruck, Unit of Applied Mechanics, Technikerstr. 13, Innsbruck, Austria

Dietmar Adam TU Wien, Institute of Geotechnics, Karlsplatz 13/220/2, Vienna, Austria

Holm Altenbach Lehrstuhl für Technische Mechanik, Institut für Mechanik, Fakultät Maschinenbau, Otto-von-Guericke-Universität Magdeburg, Universitätsplatz 2, Magdeburg, Germany

Marcus Aßmus Lehrstuhl für Technische Mechanik, Institut für Mechanik, Fakultät Maschinenbau, Otto-von-Guericke-Universität Magdeburg, Universitätsplatz 2, Magdeburg, Germany

Olga M. Babeshko Kuban state University, Krasnodar, Russia

Vladimir A. Babeshko Southern Scientific Center Russian Academy of Sciences, Rostov-on-don, Russia

Alexander K. Belyaev Institute for Problems in Mechanical Engineering of RAS, St. Petersburg, Russia

Cheng-Yi Cao Department of Civil Engineering, National Yang Ming Chiao Tung University, Hsinchu, Taiwan

Galeb El Chabaan Research Unit of Structural Dynamics and Risk Assessment, Institute of Construction, Structural Dynamics and Building Technology, TU Wien, Vienna, Austria

L. Dozio DIMEAS, Politecnico di Milano, Milan, Italy

M. D'Ottavio LEME, Université Paris Nanterre, Nanterre, France

Andreas Eitzlmayr Linz Center of Mechatronics GmbH, Linz, Austria

Olga V. Evdokimova Southern Scientific Center Russian Academy of Sciences, Rostov-on-don, Russia

Nicole Gehring Institute of Automatic Control and Control Systems Technology, Johannes Kepler University Linz, Linz, Austria

E. S. Gorkunov Institute of Engineering Science, Ural Branch of the Russian Academy of Sciences, Ekaterinburg, Russia

Rainer Haas Linz Center of Mechatronics GmbH, Area Drives, Linz, Austria

Rudolf Heuer Research Unit of Structural Dynamics and Risk Assessment, Institute of Construction, Structural Dynamics and Building Technology, TU Wien, Vienna, Austria

Helmut J. Holl Institute of Technical Mechanics, Johannes Kepler University Linz, Linz, Austria

Martin Horn Christian Doppler Laboratory for Model Based Control of Complex Test Bed Systems, Institute of Automation and Control, Graz University of Technology, Graz, Austria

Alexander Humer Institute of Technical Mechanics, Johannes Kepler University Linz, Linz, Austria

Hans Irschik Institute of Technical Mechanics, Johannes Kepler University Linz, Linz, Austria

Nataliia A. Iurlova Institute of Continuous Media Mechanics Ural Branch of RAS, Perm, Russia

Bernhard Jakoby Institute for Microelectronics and Microsensors, Johannes Kepler University Linz, Linz, Austria

Stefan Jakubek TU Wien, Institute for Mechanics and Mechatronics, Vienna, Austria

Erwin Karer Linz Center of Mechatronics GmbH, Linz, Austria

Helmut Kogler Linz Center of Mechatronics GmbH, Linz, Austria

Bernd Kolar Institute of Automatic Control and Control Systems Technology, Johannes Kepler University Linz, Linz, Austria

Anastasiia A. Kostina Institute of Continuous Media Mechanics of the UB RAS, Perm, Russia

A. Krasnobrizha LEME, Université Paris Nanterre, Nanterre, France

Michael Krommer Institute of Technical Mechanics, Johannes Kepler University Linz, Linz, Austria

Karl Ladner Linz Center of Mechatronics GmbH, Linz, Austria

Peter Ladner Linz Center of Mechatronics GmbH, Linz, Austria

Astrid Leitner Institute of Automation and Control, Graz University of Technology, Graz, Austria

Chien-Ching Ma National Taiwan University, Taipei, Taiwan (R.O.C.)

Valerii P. Matveenko Institute of Continuous Media Mechanics Ural Branch of RAS, Perm, Russia

Martin Meindlhumer Institute of Technical Mechanics, Johannes Kepler University Linz, Linz, Austria

Nikita F. Morozov Petersburg State University, St. Petersburg, Russia

Dmitriy A. Oshmarin Institute of Continuous Media Mechanics Ural Branch of RAS, Perm, Russia

Ivan Paulmichl University of Innsbruck, Unit of Applied Mechanics, Technikerstr. 13, Innsbruck, Austria

Astrid S. Pechstein Institute of Technical Mechanics, Johannes Kepler University Linz, Linz, Austria

Kurt Pichler Linz Center of Mechatronics GmbH, Area Drives, Linz, Austria

Oleg A. Plekhov Institute of Continuous Media Mechanics of the UB RAS, Perm, Russia

O. Polit LEME, Université Paris Nanterre, Nanterre, France

Markus Reichhartinger Institute of Automation and Control, Graz University of Technology, Graz, Austria

Jakob Scheidl Institute of Mechanics and Mechatronics, TU Wien, Wien, Austria

Alexander Schirrer TU Wien, Institute for Mechanics and Mechatronics, Vienna, Austria

Johannes Schröck Linz Center of Mechatronics GmbH, Linz, Austria

Markus Schöberl Institute of Automatic Control and Control Systems Technology, Johannes Kepler University Linz, Linz, Austria

Ming-Hsiang Shih Department of Civil Engineering, National Chi Nan University, Nan-Tou, Taiwan

Victoria Simader Institute of Technical Mechanics, Johannes Kepler University Linz, Linz, Austria

Alois Steindl TU Wien, Institute for Mechanics and Mechatronics, Vienna, Austria

Wen-Pei Sung Department of Landscape Architecture, Integrated Research Center for Green Living Technologies, National Chin-Yi University of Technology, Taichung, Taiwan

Petr E. Tovstik Petersburg State University, St. Petersburg, Russia

Tatyana P. Tovstik Institute for Problems in Mechanical Engineering of RAS, St. Petersburg, Russia

S. Urushadze Institute of Applied and Theoretical Mechanics, Czech Academy of Sciences, Prague, Czech Republic

E. Valot LEME, Université Paris Nanterre, Nanterre, France

Alena I. Vedernikova Institute of Continuous Media Mechanics of the UB RAS, Perm, Russia

R. Vescovini DIMEAS, Politecnico di Milano, Milan, Italy

Yury Vetyukov Institute of Mechanics and Mechatronics, TU Wien, Wien, Austria

Johannes Wenninger Linz Center of Mechatronics GmbH, Linz, Austria

Judy P. Yang Department of Civil Engineering, National Yang Ming Chiao Tung University, Hsinchu, Taiwan

Y.-B. Yang School of Civil Engineering, Chongqing University, Chongqing, China; Department of Construction Engineering, National Yunlin University of Science and Technology, Yunlin, Taiwan

J. D. Yau Department of Architecture, Tamkang University, New Taipei City, Taiwan

Chapter 1
On Dynamic Optimality of Anti-Sandwiches

Marcus Aßmus and Holm Altenbach

Abstract From the viewpoint of structural engineering, natural frequencies and associated eigenmodes of Anti-Sandwiches are crucial points in the context of their dynamic behavior. Here we suggest a general format for dynamic analysis by employing an extended layerwise theory. A finite-element implementation ensures the efficiency of the general solution approach. The set of control variables initially consists of originally 14 geometry and material parameters. The nature of this input enables to bound the space of parameters affecting the eigenbehavior. Due to the lack of any generic measure for optimality, we determine optimal values of the reduced parameters and propose general optimality criteria.

1.1 Prologue

In contrast to sandwich structures, a so-called Anti-Sandwich consists of a three-layered composite structure with thick, shear-rigid skins and a thin, shear-soft core. They are widely applied as structural bearing elements, for example, laminated glasses [16] and photovoltaic modules [21]. In the context of the design, the main challenges are among others

- excellent stiffness properties resulting in small deflections,
- effective boundary conditions [23], and
- eigenbehavior

The first two items are well studied [5, 15, 21, 23]. The optimization of the eigenbehavior is in the focus of the present contribution. The eigenbehavior of Anti-Sandwiches can be modified by the manipulation of the

---

M. Aßmus (✉) · H. Altenbach
Lehrstuhl für Technische Mechanik, Institut für Mechanik, Fakultät Maschinenbau,
Otto-von-Guericke-Universität Magdeburg, Universitätsplatz 2, 39106 Magdeburg, Germany
e-mail: marcus.assmus@ovgu.de

H. Altenbach
e-mail: holm.altenbach@ovgu.de

Fig. 1.1 Eigenmode as a
result of experimental modal
analysis by the aid of Laser
Doppler velocimetry
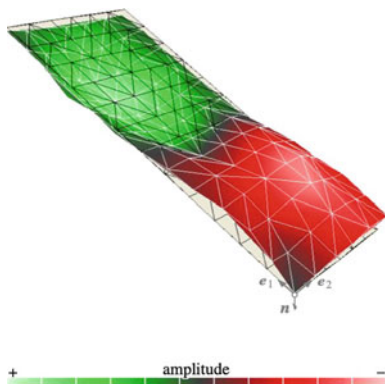
- material parameters,
- geometry parameters,
- damping properties of the core layer, and
- boundary conditions,

where K is a layer index. In the present treatise, the modification of these parameters
will be discussed from the point of view that the structural response should be outside
of any stimulus spectrum. For this purpose, the modal analysis is a powerful tool.
Figure 1.1 is representative of the results of an experimental modal analysis at Anti-
Sandwiches. Since experiments are usually very expensive, an alternative procedure
is beneficial.

A first analysis is often based on the analysis of the natural frequencies. In this
course, it is possible to reduce to geometry and material parameters when restricting
to one sample boundary condition. Considering Anti-Sandwiches, the parameters
are

- plane length dimensions $L_\alpha \ \forall \ \alpha \in \{1, 2\}$,
- layer thicknesses $h^K \ \forall \ K \in \{t, c, b\}$ (with overall thickness $H = \sum h^K$),
- Young's moduli $E^K \ \forall \ K \in \{t, c, b\}$,
- Poisson's ratios $\nu^K \ \forall \ K \in \{t, c, b\}$, and
- mass densities $\rho^K \ \forall \ K \in \{t, c, b\}$.

Herein, we make use of superscript designators t, c, b for top, core, and bottom layers
of the (three-layered) Anti-Sandwich, cf. Figure 1.3. When reviewing the relevant
literature on such structural elements, one will find a wide but restricted domain
wherein preceding parameters can be located. An overview is given in Fig. 1.2. There,
the superscript index s is used representatively for the skin layers (t, b). However, as
is typically for Anti-Sandwiches, we can state the following characteristic properties,
which are also exploited in the present work.
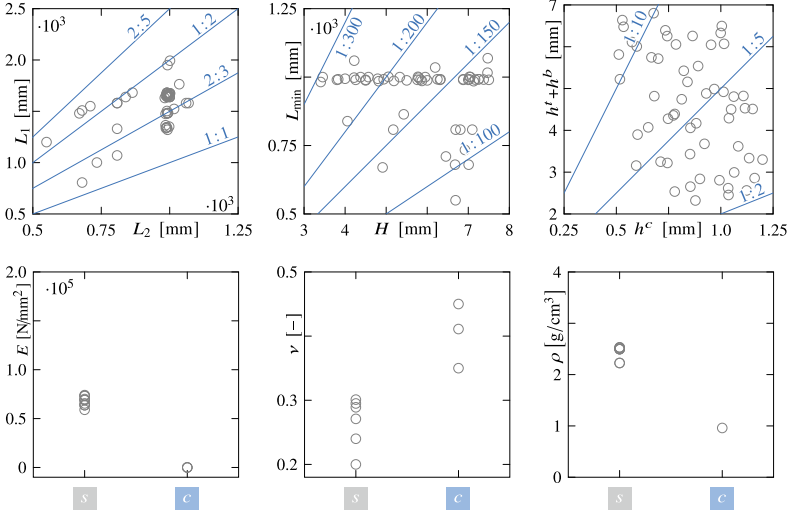
Fig. 1.2 Geometric and material variety of Anti-Sandwiches, data taken from [4]

$$L_1 \approx L_2 \tag{1.1a}$$

$$L_\alpha \gg H \tag{1.1b}$$

$$h^s \gg h^c \tag{1.1c}$$

$$G^s \gg G^c \tag{1.1d}$$

$$Z^s \gg Z^c \tag{1.1e}$$

$$\rho^s \gg \rho^c \tag{1.1f}$$

Herein, the shear modulus $G^K = E^K(2 + 2\nu^K)^{-1} \ \forall K \in \{c, s\}$ is used due to the isotropy assumed for present materials. Furthermore, $Z^K = G^K h^K \ \forall K \in \{c, s\}$ is a simple measure for the transverse shear sensitivity.

1.2 Theoretical Issues

Anti-Sandwiches are complex systems. Let us make the following model assumption allowing a simplified modeling for the analysis of the eigenbehavior of such structures. The assumed cross-section is shown in Fig. 1.3. As it was shown in previous papers [21], in dependence of the material and geometry parameters, different theories can be applied for the analysis. The simplest one is the classical layered plate theory [2]. This is an analogy to Kirchhoff's plate theory. As usual, this approach failed in the case of sandwich structures. A refined approach is related to the so-called first-order shear deformable theory [2]. Now the transverse shear is taken into account which is helpful in the case of classical sandwich structures. But even in
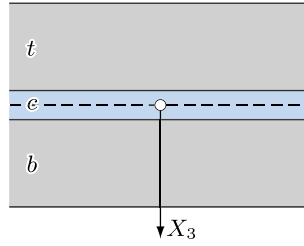
Fig. 1.3 Cross section of the assumed composite structure (*t*—top layer, *c*—core layer, *b*—bottom layer)
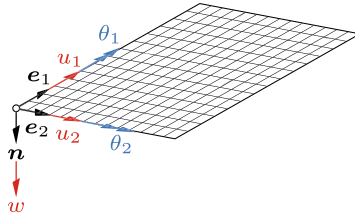
Fig. 1.4 Coordinate system and degrees of freedom of the five-parameter plate continuum (e_α, n—orthonormal base of the coordinate system, u_α—in-plane displacements, w—deflection, θ_α—rotations)

the case of a non-standard shear correction [1] some ratios of the above-mentioned parameters do not allow a correct analysis of Anti-Sandwiches. Better results one can get applying the extended layerwise theory suggested in [18]. This theory is based on the assumed cross section (Fig. 1.3), but in the first step, each layer of the three-layered composite structure is modeled separately with the help of a five-parameter plate continuum per layer based on the direct approach [3, 13, 24]. Within this theory, five independent degrees of freedom (three translational and two rotational) are used as shown in Fig. 1.4. The cross-sectional kinematic assumptions are similar to Mindlin's theory [17] for every layer separately [5]. In addition, it is assumed that

- geometrical symmetry in transverse direction w.r.t. midplane of the cross section,
- geometrically and physically linear setting,
- isotropic elastic materials,
- decoupled deformation states,
- layers are rigidly connected, and
- layers have a constant thickness.

The following statements are based on previous works performed at the Martin Luther Universität Halle-Wittenberg and the Otto von Guericke Universität Magdeburg during the last decade. The core layer behavior analysis, three-point bending tests and experimental validation to theories were presented in [8–10, 20–23]. The theoretical basics are given in [21, 23] for layerwise beams, in [18] for layerwise plates, and in [19] for layerwise shells. Solutions were presented as closed-form solu-
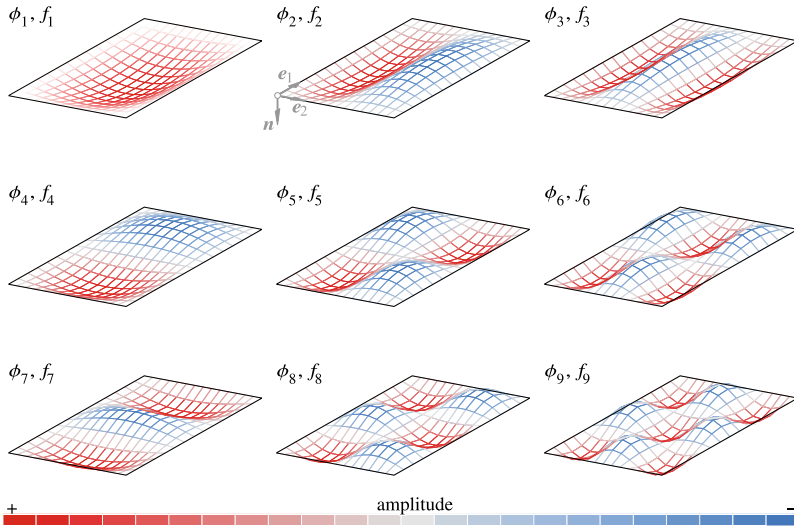
Fig. 1.5 Nine eigenform shapes ϕ_i and corresponding natural frequencies $f_i \ \forall \, i \in \{1, \ldots, 9\}$

tions in [18], computational solution strategies were introduced in [4, 5, 15]. Last but not least, application were shown for coupling with three-dimensional models in [11], for natural loading scenarios in [6] and w.r.t. borders, frontiers and limits in [7, 12, 14].

In the context of the computational solution strategy to analyze the eigenbehavior, [4, 5] introduced a special finite-element which incorporates all the degrees of freedom for all layers. The approach was implemented into the finite-element program system ABAQUS® by using a "user element" (UEL) subroutine. We denominate this computational approach FE-XLWT. The strategy developed proves itself to be particularly efficient. It has emerged as a powerful tool to analyze general three-layered composite structures [12, 14]. Examples of computational results gained are presented in Fig. 1.5.

1.3   Optimal Parameter Basis

For the determination of the structural eigenbehavior of Anti-Sandwiches, it is advantageous to analyze the natural frequencies for different geometrical and material compositions. In general, for three-layered composite structures, the parameter space is defined by a set $\mathcal{S}$ of 14 parameters. To be exact, these are five geometries

$$\mathcal{S}_{\text{geo}} := \{L_1, L_2, h^t, h^c, h^b\}, \tag{1.2}$$

and nine material parameters

$$\mathcal{S}_{\mathrm{mat}} := \{E^t, E^c, E^b, v^t, v^c, v^b, \rho^t, \rho^c, \rho^b\}, \tag{1.3}$$

while $\mathcal{S} = \mathcal{S}_{\mathrm{geo}} \cup \mathcal{S}_{\mathrm{mat}}$ holds. Since Anti-Sandwiches can be assigned to the genus of symmetric composite structures, i.e.,

$$h^t = h^b \qquad\qquad E^t = E^b \qquad\qquad v^t = v^b \qquad\qquad \rho^t = \rho^b \tag{1.4}$$

hold, the number of parameters reduces to 10. The reduced set of parameters is summarized as follows:

$$\mathcal{S}_{\mathrm{red}} := \{L_1, L_2, h^s, h^c, E^s, E^c, v^s, v^c, \rho^s, \rho^c\}, \tag{1.5}$$

while we make use of the superscript index s for the parameters of the skin layers. Another reduction of this set is based on significant ratios introduced for Anti-Sandwiches, cf. [12]. These are the thickness ratio TR, the length ratio LR, the thickness to length ratio TLR, the shear modulus ratio GR, and the mass density ratio MDR.

$$TR = \frac{h^c}{2h^s} \tag{1.6a}$$

$$LR = \frac{L_2}{L_1} \tag{1.6b}$$

$$TLR = \frac{H}{L_{\mathrm{min}}} \tag{1.6c}$$

$$GR = \frac{G^c}{G^s} \tag{1.6d}$$

$$MDR = \frac{\rho^c}{\rho^s} \tag{1.6e}$$

Obviously, ratios (1.6a), (1.6b), and (1.6c) refer to geometry parameters, while (1.6d) and (1.6e) pertain on material parameters. Following the literature review of [4], we can limit the parameter ranges due to practical applications at products available on the market.

$$TR \approx 0.125\ldots0.45 \quad LR \approx 0.25\ldots1 \quad TLR \approx 2\cdot10^{-3}\ldots1.4\cdot10^{-2}$$
$$GR \approx 7\cdot10^{-6}\ldots1.5\cdot10^{-2} \quad MDR \approx 4\cdot10^{-2}\ldots1$$

These restrictions are naturally based on the possible ranges of the set of original parameters (1.5). As a result, the new set is bounded by five parameters.

$$\mathcal{S}_{\mathrm{bound}} := \{TR, LR, TLR, GR, MDR\}, \tag{1.7}$$
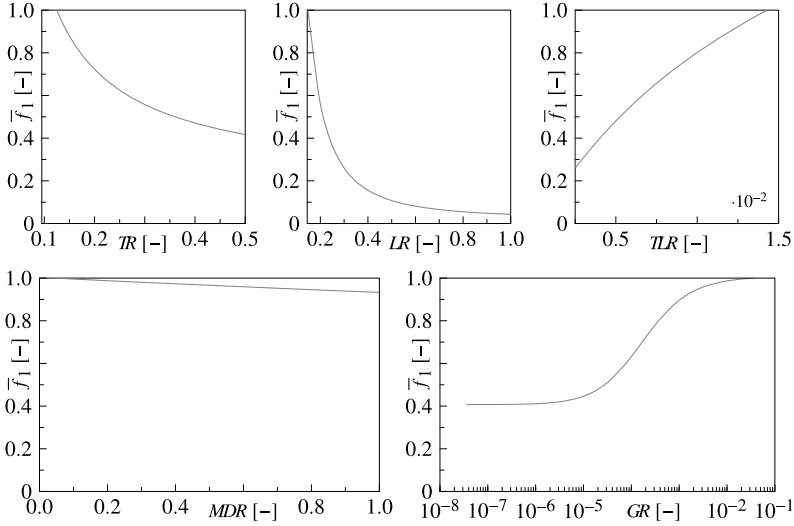
Fig. 1.6 Normalized first natural frequency in dependence of the bounded set of parameters $\mathcal{S}_{\text{bound}}$

In the sequel, these parameters are varied systematically to study their influence on the structural behavior. For the ease of evaluation, we make use of the natural frequency of the first fundamental mode $f_1 = \min(f_i)$ solely. There is a dependency on the set of reduced parameters.

$$f_1 = \mathfrak{F}(\mathcal{S}_{\text{red}}) \tag{1.8}$$

In present case, this dependence is sufficiently described the set of bounded parameters.

$$f_1 = \mathfrak{H}(\mathcal{S}_{\text{bound}}) \tag{1.9}$$

For reasons of comparability, we normalize this criteria.

$$\bar{f}_1(\square) = \frac{f_1(\square)}{\max[f_1(\square)]} \qquad \forall \square \in \{TR, LR, TLR, GR, MDR\} \tag{1.10}$$

In the present investigations, the parameters were varied individually. Resulting functional relationships are depicted in Fig. 1.6. A thorough discussion of these results is given in [4, 5].

Following the results generated, subsequent universal implications for the five reduced parameters for a low first natural frequency can be drawn.

1. *TR* high   2. *LR* high   3. *TLR* small   4. *MDR* high   5. *GR* small

By the aid of these five statements, engineers are able to estimate and regulate the vibration sensitivity, at least in the context of the product development process.

1.4 A General Optimality Criteria

Instead of working with five parameters and find optima for every parameter separately, it is our aim to establish a generic measure to achieve a general representation of the problem. For this purpose, we introduce a general parameter ratio $0 \leq S \leq 1$.

$$S \overset{\wedge}{=} \overline{\square} \quad \text{with } \overline{\square} = \frac{\square - \min(\square)}{\max(\square) - \min(\square)} \quad \forall \square \in \{TR, LR, TLR, GR, MDR\} \quad (1.11)$$

Herein, S is correlated with the structural stiffness. Based on this measure, we make use of an equally weighted normalized first natural frequency $0 \leq f_g \leq 1$. This results in a regularized function $f_g(S)$.

$$f_g(S) = \frac{1}{n} \sum_{\alpha=1}^{n} \bar{f}_1(\overline{\square}) \quad \forall \bar{\square} \in \{\overline{TR}, \overline{LR}, \overline{TLR}, \overline{GR}, \overline{MDR}\} \quad (1.12)$$

With the aid of this generic measure, it is possible to reduce the multidimensional problem.

For the set of results depicted in Fig. 1.6, this yields the function visualized in Fig. 1.7. Due to the normalizations that have been introduced, this graph has general validity, at least in the context of Anti-Sandwiches in the applied boundary conditions. Obviously, we can identify a minimum and a maximum value in the range of S. The maximum is at $S = 0.01$, while the minimum is to be found at $S = 0.36$.

The goal of the generic measure S is to have a single parameter for evaluation. Based on this parameter, it is now possible to find sets of parameters (TR, LR, TLR, MDR, GR as well as E^K, ν^K, ρ^K, L_α, h^K) for optimal S. In the present case, this reads as follows.

Fig. 1.7 Results for regularized function $f_g(S)$ with minimum and maximum
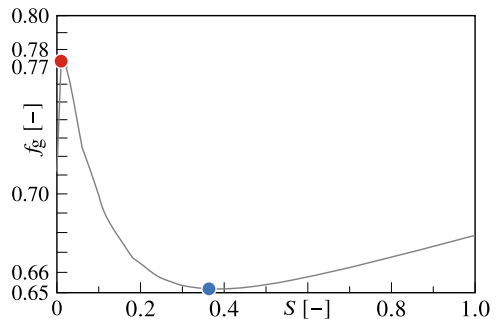
$$S_{\text{opt}} = S[\min(f_{\text{g}})] \tag{1.13}$$

Such optima, however, can be found by different algorithms. Here, the constraints on the set of parameters (1.5) depicted in Fig. 1.2 are decisive. Ultimately, this results in a variety of combinations of these parameters which fulfill the generalized optimality criteria. Thereby, every combination consists of a concrete specification of the parameters in $\mathcal{S}_{\text{red}}$.

1.5 Epilogue

In the present work, we have proposed general optimality criteria for the dynamic behavior of Anti-Sandwiches by introducing a single measure which incorporates geometry and material properties and thus describes the structural stiffness. The analysis is based on an effective and efficient approach to determine eigenbehavior of Anti-Sandwiches by the utilization of the extended layerwise theory and a computational finite-element implementation based thereon. Significant geometry and material ratios are introduced based on dimensional analysis, which reduced the parameter space considerably. In the present context, the first natural frequency is consulted as a representative sensitivity parameter for the eigenbehavior. Several variant calculations are performed to determine optimal values of the ratios introduced. In sequence, a general representation to assess an optimal eigenbehavior is established. In contrast to the previous procedure, it is thus possible to generate a large number of combinations of the original parameter set. This routine is solely limited by the physical restrictions in the possible parameters for geometry and material. On the other hand, such restrictions help to reduce the number of possible sets.

Finally, the task of selecting and applying an optimization algorithm to generate specific datasets remains open whereby finding the minimum or maximum of a function in many variables is one of the most common problems in numerical computing. Such an algorithm is then to be coupled to FE-XLWT for efficient computational analyses of parameter sets.

References

1. Altenbach, H.: An alternative determination of transverse shear stiffnesses for sandwich and laminated plates. Int. J. Solids Struct. **37**(25), 3503–3520 (2000). https://doi.org/10.1016/S0020-7683(99)00057-8
2. Altenbach, H., Altenbach, J., Kissing, W.: Mechanics of Composite Structural Elements, 2nd edn. Springer (2018). https://doi.org/10.1007/978-981-10-8935-0
3. Altenbach, H., Zhilin, P.: A general theory of elastic simple shells (in russ.). Adv. Mech. **11**(4), 107–148 (1988)
4. Aßmus, M.: Global structural analysis at photovoltaic-modules: theory, numerics, application (in german). Dissertation thesis, Otto von Guericke University Magdeburg (2018)

5. Aßmus, M.: Structural Mechanics of Anti-Sandwiches—An Introduction. SpringerBriefs in Continuum Mechanics. Springer International Publishing (2019). https://doi.org/10.1007/978-3-030-04354-4

6. Aßmus, M., Bergmann, S., Eisenträger, J., Naumenko, K., Altenbach, H.: Consideration of non-uniform and non-orthogonal mechanical loads for structural analysis of photovoltaic composite structures. In: Altenbach, H., Goldstein, R.V., Murashkin, E. (eds.) Mechanics for Materials and Technologies, Advanced Structured Materials, vol. 46, pp. 73–122. Springer, Singapore (2017). https://doi.org/10.1007/978-3-319-56050-2_4

7. Aßmus, M., Bergmann, S., Naumenko, K., Altenbach, H.: Mechanical behaviour of photovoltaic composite structures: a parameter study on the influence of geometric dimensions and material properties under static loading. Compos. Commun. **5**, 23–26 (2017). https://doi.org/10.1016/j.coco.2017.06.003

8. Aßmus, M., Jack, S., Köhl, M., Weiß, K.A.: Dynamic mechanical loads on pv-modules. In: Proceedings of the 24th European Photovoltaic Solar Energy Conference, pp. 3395–3397. Hamburg, Germany (2009). https://doi.org/10.4229/24thEUPVSEC2009-4AV.3.34

9. Aßmus, M., Jack, S., Weiss, K.A., Koehl, M.: Measurement and simulation of vibrations of PV-modules induced by dynamic mechanical loads. Prog. Photovolt. Res. Appl. **19**(6), 688–694 (2011). https://doi.org/10.1002/pip.1087

10. Aßmus, M., Köhl, M.: Experimental investigation of the mechanical behavior of photovoltaic modules at defined inflow conditions. J. Photon. Energy **2**(1), 1–11 (2012). https://doi.org/10.1117/1.JPE.2.022002

11. Aßmus, M., Naumenko, K., Altenbach, H.: A multiscale projection approach for the coupled global-local structural analysis of photovoltaic modules. Compos. Struct. **158**(-), 340–358 (2016). https://doi.org/10.1016/j.compstruct.2016.09.036

12. Aßmus, M., Naumenko, K., Altenbach, H.: Mechanical behaviour of photovoltaic composite structures: influence of geometric dimensions and material properties on the eigenfrequencies of mechanical vibrations. Compos. Commun. **6**, 59–62 (2017). https://doi.org/10.1016/j.coco.2017.10.003

13. Aßmus, M., Naumenko, K., Altenbach, H.: Subclasses of mechanical problems arising from the direct approach for homogeneous plates. In: Altenbach, H., Chróścielewski, J., Eremeyev, V.A., Wiśniewski, K. (eds.) Recent Developments in the Theory of Shells, Advanced Structured Materials, vol. 110, pp. 43–63. Springer, Singapore (2019). https://doi.org/10.1007/978-3-030-17747-8_4

14. Aßmus, M., Naumenko, K., Öchsner, A., Eremeyev, V.A., Altenbach, H.: A generalized framework towards structural mechanics of three-layered composite structures. Technische Mechanik **39**(2), 202–219 (2019). https://doi.org/10.24352/UB.OVGU-2019-019

15. Eisenträger, J., Naumenko, K., Altenbach, H., Meenen, J.: A user-defined finite element for laminated glass panels and photovoltaic modules based on a layer-wise theory. Compos. Struct. **133**, 265–277 (2015). https://doi.org/10.1016/j.compstruct.2015.07.049

16. Ivanov, I.V.: Analysis, modelling, and optimization of laminated glasses as plane beam. Int. J. Solids Struct. **43**(22), 6887–6907 (2006). https://doi.org/10.1016/j.ijsolstr.2006.02.014

17. Mindlin, R.D.: Influence of rotatory inertia and shear on flexural motions of isotropic, elastic plates. ASME J. Appl. Mech. **18**, 31–38 (1951)

18. Naumenko, K., Eremeyev, V.A.: A layer-wise theory for laminated glass and photovoltaic panels. Compos. Struct. **112**, 283–291 (2014). https://doi.org/10.1016/j.compstruct.2014.02.009

19. Naumenko, K., Eremeyev, V.A.: A layer-wise theory of shallow shells with thin soft core for laminated glass and photovoltaic applications. Compos. Struct. **178**, 434–446 (2017). https://doi.org/10.1016/j.compstruct.2017.07.007

20. Sander, M., Ebert, M.: Vibration analysis of pv modules by laser-doppler vibrometry. In: Proceedings of the 24th European Photovoltaic Solar Energy Conference, pp. 3446–3450. Hamburg, Germany (2009). https://doi.org/10.4229/24thEUPVSEC2009-4AV.3.46

21. Schulze, S.H., Pander, M., Naumenko, K., Altenbach, H.: Analysis of laminated glass beams for photovoltaic applications. Int. J. Solids Struct. **49**(15–16), 2027–2036 (2012). https://doi.org/10.1016/j.ijsolstr.2012.03.028

22. Weiß, K.A., Aßmus, M., Jack, S., Köhl, M.: Measurement and simulation of dynamic mechanical loads on pv-modules. In: Proceedings of the International Society for Optical Engineering (Reliability of Photovoltaic Cells, Modules, Components, and Systems II), vol. 7412, p. 03. San Diego, USA (2009). https://doi.org/10.1117/12.824859
23. Weps, M., Naumenko, K., Altenbach, H.: Unsymmetric three-layer laminate with soft core for photovoltaic modules. Compos. Struct. **105**, 332–339 (2013). https://doi.org/10.1016/j.compstruct.2013.05.029
24. Zhilin, P.A.: Mechanics of deformable directed surfaces. Int. J. Solids Struct. **12**(9), 635–648 (1976). https://doi.org/10.1016/0020-7683(76)90010-X

Chapter 2
On a New Model for Predicting Landslide Events

Vladimir A. Babeshko, Olga V. Evdokimova, and Olga M. Babeshko

Abstract A mathematical model of the most poorly studied pre-landslide structure, called horizontally propagating, is constructed. The spatial pre-landslide structure occupies an unbounded cylindrical area with the third quadrant in the cross section. It is filled with a medium described by the anisotropic Helmholtz equation, which is extremely fluid among other water-saturated media. Taking into account the physical and mechanical properties of the pre-slide structure, it is a vertical deformable containment wall with a deformable horizontal coating. To construct a model that is adequately formulated, we consider the boundary value problem for the three-dimensional Helmholtz equation in the specified region, taking into account the presence of deformable walls and coatings. The block element method is used to construct an exact solution of the boundary problem for the accepted coatings on the membrane boundary. The properties of the constructed model are investigated.

2.1 Introduction

Landslides and mudslides are among the most difficult to predict processes that cause huge damage to society, both material and related to victims. The complexity of predicting the events of these phenomena is associated with a large complex of physical, mechanical, hydro-mechanical, rheological, and plastic phenomena that are closely intertwined with the geometric parameters of terrain and landscape areas. This circumstance does not allow, except for certain special cases, to build a strictly

V. A. Babeshko (✉) · O. V. Evdokimova
Southern Scientific Center Russian Academy of Sciences, Chekhov str., 41, 344006
Rostov-on-don, Russia
e-mail: babeshko41@mail.ru

O. V. Evdokimova
e-mail: evdokimova.olga@mail.ru

O. M. Babeshko
Kuban state University, ul. Stavropolskaya, 149, 350040 Krasnodar, Russia
e-mail: babeshko49@mail.ru

justified mathematical theory and model of these processes. Creating a theory and models of these phenomena will allow you to get enough reliable data about the processes occurring in the zone that is dangerous for landslides, and to evaluate the steps that allow you to regularly initiate landslides or prevent them. The slow progress in modeling landslide events was largely due to the lack of a convenient mathematical apparatus for this purpose. Currently, there is some progress in this direction due to the creation of the block element method, which makes it possible to model complex processes described by linear and nonlinear boundary value problems for systems of high-order partial differential equations. Mathematically, this section of continuum mechanics is one of the most complex and least developed sections of mixed problems that have not been completely solved.

Often, these problems were presented with an extremely simplified task, which assumed that a particular task was being considered only the spreading environment, without assessing the conditions for the occurrence of such phenomena. The areas occupied by the environment were assumed to be the simplest. Only a small number of studies are devoted to attempts to account for the deformability of both the internal mass of the pre-landslide structure and the restraining coatings. This article uses a new block element method developed in Russia at the Kuban State University. Among the ten types of pre-landslide structures, a model of the least studied type, called horizontally propagating, is constructed. The area of this type of pre-landslide structure is a vertical containment wall with a horizontal coating. In this area, the landslide mass is concentrated, which is a softened fluid water-saturated medium. The limiting case of its greatest fluidity is the anisotropic model described by the anisotropic Helmholtz equation. The wall and coating are deformable and prevent the mass from spreading. At the beginning of the landslide process, either a break in the vertical wall or a break in the top cover occurs. The problem is considered as close as possible to the real one. The deformation of all contacting objects is taken into account, and the medium has a rheology, the ultimate fluidity, described by the anisotropic Helmholtz equation. In addition, taking into account that the beginning of the landslide process can be triggered by an external dynamic influence, the possibility of its presence on the coating and wall at a harmonic vibration with an arbitrary frequency is considered.

Currently, a strict theory of block structures has been developed, which is based on the block element method. Its advantage is the ability to investigate boundary value problems in almost any field since any object or structure can be considered as a real or virtual block structure. At the same time, there are few cases of applying this theory to real problems, which makes it difficult to use it in applied problems. In this paper, this approach is applied to the Helmholtz equation often used in applications in the area of a three-dimensional rectangular wedge in the presence of arbitrary boundary conditions. Despite the simplicity of the problem statement, the authors did not find a General solution to this boundary value problem. It should be noted that a large number of papers are devoted to the study of the Helmholtz equation arising in various fundamental and applied problems.

First of all, these are works in layered areas [1], where the method of integral transformations is used for research and a fairly complete list of cited literature in

this area of research is provided. In [2, 3], a ray method was developed and applied that is effective at high frequencies in boundary value problems in arbitrary domains, including for the Helmholtz equation.

In [4–7], a method is developed for presenting solutions to boundary value problems in the theory of elasticity of thermoelectroelasticity and poronasaturated Bio media using solutions of the Helmholtz equation. In [8–11], boundary problems for the Helmholtz and Laplace equations are investigated in hydrodynamics problems, in particular, the behavior of ice floes and plates on the liquid surface, and their acoustic properties. In [11], we consider the plane problem of hydrodynamics in a rectangular wedge. The author finds an original method for studying a boundary problem in a rectangular wedge by reducing it to a problem in half-space, using a mirror image of the boundary problem on a symmetrical rectangular wedge. There are other works in which researchers move away from solving the boundary value problem in a rectangular wedge by using mirror reflections and moving to a layered environment.

At the same time, the authors did not meet any studies and exact solutions of the three-dimensional Helmholtz equation in the form of packed block elements under arbitrary boundary conditions in the region of an unbounded rectangular wedge type. The possibility of studying these problems is described in [12, 13]. In this paper, we consider a three-dimensional Neumann boundary value problem for the Helmholtz equation, for which solutions for arbitrary boundary conditions are constructed using the block element method. The solution is constructed in integral form in a wedge-shaped area in the form of packed and unpacked block elements. The block element method is quite simple to use and can be used to investigate more complex problems.

2.2 Problem Statement

Let's take a rectangular coordinate system, pointing the axes x_1, ox_3 horizontally, and the axis x_2 vertically upward, see the figure. The boundary problem for the three-dimensional Helmholtz equation in a rectangular region $\Omega(|x_3| \leq \infty, x_1 \leq 0, x_2 \leq 0)$ is considered under conditions of harmonic effects. The Neumann conditions are set at the boundaries of the region Ω. Problems of this kind arise when studying the acoustic properties of unbounded areas of the wedge type, as well as when preparing initial data for the study of more complex boundary value problems for the Lame, Navier–Stokes, Maxwell, and others equations in such areas. Building solutions in the form of packed block elements is a necessary part of research when studying block structures. The specified boundary problem in a bounded area, a rectangle, was considered in [14], where pseudo-differential equations were constructed using the block element method, with the introduction of a tangent bundle of the boundary. We present one of them for the boundary value problem

$$\left[A_{11}\partial^2 x_1 + A_{22}\partial^2 x_2 + A_{33}\partial^2 x_3 + A\right]\phi(x_1, x_2, x_3) = 0$$

$$K_1 \Phi_1 = \int\limits_{-a}^{a} \int\limits_{-c}^{c} A_{33} \left(\phi'_{13} - i\alpha_3^1 \phi_1\right) \exp i \left[\alpha_1^1 \eta_1^1 + \alpha_2^1 \eta_2^1\right] d\eta_1^1 d\eta_2^1$$

$$+ \int\limits_{-c}^{c} \int\limits_{-b}^{b} A_{11} \left(\phi'_{22} + i\alpha_1^1 \phi_2\right) \exp i \left[-\alpha_1^1 a + \alpha_2^1 x_2^2 + \alpha_3^1 \left(x_1^2 - b\right)\right] dx_1^2 dx_2^2$$

$$+ \int\limits_{-a}^{a} \int\limits_{-c}^{c} A_{33} \left(\phi'_{33} + i\alpha_3^1 \phi_3\right) \exp i \left[-\alpha_1^1 x_1^3 + \alpha_2^1 x_2^3 - \alpha_3^1 2b\right] dx_1^3 dx_2^3$$

$$- \int\limits_{-c}^{c} \int\limits_{-b}^{b} A_{11} \left(\phi'_{43} - i\alpha_1^1 \phi_4\right) \exp i \left[\alpha_1^1 a + \alpha_2^1 x_2^4 - \alpha_3^1 \left(x_1^4 + b\right)\right] dx_1^4 dx_2^4$$

$$+ \int\limits_{-a}^{a} \int\limits_{-b}^{b} A_{22} \left(\phi'_{53} + i\alpha_2^1 \phi_5\right) \exp i \left[\alpha_1^1 x_1^5 - \alpha_2^1 c + \alpha_3^1 \left(x_2^5 - b\right)\right] dx_1^5 dx_2^5$$

$$+ \int\limits_{-a}^{a} \int\limits_{-b}^{b} A_{22} \left(\phi'_{63} - i\alpha_2^1 \phi_6\right) \exp i \left[-\alpha_1^1 x_1^6 + \alpha_2^1 c + \alpha_3^1 \left(x_2^6 - b\right)\right] dx_1^6 dx_2^6 \quad (2.1)$$

Here, a, b, c constants define a rectangle that is bounded if all constants are bounded, or semi-bounded if there are infinite constants among them.

In this paper, we use a variant of the block element method based on binding local coordinate systems to a single coordinate system, which, due to the shape of the area Ω, allows us to perform the study more clearly. The three-dimensional anisotropic Helmholtz equation with a reduced time multiplier is considered below $e^{-i\omega t}$

$$\left[\partial^2 x_1 + \partial^2 x_2 + A_{33}\partial^2 x_3 + Ap^2\right] u(x_1, x_2, x_3) = 0$$

in the region $\Omega (|x_3| \leq \infty, \ x_1 \leq 0, \ x_2 \leq 0)$. Here p it can be a complex number.

To apply the block element method to a boundary value problem in a block structure, you must perform three algorithms: external algebra, external analysis, and factor topology construction. Because only one block element is considered, the latter algorithm is no longer necessary.

Consider the Neumann boundary value problem for this equation.

We assume that the boundary conditions have the form

$$\frac{\partial u(0, x_2, x_3)}{\partial x_1} = f_2(x_2, x_3), \quad \frac{\partial u(x_1, 0, x_3)}{\partial x_2} = f_1(x_1, x_3)$$

Here, f_n arbitrary functions have properties sufficient for the solvability of the corresponding boundary problems in the spaces of slowly growing generalized functions, which will be discussed below. Since the region Ω contains infinitely distant points, if wave functions appear in the boundary problem, a solution is sought using the radiation principle.

By applying the Fourier transform to the differential equation for a parameter, we obtain a differential equation with a parameter of the form

$$\left(\partial^2 x_1 + \partial^2 x_2 + k^2\right) u(x_1, x_2, \alpha_3) = 0, \quad k^2 = Ap^2 - A_{33}\alpha_3^2$$

2.3 Method of Solution

Using one of the methods of tangent stratification of the boundary in the region, taking into account the adoption of a single coordinate system, after using the two-dimensional Fourier transform and introducing external forms, we come to a functional equation of the form:

$$(\alpha_1^2 + \alpha_2^2 + k^2)U(\alpha_1, \alpha_2, \alpha_3) = \int_{\partial\Omega} \omega$$

$$\omega = \frac{\partial u(0, x_2, \alpha_3)}{\partial x_1} e^{i\alpha_2 x_2} \, dx_2 - i\alpha_1 u(0, x_2, \alpha_3)e^{i\alpha_2 x_2} \, dx_2$$
$$+ \frac{\partial u(x_1, 0, \alpha_3)}{\partial x_2} e^{i\alpha_1 x_1} \, dx_1 - i\alpha_2 u(x_1, 0, \alpha_3)e^{i\alpha_1 x_1} \, dx_1$$

Notation is accepted here

$$U(\alpha_1, \alpha_2, \alpha_3) = \iiint_{\Omega} u(x_1, x_2, x_3)e^{i\langle\alpha x\rangle} \, dx_1 \, dx_2 \, dx_3,$$

$$\langle\alpha x\rangle = \alpha_1 x_1 + \alpha_2 x_2 + \alpha_3 x_3, \tag{2.2}$$

$$u(x_1, x_2, x_3) = \frac{1}{8\pi^3} \iiint_{R^3} U(\alpha_1, \alpha_2, \alpha_3)e^{-i\langle\alpha x\rangle} \, d\alpha_1 \, d\alpha_2 \, d\alpha_3$$

Taking into account the type of the coordinate system, the right part of the functional equation can be represented in the form

$$\int_{\partial\Omega} \omega = \int_{-\infty}^{0} \frac{\partial u(0, x_2, \alpha_3)}{\partial x_1} e^{i\alpha_2 x_2} \, dx_2 - i\alpha_1 \int_{-\infty}^{0} u(0, x_2, \alpha_3)e^{i\alpha_2 x_2} \, dx_2$$
$$+ \int_{-\infty}^{0} \frac{\partial u(x_1, 0, \alpha_3)}{\partial x_2} e^{i\alpha_1 x_1} \, dx_1 - i\alpha_2 \int_{-\infty}^{0} u(x_1, 0, \alpha_3)e^{i\alpha_1 x_1} \, dx_1$$

After calculating the one-dimensional integrals, which are Fourier transforms of the corresponding functions, we can present the functional equation in the form:

$$(\alpha_1^2 + \alpha_2^2 - k^2)U(\alpha_1, \alpha_2, \alpha_3) = \frac{\partial U(0, \alpha_2, \alpha_3)}{\partial x_1} - i\alpha_1 U(0, \alpha_2, \alpha_3)$$

$$+ \frac{\partial U(\alpha_1, 0, \alpha_3)}{\partial x_2} - i\alpha_2 U(\alpha_1, 0, \alpha_3) \quad (2.3)$$

In the future, the uppercase letter will denote the Fourier transforms calculated from the functions represented by the corresponding lowercase letter. We add the values of functions (2.1) to the right side of the functional equation (2.3), after calculating the Fourier transforms for all coordinates. Have

$$(\alpha_1^2 + \alpha_2^2 - k^2)U(\alpha_1, \alpha_2, \alpha_3)$$
$$= F_2(\alpha_2, \alpha_3) - i\alpha_1 U(0, \alpha_2, \alpha_3) + F_1(\alpha_1, \alpha_3) - i\alpha_2 U(\alpha_1, 0, \alpha_3)$$

To perform the external analysis algorithm, we factor the coefficient of the functional equation for each parameter, which is trivial in this case

$$(\alpha_1^2 + \alpha_2^2 - k^2) = (\alpha_1 - \alpha_{1-})(\alpha_1 + \alpha_{1-}) = (\alpha_2 - \alpha_{2-})(\alpha_2 + \alpha_{2-})$$

$$\alpha_{1-} = -i\sqrt{\alpha_2^2 - k^2}, \quad \alpha_{2-} = -i\sqrt{\alpha_1^2 - k^2}, \quad \operatorname{Im}\alpha_{1-} \le 0, \quad \operatorname{Im}\alpha_{2-} \le 0$$

The automorphism condition for the carrier and functions on it leads to pseudo-differential equations of the form [14]

$$F_2(0, \alpha_{2-}, \alpha_3) - i\alpha_1 U(0, \alpha_{2-}, \alpha_3) + F_1(\alpha_1, 0, \alpha_3) - i\alpha_{2-}U(\alpha_1, 0, \alpha_3) = 0$$

$$F_2(0, \alpha_2, \alpha_3) - i\alpha_{1-}U(0, \alpha_2, \alpha_3) + F_1(\alpha_{1-}, 0, \alpha_3) - i\alpha_2 U(\alpha_{1-}, 0, \alpha_3) = 0$$

The unknowns in the pseudo-differential equation are the functions and functions

$$U(0, \alpha_2, \alpha_3), \quad U(\alpha_1, 0, \alpha_3), \quad U(0, \alpha_{2-}, \alpha_3), \quad U(\alpha_{1-}, 0, \alpha_3)$$

The solution of pseudo-differential equations is searched for with the requirement of zero conversions outside the domain of boundary value problem solutions. This leads, after transformations, to the following kind of functional equation

$$(\alpha_1^2 + \alpha_2^2 - k^2)U(\alpha_1, \alpha_2, \alpha_3)$$
$$= \frac{1}{\alpha_{1-}\alpha_{2-}}\langle(\alpha_{2-} - \alpha_2)\left[\alpha_{1-}F_1(\alpha_1, \alpha_3) - \alpha_1 F_1(\alpha_{1-}, \alpha_3)\right]$$
$$+ (\alpha_{1-} - \alpha_1)\left[\alpha_{2-}F_2(\alpha_2, \alpha_3) - \alpha_2 F_2(\alpha_{2-}, \alpha_3)\right]\rangle$$

Then the solution in Fourier transforms representing a packed block element takes the form

$$U(\alpha_1, \alpha_2, \alpha_3) = \frac{1}{(\alpha_1^2 + \alpha_2^2 - k^2)} \frac{1}{\alpha_{1-}\alpha_{2-}} \langle (\alpha_{2-} - \alpha_2) \times$$

$$[\alpha_{1-}F_1(\alpha_1, \alpha_3) - \alpha_1 F_1(\alpha_{1-}, \alpha_3)] + (\alpha_{1-} - \alpha_1)[\alpha_{2-}F_2(\alpha_2, \alpha_3) - \alpha_2 F_2(\alpha_{2-}, \alpha_3)] \rangle$$

By reducing the same cofactors, the function $U_1(\alpha_1, \alpha_2, \alpha_3)$ can be represented as

$$U(\alpha_1, \alpha_2, \alpha_3) = i \frac{1}{\alpha_{1-}\alpha_{2-}}$$

$$\times \left\langle \frac{[\alpha_{1-}F_1(\alpha_1, \alpha_3) - \alpha_1 F_1(\alpha_{1-}, \alpha_3)]}{(\alpha_2 + \alpha_{2-})} + \frac{[\alpha_{2-}F_2(\alpha_2, \alpha_3) - \alpha_2 F_2(\alpha_{2-}, \alpha_3)]}{(\alpha_1 + \alpha_{1-})} \right\rangle (2.4)$$

The resulting representation allows us to formulate conditions for the specified boundary functions. To build a mathematical model of the pre-landslide structure, an anisotropic medium must be taken cover with a membrane sarcophagus that prevents spreading. To do this, build a mathematical model of the sarcophagus, which includes a vertical wall and a horizontal cover. We apply the method of block element.

The boundary value problem for horizontal coverage has the following formulation:

$$(\partial^2 x_1 + \partial^2 x_3 + p_1^2)w_1(x_1, x_3) = t_1(x_1, x_3),$$

$$|x_3| \leq \infty, \quad -\infty < x_1 \leq 0, \quad \partial x_1 w_1(0, x_3) = g_1(0, x_3)$$

The boundary value problem for a vertical wall is described by the equation and conditions

$$(\partial^2 x_2 + \partial^2 x_3 + p_2^2)w_2(x_2, x_3) = t_2(x_2, x_3),$$

$$|x_3| \leq \infty, \quad -\infty < x_2 \leq 0, \quad \partial x_2 w_2(0, x_3) = g_2(0, x_3)$$

Here, $t_1(x_1, x_3)$ and $t_2(x_2, x_3)$ are the amplitudes of external influences on the sarcophagus, and $g_1(0, x_3)$ and $g_2(0, x_3)$ are the angles of rotation corner ends of the wall and coating, respectively. The wall and coating are tightly mated with the mass being held.

Given that the function $u(x_1, x_2, x_3)$ represents the potential of the water-saturated mass, w_1 and w_2 are normal to the sarcophagus has a range of motion, then the following conditions must be met

$$w_1(x_1, x_3) = \partial x_2 u(x_1, x_2, x_3), \quad x_2 = 0, \quad -\infty < x_1 \leq 0$$

$$w_2(x_2, x_3) = \partial x_1 u(x_1, x_2, x_3), \quad x_1 = 0, \quad -\infty < x_2 \leq 0$$

After calculations, we get the following representation for the spreading landslide model:

$$f_1(x_1, x_3) = \mathbf{F}_2^{-1}(x_1, x_3) \left[\frac{\alpha_1 \alpha_{1-}^{-1} T_1(\alpha_{1-}, \alpha_3) - T_1(\alpha_1, \alpha_3)}{(\alpha_1^2 + \alpha_3^2 - p_1^2)} - \frac{\alpha_{1-} g_1(0, \alpha_3)}{(\alpha_1 - \alpha_{1+})} \right]$$

$$f_2(x_2, x_3) = \mathbf{F}_2^{-1}(x_2, x_3) \left[\frac{\alpha_2 \alpha_{2-}^{-1} T_2(\alpha_{2-}, \alpha_3) - T_2(\alpha_2, \alpha_3)}{(\alpha_2^2 + \alpha_3^2 - p_2^2)} - \frac{\alpha_{2-} g_2(0, \alpha_3)}{(\alpha_2 - \alpha_{2+})} \right]$$

Adding these function values to formulas (2.4) and (2.2) allows you to get an analytical representation in the form of integrals of the model of a horizontally propagating landslide. Here, $\mathbf{F}_2^{-1}(x_1, x_3)$, and $\mathbf{F}_2^{-1}(x_2, x_3)$ are two-dimensional inverse Fourier operators.

2.4 Conclusions

By construction, the function represents a potential that is proportional to the pressure. The constructed solution of the problem allows it to be evaluated at any point in the considered area, including near the border. In the model, you can choose different problem statements, changing the effects on the walls and coatings, and also vary the anisotropy parameters, thereby revealing the extremely critical States of the landslide structure, after which there will be a gap between the sarcophagus and the landslide process will begin.

References

1. Brekhovskikh, L.M.: Waves in layered media. Nauka, Moscow (1973) (In Russian)
2. Babich, V.M.: On the short-wave asymptotics of the green function for the Helmholtz equation. Math. Collect. **65**, 577–630 (1964) (In Russian)
3. Babich, V.M., Buldyrev, V.S.: Asymptotic methods in the problem of short-wave diffraction. Nauka, Moscow (In Russian) (1972)
4. Mukhina, I.V.: Approximate reduction to the Helmholtz equations of the equations of elasticity theory and electrodynamics for inhomogeneous media. PMM **36**, 667–671 (1972) (In Russian)
5. Molotkov, L.A.: Investigation of wave propagation in porous and fractured media on the basis of effective models of Biot and layered media. Nauka, Saint-Petersburg (In Russian) (2001)
6. Novatsky, V.: Theory of elasticity. Mir, Moscow (In Russian) (1975)
7. Nowacki, V.: Electromagnetic effects in solid bodies. Mir, Moscow (In Russian) (1986)

8. Tkacheva, L.A.: Vibrations of a floating elastic plate, with periodic displacements of the bottom section. Appl. Mech. Tech. Phys. **46**(5), 166–179 (2005) (In Russian)
9. Tkacheva, L.A.: Flat problem of vibrations of a floating elastic plate under the action of periodic external load. Appl. Mech. Tech. Phys. **45**(5), 136–145 (2004) (In Russian)
10. Tkacheva, L.A.: Behavior of a floating plate under vibrations of the bottom section. Appl. Mech. Tech. Phys. **46**(2), 98–108 (2005) (In Russian)
11. Tkacheva, L.A.: Interaction of surface and Flexural-gravitational waves in an ice cover with a vertical wall. Appl. Mech. Tech. Phys. **54**(4), 158–170 (2013) (In Russian)
12. Babeshko, V.A., Evdokimova, O.V., Babeshko, O.M., et al.: A method of designing inhomogeneous materials and block structures. Doklady Phys. (2018). https://doi.org/10.1134/S1028335818100014
13. Babeshko, V.A., Evdokimova, O.V., Babeshko, O.M.: Stages of transformation of block elements. Doklady Phys. (2016). https://doi.org/10.1134/S1028335816050049
14. Babeshko, V.A., Babeshko, O.M., Evdokimova, O.V.: On the Sadovskii problem of block structures. Doklady Phys. (2009). https://doi.org/10.1134/S1028335809080060

Chapter 3
Variable Kinematics Models for Advanced Composite Plates

M. D'Ottavio, A. Krasnobrizha, E. Valot, O. Polit, R. Vescovini, and L. Dozio

Abstract This paper presents the application of a sublaminate-based variable kinematics approach to *advanced* composite structures with enhanced damping treatments such as viscoelastic layers or piezoelectric plies. The Sublaminate Generalized Unified Formulation (SGUF) is applied in conjunction with an efficient Ritz-type solution to free-vibration problems involving various mechanical and electrical boundary conditions. Conventional viscoelastic sandwich and piezoelectric bimorph structures are considered as well as more complex double-core plates. The role of thickness stretch in viscoelastic cores is pointed out and the possibility of reducing the number of degrees of freedom by virtue of the sublaminate approach is highlighted. The possibility of tailoring the accuracy and the number of degrees of freedom will be particularly meaningful for computationally intensive algorithms searching optimal configurations.

3.1 Introduction

Vibration suppression is one of the most relevant challenges for lightweight structural components, as it drives relevant design aspects, e.g. noise attenuation and fatigue life. A traditional way of improving the damping properties consists of embedding viscoelastic material (VEM) plies within stiff layers [23]. The embedment of piezoelectric sensors and/or actuators has been demonstrated to be among the most indicated solutions for implementing an adaptive control strategy [21]. Solutions involving both VEM and piezoelectric transducers have also attracted great interest [4]. The design of such *advanced composite structures* requires dedicated tools for coping with the complex underlying physical mechanisms and structural response. In particular, *efficient* numerical tools are desired that allow to perform optimisation

M. D'Ottavio (✉) · A. Krasnobrizha · E. Valot · O. Polit
LEME, Université Paris Nanterre, Nanterre, France
e-mail: michele.d_ottavio@parisnanterre.fr

R. Vescovini · L. Dozio
DIMEAS, Politecnico di Milano, Milan, Italy

loops by grasping the structural response up to the desired degree of accuracy (e.g. global and/or local analysis).

Among the very intensive research activity that is being dedicated to the development of such numerical simulation tools for more than 30 years, the so-called *variable kinematics* approach systematically developed by Carrera and co-workers appears to be very efficient [7, 9, 11]. The basic idea is to provide within a unique software, the possibility of tailoring the accuracy—thus the computational cost—by adopting different models depending on the desired output quantity. The variable kinematics approach has been shown to be particularly meaningful for multifield problems, in which gradients of different field variables require an appropriate resolution [3, 8, 15]. The variable kinematics approach also facilitates the implementation of global–local strategies [25], and it can be also employed for identifying the problem-dependent *best theory* in an axiomatic/asymptotic sense [10].

This contribution summarises a variable kinematics approach called Sublaminate Generalized Unified Formulation (SGUF) [12] and presents its application to advanced composite plate structures including piezoelectric and viscoelastic materials. The two-dimensional partial differential equations governing the plate models are solved numerically by means of a Ritz method, which allows to efficiently deal with structural vibration problems including arbitrary boundary conditions and anisotropic coupling [13, 24]. The efficiency and accuracy of the proposed approach are demonstrated by referring to free-vibration problems of composite plates with embedded viscoelastic or piezoelectric plies, including proper electric boundary conditions for these latter.

3.2 Modelling Approach

This section describes the axiomatic variable kinematics plate models employed in conjunction with a Ritz-type approach for solving free-vibration problems in a small perturbation setting. The piezoelectric coupling is taken into account by referring to the "generalised displacements" formulation based on electric enthalpy. The weak form of d'Alembert's principle for traction- and electric charge-free vibrations of a piezoelectric continuum is then expressed as

$$\int_V \delta S_{ij} T_{ij} - \delta E_i D_i + \delta u_i \, \rho \ddot{u}_i \, \mathrm{d}x_1 \, \mathrm{d}x_2 \, \mathrm{d}x_3 = 0 \tag{3.1}$$

$V = \Omega \times [-\frac{h}{2} \leq x_3 \leq \frac{h}{2}]$ is the volume occupied by the plate, that is considered to have a uniform thickness h over the reference surface Ω lying in the plane $x_3 = 0$. Adopting the standard notation of [1], the primary mechanical field variables are the three components of the displacement vector $u_i(x_1, x_2, x_3)$ and the primary electrical field variable is the electrostatic potential $\varphi(x_1, x_2, x_3)$. Linear gradient equations, not reported here for the sake of brevity, are used to define the mechanical strain tensor S_{ij} and the electric field vector E_i from the primary variables. The classical

constitutive law of linear piezoelectricity is employed for defining the mechanical stress tensor T_{ij} and the electric displacement vector D_i [1]:

$$T_{ij} = \tilde{c}^E_{ijkl}\, S_{kl} - e_{kij}\, E_k; \quad D_i = e_{ikl} S_{kl} + \varepsilon^S_{ik}\, E_k \tag{3.2}$$

3.2.1 Complex Modulus Approach for VEM

Free-vibration problems involving VEM are suitably described within the complex modulus approach, in which the time-dependent constitutive law is expressed in the frequency domain as

$$T_{ij} = \tilde{c}^*_{ijkl}(\omega)\, S_{kl} \tag{3.3}$$

Throughout the paper, complex quantities are characterised by an asterisk. The complex stiffness coefficients are defined in terms of complex engineering moduli and real Poisson's ratios. Two models are considered for introducing the dependency on the circular frequency ω. The well-known Anelastic Displacement Field model (ADF) represents the VEM behaviour as a series of n Kelvin–Voigt elements and an elastic spring [19]:

$$G^*(\omega) = G_0 \left(1 + \sum_{j=1}^{n} \frac{\Delta_j\, \omega}{\omega - \hat{\imath}\, \Omega_j} \right) \tag{3.4}$$

Alternatively, the four-parameter Zener fractional derivatives model (FDZ) is considered [22]:

$$G^*(\omega) = \frac{G_0 + G_\infty(\hat{\imath}\, \omega\, \tau)^\alpha}{1 + (\hat{\imath}\, \omega\, \tau)^\alpha} \tag{3.5}$$

In the above equations, $\hat{\imath} = \sqrt{-1}$ is the imaginary unit, G_0 represents the static modulus and $G_\infty = G^*(\omega \to \infty)$ the unrelaxed modulus; in the ADF model, $1/\Omega_j$ and Δ_j are the relaxation time and strength, respectively, of the jth Kelvin–Voigt element; in the FDZ model, α is the fractional order of derivatives and τ the relaxation time. Thermodynamic consistency of the FDZ model is ensured provided $G_\infty > G_0 > 0$, $\tau > 0$ and $0 < \alpha \leq 1$ [2].

Fig. 3.1 Subdivision of the composite stack (left) in sublaminates (right): employed coordinates for describing the kinematic assumptions
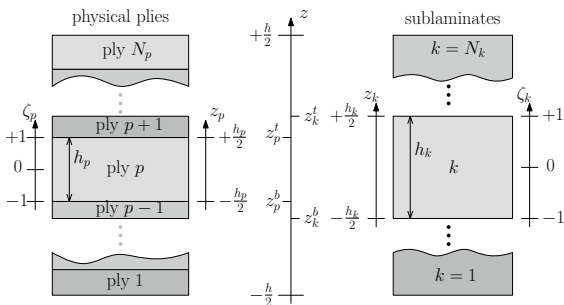
3.2.2 SGUF Variable Kinematics Modelling and Ritz-Type Solution

The SGUF variable kinematics approach describes the composite plate as a stack along its thickness direction $x_3 \equiv z$ of $k = 1, 2 \ldots N_k$ numerical layers, the *sublaminates*, each may regroup several physical plies or a fraction of a single physical ply, see Fig. 3.1. In each ply p within the sublaminate k, the generic field variable $\mathcal{U}_r^{p,k}(x_1, x_2, z_p)$ is axiomatically assumed in the form expressed in Generalized Unified Formulation (GUF) [11] as

$$\mathcal{U}_r^{p,k}(x_1, x_2, \zeta) = \sum_{\alpha_{\mathcal{U}_r}=0}^{N_{\mathcal{U}_r}^k} F_{\alpha_{\mathcal{U}_r}}(\zeta)\, \hat{\mathcal{U}}_{r\alpha_{\mathcal{U}_r}}^{p,k}(x_1, x_2) \tag{3.6}$$

The index $r \in [1, 4]$ identifies the field variable, which is the displacement component u_r for $r = 1, 2, 3$, or the electrostatic potential φ for $r = 4$. Note that the electrostatic potential variables are only present in piezoelectric plies. The *thickness functions* $F(\zeta)$ describe the gradient across the sublaminate's thickness either in a LayerWise (LW) or in an Equivalent Single Layer (ESL) sense: the non-dimensional coordinate ζ is thus defined over either the ply thickness h_p, or the sublaminate thickness h_k, respectively. The through-the-thickness approximation is defined as the sum of a linear Lagrange interpolation and orthogonal Legendre polynomials of order $N_{\mathcal{U}_r}^k$. This allows a hierarchic model enrichment while preserving direct access to the top and bottom values and, hence, facilitating the subsequent assembly. The overall kinematic model for the whole composite plate is obtained as an LW assembly of the individual sublaminate contributions. More details can be found in [14].

The solution over the reference plane Ω is sought according to Ritz' method in the following form [13]:

$$\hat{\mathcal{U}}_{r\alpha_{\mathcal{U}_r}}^{p,k}(x_1, x_2) = \sum_{j=1}^{M} N_{\mathcal{U}_r j}(x_1, x_2)\, \mathcal{U}_{r\alpha_{\mathcal{U}_r} j}^{p,k} \tag{3.7}$$

The two-dimensional shape functions $N_{\mathcal{U}_r j}(x_1, x_2)$ are constructed by multiplying the products of one-dimensional orthogonal basis functions $P_m(x_1)$ and $P_n(x_2)$ defined by Legendre polynomials, with appropriate boundary functions $f(x_1)$ and $g(x_2)$ that represent the clamped, simply supported and free edge conditions [24]:

$$N_{\mathcal{U}_r j}(x_1, x_2) = \Phi_{\mathcal{U}_r m}(x_1)\, \Psi_{\mathcal{U}_r n}(x_2) \quad \text{with} \begin{cases} \Phi_{\mathcal{U}_r m}(x_1) = P_m(x_1) f(x_1) \\ \Psi_{\mathcal{U}_r n}(x_2) = P_n(x_2) g(x_2) \end{cases} \quad (3.8)$$

Taking $m \in [1, R]$, $n \in [1, S]$, the order of Ritz' approximation is thus $M = RS$.

3.2.3 The Discrete Algebraic System

The through-the-thickness approximation of the plate model expressed by Eq. (3.6) and the in-plane approximation expressed by Eq. (3.7) are introduced in the variational formulation Eq. (3.1); the thickness and in-plane integrals are carried out separately and subsequently assembled to build the system matrices. Details about the implied procedures can be found elsewhere [12–14], including the definition of *fundamental nuclei* that characterise the implementation of unified formulation approaches, their expansion and assembly. It is worth emphasising that the present implementation is highly efficient since it employs analytically computed integrals, see [24]: as a result, high-order approximations can be used without ill-conditioning and the system matrices are shown to have a high degree of sparsity. One eventually arrives at the discrete algebraic system defining the eigenvalue problem associated to the free-vibration problem. Different solution procedures are adopted depending on whether the structure contains a VEM or a piezoelectric ply, as described in the following.

3.2.3.1 The Viscoelastic Case

In case of a viscoelastically damped structure, the eigenvalue problem is complex and written as

$$(K^* - \lambda^2 M)U^* e^{\hat{\imath}\omega t} = 0, \quad \text{with } K^* = K_R + \hat{\imath} K_I \quad (3.9)$$

where only the complex part K_I of the stiffness matrix contains the frequency-dependent VEM behaviour. In case of a frequency-*independent* VEM, the complex eigenvalue problem is directly solved yielding the damped modal eigenfrequencies and corresponding damping factors as

$$\omega_j = \sqrt{\Re(\lambda_j^2)} \quad \text{and} \quad \eta_j = \frac{\Im(\lambda_j^2)}{\Re(\lambda_j^2)} \quad (3.10)$$

In the presence of a frequency-*dependent* VEM, $K_I = K_I(\omega)$ and the complex eigenvalue is nonlinear: an iterative fixed-point approach is adopted in conjunction with the direct complex eigensolver to obtain the solution. Starting from an initial guess defined by the undamped system, four to five iterations are in general required to reach a converged solution with a tolerance of 10^{-6}.

An alternative solution approach that avoids the use of the Complex Eigen-Solver (CES), relies on the Modal Strain Energy (MSE) approach [16]. In this case, a real eigenproblem is solved for obtaining the undamped eigenfrequencies and corresponding modes, from which the loss factor for mode j is estimated *a posteriori* as

$$\eta_j = \frac{U_j^T \, K_I \, U_j}{U_j^T \, K_R \, U_j} \tag{3.11}$$

3.2.3.2 The Piezoelectric Case

The vibratory response of plates with piezoelectric plies should properly take into account the electrical boundary conditions at the electrodes. The essential boundary condition for the electrostatic potential on an equipotential surface located at z_e is exactly verified by adopting a one-term, constant Ritz approximation $\varphi(x_1, x_2, z_e) = \varphi_e$, see also [14]: this approximation is used for both, a prescribed electrostatic potential, e.g. in the Short-Circuit (SC) condition $\varphi_e = 0$, and a prescribed zero-charge condition of the Open-Circuit (OC) configuration, for which φ_e remains unknown.

After having condensed out all *internal* degrees-of-freedom (DOF) related to the electrostatic potential, the following electromechanically coupled linear and real eigenvalue problem is obtained:

$$\left(\begin{bmatrix} \tilde{K}_{uu} & \tilde{K}_{u\varphi_e} \\ \tilde{K}_{u\varphi_e}^T & \tilde{K}_{\varphi_e\varphi_e} \end{bmatrix} - \omega^2 \begin{bmatrix} M & 0 \\ 0 & 0 \end{bmatrix} \right) \begin{bmatrix} U \\ \varphi_e \end{bmatrix} = \begin{bmatrix} 0 \\ 0 \end{bmatrix} \tag{3.12}$$

where the only electrostatic potential DOF are those associated to the electrodes. The appropriate electrical boundary conditions are subsequently applied and a purely mechanical eigenvalue problem is finally obtained, see e.g. [5]

$$\left(\tilde{\tilde{K}}_{uu} - \omega^2 M \right) U = 0 \tag{3.13}$$

where $\tilde{\tilde{K}}_{uu} = \tilde{K}_{uu} - \tilde{K}_{u\varphi_e}^T \tilde{K}_{\varphi_e\varphi_e}^{-1} \tilde{K}_{u\varphi_e}$ is the equivalent mechanical stiffness matrix that accounts for the unknown electrostatic potential DOF at OC electrodes.

3.3   Numerical Results

The proposed modelling approach is next applied to some case problems available in open literature in order to demonstrate its accuracy and versatility. At first, we shall introduce the naming convention employed to identify the plate models that can be implemented within the SGUF approach.

3.3.1   Naming Convention for the Models

The model adopted *in each sublaminate* is uniquely denoted by an acronym of the form $D_{XN_{u_\alpha},XN_{u_3}}^{XN_\varphi}$, in which the letter 'D' indicates that a (generalised) displacements' approach has been used. The subscripts indicate the assumptions for the in-plane displacements $u_\alpha = u_1$, u_2 (the same model will be employed for the displacements along x_1 and x_2 for simplicity), and the transverse displacement u_3. The letter 'X' is a placeholder that is replaced by 'E' if the displacement component is described in an ESL sense, or by 'L' if an LW description is adopted. The integers N_{u_α} and N_{u_3} correspond to the order of the polynomial expansion. The superscript is used to define the approximation for the electrostatic potential and follows the same convention. If the sublaminate consists of only one ply, the 'X' letters are dropped out; furthermore, if all variables are described in the same manner, the 'X' is placed before the 'D'. So, the model corresponding to the first-order shear deformation theory is $ED_{1,0}$, while an LW model with FSDT kinematics in each ply is $LD_{1,0}$. Note that the reduced constitutive law is employed enforcing the constraint $T_{33} = 0$ is used whenever $N_{u_3} = 0$.

3.3.2   Sandwich Plates with VEM Cores

A thin sandwich plate with a frequency-*independent* VEM core and metallic faces is first considered as proposed by Zhang and Sainsbury, who provided accurate FEM results for the first 100 modes of a rectangular plate with all edges free [26]. Figure 3.2 (left) displays the convergence of the present Ritz solution for a $LD_{1,0}$ model in terms of eigenfrequency and modal loss factor for a VEM core whose loss factor is $\eta_c = 0.5$. The relative errors between the results obtained by the MSE approach with respect to the CES are illustrated in Fig. 3.2 (right). Three different VEM loss factors have been considered and it is obvious that the MSE approach provides accurate results as long as the damping is low. However, it should be noted that the MSE solution took only approximately half of the time required by the CES for computing the 100 modes.

A fully clamped, thin sandwich plate with metallic faces and a frequency-*dependent* VEM core is next considered as proposed by Bilasse et al. [6], who
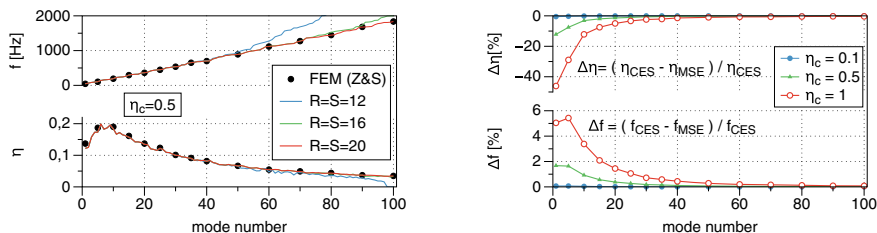
Fig. 3.2 First 100 modes of a rectangular sandwich plate with frequency-independent VEM: convergence of the present Ritz solution for $\eta_c = 0.5$ (left) and comparison between the MSE and the CES for different damping values η_c of the VEM

Table 3.1 Sandwich plate with frequency-dependent VEM: present results with ADF and FDZ models obtained with the iterative CES, results in Ref. [6] obtained with ADF and ANM

Mode	Reference [6]		ADF model			FDZ model		
	f (Hz)	η_l	f (Hz)	η_0	η	f (Hz)	η_0	η
1	83.01	0.246	83.10	0.247	0.254	82.80	0.231	0.241
2	146.61	0.258	146.91	0.259	0.269	146.64	0.260	0.272
3	168.92	0.257	168.76	0.257	0.269	168.74	0.260	0.272
4	225.27	0.270	225.59	0.269	0.283	226.35	0.271	0.284

adopted the Asymptotic Numerical Method (ANM) to solve the nonlinear complex eigenvalue problem arising from an ADF model for the VEM core. Present results are obtained with the iterative complex eigensolver for an $LD_{1,0}$ kinematics adopting either the ADF or the FDZ model. Table 3.1 shows that present results compare in a satisfactory manner with the reference solution. Some small discrepancies are found for the FDZ model which are due to the identification of the four parameters starting from the ADF model.

In the following, the influence of the kinematics assumptions is addressed. The third case problem concerns a moderately thick, double-core sandwich beam, composed of three metallic plies and two frequency-dependent VEM cores described by an FDZ model. This configuration has been analysed by Lewandowski and Baum with a model adopting Classical Plate Theory (CPT) for the metallic plies and FSDT for the VEM cores [20]. The plane beam has been modelled within the present approach by setting $S = 1$ in the Ritz expansion with free–free conditions at the edges parallel to the beam axis x_1, and upon using reduced stiffness coefficients that correspond to the plane stress condition $T_{22} = 0$ along the beam width. The present results for the modal loss factors obtained for different boundary conditions are reported in Fig. 3.3 along with the solution proposed by Lewandowski and Baum. Three different kinematics are compared: the $LD_{1,0}$ model follows the results of Ref. [20], but the quasi-3D model LD4 and the high-order model $ED_{1,0}/ED_{1,2}$, in which FSDT is used for the metallic plates and the $ED_{1,2}$ kinematics for the VEM cores, show significant differences. The reason for the discrepancy is attributed to the full 3D constitutive law
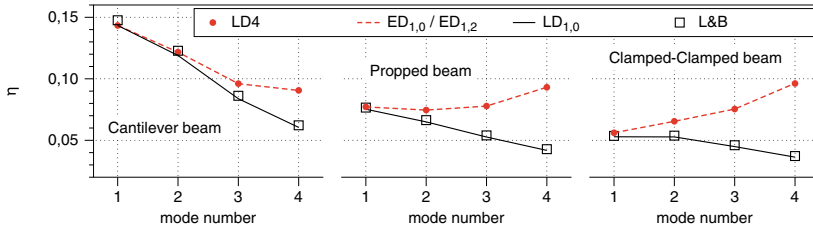
Fig. 3.3 Double-core sandwich beam with different boundary conditions: influence of the model kinematics on the modal loss factor

retained by these refined models for the VEM cores: the through-thickness stretch in the VEM cores entails an *increase* of the modal loss factor of higher modes, an effect that is emphasised by the degree of hyperstaticity of the structure.

3.3.3   Plates with Piezoelectric Plies

A first case problem is considered for highlighting the role of electrical boundary conditions on the free-vibration response of piezoelectric plates. A piezoelectric parallel bimorph wide plate (cylindrical bending) is examined, for which Krommer provided reference solutions based on an FSDT kinematics [18]. The plate is either cantilevered (CF) or simply supported (SS); three sets of electrical boundary conditions are considered for the top and bottom surfaces of the bimorph (the interlaminar electrode being grounded): a Short-Circuit (SC) configuration with $\varphi(x_1, x_2, z = \pm h/2) = 0$, an Open-Circuit (OC) configuration with $\varphi(x_1, x_2, z = \pm h/2) = $ const, and a Not-Electroded (NE) configuration with $\varphi(x_1, x_2, z = \pm h/2)$ let free to vary without any equipotentiality constraint. Figure 3.4 reports the ratio between the eigenfrequencies of the piezoelectric system and those of the purely elastic system for the first 6 modes. The same FSDT model of Ref. [18] has been used as well as a refined LD_{32} model that retains the 3D constitutive law. Results for the SC and OC configurations compare very accurately with the corresponding reference solution. The refined model provides results that are only marginally different from those obtained by FSDT. It

Fig. 3.4 Piezoelectric coupling effect of a bimorph plate: influence of mechanical and electrical boundary conditions, and comparison between $ED_{1,0}$ (FSDT) and a high-order model with 3D constitutive law ($LD_{3,2}$)
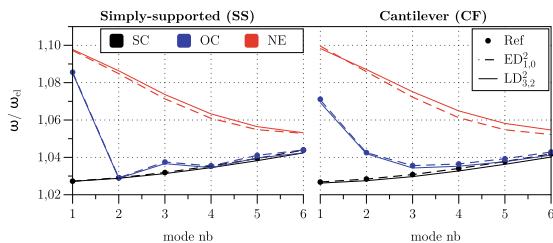
Fig. 3.5 Double-core basis plate with bonded piezoelectric plies (left) and three SGUF models (right): two models with three sublaminates (**a1**) and (**a2**) and one model with seven sublaminates (**b**)
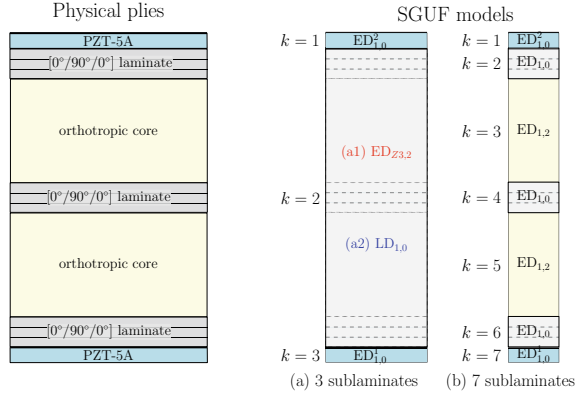
is worth noticing the different trends obtained by the NE configuration, which confirms the important role played by the equipotentiality condition on the piezoelectric coupling.

A final case problem is considered, which allows to give evidence of the computational advantage gained by virtue of the SGUF approach. It consists of a double-core sandwich plate with three composite faces and two thick orthotropic cores, with two piezoelectric plies bonded at its top and bottom surfaces, see Fig. 3.5 (left). Ply thicknesses and material data can be found in [17]. The plate is square of edge length a and simply supported; different electrical boundary conditions are applied to the piezoelectric plies: the ply at the bottom works in OC, while that at the top is shunted (SC). The interfaces between the piezoelectric plies and the basic structure are electroded and grounded. Separate sublaminates are used for the piezoelectric plies in order to introduce dedicated assumptions depending on the electrical boundary conditions [15]: FSDT kinematics is used along with a linear and quadratic approximation for $\varphi(z)$ for the OC and SC piezoelectric ply, respectively. The basis double-core plate has no electrostatic potential DOF and is modelled with either (a) a single sublaminate or (b) with five sublaminates, see Fig. 3.5 (right). Two models shall be declined within description (a), namely (a1) the higher order ESL model $ED_{3,2}$ retaining the 3D constitutive law, and (a2) the conventional $LD_{1,0}$ model. Adopting five sublaminates for the basis plate, model (b) employs FSDT for the stiff laminated faces and the refined model $ED_{1,2}$ for the thick and soft cores; the resulting model will thus be labelled $ED_{1,0}/ED_{1,2}$.

The results are reported in Fig. 3.6 for three different length-to-thickness ratios $S = a/h = 5, 10, 20$ in terms of percentage difference with respect to the exact 3D solution of the non-dimensional eigenfrequencies $\bar{\omega}$ for the three modes with (1, 1), (1, 2) and (1, 3) halfwaves. The legend reports also the number of DOF for the three considered models. It is obvious that higher errors are introduced for thick plates and for higher modes (shorter wavelength). When adopting a single sublaminate for the whole basis structure, model (a1) produces with 20 DOF a maximum error of about 20%, whereas the full LW model (a2) shows a maximum error of approximately 1%

Fig. 3.6 Eigenfrequencies of the double-core sandwich plate with bonded outer piezoelectric plies: percentage errors with respect to the 3D solution for three different length-to-thickness ratios S and three different SGUF models
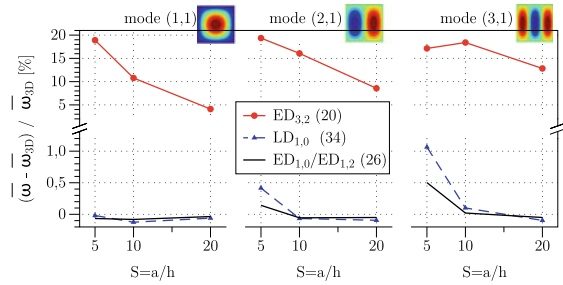
with 34 DOF. Model (b) requires only 26 DOF and is affected by a maximum error of approximately 0.5% for mode (1, 3) and for the thick plate case.

3.4   Conclusion

This paper has extended the variable kinematics SGUF approach to the free-vibration analysis of advanced composite plates including viscoelastic and piezoelectric materials. VEM can display frequency-dependent damping properties, and different electrical boundary conditions can be considered with good accuracy. The variable kinematics approach could highlight the important role of the transverse stretch in VEM cores. Moreover, thanks to the sublaminate description, the accuracy of the axiomatic models can be enhanced without an excessive use of DOF.

Future work shall be directed towards the FEM implementation of the SGUF approach for an efficient simulation of structures with piezoelectric and/or viscoelastic patches. The simultaneous solution of structures including both, piezoelectric plies and VEM shall provide a flexible numerical tool for the optimisation of advanced structures with hybrid active–passive damping treatments.

References

1. American National Standard Institute. IEEE Standard on Piezoelectricity (1987)
2. Bagley, R.L., Torvik, P.J.: On the fractional calculus model of viscoelastic behavior. J. Rheol. **30**(3), 133–155 (1986)
3. Ballhause, D., D'Ottavio, M., Kröplin, B., Carrera, E.: A unified formulation to assess multi-layered theories for piezoelectric plates. Comput. Struct. **83**(15–16), 1217–1235 (2005)
4. Baz, A.M.: Active and Passive Vibration Damping. Wiley (2019)
5. Benjeddou, A., Belouettar, S.: On the evaluation and application of the modal properties of piezoelectric adaptive structures. In: Topping, B.H.V., Montero, G., Montenegro, R. (eds.) Innovation in Computational Structures Technology, pp. 287–302. Saxe-Coburg Publications, Kippen, UK (2006)
6. Bilasse, M., Azrar, L., Daya, E.M.: Complex modes based numerical analysis of viscoelastic sandwich plates vibrations. Comput. Struct. **89**, 539–555 (2011)

7. Carrera, E.: Theories and finite elements for multilayered plates and shells: a unified compact formulation with numerical assessment and benchmarking. Arch. Comput. Meth. Eng. **10**, 215–296 (2003)

8. Carrera, E., Brischetto, S., Nali, P.: Plates and Shells for Smart Structures. Classical and Advanced Theories for Modeling and Analysis. Wiley (2011)

9. Carrera, E., Cinefra, M., Petrolo, M., Zappino, E.: Finite Element Analysis of Structures through Unified Formulation. Wiley, Chichester, UK (2014)

10. Cinefra, M., Carrera, E., Lamberti, A., Petrolo, M.: Best theory diagrams for multilayered plates considering multifield analysis. J. Intell. Math. Syst. Struct. **28**, 2184–2205 (2017)

11. Demasi, L.: ∞^3 hierarchy plate theories for thick and thin composite plates: the generalized unified formulation. Compos. Struct. **84**, 256–270 (2008)

12. D'Ottavio, M.: A sublaminate generalized unified formulation for the analysis of composite structures and its application to sandwich plates bending. Compos. Struct. **142**, 187–199 (2016)

13. D'Ottavio, M., Dozio, L., Vescovini, R., Polit, O.: Bending analysis of composite laminated and sandwich structures using sublaminate variable-kinematic Ritz models. Compos. Struct. **155**, 45–62 (2016)

14. D'Ottavio, M., Dozio, L., Vescovini, R., Polit, O.: The Ritz—sublaminate generalized unified formulation approach for piezoelectric composite plates. Int. J. Smart Nano Mater. **9**(1), 1–22 (2018)

15. D'Ottavio, M., Polit, O.: Sensitivity analysis of thickness assumptions for piezoelectric plate models. J. Intell. Mater. Syst. Struct. **20**(15), 1815–1834 (2009)

16. Johnson, C.D., Kienholz, D.A.: Finite element prediction of damping in structures with constrained viscoelastic layers. AIAA J. **20**, 1284–1290 (1982)

17. Kapuria, S., Nath, J.K.: Coupled global-local and zigzag-local laminate theories for dynamic analysis of piezoelectric laminated plates. Compos. Struct. **95**, 163–172 (2013)

18. Krommer, M.: Piezoelastic vibrations of composite Reissner-Mindlin-type plates. J. Sound Vib. **263**, 871–891 (2003)

19. Lesieutre, G.A., Bianchini, E.: Time domain modeling of linear viscoelasticity using anelastic displacement fields. J. Vib. Acoust. **117**, 424–430 (1995)

20. Lewandowski, R., Baum, M.: Dynamic characteristics of multilayered beams with viscoelastic layers described by the fractional Zener model. Arch. Appl. Mech. **85**, 1793–1814 (2015)

21. Moheimani, S.O.R., Fleming, A.J.: Piezoelectric Transducers for Vibration Control and Damping. Springer, London (2006)

22. Pritz, T.: Analysis of four-parameter fractional derivative model of real solid materials. J. Sound Vib. **195**, 103–115 (1996)

23. Rao, M.D.: Recent applications of viscoelastic damping for noise control in automobiles and commercial airplanes. J. Sound Vib. **262**, 457–474 (2003)

24. Vescovini, R., Dozio, L., D'Ottavio, M., Polit, O.: On the application of the Ritz method to free vibration and buckling analysis of highly anisotropic plates. Compos. Struct. **192**, 460–474 (2018)

25. Zappino, E., Li, G., Pagani, A., Carrera, E.: Global-local analysis of laminated plates by node-dependent kinematic finite elements with variable ESL/LW capabilities. Compos. Struct. **172**, 1–14 (2017)

26. Zhang, Q.J., Sainsbury, M.G.: The Galerkin element method applied to the vibration of rectangular damped sandwich plates. Comput. Struct. **74**, 717–730 (2000)

Chapter 4
Magnetoelastic Phenomena and Their Applications in Diagnostics and Technology

E. S. Gorkunov

Abstract The paper studies the nature of magnetostriction and magnetoelastic phenomena in ferromagnets and their application to the creation of transducers different types. It also demonstrates the applicability of magnetoelastic parameters for nondestructive evaluation of the level of macroscopic and microscopic stresses in ferromagnetic parts and structural components.

4.1 Introduction

The study of the effect of elastic and plastic strains on the magnetization reversal of ferromagnetic materials has both theoretical and practical aspects. Therefore, specialists engaged in basic research and practical application of magnetoelastic phenomena may talk entirely different languages and use different terms. In practical terms, the knowledge of magnetic behavior under elastic strains enables one to use magnetoelastic phenomena when creating new types of transducers and, accordingly, offering new capabilities of measuring equipment [4, 7] and nondestructive testing [3, 6, 8, 9]. In the field of nondestructive testing, the study of magnetoelastic phenomena in structural ferromagnetic materials allows one to progress in the evaluation of the stress-strain parameters of individual structural components, and, in the future, to evaluate the state and service life of a whole structure using these parameters and model representations of fracture mechanics. Magnetoelastic phenomena in ferromagnetic metals and alloys began to be studied long ago [2]. As early as in mid-1800s, Villari found that, affected by elastic tensile and compressive stresses, the magnetic permeability of ferromagnetic bodies undergoes some changes depending on magnetization. This phenomenon was supported by a number of later studies.

E. S. Gorkunov (✉)
Institute of Engineering Science, Ural Branch of the Russian Academy of Sciences, 34 Komsomolskaya st., 620049 Ekaterinburg, Russia
e-mail: ges@imach.uran.ru

4.2 The Basics of the Phenomenon

Magnetoelastic effects are based on the phenomenon of magnetostriction (a change in the shape and dimensions of a body under magnetization) discovered in iron by James Prescott Joule in 1842. The phenomenon of magnetostriction is inherent in all substances, both strong magnetic magnets and dia- or paramagnets. In ferromagnets, magnetostriction (percentage elongation $\lambda = \Delta l / l$) reaches 10^{-2}. For iron-based alloys, λ amounts to 10^{-6}. In dia- and paramagnets, magnetostriction is low (10^{-7} to 10^{-5}), except for Bi (diamagnet) and rare-earth paramagnets, where it reaches 10^{-4}. Magnetostriction is widely used for generating and receiving oscillations of various frequencies (ultra- and hypersound) in ultrasonic technique and hydroacoustics, as well as for creating various transducers [5]. The magnetoelastic effect is inverse to magnetostriction. The operation of a magnetoelastic transducer is based on the variation of its magnetic state under magnetization by a direct or alternating current and due to the effect of elastic strain. Devices of this type are used for data storage, for measuring magnetic field parameters, as magnetic amplifiers, and for measuring nonelectric quantities (location, displacements (rotation), forces, strains, fluid level, etc.) [4, 7]. Various effects are used in the design of transducers.

- **The Villari effect** (inverse to magnetostriction) consists in the variation of ferromagnet magnetization in the direction of mechanical strain (longitudinal and lateral), Fig. 4.1a.
- **The Guillemin effect** implies that a ferromagnetic bar straightens up when placed in a magnetic field.
- **The Wiedemann effect** (direct), discovered in 1858, means that, under circular magnetization by a current (J), the emerging torsion strain (τ) generates an emf (e) in the inductance coil (W), and vice versa (*the Matteucci effect*).
- **The Wertheim effect** is as follows: as a magnetized rod (M) is twisted (τ), an emf (e) is generated between the two rod ends (the direct effect); as an alternating current is applied to a magnetized rod, torsion strains appear in it (the inverse effect).

(a)   (b)
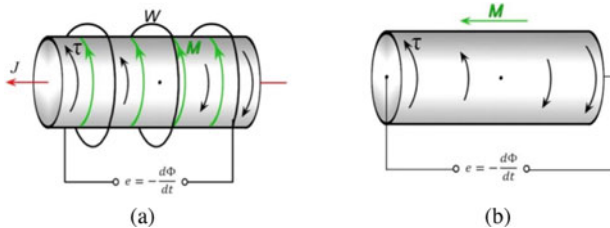
Fig. 4.1 Schematic work of a transducer using the Villari effect (**a**) and the Wertheim effect (**b**)

4.2.1 The Nature of Magnetostriction

The physical foundations of these processes are as follows. The shape and dimensions of a ferromagnet change under magnetization, i.e., elastic deformation forces appear; therefore, when evaluating the overall energy state, one must take into account four kinds of energies in a ferromagnet [1, 10]. Magnetostriction appears at temperatures below the Curie point (T_C) due to the action of exchange and magnetic bonding forces. The four kinds of energies are as follows:

$$E_{exch} = -2 \sum_{ij} A_{ij} \left(\mathbf{S}_i \mathbf{S}_j \right), \tag{4.1}$$

where E_{exch} is exchange energy, A_{ij} is the exchange integral for the atoms i and j, depending on the ratio of the lattice constant a to the effective radius r of the 3D level, and ϕ_{ij} is the angle between the spin moment vectors $\mathbf{S}_i$ and $\mathbf{S}_j$ the units $\hbar$;

$$E_K = K_0 + K_1 \alpha^2, \tag{4.2}$$

where E_K is crystallographic anisotropy energy and K_1 is the anisotropy constant;

$$E_\lambda = \frac{E \lambda_S^2}{2}, \tag{4.3}$$

where E_λ is magnetostrictive strain energy, E is Young's modulus, and λ_S is saturation magnetostriction;

$$E_\sigma = -\frac{3}{2} \lambda_S \sigma \cos^2 \varphi, \tag{4.4}$$

where E_σ is magnetoelastic energy for the case of isotropic magnetostriction, σ is applied stresses, and $\cos \varphi$ is a direction cosine taking into account the magnetization direction and the acting force direction. The effect of these energies changes the volume and shape of a ferromagnet. In what follows, this will be exemplified by iron.

Spontaneous (volume) magnetostriction If an iron ball, which is in the paramagnetic state above the Curie point $T > T_C$ (the spin magnetic moments are disordered) is cooled, exchange energy appears as the Curie point T_C is passed (the exchange interaction of the electrons is accompanied by a parallel arrangement of the electron spin moments and the appearance of spontaneous magnetization), and the paramagnetic ball changes its radius (Fig. 4.2a), thus changing its volume $\Delta V / V$, i.e., causing spontaneous (volume) magnetostriction. The ball becomes ferromagnetic and grows in size. At the same instant, the second-order phase transition occurs at the Curie point, and the appearance of spontaneous magnetostriction generates an elastic wave in the ferromagnet, which can be used for performing test operations.
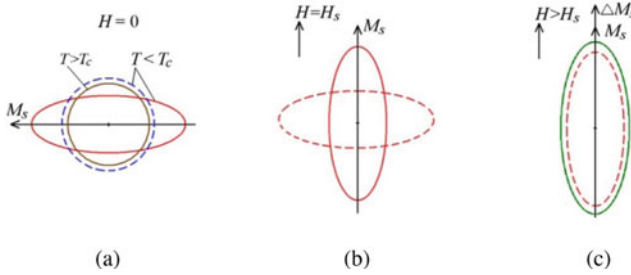
Fig. 4.2 Magnetostrictive effects in a ball-shaped one-domain crystal

For example, the thickness of locally water-cooled hot-rolled metal is tested this way.

Crystallographic anisotropy energy At the same time, with the appearance of spontaneous magnetostriction, below the Curie point there appear magnetic forces of the lattice, having anisotropy, and the ferromagnetic ball turns into an ellipsoid (Fig. 4.2a). The lower the temperature, the stronger is the manifestation of the anisotropic magnetic forces. For different crystallographic directions of iron, magnetostriction has different behaviors under magnetization (Fig. 4.3).

Linear magnetostriction and paraprocess magnetostriction When an ellipsoid (Fig. 4.2a) is placed in a growing magnetic field H, the vector M begins to rotate and, accordingly, the ellipsoid changes its shape and spatial position (linear magnetostriction), Fig. 4.2b. Linear magnetostriction increases with the field and reaches saturation λ_S in the field H_s. In fields above technical saturation ($H > H_s$), magnetization in the paraprocess region acquires an increment ΔM_s, and the ellipsoid slightly changes its volume (Fig. 4.2c), this being paraprocess magnetostriction. The case of the one-domain state under study is the model. In actual ferromagnets, a multidomain structure appears below the Curie point, which is also shown in Fig. 4.4 as the Landau–Livshits model. A ferromagnet is divided into individual magnetic domains, each being magnetized to saturation. Principal (180°) and closure (90°, reducing the magnetostatic energy) domains are formed in iron. A schematic change in the orientation of magnetic moments inside a 180°. Bloch domain wall (a transi-

Fig. 4.3 Magnetostriction in an iron single crystal for different crystallographic directions
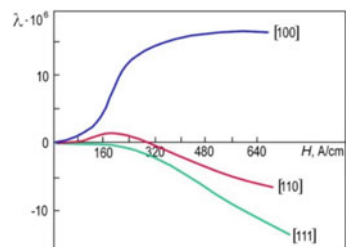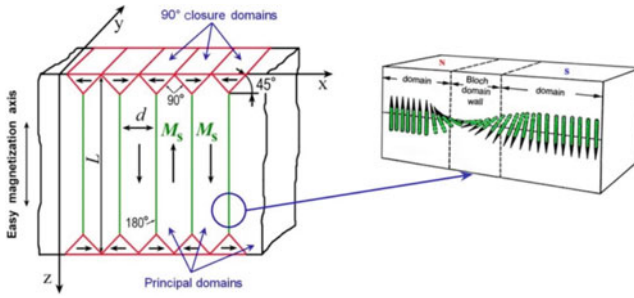
Fig. 4.4 The structure of plane parallel 180° and 90° closure domains in a magnetically uniaxial crystal

tion layer between the domains) is shown in Fig. 4.4. The appearance of 90° closure domains induces magnetostrictive strain energy represented by equation (4.4). The volume of the domains changes under magnetization, and so do the magnetization directions in each of them; however, the change in the magnetostrictive strain energy is affected only by a change in the volume of 90° domains. Magnetostrictive strain in 180° domain walls is here omitted since its value is too low.

4.3 The Effect of Changes in Metal Structure and Stress-Strain State

The change in the structural state under external action (e.g., heat treatment or deformation) is accompanied by a change in all the here-discussed kinds of energies and, consequently, the domain structure of a ferromagnet, and this is reflected in the magnetoelastic behavior, Fig. 4.5. Magnetostriction is sensitive to the structural changes occurring under heat treatment; therefore, the magnetoelastic parameters must also sense the changes taking place in the structure of a material, i.e., magnetostriction and the magnetoelastic parameters can be used to evaluate structural changes in ferromagnetic materials.

Formation of magnetic texture Acting elastic strains form a special domain structure (the so-called magnetic texture), which governs the processes of magnetization and magnetic reversal in a ferromagnet. Figure 4.6 demonstrates that, if magnetostriction is positive ($\lambda > 0$) and there are tensile strains ($\sigma > 0$), the domain structure is rearranged so that there appears a predominant "easy axis" direction of the magnetization vectors, and magnetization reversal in the direction of stresses becomes easier, see Fig. 4.6. Under compression ($\sigma < 0$), an "easy plane" magnetic texture is formed, so that a perpendicular arrangement of magnetic vectors becomes prevailing and magnetization reversal becomes more difficult, see Fig. 4.6. In turn, the rearrangement of the domain structure affects the behavior of magnetostriction. It
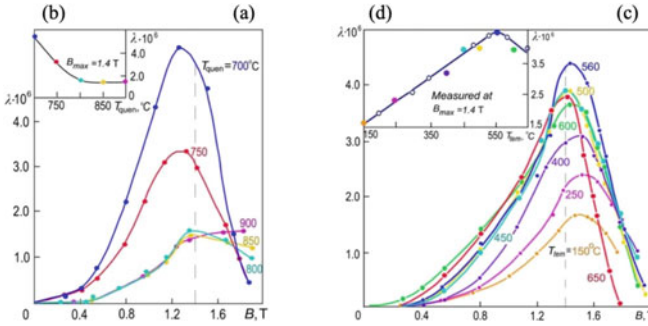
Fig. 4.5 The effect of heat treatment (quenching (**a**, **b**) and tempering (**c**, **d**)) on the magnetostriction of the 34KhN3M structural steel (0.34% C, 1% Cr, 1% Ni, and 35% Mo)

Fig. 4.6 Formation of the "easy axis" and "easy plane" magnetic textures under tension and compression, respectively
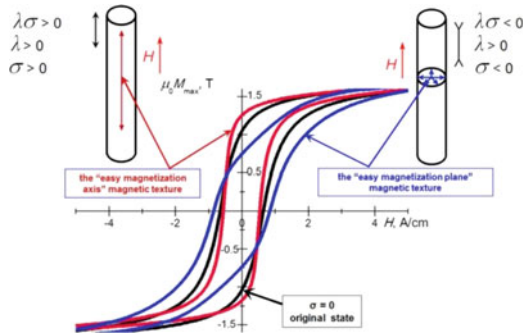
decreases under tension to become negative and increases under compression. This is visualized by the field dependences of longitudinal magnetostriction various values of applied tensile and compressive stresses for steel 45 (Fig. 4.7). An increase in the degree of alloying is accompanied by a change in the behavior of $\lambda(H)$. In high-alloyed steels, the region of negative values of λ decreases under tension or vanishes, this being due to the increasing elastic modulus, Poisson ratio, and magnetostrictive strain energy in alloyed steels (Fig. 4.8). Elastic strains form a magnetic texture in a ferromagnet and affect the processes of magnetization reversal. Figure 4.9 shows the evolution of hysteresis loops under uniaxial compression and tension. It is obvious that the hysteresis loops measured at different stresses, firstly, are sensitive to applied stresses and, secondly, have regions of intersection, where induction is poorly sensitive to stresses. Thus, the magnetoelastic characteristics determined in these induction regions are poorly sensitive to elastic strains.

It is seen from Fig. 4.9 that the applied stresses differently affect magnetization reversal in weak and strong magnetic fields. This can be more clearly exemplified by coercive force. The behavior of the coercive force H_c depending on stresses σ in strong fields is practically opposite to that in weak fields (Fig. 4.10a, b), i.e., the choice of the value of the magnetized field can affect the magnetoelastic behav-
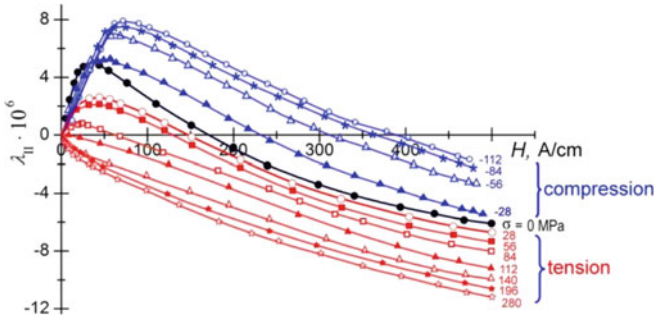
Fig. 4.7 The field dependences of magnetostriction under elastic compression and tension for steel 45 (C ∼ 0.45%)
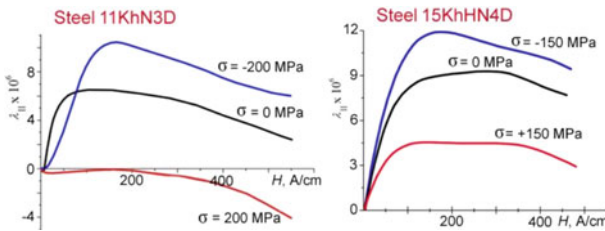
Fig. 4.8 The field dependences of magnetostriction for the steels 11KhN3D(0.11% C, 0.68% Mn, 0.88% Cr, 2.96% Ni, 0.27% Mo, 0.28% Si, 0.7% Cu) and 15KhN4D (0.15% C, 0.34% Mn, 0.69% Cr, 4.11% Ni, 0.13% Si, 1.23% Cu)
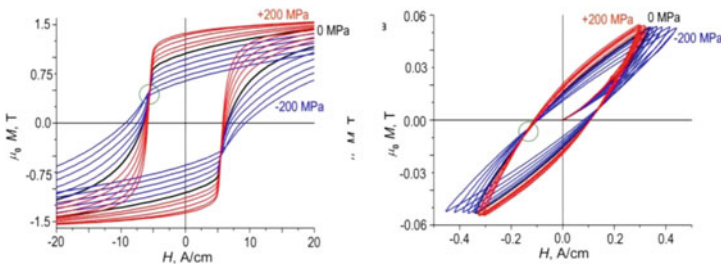
Fig. 4.9 Magnetic hysteresis loops for the 11KhN3D steel measured in strong (**a**—major loops) and weak magnetic fields (**b**—$B_{max} = 0.05$ T) as dependent on applied stresses. The loops change from the zero stress value, with a step of 40 MPa, to +200 MPa under tension and to −200 MPa under compression

ior. The effect of elastic strains (macrostresses) on the magnetic parameters of a ferromagnet provides a basis for creating various devices, such as force-measuring gauges, position sensors, displacement transducers, etc. [4, 7].

Up to now, we have been discussing the effect of macroscopic stresses on magnetic parameters. However, there are methods for evaluating microscopic stresses by magnetic parameters.
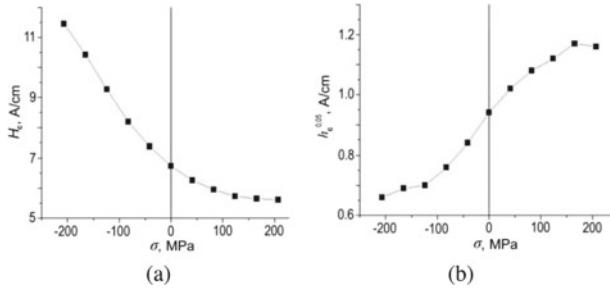
Fig. 4.10 The coercive force of the major (**a**) and minor cycles ($B_{max} = 0.05\,\text{T}$) (**b**) as dependent on compressive and tensile stresses

4.4 Microstress Evaluation Methods

All the evaluation methods deal with the redistribution of magnetoelastic energy under magnetization reversal in the course of the motion of 90° domain walls. Two evaluation methods are discussed in what follows, namely magnetoelastic acoustic emission and double electromagnetic acoustic transduction (EMAT). When moving, 180° and 90° domain walls interact with magnetic imperfections, e.g., inclusion-type defects. At the moment of 180° domain wall unpinning, an electromagnetic wave is emitted (Barkhausen electromagnetic effect); at the moment of 90° domain wall unpinning, both an electromagnetic wave and an ultrasonic wave (magnetoelastic acoustic emission) are emitted, the nature of the latter being associated with the redistribution of magnetoelastic energy with the motion of 90° domain walls. The recorded parameters of magnetoelastic acoustic emission correlate with the level of microstresses in a ferromagnet.

Magnetoelastic acoustic emission Using various parameters, one can correlatively evaluate macroscopic and microscopic stresses by the parameters of magnetoelastic acoustic emission (MAE) and Barkhausen jumps (BJ). It follows from Fig. 4.11 that the BJ parameters had better be used to evaluate compressive stresses (red curve), the parameters of magnetoelastic acoustic emission (blue curve) being preferable for tension. It is obvious from Fig. 4.12, where the heat-treated 34Kh3M steel is used as an example, that in certain heat treatment ranges (quenching followed by different temperings) the level of microstresses (blue curve) can be evaluated by the correlation method with the use of magnetoelastic acoustic emission (green curve).

Double electromagnetic acoustic transduction. Another way of making 90° domain walls move is double electromagnetic-acoustic transduction. In a ferromagnet placed in a strong polarizing field, an electromagnetic wave of a certain frequency is generated by an exciting coil at the air-ferromagnet interface; this wave makes 90° domain walls move and generates an elastic wave; the latter, in turn, going through the ferromagnet, excites an electromagnetic wave at the ferromagnet-air interface, which is recorded by a receiving coil. The recorded parameters are associated with
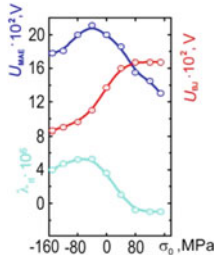
Fig. 4.11   Effect of elastic strain in the Fe+3%Si alloy on magnetostriction, the RMS values of the parameters of electromagnetic and magnetoelastic acoustic emissions
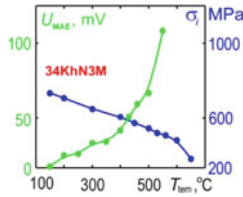
Fig. 4.12   The tempering temperature dependence of the parameters of magnetoelastic acoustic emission and the level of microstresses
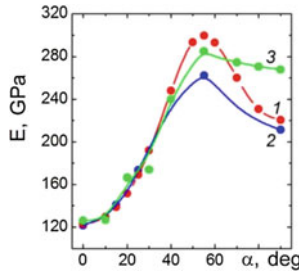
Fig. 4.13   The effect of crystallographic anisotropy on the values of the elastic modulus determined by different methods: calculated from sound velocity measurements (1); obtained from the EMAT spectrum for Fe-3%Si single-crystal strips (2); obtained from the EMAT spectrum for a Fe+3%Si single-crystal disk (3)

the elastic subsystem of the ferromagnet, and they correlate with some magnetoelastic parameters of the material, including the level of microstresses.

The applicability of the EMAT parameters is exemplified in Fig. 4.13 by the elastic modulus as dependent on the angle α between the [001] crystallographic direction of the specimen and the polarizing field. We can establish the existence of a correlation between the elastic modulus calculated from the direct measurements of sound velocity and the data obtained from the EMAT spectrum for single-crystal strips and a single-crystal disk in the case of the existing crystallographic anisotropy of the elastic modulus. It follows from Fig. 4.14 that the microdistortions (stresses)
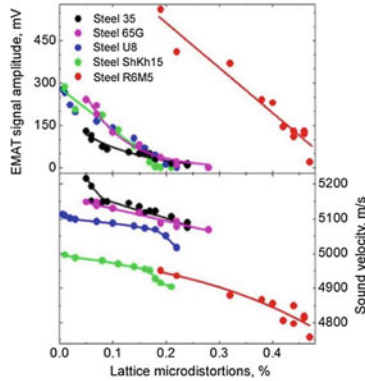
Fig. 4.14 The correlation of the EMAT signal and sound velocity parameters with crystal lattice microdistortions in heat-treated (quenched and tempered at different temperatures ranging between 150 and 650 °C) steels, namely 35($\sim$0.35% C), 65G ($\sim$0.65% C, $\sim$1% Mn), U8($\sim$0.8% C), ShKh15($\sim$0.9% C, $\sim$1.5% Cr), P6M5($\sim$0.85% C, $\sim$6% W, $\sim$5% Mo, $\sim$4% Cr, $\sim$2% V)
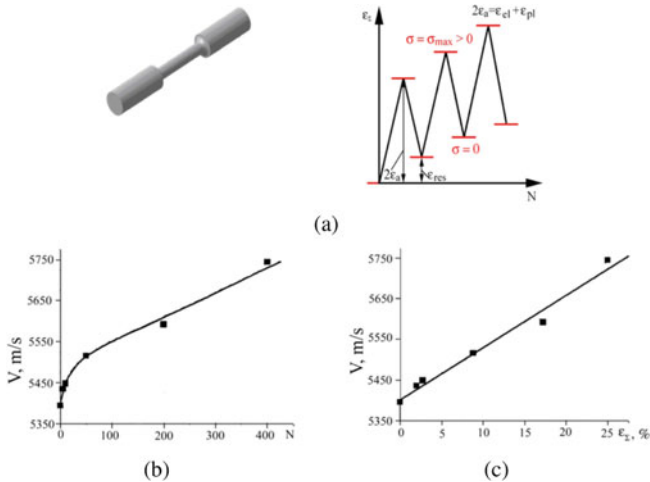
Fig. 4.15 Schematic diagram of the cyclic loading of a specimen (**a**); longitudinal sound wave ve-locity as dependent on the number of loading cycles (**b**) and the value of accumulated plastic strain (**c**) for specimens made of steel 45

in heat-treated steels can be evaluated by means of EMAT. The electromagnetic-acoustic characteristics can be used to evaluate strain-induced damage. Thus, for example, to evaluate low-cycle strain-induced damage, it is possible to use the value of sound velocity determined by means of double electromagnetic-acoustic trans-duction (Fig. 4.15). Besides, to evaluate damage high-cycle fatigue damage, we can use magnetic parameters, such as the Barkhausen jump parameters N and U measured in mutually perpendicular directions with the use of attached magnetic devices
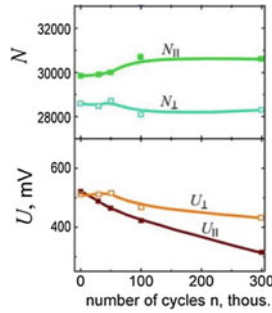
Fig. 4.16 The number of jumps N and the RMS values of Barkhausen noise voltage U, measured by attached magnetic devices, as dependent on the number of loading cycles for the 08G2B pipe steel (~0.08% C, ~1.7% Mn, ~0.3% Si, ~0.07% Nb)
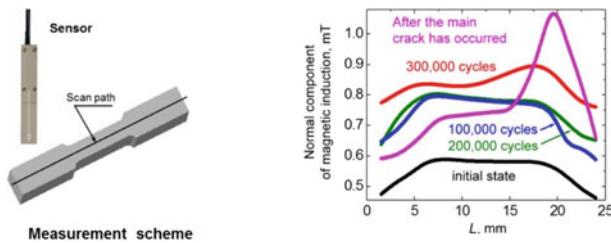
Fig. 4.17 The distribution of the normal component of the magnetic induction vector along the gauge part of a U10 steel specimen(~1% C) as dependent on the number of unidirectional zero-to-tension cycles with an amplitude of 0.6 yield stress
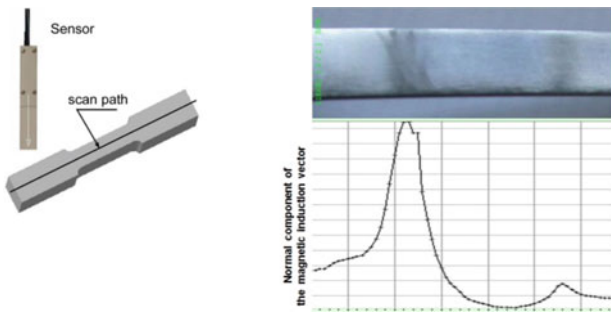
Fig. 4.18 The effect of plastic strain localization bands in a carbon steel specimen on its magnetic field

(Fig. 4.16). Using fluxgate transducers recording leakage magnetic fields, we can record the pre-failure stage, which precedes the formation of the main crack (red curve), see Fig. 4.17. In the case of plastic strain and localization of slip bands, they can also be detected, even under a paint layer, by surface scanning and recording the leakage fields from these bands (see Fig. 4.18).

4.5 Conclusion

Magnetoelastic phenomena area basis for creating various transducers designed to measure position, displacement (rotation), force, strain, and a liquid level using the well-known Villari, Guillemin, Wiedemann, Wertheim, and Matteucci effects. A number of magnetoelastic parameters can be used in nondestructive testing to evaluate applied macrostresses. Magnetoelastic parameters associated with the displacements of 90° domain walls, which correlate with changes occurring in the magnetoelastic subsystem of a ferromagnet, have been proposed to be used for evaluating microdistortions (microstresses).

References

1. Belov, K.P.: Elastic, Thermal and Electrical Phenomena in Ferromagnets. Izd-vo Tekh.-Teor. Liter, Moscow (1957). (in Russian)
2. Bozorth, R.M.: Ferromagnetism. Wiley-IEEE Press (1993). https://doi.org/10.1109/9780470544624
3. Garshelis, I.: A study of the inverse Wiedemann effect on circular remanence. IEEE Trans. Magn. **10**(2), 344 (1974)
4. Ginzburg, V.B.: Magnetoelastic Transducers. Energiya, Moscow (1970). (in Russian)
5. Golyamina, I.P.: (ed.): Ultrasound. Sovetskaya Entsiklopediya, Moscow (1979). (in Russian)
6. Gorkunov, E.S., Dragoshanskii, Yu.N., Khamitov, V.A.: Magnetoelastic acoustic emission in ferromagnetic materials. II. Effect of elastic and plastic strains on parameters of magnetoelastic emission. J. Nondestr. Test. **37**(12), 835 (2001). https://doi.org/10.1023/A:1016808500512
7. Gumanyuk, M.N.: Magnetoelastic Transducers in Automation. Tekhnika, Kiev (1972). (in Russian)
8. Klyuev, V.V. (ed.): Nondestructive Testing. Handbook, vol. 6, book 1: Magnetic Testing Methods. Mashinostroenie, Moscow (2004). (in Russian)
9. Lahyaoui, O., Lanfranchi, V., Buiron, N., Martin, F., Aydin, U., Belahcen, A.: Effect of mechanical stress on magnetization and magnetostriction strain behavior of non-oriented Si-Fe steels at different directions and under pseudo-DC conditions. Int. J. Appl. Electromagn. Mech. **60**(2), 299 (2019)
10. Vonsovsky, S.V.: Magnetism. Nauka, Moscow (1971). (in Russian)

Chapter 5
Fault Diagnosis in a Hydraulic Circuit Using a Support Vector Machine Trained by a Digital Twin

Rainer Haas and Kurt Pichler

Abstract This paper presents a novel approach for detecting failures in a hydraulic accumulator loading circuit. By measuring only the accumulator pressure, pump leakage and changes in the accumulator's pre-fill pressure can be detected. A hydraulic circuit model, which is part of the digital twin, is used to acquire simulated data for the development and training of the condition monitoring method. Especially, it is used to generate data containing different system failures. In a feature engineering step, these data are used to extract meaningful features from the pressure signal. Then an SVM classifier is applied to the feature space to classify the different failure modes. For evaluation, the classifier is applied to different failure cases, and the proposed approach is compared to a commonly used approach that observes the loading time. The results show that the proposed approach is significantly better than the commonly used one especially in the case of multiple failures.

5.1 Introduction

Digital Layers (DL) of industrial products are more and more on the spot. These entities are also called Digital Twins (DT), see [2] p. 92ff, [15], [10]—just to list a few papers dealing with digital twins. Grieves and Vickers [2] state a distinction between two DT types, the Digital Twin Prototypes (DTP) and Digital Twin Instances (DTI). Shortly, it can be summarized that the DTP contains all artifacts and information needed to design, optimize, and produce a certain product. This includes, e.g., the physical system models used in the development process. Where, however, the DTI type is linked to a certain product instance, containin all needed design artifacts, as well as the product's life time information like measurement data (from production or operation).

R. Haas (✉) · K. Pichler
Linz Center of Mechatronics GmbH, Area Drives, Altenberger Strasse 69, 4040 Linz, Austria
e-mail: rainer.haas@lcm.at

K. Pichler
e-mail: kurt.pichler@lcm.at

47

Besides DTs, it is important to say a few words about Cyber Physical Systems (CPS), see [7] and [14], and how this concept is related to our work. As written in the previous two cited references, CPSs are integrations of computational resources and physical mechanisms in different tiers of interlacement. As an example, the computational resource can monitor (observe) or even control the mechanism, whereas this can be done at the machine controller or from more abroad computational resources. For the sake of simplicity, we break this concept down to the following three cases, taking the time synchronicity between the simulation time of the DT's model and the real-time system, as well as the distance of the computational resource from the mechanism into account.

1. Online and synchronous DTs,
2. online but asynchronous DTs,
3. offline and therefore asynchronous DTs.

Regarding the list above, so to say the classical one is working like a conventional observer according to control theory. The second kind is also running on embedded computers but the evaluation is not done in "real time"—it is done in parallel whenever required. A much larger class of problems can be treated because real-time restrictions can almost exclusively be neglected accepting an increase of needed data storage. The last one, the offline one, needs the same data requirements as the online asynchronous one but has the ability to use computation resources, which are not necessarily located in the vicinity.

This paper won't go deeper into this field of abstract definitions. Our goal is to bring this concept closer to practical applications presenting a realized example. At first glance, we are dealing with the third case especially using the DTI concept because the used data is gathered by an embedded system and post-processed by a distant computing resource using a model created during the design process. Results are obtained in a way that they should be easily portable to the DTs of the second kind.

The main concept for creating a DT can be summarized in the following steps:

1. Definition of system goals and requirements;
2. Create mathematical and geometric system models for system development;
3. Set up the real system;
4. Gather measurements data in order to validate the final design model;
5. If necessary, update the final model in order to fit the real entity
   ⇒ Digital Layer/Digital Twin;
6. Use the DT for further purposes like condition monitoring, …

This paper is organized as follows: In Sect. 5.2, the technical problem and the favored solution technique are discussed whereas Sect. 5.3 contains the structure of the hydraulic circuit and the equations for physical modeling. The built DT is used in Sect. 5.4 dealing with fault diagnosis. Finally, results and conclusions are provided in Sects. 5.5 and 5.6, respectively.

5.2 Problem Statement

The complexity of fault diagnostics, respectively, condition monitoring in hydraulics relates strongly with the system under study. Especially in the case of large hydraulic systems containing various elements, simple—respectively trivial—Condition Monitoring (CM) features do not always lead to a good fault diagnostics.

In the following, we will have a look at a broadly used simple hydraulic circuit, the accumulator loading circuit. Even this example shows that simple CM features can lead to misinterpreted faults, respectively, hidden fault cases. Nevertheless, it is important to build up proper simulation models, modeling all necessary physical effects of the system under study. Such models can later be used to train classification algorithms without or even be less reliant on real-world measurements. A photo and a hydraulic scheme of the system are depicted in Fig. 5.1a, b. The system contains three relevant main elements, i.e., the pump, the hydraulic accumulator, and the pressure relief valve. The following points describe a typical operation mode.

- The motor of the pump is started if the pressure drops below a critical pressure level. It runs at a constant speed.
- If the pressure in the accumulator exceeds a certain level p_2, the motor is turned off.
- The system waits until the pressure drops again below the lower threshold—the consuming elements of the connected hydraulic circuit take energy out of the accumulator.

In the following paper, a model of the hydraulic circuit is built and fitted to measurements of the real hydraulic system. This updated model is later called a

(a) Photo of the test rig

(b) Hydraulic scheme
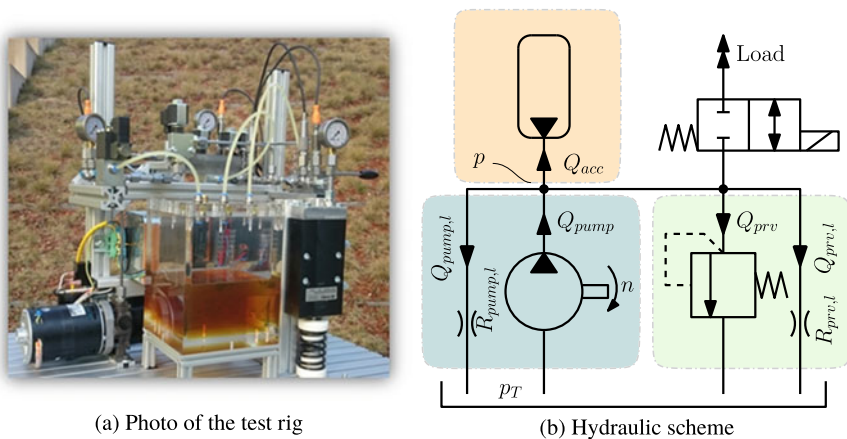
Fig. 5.1 Hydraulic system

digital twin. Finally, the DT is used to generate data in order to train the classification algorithm.

The performance of the algorithm is certainly limited by the quality of the training data. Due to the fact that it is generally not trivial to model a pump or an accumulator fault, we focused in the first step on two effects that can be modeled with reasonable effort, i.e., the accumulator's pre-filling pressure and a pump leakage change. At this point, it has to be stated that the assumptions, taken as physical fault models, are a simple approach and can therefore not be strictly applied to any other hydraulic accumulator loading circuit. The detailed system under study has to be analyzed properly. In our case, the used models are sufficient.

5.3   Hydraulic Circuit and Its Digital Layer

The simulation model representing the Digital Layer is declared in the current section. As previously discussed, this paper focuses on the application of the concept of digital representatives in the overall system design process. Therefore, the hydraulic simulation model is kept simple not to lose focus on the underlying overall concept, see Sect. 5.1.

The hydraulic pump is modeled as a fixed displacement pump with the displacement ΔV, see [9] p. 139ff. It is driven at nominal speed n or stopped. The flow rate Q_{pump} can be calculated according to

$$Q_{pump} = \Delta V \cdot n. \tag{5.1}$$

The system also contains a pressure relief valve which is modeled by the flow characteristic of an orifice, see [9] p. 48ff, supplemented with a linear pressure depending opening.

$$Q_{prv} = \begin{cases} 0 & p \leq p_{prv,0} \\ Q_{prv,n} \cdot \sqrt{\frac{p_{prv,S}}{p_{prv,n}}} \cdot \frac{p - p_{prv,0}}{p_{prv,S} - p_{prv,0}} & p_{prv,0} < p \leq p_{prv,S} \\ Q_{prv,n} \cdot \sqrt{\frac{p}{p_{prv,n}}} & p > p_{prv,S}. \end{cases} \tag{5.2}$$

In the typical operating mode, the opening pressure of the valve is turned up to a level higher than the max. accumulator loading pressure in order to be able to load it. So it has no direct suggested influence on the operating system. Nevertheless, measurements showed that this component has a not negligible leakage. In order to fit the measured pressure during the charging, it is important to model the leakage of the pressure relief valve. A sufficient model is a constant hydraulic resistance $R_{prv,leak}$. In particular, the laminar flow through a rectangular gap, [9] p. 45ff, was used writing

(a) Screenshot of the simulation model

(b) Pressure during accumulator loading, with and without leakage model for the pressure relief value
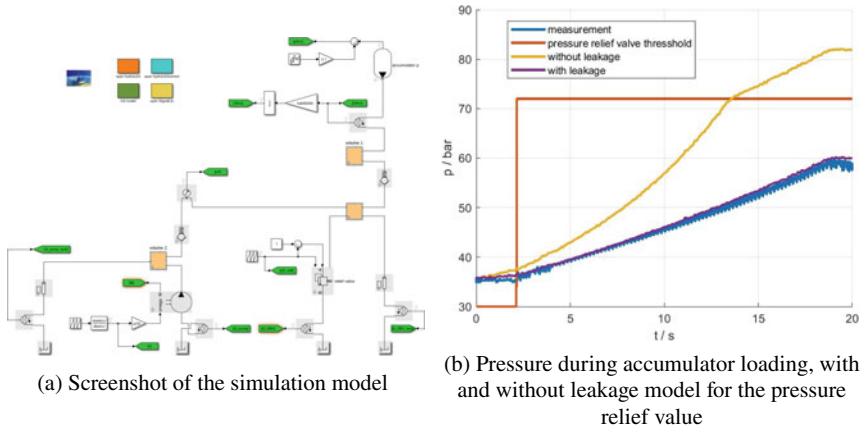
Fig. 5.2 Simulation model and results

$$R_{prv,leak} = \frac{12 \cdot \eta \cdot L}{b \cdot h^3}, \tag{5.3}$$

$$Q_{prv,leak} = \frac{\Delta p}{R_{prv,leak}}. \tag{5.4}$$

The pressure build up in the accumulator reads

$$\frac{dp}{dt} = \frac{p \, \kappa}{V_{gas,0} \cdot \left(\frac{p_{gas,0}}{p}\right)^{\frac{1}{\kappa}}} \cdot \left(Q_{pump} - Q_{prv} - Q_{prv,leak}\right). \tag{5.5}$$

Figure 5.2b shows the comparison of the simulation result and the measurement. It can be seen that the leakage model of the pressure relief valve is essential for a good model measurement correlation.

The resulting model can now be extended by the suggested failure cases/models:

- Pump leakage and
- reduction of the accumulator's pre-filling pressure.

The pump leakage $Q_{pump,leak}$ is modeled using a laminar hydraulic resistance $R_{pump,init}$. The degree of wear is emulated using the scaling factor m_p. A measure of the pressure drop of the accumulator is the subtractor s_a. It denotes the amount of lost gas pre-fill pressure. The resulting equations read

$$R_{pump,leak} = m_p \cdot R_{pump,init},\tag{5.6}$$

$$Q_{pump,leak} = \frac{p - p_T}{R_{pump,leak}},\tag{5.7}$$

$$p_{gas,0,fail} = p_{gas,0} - s_a.\tag{5.8}$$

The resulting dynamical model of the DT reads

$$\frac{dp}{dt} = \frac{p\,\kappa}{V_{gas,0} \cdot \left(\frac{p_{gas,0,fail}}{p}\right)^{\frac{1}{\kappa}}} \cdot \left(Q_{pump} - Q_{pump,leak} - Q_{prv} - Q_{prv,leak}\right).\tag{5.9}$$

Data generated using this model can now be used to train and test fault diagnosis methods.

5.4 Fault Diagnosis

For fault diagnosis in the hydraulic circuit, we employed a data-driven approach trained with data from the digital twin. For that purpose, data with different pump leakage and accumulator pressure were simulated. In particular, we simulated data on a grid of $m_p \in [0.5, 4]$ and $s_a \in [0, 8]$. Data of the different fault states,

- no fault $\left(m_p \leq 1.6 \text{ and } s_a \leq 0.8\right)$,
- only pump leakage $\left(m_p > 1.6 \text{ and } s_a \leq 0.8\right)$,
- only decreased accumulator pressure $\left(m_p \leq 1.6 \text{ and } s_a > 0.8\right)$,
- pump leakage and decreased accumulator pressure $\left(m_p > 1.6 \text{ and } s_a > 0.8\right)$,

were used for feature engineering. The extracted features and the classification method are described in more detail in the following subsections.

5.4.1 Feature Extraction

In feature engineering, we extracted a number of features from the raw data. By performing some tests with the wrapper as well as filter feature selection, the combination of two features turned out to be best. The first feature is the loading time Δt, which is defined as the time from starting the pump until the target pressure is reached, i.e.,

$$\Delta t = t_n - t_1,\tag{5.10}$$
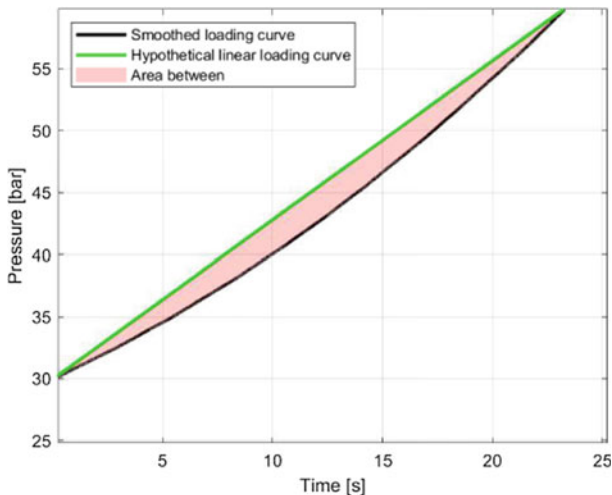
Fig. 5.3 Definition of feature $\Delta\kappa$: area between the smoothed pressure loading curve and the hypothetical linear loading curve

where t_1 denotes the time when the pump starts and t_n denotes the time when the target pressure in the accumulator is reached.

The second feature $\Delta\kappa$ is somehow related to the curvature of the pressure loading cycle. It measures the area between the actual pressure loading curve over time and the (hypothetical) linear loading curve (Fig. 5.3). In the first step, the actual pressure loading curve $p(t)$ is smoothed. Since the signal $p(t)$ is actually discrete with values $p_1, \ldots, p_n$ at equidistant time instances $t_1, \ldots, t_n$, we can utilize the Whittaker smoother [16] for removing measurement noise. In this approach, the smoothed signal $p_1^s, \ldots, p_n^s$ is determined by minimizing the cost function

$$f = \sum_{i=1}^{n} \left(p_i - p_i^s \right)^2 + \lambda \cdot \sum_{i=i}^{n-d} \left(\Delta^d p_i^s \right)^2. \qquad (5.11)$$

The parameter $d \in \mathbb{N}$ defines the order of the smoothness measure, for instance, $\Delta^1 p_i^s = p_{i+1}^s - p_i^s$ and $\Delta^2 p_i^s = \left(p_{i+2}^s - p_{i+1}^s \right) - \left(p_{i+1}^s - p_i^s \right)$; typical values are $d = 1$ and $d = 2$. The Lagrange multiplier λ [13] weights the contribution of the smoothness measure to the cost function: the higher λ, the smoother the resulting signal p^s. Rewriting the cost function in matrix form (for details see [3]) yields

$$f = \left\| p - p^s \right\|_2^2 + \lambda \cdot \left\| D \cdot p^s \right\|_2^2, \qquad (5.12)$$

with a matrix $D \in \mathbb{R}^{(n-d)\times n}$ such that

$$D \cdot p^s = \sum_{i=1}^{n-d} \Delta^d p_i^s \cdot e_i. \tag{5.13}$$

Here,

$$e_i = \begin{pmatrix} 0 \\ \vdots \\ 0 \\ 0 \\ 1 \\ 0 \\ \vdots \\ 0 \end{pmatrix} \begin{array}{l} \\ \\ \leftarrow i-1 \\ \leftarrow i \\ \leftarrow i+1 \\ \\ \end{array} \tag{5.14}$$

is the i-th vector of the canonical basis [6] of $\mathbb{R}^{n-d}$. By computing the first partial derivative of the cost function f with respect to p^s and solving it for zero, the cost is minimized. Thus, the partial derivative

$$\frac{\partial f}{\partial p^s} = -2 \cdot (p - p^s) + 2 \cdot \lambda \cdot D^T \cdot D \cdot p^s \tag{5.15}$$

is solved for zero. This leads to the solution

$$p^s = \left(I + \lambda \cdot D^T \cdot D\right)^{-1} \cdot p \tag{5.16}$$

with $I \in \mathbb{R}^{n \times n}$ representing the unit matrix.

In the second step, the hypothetical linear loading curve is constructed. This is done by solving the system of equations

$$\begin{aligned} t_1 \cdot k + d &= p_1 \\ t_n \cdot k + d &= p_n \end{aligned} \tag{5.17}$$

for k and d. This gives the solution

$$k = \frac{p_1 - p_n}{t_1 - t_n} \tag{5.18}$$

and

$$d = \frac{p_n t_1 - p_1 t_n}{t_1 - t_n} \tag{5.19}$$

and therefore, the linear equation

$$p^l(t) = \frac{p_1 - p_n}{t_1 - t_n} \cdot t + \frac{p_n t_1 - p_1 t_n}{t_1 - t_n} \qquad (5.20)$$

for the linear loading curve p^l. The area A between the linear loading curve p^l and the smoothed actual loading curve p^s is subsequently the integral value

$$A = \int_{t_1}^{t_n} \left| p^l(t) - p^s(t) \right| \cdot dt. \qquad (5.21)$$

Since the smoothed actual loading curve p^s is a discrete measurement vector, the integral is substituted by a sum, and the second feature $\Delta\kappa$ is defined as

$$\Delta\kappa = \sum_{i=1}^{n-1} \frac{\left| \left(p_i^l - p_i^s\right) + \left(p_{i+1}^l - p_{i+1}^s\right) \right|}{2} \cdot (t_{i+1} - t_i) \qquad (5.22)$$

where $p_i^l = p^l(t_i)$.

5.4.2 Classification

As in a lot of application settings, the degree of non-linearity is unknown in advance, a very flexible type of machine learning classifier is used for classification, the SVMs [12], which can handle decision boundaries between classes with arbitrary complexities. SVMs are widely used for a great range of classification problems [8, 17]. Let $y \in \{-1, 1\}$ be the class information of an n-dimensional feature vector $z \in \mathbb{R}^n$; in this application, the feature vector $z \in \mathbb{R}^2$ would be

$$z = \begin{pmatrix} \Delta t \\ \Delta\kappa \end{pmatrix}. \qquad (5.23)$$

Let y_i, $i = 1, \ldots, m$ be the known class information of m feature vectors z_i, $i = 1, \ldots, m$, i.e., of accumulator loading cycles. SVMs try to find a decision boundary which maximizes the margin between two classes. Based on this motivation, it falls into the class of "flexible discriminants" [4], and an optimization problem can be analytically derived and formulated in the following way:

$$\begin{aligned} \min_{w,b,\xi} \quad & \frac{1}{2} \cdot w^{\mathsf{T}} \cdot w + C \cdot \sum_{i=1}^{n} \xi_i \\ \text{subject to} \quad & y_i \left(w^{\mathsf{T}} \cdot \phi(z_i) + b \right) \geq 1 - \xi_i \\ & \xi_i \geq 0. \end{aligned} \qquad (5.24)$$

Here, w denotes the weights and b denotes the bias; for more details, see for instance [12]. The function ϕ maps the feature vectors into a higher dimensional space. In this higher dimensional space, a linear separating hyperplane with maximal margin is found. The parameter $C > 0$ penalizes the error term. Since SVM only needs to compute scalar products in the high-dimensional space, it uses the kernel trick [11]. The scalar products in the higher dimensional space are computed by a kernel function $K\left(z_i, z_j\right)$ without actually transforming the data to the high-dimensional space using the function ϕ. The kernel function has to fulfill Mercer's condition [1]. A number of kernel functions have been proposed by researchers. In this application, one of the basic ones is used, the radial basis function, which gave the best results for the application scenario. This kernel is defined as

$$K\left(z_i, z_j\right) = \mathrm{e}^{-\gamma\|z_i - z_j\|^2}, \ \gamma > 0. \tag{5.25}$$

Finally, the estimated class of a new feature vector z is determined by

$$y = \mathrm{sgn}\left(w^\mathsf{T} \cdot \phi\left(z\right) + b\right). \tag{5.26}$$

Using the kernel function instead of transforming to the high-dimensional space and calculating the scalar products there, the estimated class information can be easily evaluated. The time consumption of training the classifier strongly depends on the size of the training set and the parameters (basically C and γ). For obtaining good parameters, grid search can be applied [5]. The classification method can be extended to more than the two target classes that are described here.

5.5 Results

Before applying the proposed approach to the running system, a classifier has to be trained. For that purpose, we acquire training data on a meaningful grid for m_p and s_a with different fault states as mentioned in Sect. 5.4. This results in feature space as shown in Fig. 5.4. Based on that feature space, an SVM classifier as described in Sect. 5.4.2 was trained.

For evaluation of the method, we created some interesting test cases and compared the output of the SVM to the commonly used approach of observing the loading time Δt of the accumulator. In the commonly used approach, a pump leakage is detected when the loading time is significantly longer than in the nominal (fault-free) case. On the other hand, if the loading time is shorter than in the nominal case, a too low initial pressure of the accumulator is detected. The test cases (in the form of values of m_p and s_a), the true system state, and the system states inferred with the commonly used approach and the proposed approach are listed in Table 5.1. Furthermore, for each test case, the actual loading cycle (pressure over time) in comparison to a nominal loading cycle as well as the position of the actual cycle in the feature space is presented in
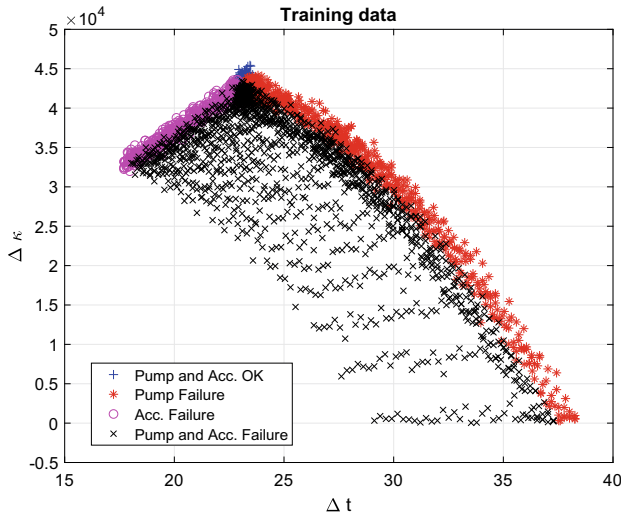
Fig. 5.4 Feature space for classifier training

Table 5.1 Application results

m_p	s_a	True system state	Approach Δt	Proposed approach
1	0	OK	OK	OK
3	0	Pump leakage	Pump leakage	Pump leakage
1	4	Low acc. pressure	Low acc. pressure	Low acc. pressure
3.9	7.6	Pump leakage and low acc. pressure	OK	Pump leakage and low acc. pressure
2	6.9	Pump leakage and low acc. pressure	Low acc. pressure	Pump leakage and low acc. pressure

Fig. 5.5a–e. In these figures, the colored areas represent the SVM classes according to the classes in Fig. 5.4.

The results show that the first three trivial cases (no fault/only pump leakage/only low accumulator pressure) are easily detectable by both methods. However, the latter two cases are more interesting. In the case of $m_p = 3.9$ and $s_a = 7.6$ (i.e., pump leakage and low accumulator pressure), the absolute loading time is approximately equal to the nominal case (Fig. 5.5d). Hence, the commonly used approach detects no fault. Since the curvature of the loading curve is different, the feature-based proposed approach detects both failures correctly. Moreover, in the case of $m_p = 2$ and $s_a = 6.9$ (i.e., pump leakage and low accumulator pressure), the absolute loading time is significantly shorter than in the nominal case (Fig. 5.5e). The commonly used
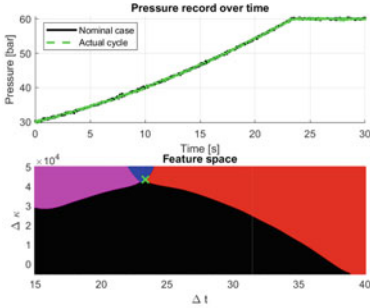
(a) Comparison of actual and nominal loading cycle (top) and position in feature space of actual cycle (bottom) for $m_p = 1$ and $s_a = 0$
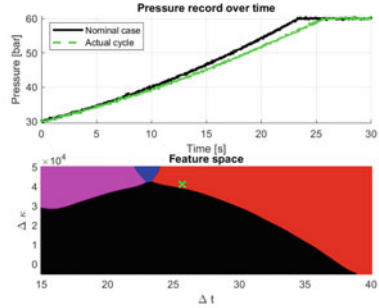
(b) Comparison of actual and nominal loading cycle (top) and position in feature space of actual cycle (bottom) for $m_p = 3$ and $s_a = 0$
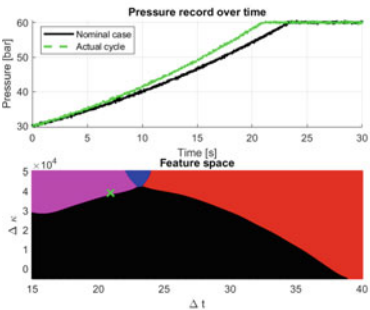
(a) Comparison of actual and nominal loading cycle (top) and position in feature space of actual cycle (bottom) for $m_p = 1$ and $s_a = 4$
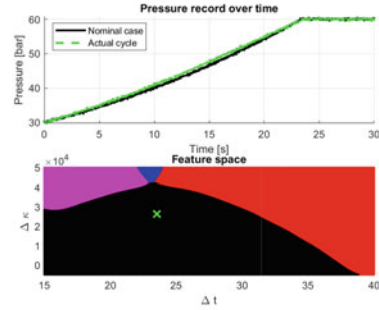
(d) Comparison of actual and nominal loading cycle (top) and position in feature space of actual cycle (bottom) for $m_p = 3.9$ and $s_a = 7.6$
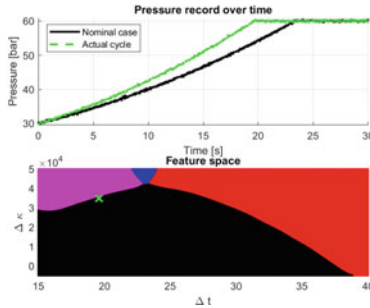
(e) Comparison of actual and nominal loading cycle (top) and position in feature space of actual cycle (bottom) for $m_p = 2$ and $s_a = 6.9$

Fig. 5.5 Examples in feature space

approach detects accordingly just low accumulator pressure, while the proposed feature-based approach detects again both failures correctly.

5.6 Conclusions

In this paper, a novel approach for detecting failures in a hydraulic accumulator loading circuit is proposed. Based on the shape of the pressure record over time, features are extracted and used for classification via SVM. The proposed method proves its advantage over the commonly used observation of the loading time especially in case of the multiple failures. Hence, the method can be used for monitoring the pump as well as the accumulator of the hydraulic circuit by measuring only the accumulator pressure. Compared to monitoring each component separately, this saves required sensors and therefore costs.

References

1. Courant, R., Hilbert, D.: Methods of Mathematical Physics. Interscience Publishers, Inc. (1953)
2. Grieves, M., Vickers, J.: Digital twin: mitigating unpredictable, undesirable emergent behavior in complex systems. Transdisciplinary Perspectives on Complex Systems, pp. 85–113. Springer (2017). https://doi.org/10.1007/978-3-319-38756-7_4
3. Eilers, P.H.: A perfect smoother. Anal. Chem. **75**(14), 3631–3636 (2003)
4. Hastie, T., Tibshirani, R., Friedman, J.: The Elements of Statistical Learning: Data Mining, Inference and Prediction. Springer, New York, Berlin, Heidelberg (2009)
5. Hsu, C.W., Chang, C.C., Lin, C.J.: A practical guide to support vector classification. Department of Computer Science, National Taiwan University (2003)
6. Kowalsky, H.J., Michler, G.: Lineare Algebra. de Gruyter (2003)
7. Lee, E.A.: Cyber physical systems: design challenges. Electrical Engineering and Computer Sciences University of California at Berkley, 23 Jan 2008
8. Ma, Y., Guo, G.: Support Vector Machines Applications. Springer, New York (2014)
9. Murrenhoff, H.: Grundlagen der Fluidtechnik, Teil 1: Hydraulik, 4. Shaker Verlag, Auflage (2005). ISBN 3-8265-9446-0
10. Rosen, R., Fischer, J., Boschert, St.: Next generation digital twin: an ecosystem for mechatronic systems? Siemens AG, Corporate Technology, 2019, 8th IFAC Symposium on Mechatronic Systems, 4–6 Sept 2019, Vienna, Austria
11. Schölkopf, B., Smola, A.J.: Learning with Kernels—Support Vector Machines, Regularization, Optimization and Beyond. MIT Press, London (2002)
12. Vapnik, V.N.: The Nature of Statistical Learning Theory. Springer, New York (1995)
13. Vapnyarskii, I.B.: Lagrange multipliers. In: Hazewinkel, M. (ed.) Encyclopedia of Mathematics. Springer (2001)
14. WikiPedia: Cyber-physical system. https://en.wikipedia.org/wiki/Cyber-physical_system
15. WikiPedia: Digital twin. https://en.wikipedia.org/wiki/Digital_twin

16. Whittaker, E.T.: On a new method of graduation. Proc. Edinb. Math. Soc. **41**(1), 63–75 (1923)
17. Wu, X., Kumar, V., Quinlan, J.R., Gosh, J., Yang, Q., Motoda, H., MacLachlan, G.J., Ng, A., Liu, B., Yu, P.S., Zhou, Z.H., Steinbach, M., Hand, D.J., Steinberg, D.: Top 10 algorithms in data mining. Knowl. Inf. Syst. **14**(1), 1–37 (2006)

Chapter 6
On Nonlinear Vibrations of Bimodular Beam Structures

Rudolf Heuer and Galeb El Chabaan

Abstract   The paper is concerned with the modeling and numerical solution of the dynamic response of the Bernoulli–Euler beams rigid in shear due to time-variant excitation. The beams are assumed to be homogeneous and show classical boundary conditions. However, they are composed of a bimodular material, thus behaving differently in tension and compression. Generally, bimodular beams can be modeled as effective two-layer laminates. However, their neutral axis depends on the curvature's sign. Thus, the equations of motion for flexural oscillations are developed by defining an effective composite layered structure with a discontinuous natural beam axis. The position of the natural axis follows from a (highly) nonlinear equation that is dependent on both the geometry of the cross-section and the elastic material properties. After an appropriate transformation, all calculations are formulated respecting an independent reference axis of the bimodular beam structure. Within a numerical study, structures of various cross-sections are considered showing the influence of the bimodular material on the dynamic response. When considering mode shape expansion, beams can be analyzed numerically by means of a modified Newmark method.

6.1   Introduction

Composites exhibiting load-dependent elastic properties cannot be treated as structures with, e.g., effective isotropic parameters. The stress–strain curve of these so-called bimodular materials is usually approximated by two straight lines with a slope discontinuity at the origin, see, e.g., [5]. A comprehensive study about the mechanical behavior of bimodular composite structures can be found in [1]. Publication [3]

R. Heuer (✉) · G. E. Chabaan
Research Unit of Structural Dynamics and Risk Assessment, Institute of Construction, Structural Dynamics and Building Technology, TU Wien, Vienna, Austria
e-mail: rudolf.heuer@tuwien.ac.at

G. E. Chabaan
e-mail: galeb.el.chabaan@tuwien.ac.at

focuses on the nonlinear bending of laminated fibrous composite beams by incorporating a higher-order shear deformation beam theory. Bert and Tran [2] analyze the transient response of moderately thick bimodular beams by means of the transfer-matrix method. An analytical solution of tapered bimodular beams can be found in [4]. The present contribution studies plane flexural vibrations of the bimodular Bernoulli–Euler beams. The equations of motion for flexural oscillations are developed by defining an effective composite layered structure. The position of the natural axis follows from a (highly) nonlinear equation that is dependent on both the geometry of the cross-section and the elastic material properties.

Beams of trapezoidal as well as the limit cases "rectangular" and "triangular" cross-sections are considered showing the nonlinear influence of the discontinuous natural beam axis on the dynamic response.

6.2 Mechanical Modeling

6.2.1 Kinematic Relations

Considering the beam to bend cylindrically, the displacement field is expressed as

$$
\begin{pmatrix} u(x,\zeta;t) \\ v(x,\zeta;t) \\ w(x,\zeta;t) \end{pmatrix} = \begin{pmatrix} u_S(x;t) + \zeta\,\psi(x;t) \\ 0 \\ w(x;t) \end{pmatrix} = \begin{pmatrix} \left(u_0(x;t) - \zeta_0(t)\,\psi(x;t)\right) + \zeta\,\psi(x;t) \\ 0 \\ w(x;t) \end{pmatrix}
$$
(6.1)

where the origin of the Cartesian (x,ζ)-coordinate system is located in the geometrical centroid of the cross-section, S. The axial and transverse (vertical) displacements are described by u and w, respectively. x represents the axial beam coordinate and $\psi(x;t)$ denotes the cross-sectional rotation, see Fig. 6.1. Neglecting the effect of transverse shear results in the kinematic Bernoulli–Euler hypothesis,

$$
\psi = -\partial w/\partial x = -w_{,x}
$$
(6.2)

and thus the linearized axial and shear strains become

$$
\begin{pmatrix} \varepsilon \\ \gamma \end{pmatrix} \equiv \begin{pmatrix} \varepsilon_x \\ \gamma_{xz} \end{pmatrix} = \begin{pmatrix} u_{,x} \\ \gamma_{xz} \end{pmatrix} = \begin{pmatrix} u_{0,x} + (\zeta_0 - \zeta)\,w_{,xx} \\ w_{,x} + \psi \end{pmatrix} = \begin{pmatrix} \varepsilon_0 + (\zeta_0 - \zeta)\,w_{,xx} \\ 0 \end{pmatrix}
$$
(6.3)
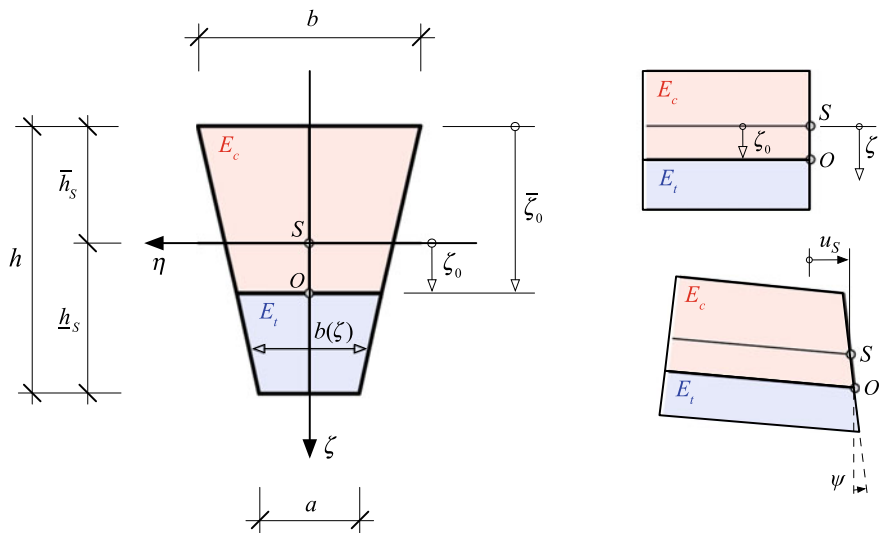
Fig. 6.1 Geometry and axial deformation of a bimodular beam in case of upward bending $(w_{,xx} < 0)$

6.2.2   Governing Equations of Elastic Bimodular Beams

The constitutive relations for a linear elastic beam can be formulated according to Hooke's law,

$$\sigma(x, \zeta; t) = E\varepsilon = E\left[\left(\zeta_0 - \zeta\right) w_{,xx} + \varepsilon_0\right] \tag{6.4}$$

where σ denotes the component of normal stress and E is time-independent Young's modulus. By spatial integration, the stress resultants, axial force N, and bending moment M become

$$\begin{pmatrix} N \\ M \end{pmatrix} = \begin{pmatrix} \int\limits_A \sigma \, \mathrm{d}A \\ \int\limits_A \sigma\zeta \, \mathrm{d}A \end{pmatrix} = \begin{pmatrix} \left(\overline{A}\,\zeta_0 - B\right) w_{,xx} + \overline{A}\,\varepsilon_0 \\ \left(B\,\zeta_0 - D\right) w_{,xx} + B\,\varepsilon_0 \end{pmatrix} \tag{6.5}$$

where $\overline{A}$ and D define extensional and bending stiffness, respectively, as

$$\overline{A} = \int\limits_A E \, \mathrm{d}A = \int\limits_h E(\zeta)\, b(\zeta) \, \mathrm{d}\zeta \tag{6.6}$$

$$D = \int\limits_A E \, \zeta^2 \, \mathrm{d}A = \int\limits_h E(\zeta) \, \zeta^2 \, b(\zeta) \, \mathrm{d}\zeta \tag{6.7}$$

B represents a coupling term that arises due to the reference coordinate system (η, ζ) which is kept fixed during the dynamic response,

$$B = \int\limits_A E \, \zeta \, \mathrm{d}A = \int\limits_h E(\zeta) \, \zeta \, b(\zeta) \, \mathrm{d}\zeta \tag{6.8}$$

Furthermore, the vertical distance to the neutral axis ζ_0 can be determined by means of the following condition,

$$\zeta_0 = \frac{B}{A} = \frac{\int_A E \, \zeta \, \mathrm{d}A}{\int_A E \, \mathrm{d}A} = \frac{\sum_{i=1}^2 \zeta_{s_i} E_i A_i}{\sum_{i=1}^2 E_i A_i} \tag{6.9}$$

that leads to a nonlinear algebraic equation for ζ_0. Expressing the stress resultants according to Eq. (6.5) and subsequent application of both the conservation of momentum and the conservation of angular momentum for an infinitesimal beam element render

$$N_{,x} = \left(\overline{A} \, \zeta_0 - B \right) w_{,xx} + \overline{A} \, \varepsilon_{0,x} = 0 \tag{6.10}$$

$$M_{,xx} = \left(B \, \zeta_0 - D \right) w_{,xxxx} + B \, \varepsilon_{0,xx} = \mu \, \ddot{w} - p \tag{6.11}$$

where

$$\mu = \int\limits_A \rho \, \mathrm{d}A = \int\limits_h \rho(x, \zeta) \, b(\zeta) \, \mathrm{d}\zeta \tag{6.12}$$

denotes the mass per unit length. When considering only vertical loads, p, the strain of the neutral axis ε_0 and its derivatives can be neglected in the equation of flexural deformation, Eq. (6.11), which finally leads to

$$\left(D - B \, \zeta_0 \right) w_{,xxxx} + \mu \, \ddot{w} = p \tag{6.13}$$

6.3 Considered Geometries

In the following section, beams of symmetric trapezoidal as well as the limit cases "rectangular" and "triangular" cross-sections are taken into account.

6.3.1 Trapezoidal Cross-Section

Considering beams with symmetric trapezoidal cross-section (see Fig. 6.1), the width can be expressed by a linear function as

$$b(\zeta) = b_0 + b_1\,\zeta \qquad b_0 = \frac{2\big(b^2 + b\,a + a^2\big)}{3\big(b + a\big)} \qquad b_1 = -\frac{2\,b^2 - b\,a - a^2}{h\big(2\,b + a\big)} \quad (6.14)$$

Determination of the stiffness parameters according to Eqs. (6.6–6.8) renders in case of the configuration "upward bending", $w_{,xx} < 0$,

$$\overline{A}^{(-)} = E_c\left[b_0\Big(\underline{h}_s\,\delta + \overline{h}_s\Big) + \frac{b_1}{2}\Big(\underline{h}_s^2\,\delta - \overline{h}_s^2\Big) - b_0\big(\delta - 1\big)\zeta_0 - \frac{b_1}{2}\big(\delta - 1\big)\zeta_0^2 \right]$$
(6.15)

$$B^{(-)} = E_c\left[\frac{b_0}{2}\Big(\underline{h}_s^2\,\delta - \overline{h}_s^2\Big) + \frac{b_1}{3}\Big(\underline{h}_s^3\,\delta + \overline{h}_s^3\Big) - \frac{b_0}{2}\big(\delta - 1\big)\zeta_0^2 - \frac{b_1}{3}\big(\delta - 1\big)\zeta_0^3 \right]$$
(6.16)

$$D^{(-)} = E_c\left[\frac{b_0}{3}\Big(\underline{h}_s^3\,\delta + \overline{h}_s^3\Big) + \frac{b_1}{4}\Big(\underline{h}_s^4\,\delta - \overline{h}_s^4\Big) - \frac{b_0}{3}\big(\delta - 1\big)\zeta_0^3 - \frac{b_1}{4}\big(\delta - 1\big)\zeta_0^4 \right]$$
(6.17)

and for "downward bending", $w_{,xx} > 0$,

$$\overline{A}^{(+)} = E_c\left[b_0\Big(\overline{h}_s\,\delta + \underline{h}_s\Big) - \frac{b_1}{2}\Big(\overline{h}_s^2\,\delta - \underline{h}_s^2\Big) + b_0\big(\delta - 1\big)\zeta_0 + \frac{b_1}{2}\big(\delta - 1\big)\zeta_0^2 \right] \quad (6.18)$$

$$B^{(+)} = E_c\left[-\frac{b_0}{2}\Big(\overline{h}_s^2\,\delta - \underline{h}_s^2\Big) + \frac{b_1}{3}\Big(\overline{h}_s^3\,\delta + \underline{h}_s^3\Big) + \frac{b_0}{2}\big(\delta - 1\big)\zeta_0^2 + \frac{b_1}{3}\big(\delta - 1\big)\zeta_0^3 \right]$$
(6.19)

$$D^{(+)} = E_c\left[\frac{b_0}{3}\Big(\overline{h}_s^3\,\delta + \underline{h}_s^3\Big) - \frac{b_1}{4}\Big(\overline{h}_s^4\,\delta - \underline{h}_s^4\Big) + \frac{b_0}{3}\big(\delta - 1\big)\zeta_0^3 + \frac{b_1}{4}\big(\delta - 1\big)\zeta_0^4 \right] \quad (6.20)$$

where the modular ratio

$$\delta = \frac{E_t}{E_c} \tag{6.21}$$

contains both Young's modulus of tension, E_t, and of compression, E_c. The geometric parameters $\underline{h}_s$ and $\overline{h}_s$ are shown in Fig. 6.1. The cross-section with the areas of compression and tension for both cases is presented in Fig. 6.2, where it is assumed that $E_t > E_c$. The position of neutral axis can be obtained from the lowest root of an algebraic equation of fifth order, that follows from Eq. (6.9). Equation (6.22) shows that equation exemplarily for the configuration of negative curvature, $w_{,xx} < 0$,
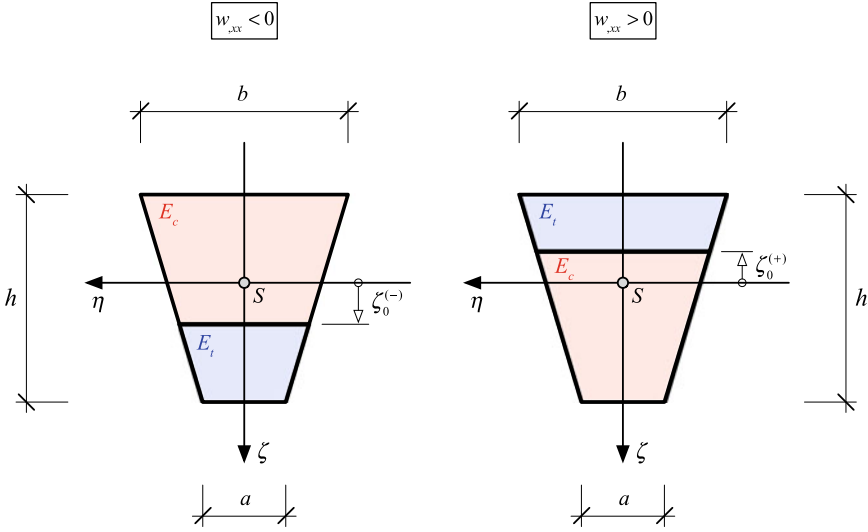
Fig. 6.2 Trapezoidal cross-section of a bimodular beam in the deformed state of negative and positive curvature

$$\left(b-a\right)^3\left(\delta-1\right)\overline{\zeta}_0^5 - h\left(6b^3 - 11b^2a + 4ba^2 + a^3\right)\left(\delta-1\right)\overline{\zeta}_0^4 +$$

$$+h^2\left[b^3\left(14\delta - 11\right) - b^2a\left(9\delta - 6\right) - ba^2\left(8\delta - 5\right) + 3a^3\delta\right]\overline{\zeta}_0^3 -$$

$$-h^3\left[b^3\left(16\delta - 6\right) + b^2a\left(9\delta - 6\right) - 12ba^2\delta - a^3\delta\right]\overline{\zeta}_0^2 +$$

$$+h^4\left(9b^3 + 16b^2a + ba^2 - 2a^3\right)\delta\overline{\zeta}_0 - 2h^5\left(b^3 + 3b^2a + 2ba^2\right)\delta = 0 \quad (6.22)$$

6.3.2 Limit Cases

In case of $a = b$, see Fig. 6.2, the governing equations lead to those of a bimodular beam with rectangular cross-section. Setting $a = 0$ describes a beam with the cross-section's geometry of an isosceles triangle.

Assuming again that $w_{,xx} < 0$, Eq. (6.22) reduces to

$$\left(\delta-1\right)\overline{\zeta}_0^2 - 2h\delta\overline{\zeta}_0 + h^2\delta = 0 \tag{6.23}$$

for the rectangular cross-section, and in case of the shape of an isosceles triangle,
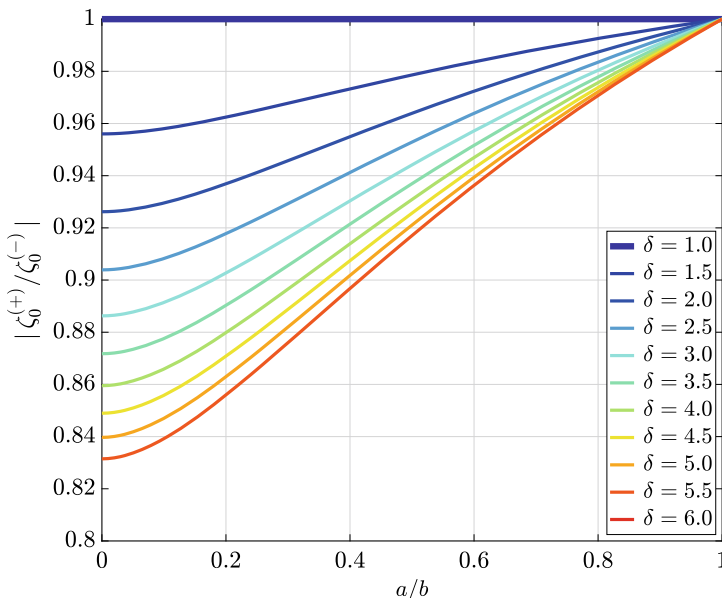
Fig. 6.3 $\left|\zeta_0^{(+)}/\zeta_0^{(-)}\right|$ depending on the aspect ratio a/b; $a = b$... limit case "rectangle"; $a = 0$... limit case "isosceles triangle"

$$\left(\delta - 1\right)\overline{\zeta}_0^5 - 6h\left(\delta - 1\right)\overline{\zeta}_0^4 + h^2\left(14\delta - 11\right)\overline{\zeta}_0^3 - h^3\left(16\delta - 6\right)\overline{\zeta}_0^2 + 9h^4\delta\overline{\zeta}_0 - 2h^5\delta = 0$$

(6.24)

In Eqs. (6.23) and (6.24), the parameter δ is again defined according to Eq. (6.21). Figure 6.3 shows the result of an extensive parameter study $\left|\zeta_0^{(+)}/\zeta_0^{(-)}\right|$ depending on the aspect ratio a/b, where both limit cases $a = b$ and $a = 0$ are included.

6.4 Numerical Studies

This numerical study deals with a simply supported beam of length of $l = 8$ m subjected to uniformly distributed vertical dynamic load, $p_0 = 5$ kN/m. The material of the beam is characterized by the following properties: Young's modulus of tension, $E_t = 12\,000$ kN/cm^2, Young's modulus of compresion, $E_c = 3\,000$ kN/cm^2, and density, $\rho = 2\,500$ kg/m^3. The damping effects are included by the assumption of a viscous damping with a modal damping ratio of $\zeta_n = 0.03$. Within this analysis, two cross-sections are considered, namely the trapezoidal and rectangular cross-section, whose parameters are listed in Table 6.1.

From Table 6.1, it is obvious that the dimensions of both cross-sections are chosen in such a way so that they have approximately equal cross-sectional area as well as approximately equal moment of inertia with respect to the η-axis. Table 6.2 contains

Table 6.1 Cross-section parameters

			Trapezoidal cross-section	Rectangular cross-section
Height	h	(cm)	33.00	30.00
Top width	b	(cm)	31.50	20.00
Bottom width	a	(cm)	5.00	20.00
Cross-sectional area	A	(cm^2)	602.25	600.00
Moment of inertia about η-axis	I_η	(cm^4)	45 051.16	45 000.00
Neutral axis position $(w_{,xx} < 0)$	$\zeta_0^{(-)}$	(cm)	5.25	5.00
Neutral axis position $(w_{,xx} > 0)$	$\zeta_0^{(+)}$	(cm)	−4.59	−5.00

Table 6.2 Numerical comparison of natural circular frequencies ω_0 (rad/s)

	Trapezoidal cross-section		Rectangular cross-section
	$\omega_0^{(-)}$	$\omega_0^{(+)}$	$\omega_0^{(-)} = \omega_0^{(+)}$
n = 1	65.38	58.68	61.68
n = 2	261.51	234.70	246.74
n = 3	588.39	528.08	555.16
n = 4	1 046.02	938.81	986.96
n = 5	1 634.41	1 466.90	1 542.13
n = 6	2 353.55	2 112.33	2 220.66
n = 7	3 203.44	2 875.12	3 022.56
n = 8	4 184.09	3 755.25	3 947.84

a comparison between the natural circular frequencies in the case of upward, $\omega_0^{(-)}$, and downward, $\omega_0^{(+)}$, bending motion for the first eight vibration modes.

In a first step, mode shape expansion in combination with Galerkin's procedure is applied to Eq. (6.13) to lead to a set of ordinary time-differential equations. The corresponding initial conditions of displacement and velocity are assumed to be zero. Their solution is found by Newmark's method by using *MATLAB R2018a*. Within this numerical investigation, the following two dynamic load cases are analyzed separately:

Load case 1—Sinusoidal periodic excitation

$$p(x, t) = p_0 \sin(\nu t)$$
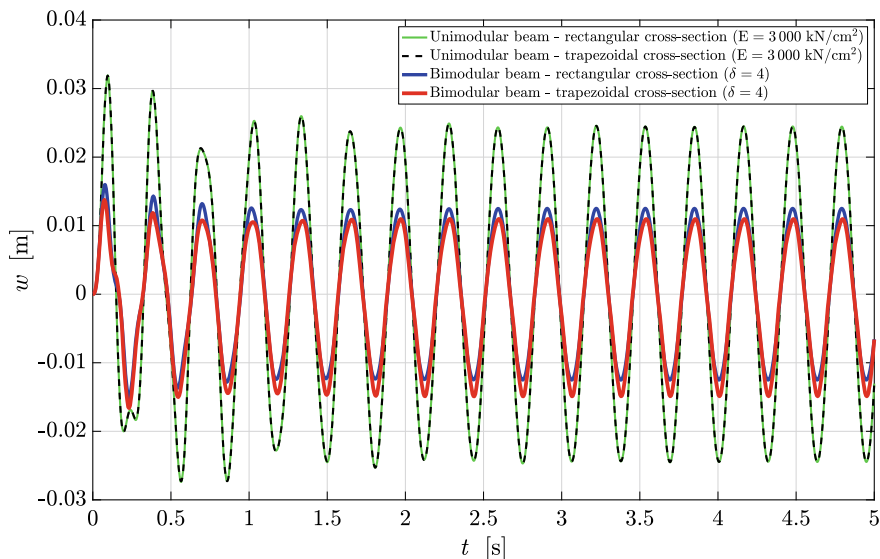
Fig. 6.4 Load case 1—comparison of displacement response $w(l/2; t)$

where $\nu = 20$ rad/s represents the exciting frequency.

Load case 2—Exponential pulse force

$$
p(x, t) = \begin{cases} p_0 \left(1 - \dfrac{t}{t_d}\right) e^{-2\, t/t_d} & t \leq t_d \\[2mm] 0 & t \geq t_d \end{cases}
$$

where $t_d = 0.5$ s is the exponential pulse duration.

The dynamic responses of the systems are compared in Figs. 6.4 and 6.5.

The dynamic response of the bimodular beam strongly depends not only on the modular ratio δ but also on the geometry of the cross-section. Figures 6.4 and 6.5 indicate that, based on different bending stiffness, there are significant differences between the amplitudes of displacement response of unimodular and bimodular beam. The effect of the geometry of the cross-section on the amplitude and period of the vibration is also graphically illustrated. As can be seen, if $E_t > E_c$, the downward bending amplitudes of the bimodular beam with trapezoidal cross-section are larger than the upward one, while the beam with rectangular cross-section has equal amplitudes in both bending cases. The reason for that is the influence of the cross-section geometry on finding the neutral axis position (hence on determining the stiffness and frequency), whose absolute values are different for negative and positive curvatures in the case of the trapezoidal but equal in the case of the rectangular cross-section.
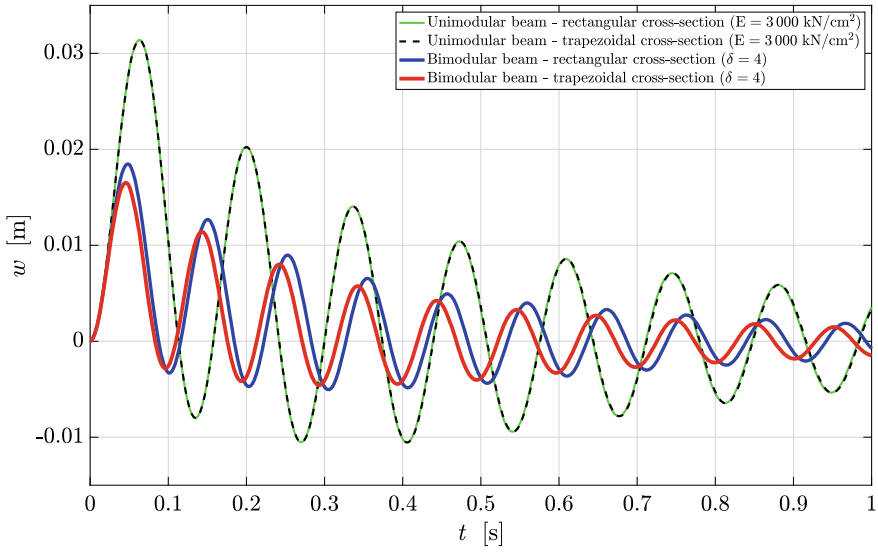
Fig. 6.5 Load case 2—comparison of displacement response $w(l/2; t)$

Because of that, the period of vibration of the bimodular beam with trapezoidal cross-section is also affected by curvature-dependent frequency.

6.5 Conclusions

Bimodular beams can be modeled as effective two-layer laminates. However, their neutral axis depends on the curvature's sign and therefore shows discontinuous behavior. The position of that natural axis follows from a nonlinear equation depending on both the geometry of the cross-section and the elastic material properties. Thus, an independent reference axis must be used when formulating the equations of motion for flexural oscillations.

Within numerical studies, the dynamic response of simply supported beams with trapezoidal as well as rectangular cross-section is analyzed for transient sinusoidal and exponential excitation. Comparison to the response of unimodular beams shows a significant influence of the nonlinear bimodular effect.

References

1. Bert, C.W., Reddy, J.N.: Mechanics of bimodular composite structures. Report OUAMNE-82-4, Office of naval Research, Arlington (1982)
2. Bert, C.W., Tran, A.D.: Transient response of a thick beam of bimodular material. Earthq. Eng. Struct. Dyn. **10**, 551–560 (1982)
3. Ghazavi, A., Gordaninejad, F.: Nonlinear bending of thick beams laminated from bimodular composite materials. Compos. Sci. Technol. **36**, 289–298 (1989)
4. Jardan, D.K.: Analytical solution of tapered bimodular beams. Anbar J. Eng. Sci. 79–101 (2012)
5. Tseng, Y.-P., Lee, C.-T.: Bending analysis of bimodular laminates using a higher-order finite strip method. Compos. Struct. **30**, 341–350 (1995)

Chapter 7
Dynamic Modelling and Simulation of a Production Machine with Moving Loads

Helmut J. Holl and Victoria Simader

Abstract In this contribution, a dynamic model for a production machine is discussed, that includes some submodels like belt drives, a moving beam and a moving mass. For the derivation of a mechanical model of an industrial machine, these submodels and their interactions are considered. The equations of motion of these submodels are derived from the potential and kinetic energy applying the equation of Lagrange. The model of the moving beam involves approximation functions for bending and torsional motion. Furthermore, the friction is taken into account with a modified Coulomb model. The interactions of the submodels are considered in the derived equations, a numerical solution with reference parameters is calculated and some test cases are shown.

7.1 Introduction

When designing a production machine, it is important to study the effects of different components and their interaction carefully. Furthermore, if the machine should be adapted to other production conditions or another size of the product, it has to be evaluated by a suitable mechanical model. The accuracy and the quality of the manufactured work-pieces have to be independent of the specific operating parameters of the machine. The goal is to simulate the production process and predict derivations and vibrations in the early phase of development. Therefore, our analysis starts with a basic mechanical model, which is derived from the potential and kinetic energy, see [3, 8, 9]. Essential equations for details, submodels and knowledge as well as identified parameters from measurements can be added subsequently to improve the dynamic model.

H. J. Holl (✉) · V. Simader
Institute of Technical Mechanics, Johannes Kepler University Linz, Altenberger Straße 69, 4040 Linz, Austria
e-mail: helmut.holl@jku.at

V. Simader
e-mail: victoria.simader@jku.at

Different submodels have been analysed for driving systems for linear motion and there is a lot of literature with respect to some special effects. The characteristics of the dynamics and application for belt drives are discussed in [4], where also some examples and simulations are given. In [10], some further important aspects are discussed, like precision, vibrations, noise and force distribution. In such machines, moving masses are present, and in [5], the vibration behaviour with applied moving loads are analysed for various boundary conditions. As in the final equations of motion, the mass matrix is not constant but a function of time, the behaviour of variable mass machines is involved, see [2]. The accurate computation of such non-linear dynamic systems with variable parameters is discussed in [6]. For the model derived in this contribution, the most important effects have been considered and some further details are kept for future analysis. The equations of motion for the entire machine are derived using the equation of Lagrange. This allows a combination with further submodels and systems using approximation functions. The modelling of the used submodels is described, which are combined to give the model of the entire machine.

7.2 Dynamic Submodel of a Belt Drive

The equations of motion of the submodel of a belt drive shown in Fig. 7.1 are derived using the potential and kinetic energy and approximation functions for the deformation of the elastic timing belt. The degrees of freedom are the rotation of the pulley wheels on the left side q_1 and on the right side q_2. q_3 represents the translational motion of the mass m_3. This mass is guided in the horizontal direction where a friction force F_f is present. The model considers only the longitudinal elasticity of the timing belt and no transversal vibrations. The transversal motion can be considered by an approximation function analogous to that used in [7], which will be done within a refinement study of the present model. The detailed kinematic motion of the timing belt on the pulley wheel is replaced by the condition of no relative slip. The pulley wheels rotate due to an appropriate moment M_{T_1} and M_{T_2}. They are connected with a timing belt with position-dependent length. The parts of the timing belt are represented by springs with the position-dependent axial stiffness EA/L, see [8]. Due to these assumptions, the potential energy of this subsystem is

$$V = \frac{EA}{2} \frac{(r_1 q_1 - q_3)^2}{(L_1 + q_3)} + \frac{EA}{2} \frac{(r_2 q_2 - q_3)^2}{(L_3 - L_1 - q_3)} + \frac{1}{2} \frac{EA}{L_3} (r_1 q_1 - r_2 q_2)^2. \quad (7.1)$$

EA is the longitudinal stiffness, and the geometric parameters and degrees of freedom are shown in Fig. 7.1. The kinetic energy

$$T = \frac{1}{2} J_1 \dot{q}_1^2 + \frac{1}{2} J_2 \dot{q}_2^2 + \frac{1}{2} m_3 \dot{q}_3^2 \qquad (7.2)$$
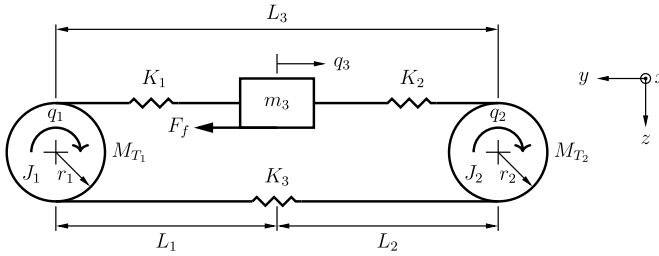
Fig. 7.1 Dynamic submodel of a belt drive

includes the second moment of inertia of the two rotating parts from the pulley wheels J_1 and J_2 and the kinetic energy of the motion of the guided mass. Based on Eqs. (7.1) and (7.2), the equation of motion can be derived using

$$\frac{\mathrm{d}}{\mathrm{d}t}\left(\frac{\partial T}{\partial \dot{q}_i}\right) - \frac{\partial T}{\partial q_i} + \frac{\partial V}{\partial q_i} = Q_i, \tag{7.3}$$

where $\mathbf{Q} = \begin{bmatrix} M_{T_1} & M_{T_2} & F_f \end{bmatrix}^T$ represents the vector of the external excitation moments and the friction force. This submodel is used in the derivation of the mechanical model of a production machine, as it allows to compute the basic vibrations. Further degrees of freedom like transversal vibrations, can be added for a more complex simulation of coupled vibrations, see [7, 10]. As the stiffness parameters are position-dependent, the vibration behaviour of this driving unit shows different eigenfrequencies, which can be detected also experimentally, see [1] and confirmed by a detailed numerical finite-element computation.

7.3 Submodel of Two Combined Belt Drives

In production machines with a plane rectangular working space, two linear belt drives are combined and connected with torsional shafts as can be seen in Fig. 7.2. The torsional shafts have a characteristic length, radius, cross section, moment of inertia and shear modulus and, for different time-dependent moments, the difference of the motion of both sides should be small and the relative longitudinal motion also should be as small as possible. With the torsional stiffness $G_i I_{Ti}/L_i$ of the i-th shaft, the potential energy for the two shafts is

$$V_{s_1} = \frac{1}{4}\frac{G_{s_1}\pi r_{s_1}^4}{L_{s_1}}(q_1 - q_4)^2 \quad \text{and} \quad V_{s_2} = \frac{1}{4}\frac{G_{s_2}\pi r_{s_2}^4}{L_{s_2}}(q_2 - q_5)^2, \tag{7.4}$$
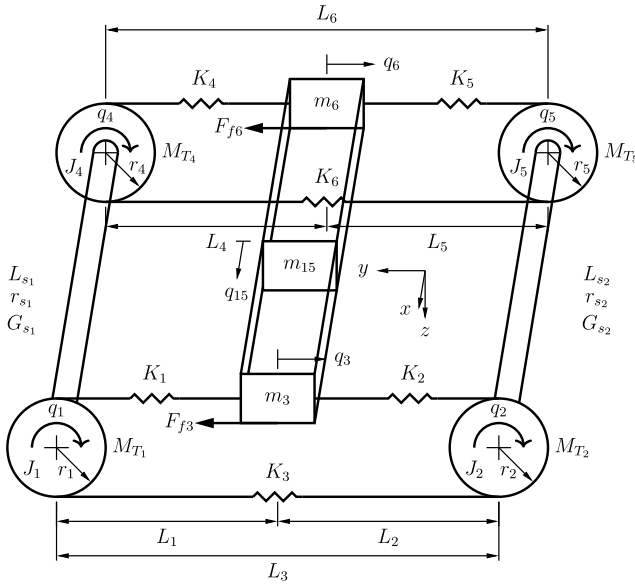
Fig. 7.2 Submodel of belt drives and moving beam

where the second polar moment of area $I_p = I_T = \dfrac{r^4\pi}{2}$ for a circular cross section is used. The kinetic energy of the torsional shafts is considered with a linear Ritz approximation function

$$T_{s_1} = \frac{1}{2}\rho I_p \int_0^{L_{s_1}} \left(\dot{q}_1 + (\dot{q}_4 - \dot{q}_1)\frac{x}{L_{s_1}}\right)^2 dx = \frac{1}{12}\pi\rho r_{s_1}^4 L_{s_1}\left(\dot{q}_1^2 + \dot{q}_4^2 + \dot{q}_1\dot{q}_4\right), \quad (7.5)$$

$$T_{s_2} = \frac{1}{12}\pi\rho r_{s_2}^4 L_{s_2}\left(\dot{q}_2^2 + \dot{q}_5^2 + \dot{q}_2\dot{q}_5\right). \tag{7.6}$$

The degrees of freedom and the external moments and friction forces are shown in Fig. 7.2 and the vector of generalized forces is $\mathbf{Q} = \begin{bmatrix} M_{T_1} & M_{T_2} & F_{f3} & M_{T_4} & M_{T_5} & F_{f6} \end{bmatrix}^T$. Simulations with this model can evaluate the necessary parameters of the torsional shafts in order to minimize the difference of the motion of both sides q_3 and q_6. Additionally, the position-dependent eigenfrequencies of the belt drive systems are modified due to the coupling caused by the torsional shafts.

7.4 Submodel of Belt Drives and Moving Beam

In the production machine under consideration, a moving beam is added between the belt drives at the position of the masses m_3 and m_6, see Fig. 7.2. This beam can have translational vibrations in y- and z-direction and also allows torsional rotations. As
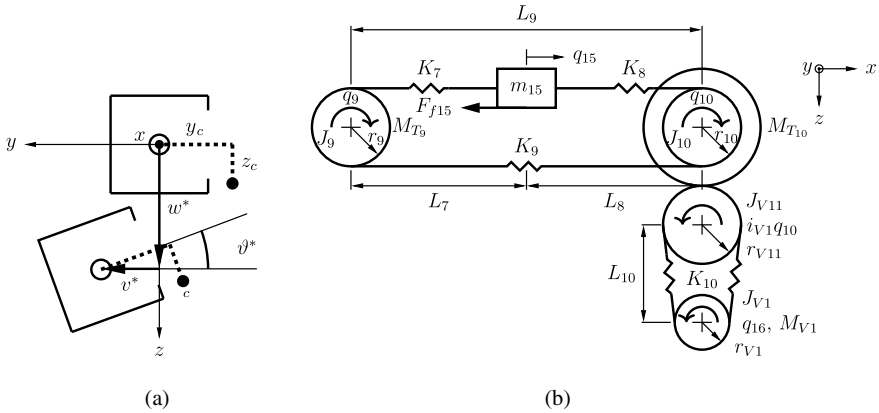
Fig. 7.3 Rotation of mass m_{15} (**a**) and detail of the driving timing belt in the beam (**b**)

this beam can have an open thin-walled multi-cell cross section, the centre of the cross section and the centre of gravity are different. The bending and torsional vibrations are coupled in such a configuration. The mass m_{15} with the centre of gravity at a defined position y_c and z_c, see Fig. 7.3a, is moving in longitudinal direction with the coordinate q_{15} relative to the initial position L_7. With the approximation for the bending deflection $v^*(x, t)$ and $w^*(x, t)$ and the torsional rotation $\vartheta^*(x, t)$, the position vector of the centre of gravity is given by

$$
\boldsymbol{r_c} = \begin{bmatrix} L_7 + q_{15}(t) \\ v^*[L_7 + q_{15}(t), t] \\ w^*[L_7 + q_{15}(t), t] \end{bmatrix} + \begin{bmatrix} 0 \\ -y_c \cos\{\vartheta^*[L_7 + q_{15}(t), t]\} - z_c \sin\{\vartheta^*[L_7 + q_{15}(t), t]\} \\ -y_c \sin\{\vartheta^*[L_7 + q_{15}(t), t]\} + z_c \cos\{\vartheta^*[L_7 + q_{15}(t), t]\} \end{bmatrix}.
$$
(7.7)

The actual speed of the centre of gravity of the mass m_{15} after a linearization for small angles is computed to

$$
\boldsymbol{\dot{r}_c} \approx \begin{bmatrix} \dot{q}_{15}(t) \\ \dot{v}^* + v^{*\prime}\dot{q}_{15}(t) - z_c\left(\vartheta^{*\prime}\dot{q}_{15}(t) + \dot{\vartheta}^*\right) \\ \dot{w}^* + w^{*\prime}\dot{q}_{15}(t) - y_c\left(\vartheta^{*\prime}\dot{q}_{15}(t) + \dot{\vartheta}^*\right) \end{bmatrix}.
$$
(7.8)

As can be seen in Fig. 7.3b, there is also an additional timing belt drive installed to control the motion of the mass in longitudinal direction q_{15}. The equations of motion have to consider the additional degrees of freedom, see Fig. 7.3b. The potential and kinetic energies of the beam with the length L_B are

Fig. 7.4 Sketch for bending in the x–y-plane
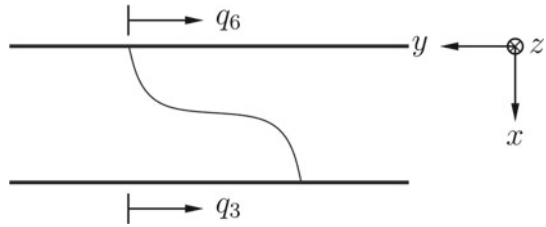
$$V_{\text{Beam}} = \frac{E I_y}{2} \int_0^{L_B} (w^{*\prime\prime})^2 \, dx + \frac{E I_z}{2} \int_0^{L_B} (v^{*\prime\prime})^2 \, dx + \frac{G I_T}{2} \int_0^{L_B} (\vartheta^{*\prime})^2 \, dx - \rho A g \int_0^{L_B} w^* dx$$

$$T_{\text{Beam}} = \frac{\rho A}{2} \int_0^{L_B} (\dot{w}^*)^2 \, dx + \frac{\rho A}{2} \int_0^{L_B} (\dot{v}^*)^2 \, dx + \frac{\rho I_p}{2} \int_0^{L_B} (\dot{\vartheta}^*)^2 \, dx \qquad (7.9)$$

and the energy of mass m_{15} is

$$V_m = -m_{15} \, g \, \{w^*[L_7 + q_{15}(t), t] - y_c \vartheta^*[L_7 + q_{15}(t), t]\}$$
$$T_m = \frac{1}{2} m_{15} \left(\dot{r}_{cy}\right)^2 + \frac{1}{2} m_{15} \left(\dot{r}_{cz}\right)^2 + \frac{1}{2} J_{15} \left(\dot{\vartheta}^*[L_7 + q_{15}(t), t]\right)^2 . \qquad (7.10)$$

For the integration of these equations, three approximation functions are needed. The bending deflection of the beam in the x–y-plane, see Fig. 7.4, is assumed as a superposition of the static bending and an approximation function for the dynamic bending. For the position of both ends, q_3 and q_6 and the consideration of clamped boundary conditions, a polynom can be computed for the static deflection. For the dynamic deflection, an approximation function representing the first mode of vibration of a beam clamped on both ends with a constant cross section is assumed.

$$v^*(x, t) = \left(\frac{x}{L_B}\right)^2 \left[3 - 2\frac{x}{L_B}\right] [q_6(t) - q_3(t)] + q_7(t) \frac{1}{2} \left[1 - \cos\left(2\pi \frac{x}{L_B}\right)\right]$$
$$(7.11)$$

For the deflection in the x–z-plane, hinged boundary conditions are used on both ends. As an approximation function, a series expansion is used

$$w^*(x, t) = \sum_{n=1}^{\infty} q_{8_n}(t) \sin\left(\frac{n\pi x}{L_B}\right) . \qquad (7.12)$$

Here, only the first vibration mode with $n = 1$ is considered and the influence of higher modes is analysed in a separate study. The boundary conditions can be extended with torsional springs on both ends, where the parameters can be identified by measurements.

The approximation function for the rotation about the x-axis is chosen similarly to the bending mode. The rotation is zero at $x = 0$ and $x = L_B$ so for the rotation

$$\vartheta^*(x, t) = \sum_{n=1}^{\infty} q_{\vartheta_n}(t) \sin\left(\frac{n\pi x}{L_B}\right) \tag{7.13}$$

a sine-function is selected and again only the first mode $n = 1$ is considered. This is a more general approach than a linear function representing the static deflection. Additionally, a torsional spring can be considered on both ends as an extension and refinement of the model. With these approximation functions the potential and kinetic energy can be computed and the equations of motion can be derived which results in lengthy equations which cannot be given here.

7.5 Description of the Friction Model

In the present model, friction occurs in all moving and guided parts. It is considered only in the three motions q_3, q_6 and q_{15} and neglected in the other guides. Friction is a complicated velocity-dependent reaction force. As a first approach the Coulomb friction force $F_f = -\mu F_N \mathrm{sgn}(\dot{q})$ was chosen, see [3]. As the numerical solution of the whole model is computed, there are some jumps of the force when the velocity is zero, so that vibrations occur at the beginning of the simulation. Therefore, the Coulomb friction was modified as shown in Fig. 7.5, where three different forcing functions are shown which have been analysed. Based on the simulation results, the following friction force function F_1 is used.
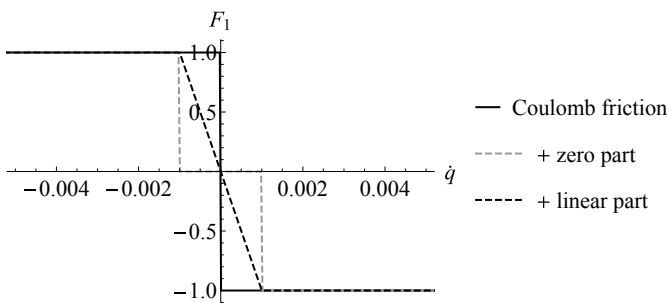
Fig. 7.5 Different friction force functions depending on the relative velocity

$$F_{fi}(\dot{q}_i) = \mu F_N \cdot F_1(\dot{q}_i) \quad \text{with} \quad F_1 = \begin{cases} 1, & \dot{q}_i < -0.001 \\ 0 & -0.001 \leq \dot{q}_i \leq 0.001 \\ -1, & \dot{q}_i > 0.001 \end{cases} \qquad (7.14)$$

The friction force function vanishes below a defined threshold value of ± 0.001 m/s. The normal force $F_N = m_{gi}\, g$ in Eq. (7.14) considers each mass m_3, m_6 and m_{15}, where half of the mass of the beam $\rho A L_B$ and the moving mass m_{15} is added:

$$m_{g3} = m_3 + \frac{\rho A L_B}{2} + \frac{m_{15}}{2},\ m_{g6} = m_6 + \frac{\rho A L_B}{2} + \frac{m_{15}}{2} \ \text{and}\ m_{g15} = m_{15}.$$

7.6   Simulation of Operation Conditions

The developed model allows the numerical calculation of reference test cases, where the parameters from Table 7.1 have been used in the following simulations. There are several configurations and operating conditions which have been simulated. Two reference cases of the motion without external load and with a defined driving load are shown.

In the first test case, all external moments, the friction forces, the distance to the centre of gravity of the mass m_{15} and the initial conditions of all degrees of freedom are homogeneous. Due to the gravity the deflection of the beam in z-direction, with the degree of freedom $q_8(t)$, starts to oscillate around the associated static position, as can be seen in Fig. 7.6a. A translational motion of mass m_{15} starts towards the centre of the beam and there is an accompanying rotation of the pulley wheels with the degrees of freedom $q_9(t)$, $q_{10}(t)$ and $q_{16}(t)$, as depicted in Fig. 7.6b. As the mass m_{15} initially is not in the centre of the beam, i.e. $L_7 \neq L_8$, the slope at the position of the mass leads to a motion towards the lowest position on the beam. If the distances $L_7 = L_8$ are chosen initially, the result for $q_{15}(t)$ is a homogeneous solution. With this test case, to evaluate the static deflection, the importance of the suitable initial conditions representing the static deflection for the calculation has been shown and, in the further example, the static deflections are chosen as initial conditions, which are inhomogeneous for the degrees of freedom q_8 and q_ϑ with the parameters from Table 7.1. Two different moments are applied to the system, which are defined in Eq. (7.15) with some given time parameters.

$$M_i = 4 \begin{cases} 0 & t < T_1 \\ 1/2\ \{1 - \cos[25\pi(t - T_1)]\} & T_1 \leq t \leq T_2 \\ 1 & T_2 \leq t \leq T_3 \\ 1/2\ \{1 + \cos[25\pi(t - T_3)]\} & T_3 \leq t \leq T_4 \\ 0 & t > T_4 \end{cases} \qquad (7.15)$$

The moment M_{T1} with $T_1 = 0.1$ s, $T_2 = 0.14$ s, $T_3 = 0.2$ s and $T_4 = 0.24$ s acts on the timing belt on one side of the beam and the moment M_{V1} with $T_1 = 0.2$ s,

Table 7.1 Model parameters for the simulation

$J_1 = J_2 = J_4 = J_5$, moment of inertia	$5.6 \cdot 10^{-4}$ kgm^2
$m_3 = m_6$, mass	7.7 kg
r_1, r_2, r_4, r_5, radius of the pulley wheels	0.0375 m
L_1, L_4, belt length 1 and 4	0.46 m
$L_2 = L_3 - L_1, L_5 = L_6 - L_4$, belt length 2 and 5	3.0 m
L_3, L_6, total belt length 3 and 6	3.46 m
EA, strain stiffness of the belt	2 120 000 N
$M_{T_1}, M_{T_2}, M_{T_4}, M_{T_5}$, moments at pulley wheels	$M_{T_1} = 0$ Nm or Eq. (7.15)
	$M_{T_2} = M_{T_4} = M_{T_5} = 0$ Nm
$F_{f3} = F_{f6}$, friction force	$F_{f3} = F_{f6} = 0$ N
	or $F_{f3} = F_{f6} = $ Eq. (7.14)
ρ_s, density of torsional shaft	2700 kg/m^3
$L_{s_1} = L_{s_2}$, length of torsional shafts	2.1 m
$r_{s_1} = r_{s_2}$, radius of torsional shafts	0.03 m
$G_{s_1} = G_{s_2}$, shear modulus of torsional shafts	$25.5 \cdot 10^9$ N/m^2
L_7, belt length 7	1.4 m
$L_8 = L_9 - L_7$, belt length 8	1.1 m
L_9, total belt length 9	2.5 m
L_{10}, total belt length 10	0.06 m
y_c, distance to the centre of gravity of mass m_{15}	0.03 m
z_c, distance to the centre of gravity of mass m_{15}	0.1 m
m_{15}, moving mass on the beam	4 kg
J_{15}, moment of inertia of mass m_{15}	$J_{15} = m_{15} \cdot i_{15}^2 = 4 \cdot 0.02^2 = 0.0016$ kgm^2
$r_9, r_{10}, r_{V1}, r_{V11}$, radius of pulley wheels	0.0375 m
J_9, moment of inertia pulley wheel 9	$2.4 \cdot 10^{-4}$ kgm^2
J_{10}, moment of inertia pulley wheel 10	$1.7 \cdot 10^{-4}$ kgm^2
J_{V1}, moment of inertia pulley wheel $V1$	$3.1 \cdot 10^{-7}$ kgm^2
J_{V11}, moment of inertia pulley wheel $V11$	$5.6 \cdot 10^{-7}$ kgm^2
$\rho = \rho_B$, density of the beam	2700 kg/m^3
A, cross sectional area of the beam	0.006 m^2
L_B, length of the beam	2.5 m
EI_y, bending stiffness of the beam	$4.2 \cdot 10^5$ Nm^2
EI_z, bending stiffness of the beam	$3.7 \cdot 10^5$ Nm^2
GI_T, torsional stiffness of the beam	$1.2 \cdot 10^5$ Nm^2
I_p, second polar moment of area of the beam	$5.3 \cdot 10^{-8}$ m^4
EA_v, strain stiffness of the small belt	212 000 N
i_{V1}, transmission ratio	1
M_{T9}, M_{T10}, M_{V1}, moments at pulley wheels	$M_{T9} = M_{T10} = 0$ Nm
	$M_{V1} = 0$ Nm or Eq. (7.15)
F_{f15}, friction force m_{15}	0 N or $F_{f15} = $ Eq. (7.14)
μ, coefficient of friction	0.01
g, gravity of Earth	9.81 m/s^2
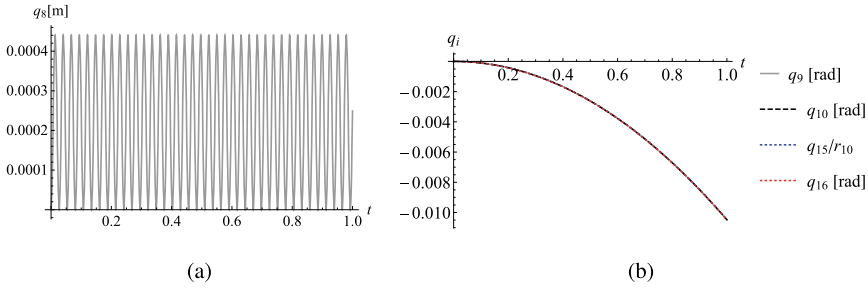
Fig. 7.6 Deflection in z-direction (**a**) and solution for the motion of mass (**b**)
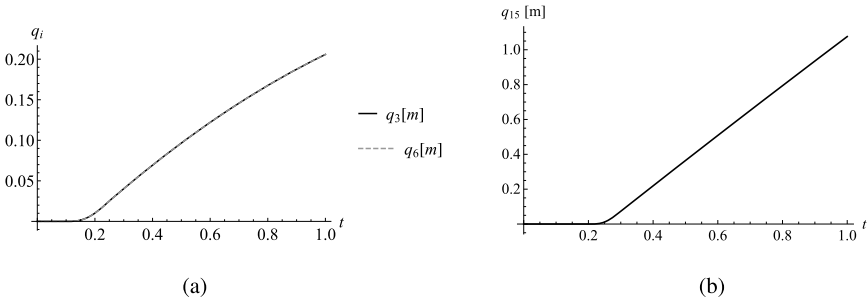
Fig. 7.7 Motion of mass m_3, m_6 (**a**) and m_{15} (**b**)

$T_2 = 0.24$ s, $T_3 = 0.26$ s and $T_4 = 0.3$ s acts on the timing belt for the motion of the mass m_{15}. Both moments have a maximum of 4 Nm. For the given moments and parameters the motion is computed. Figure 7.7a shows the motion of the masses m_3 and m_6 in y-direction. As can be seen, the beam starts to move at $t = 0.1$ s and speeds up until 0.24 s. After that time, the moment is zero and the decreasing slope of the curve corresponds to the effect of the friction force. Figure 7.7b displays the motion of the mass m_{15} in x-direction. This motion starts at $t = 0.2$ s. Due to the small value of the mass m_{15} the influence of the friction force is not visible in the diagram for the period of 1 s.

The beam moved about 0.2 m and the smaller mass m_{15} on the beam travels a distance longer than 1 m. It is important to predefine the acting moments properly because the end of the machine must not be reached and no collisions are checked in the present model. The corresponding equations for the restrictions can be added to consider these geometric constraints. In Fig. 7.8a the velocities of the masses m_3 and m_6 are depicted. This velocity is increasing in the period when the moment M_{T_1} is different from zero and decreasing afterwards because of the friction force. The friction force according to Eq. (7.14) is shown in Fig. 7.8b. There are no fluctuations before the motion starts at $t = 0.1$ s as required.

The following pictures show the approximation functions of the beam over its length and over the simulation time on the left-hand side and the relevant degrees
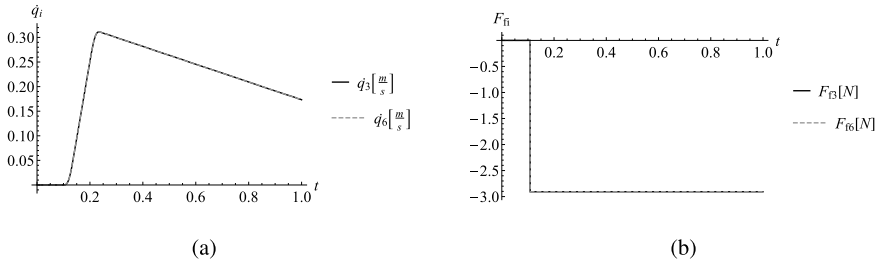
Fig. 7.8 Velocity of mass m_3 and m_6 (**a**) and friction force at m_3 and m_6 (**b**)
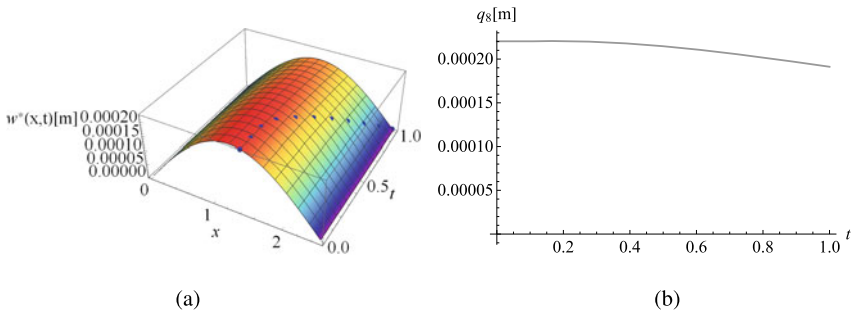
Fig. 7.9 Approximation function for bending deflection in the z-direction (**a**) and DOF for deflection (**b**)

of freedom on the right-hand side. $w^*(x, t)$ in Fig. 7.9a shows the deflection in z-direction for the hinged beam. At the beginning of the simulation, the mass m_{15}, depicted with the blue points, is near the centre of the beam. When the mass starts to move towards the end of the beam, the deflection decreases. This corresponds with the diagram for the degree of freedom $q_8(t)$ shown in Fig. 7.9b.

The behaviour of the deflection in y-direction is different and much smaller, see Fig. 7.10. After 0.1 s, the moment M_{T_1} is increasing. In the next 0.14 s, the difference between $q_3(t)$ and $q_6(t)$ is computed due to the moment M_{T_1} acting on the side of the system with mass m_3. After that time, the moment vanishes and the difference oscillates with a very small amplitude. The motion of the beam causes an oscillation with small amplitudes that still remains after M_{T_1} is zero again. The blue points, that mark the position of mass m_{15} are not visible all the time, because they are hidden behind the amplitude function in the three-dimensional plot. The degree of freedom $q_7(t)$ is depicted in Fig. 7.10b and shows the vibration amplitude in the approximation function $v^*(x, t)$.

The approximation function for the rotation about the x-axis is shown in Fig. 7.11. The mass m_{15} remains in the initial position for the first 0.1 s. Then the beam begins to move and some small oscillation starts. The amplitude of vibration gets smaller the closer the position of mass m_{15} is to the end of the beam. Also, the absolute value of the rotational angle decreases as can be seen in Fig. 7.11b.
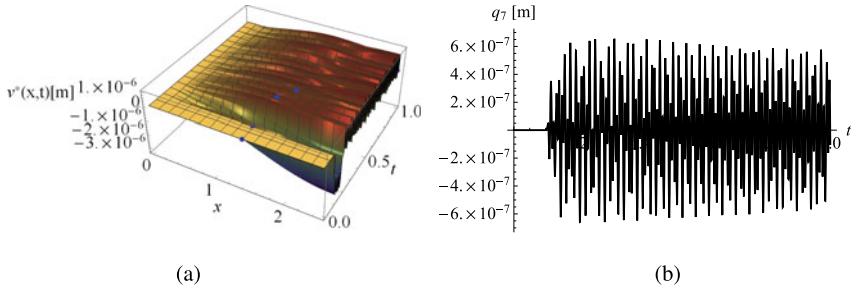
Fig. 7.10 Approximation function for bending deflection in the y-direction (**a**) and DOF for oscillation (**b**)
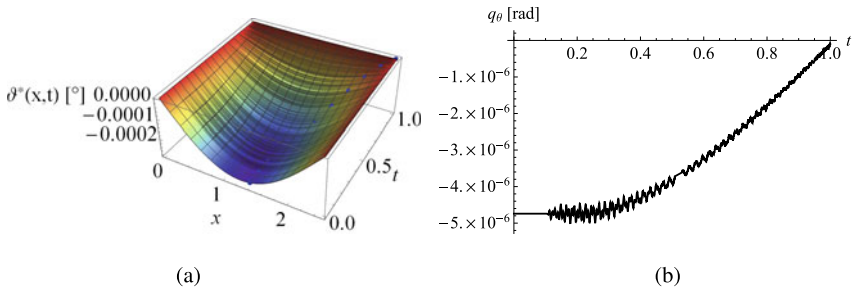
Fig. 7.11 Approximation function for rotation about the x-axis (**a**) and DOF for rotation (**b**)

7.7 Conclusions and Outlook

The dynamic model of the production machine combines effects from different submodels. The numerical results without loads show the importance of the correct initial values to compute suitable and reliable solutions. Due to the depiction of the approximation functions and several degrees of freedom for some test cases, the mechanical model is verified. The goal is to further improve the present model and implement additional refined submodels. This will help to optimize the quality and the accuracy of the production machine as some additional knowledge can be derived from the analysis of the simulation results.

References

1. Cojocaru, E.C., Holl, H.J., Brandl, A.: Theoretical and experimental frequency analysis of a transmission system with timing belts. In: Borbás, L. (ed.) Proceedings of the 28th Danubia-Adria Symposium on Advances in Experimental Mechanics, 28 Sept–01 Oct 2011, Siófok, pp. 105–106 (2011)
2. Cveticanin, L.: Dynamics of Bodies with Time-Variable Mass, 7th edn. Springer
3. Dankert, H., Dankert, J.: Technische Mechanik: Statik, Festigkeitslehre, Kinematik/Kinetik, 7th edn. Springer (2013)
4. Dresig, H., Fidlin, A.: Schwingungen mechanischer Antriebssysteme, 3th edn. Springer (2014)
5. Fryba, L.: Vibration of Solids and Structures Under Moving Loads, 3th edn. Thomas Telford (1993)
6. Holl, H.J.: Analysis of dynamic variable mass and variable parameter systems applying semi-analytic time-integration. In: Gutschmidt, S., Hewett, J.N., Sellier, M. (eds.) IUTAM Symposium on Recent Advances in Moving Boundary Problems in Mechanics, IUTAM Bookseries, vol. 34, pp. 239–252. Springer (2019)
7. Holl, H.J., Hammelmüller, F.: Analysis of the coupled oscillations of strip and coiling drum in a winding process. In: Kim, K.-W., Kim, Y.-C. (eds.) Proceedings of the 8th IFToMM International Conference on Rotor Dynamics (on USB), 12–15 Sept 2010, Seoul, paper-ID WeD2-4(S-1011), pp. 962–969 (2010)
8. Isermann, R.: Mechatronische Systeme: Grundlagen, 2nd edn. Springer (2008)
9. Parkus, H.: Mechanik der festen Körper, 2nd edn. Springer (2005)
10. Perneder, R., Osborne, I.: Handbook Timing Belts, 7th edn. Springer (2012)

Chapter 8
A Derivation of the Beam Theory of Second-Order with Shear, Starting from a Continuum Mechanics-Based Extension of the Reissner Finite-Strain Beam Theory

Hans Irschik

Abstract A consistent derivation of the beam theory of second order with shear is presented. The geometrically exact Reissner finite-strain beam theory is taken as the starting point, utilizing a continuum mechanics-based extension with respect to stress–strain constitutive formulations. Corresponding incremental relations for small deformations superimposed upon an intermediate configuration with (possibly) finite deformations are presented, from which the second-order beam theory with shear eventually is derived using two slight approximations.

8.1 Introduction

The present contribution is concerned with a consistent derivation of the beam theory of second order, taking into account the effect of shear, see Rubin and Vogel [9], Rubin and Schneider [8]. The increase of the practical usage of the beam theory of second order generally is due to both, economic and safety reasons, e.g. Petersen [6] for steel structures. However, the fundamental relations of the beam theory of second order have been stated in a somewhat ad hoc manner in the literature. Our present derivation attempts to provide a consistent connection to non-linear structural and continuum mechanics. From space restrictions, we consider plane deformations of originally straight shear-deformable beams, utilizing the Timoshenko hypothesis of cross sections remaining plane and un-deformed in the deformed configuration, but, due to the effect of shear, not necessarily perpendicular to the deformed beam axis, see Ziegler [12]. The geometrically exact Reissner finite-strain beam theory [7] is taken as a starting point. In Sect. 8.2 below, we shortly recall the corresponding fundamental relations of this theory, which is geometrically exact within the Timo-

H. Irschik (✉)

Institute of Technical Mechanics, Johannes Kepler University Linz, Linz, Austria
e-mail: hans.irschik@jku.at

shenko hypothesis. Using virtual work considerations, Reissner in [7] showed that the constitutive relations for the stress resultants must be formulated as functions of certain generalized strains. In the Reissner finite-strain theory [7], the mathematical form of the constitutive relations however needs to be stipulated. In order to overcome this problem, Irschik and Gerstmayr [5] presented an extension of the Reissner finite-strain beam theory, where local stress–strain relations can be utilized, the formulation being also geometrically exact within the Timoshenko hypothesis. A three-dimensional hyperelastic stress-strain constitutive relation, dating back to Ciarlet [1] and proposed by Simo and Hughes [10], was treated exemplarily in [5], see Sect. 8.3 below for an overview. Based on this continuum mechanics-based extension, the case of (infinitesimally) small deformations superimposed upon an intermediate configuration with (possibly) large deformations are studied in Sect. 8.4, where a method by DaDeppo [2] for beams rigid in shear is adopted, see Irschik [3] for the Reissner finite-strain beam theory. Correspondingly, the fundamental relations are differentiated with respect to a non-dimensional generalized time, e.g. a characteristic load parameter, from which the incremental (rate) forms of the equilibrium relations, of the kinematic relations, as well as of the hyperelastic constitutive beam relations are obtained directly. These relations form a system of linear algebraic and ordinary differential equations for the rates, where generalized strains and stress resultants of the intermediate configuration serve as generally non-constant but known coefficients. We particularly study a straight intermediate configuration under the single action of a constant normal (axial) force. In Sect. 8.5 below, we eventually show that two slight approximations are needed only to approach the beam theory of second order from the exact linearization of the extended Reissner finite-strain beam theory given in Sect. 8.4. The notational transitions necessary to obtain coincidence with the relations introduced by Rubin and Vogel [9] are stated in some detail at the end of the paper.

8.2 The Reissner Finite-Strain Beam Theory

In this Section, we shortly recall the Reissner shear-deformable, finite-strain beam theory [7], which is geometrically exact within the Timoshenko hypothesis. We study an initially straight beam, see Fig. 8.1 for the meaning of the subsequently used static and kinematic entities.

The differential forms of the local equilibrium relations read

$$\mathbf{R}' + \mathbf{p} = \mathbf{0}, \tag{8.1}$$

$$\mathbf{M}' + \mathbf{r}' \times \mathbf{R} + \mathbf{m} = \mathbf{0}, \tag{8.2}$$

where

Fig. 8.1 Kinematic and static entities in the finite-strain beam theory
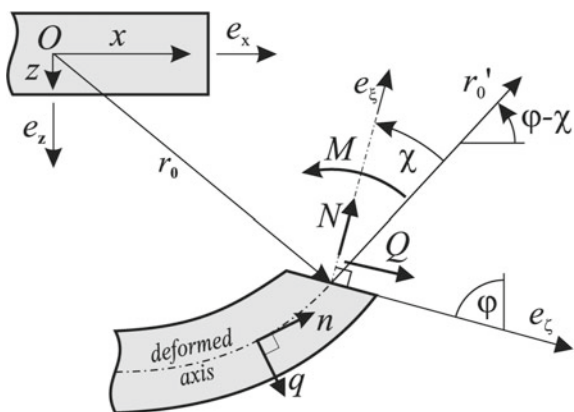
$$\mathbf{R} = R_x\mathbf{e}_x + R_z\mathbf{e}_z = N\mathbf{e}_1 + Q\mathbf{e}_3, \tag{8.3}$$

$$\mathbf{M} = M\mathbf{e}_y. \tag{8.4}$$

In the Reissner formulation [7], the normal force N is taken as perpendicular to the cross section in the deformed configuration, the shear force Q being in the direction of the cross section, see Fig. 8.1. The y-axis is perpendicular to the plane of deformation, the corresponding moment M representing the bending moment. The position vector of the deformed axis is

$$\mathbf{r}_0 = \mathbf{r} = x\mathbf{e}_x + \mathbf{u} \tag{8.5}$$

with the displacement vector of the axis

$$\mathbf{u} = u_x\mathbf{e}_x + u_z\mathbf{e}_z = u\mathbf{e}_x + w\mathbf{e}_z. \tag{8.6}$$

We utilize the Lagrange description of continuum mechanics; hence, every entity is understood as a function of the axial coordinate x in the un-deformed configuration. The global (x, z)- and the local (ξ, η)-coordinate systems are related by, see Fig. 8.1,

$$\mathbf{e}_\xi = \mathbf{e}_1 = \mathbf{e}_x \cos\varphi - \mathbf{e}_z \sin\varphi, \qquad \mathbf{e}_\zeta = \mathbf{e}_3 = \mathbf{e}_x \sin\varphi + \mathbf{e}_z \cos\varphi. \tag{8.7}$$

Derivatives with respect to the coordinate x and rates with respect to a generalized non-dimensional time t are indicated by superimposed primes and dots, respectively:

$$f' = \frac{\partial f}{\partial x}, \quad \dot{f} = \frac{\partial f}{\partial t} : \quad \mathbf{e}_1' = -\varphi'\mathbf{e}_3, \quad \dot{\mathbf{e}}_1 = -\dot{\varphi}\mathbf{e}_3, \quad \mathbf{e}_3' = \varphi'\mathbf{e}_1, \quad \dot{\mathbf{e}}_3 = \dot{\varphi}\mathbf{e}_1. \tag{8.8}$$

Particularly, the deformation gradient vector of the axis, being tangential to the latter, is

$$\mathbf{r}' = (1 + u')\mathbf{e}_x + w'\mathbf{e}_z = \Lambda(\cos \chi \mathbf{e}_1 - \sin \chi \mathbf{e}_3), \tag{8.9}$$

where Λ denotes the axial stretch,

$$\Lambda = \|\mathbf{r}'\|. \tag{8.10}$$

Substituting Eq. (8.7), we find that

$$1 + u' = \Lambda \cos(\varphi - \chi), \qquad w' = -\Lambda \sin(\varphi - \chi). \tag{8.11}$$

External forces and moments per unit axial length in the un-deformed configuration are

$$\mathbf{p} = p_x\mathbf{e}_x + p_z\mathbf{e}_z = n\mathbf{e}_1 + q\mathbf{e}_3, \tag{8.12}$$
$$\mathbf{m} = m\mathbf{e}_y. \tag{8.13}$$

The local equilibrium relations of the Reissner theory eventually can be written as

$$\mathbf{R}' + \mathbf{p} = \left(N' + \varphi'Q + n\right)\mathbf{e}_1 + \left(Q' - \varphi'N + q\right)\mathbf{e}_3 = \mathbf{0}, \tag{8.14}$$
$$M' - \Lambda\left(Q \cos \chi - N \sin \chi\right) + m = 0. \tag{8.15}$$

The problem must be closed by constitutive relations for normal force N, shear force Q and bending moment M. Using virtual work arguments, Reissner [7] showed that these constitutive relations must be formulated as functions of corresponding generalized strains:

$$\varepsilon = \Lambda \cos \chi - 1, \qquad \gamma = \Lambda \sin \chi, \qquad \kappa = \varphi'. \tag{8.16}$$

Reissner [7] exemplarily discussed the appropriateness of linear matrix-type constitutive relations, where, in an example, he simplified to a decoupled form:

$$N = C^{-1}\varepsilon, \qquad Q = B^{-1}\gamma, \qquad M = D\kappa. \tag{8.17}$$

In Eqs. (8.17), D represents a cross-sectional bending stiffness, and C and B are cross-sectional extensional and shear compliances, respectively.

8.3 Extension of the Reissner Theory with Respect to Stress-Strain-Based Constitutive Relations

A problem associated with the phenomenological constitutive approach discussed in [7] is that the mathematical form of the constitutive relations must be stipulated. In order to allow a formulation utilizing the continuum mechanics level of stress–strain

constitutive relations, the Reissner theory [7] was extended by Irschik and Gerstmayr [5], see also [4] for beams rigid in shear, $\chi = 0$. It was shown in [5] that the following constitutive relations are work equivalent to the ones derived in [7]:

$$N = \int_A S_{xx} J \, dA, \quad Q = \int_A (S_{xz} + S_{xx} \gamma) \, dA, \quad M = \int_A S_{xx} z J \, dA. \quad (8.18)$$

In Eq. (8.18), integration is with respect to the beam cross section A in the undeformed reference configuration, and S_{xx} and S_{xz} represent respective components of the matrix of the second Piola–Kirchhoff stress tensor in the global (x, z)-coordinate system, see Washizu [11] for an enlightening geometric interpretation. The Jacobian determinant of the deformation gradient tensor is denoted by J. For the Timoshenko-type deformation assumed here, J reads

$$J = \Lambda \cos \chi + z \varphi' = 1 + \varepsilon + z \kappa. \quad (8.19)$$

In order to exemplary illustrate the use of Eq. (8.18) in a non-linear context, we address a hyperelastic constitutive relation dating back to Ciarlet [1], see also Simo and Hughes [10]:

$$\underline{S} = \frac{\lambda}{2} \left(J^2 - 1 \right) \underline{C}^{-1} + \mu \left(\underline{1} - \underline{C}^{-1} \right). \quad (8.20)$$

The second Piola–Kirchhoff stress tensor is denoted by $\underline{S}$, and $\underline{C}$ is the right Cauchy–Green tensor. The Lamé parameters are λ and μ, and the unit tensor is written as $\underline{1}$. Within the Timoshenko-type kinematic hypothesis, the matrix of the inverse tensor $\underline{C}^{-1}$ is, see [5]:

$$\left[\underline{C}^{-1} \right] = \begin{bmatrix} \frac{1}{J^2} & 0 & -\frac{\gamma}{J^2} \\ 0 & 1 & 0 \\ -\frac{\gamma}{J^2} & 0 & 1 + \frac{\gamma^2}{J^2} \end{bmatrix}. \quad (8.21)$$

Substituting Eqs. (8.20) and (8.21) into Eqs. (8.18), the following constitutive relations for normal force N, shear force Q, and bending moment M is obtained, see again [5]:

$$N = \frac{1}{2} \left(2\mu + \lambda \right) \int_A \left(J - \frac{1}{J} \right) dA, \quad (8.22)$$

$$Q = \mu A \gamma, \quad (8.23)$$

$$M = \frac{1}{2} \left(2\mu + \lambda \right) \int_A \left(J - \frac{1}{J} \right) z \, dA. \quad (8.24)$$

In Eqs. (8.22)–(8.24), it has been assumed that the beam is homogeneous in the un-deformed reference configuration, such that the material parameters can be put

in front of the cross-sectional integrals, and that the beam axis is formed by the cross-sectional centroids, such that

$$\int_A z \, dA = 0. \tag{8.25}$$

Note that Eqs. (8.22)–(8.24) indeed represent functions of the generalized strains introduced by Reissner [7], as this should be, cf. Eqs. (8.16) and (8.19) above.

8.4 Infinitesimally Small Deformations Superimposed Upon an Intermediate Configuration

We now study (infinitesimally) small deformations that are superimposed upon some intermediate configuration with a (possibly) large pre-deformation. For this sake, we perform derivatives of the relations in Sect. 8.3 with respect to a generalized time, following DaDeppo [2] and Irschik [3], see Eqs. (8.8). This yields the following set of relations:

$$\dot{\varepsilon} = \dot{\Lambda} \cos \chi - \Lambda \dot{\chi} \sin \chi, \tag{8.26}$$

$$\dot{\gamma} = \dot{\Lambda} \sin \chi + \Lambda \dot{\chi} \cos \chi, \tag{8.27}$$

$$\dot{\kappa} = \dot{\varphi}', \tag{8.28}$$

$$\dot{J} = \dot{\varepsilon} + z\dot{\kappa}, \tag{8.29}$$

$$\dot{u}' = \dot{\Lambda} \cos(\varphi - \chi) - \Lambda(\dot{\varphi} - \dot{\chi}) \sin(\varphi - \chi), \tag{8.30}$$

$$\dot{w}' = -\dot{\Lambda} \sin(\varphi - \chi) - \Lambda(\dot{\varphi} - \dot{\chi}) \cos(\varphi - \chi), \tag{8.31}$$

$$\dot{N}' + \dot{\kappa} Q + \kappa \dot{Q} + \dot{\varphi} Q' - \dot{\varphi}\kappa N + \dot{n} + \dot{\varphi}q = 0, \tag{8.32}$$

$$\dot{Q}' - \dot{\kappa} N - \kappa \dot{N} - \dot{\varphi} N' - \dot{\varphi}\kappa Q + \dot{q} - \dot{\varphi}n = 0, \tag{8.33}$$

$$\dot{M}' - Q\dot{\varepsilon} - \dot{Q}(\varepsilon + 1) + N\dot{\gamma} + \dot{N}\gamma + \dot{m} = 0, \tag{8.34}$$

$$\dot{N} = \frac{1}{2}(2\mu + \lambda) \int_A \dot{J} \left(1 + \frac{1}{J^2}\right) dA, \tag{8.35}$$

$$\dot{Q} = \mu A \dot{\gamma}, \tag{8.36}$$

$$\dot{M} = \frac{1}{2}(2\mu + \lambda) \int_A \dot{J} \left(1 + \frac{1}{J^2}\right) z \, dA. \tag{8.37}$$

We particularly are interested in a straight intermediate configuration without shear deformation, $\varphi = 0$, $\chi = 0$. From Eq. (8.16), it follows that $\gamma = 0$, $\kappa = 0$, and Eq. (8.19) implies that $J = \Lambda = 1 + \varepsilon$ does not depend on the transverse coordinate z. From Eqs. (8.22)–(8.25), we yield that $M = 0$, $Q = 0$, while $N = const$. Moreover, Eqs. (8.14) and (8.15) clarify that there must be no distributed loadings

then, $n = 0, q = 0, m = 0$. The kinematic relations for small deformations from this straight intermediate deformation become, see Eqs. (8.26)–(8.31):

$$\dot{\varepsilon} = \dot{\Lambda}, \qquad \dot{\gamma} = \Lambda \dot{\chi} = (1 + \varepsilon)\dot{\chi}, \qquad\qquad \dot{\kappa} = \dot{\varphi}', \qquad (8.38)$$

$$\dot{J} = \dot{\varepsilon} + z\dot{\kappa}, \qquad\qquad (8.39)$$

$$\dot{u}' = \dot{\Lambda} = \dot{\varepsilon}, \qquad \dot{w}' = -\Lambda(\dot{\varphi} - \dot{\chi}) = -(1 + \varepsilon)\dot{\varphi} + \dot{\gamma}. \qquad (8.40)$$

The incremental equilibrium relations, Eqs. (8.32)–(8.34), read

$$\dot{N}' + \dot{n} = 0, \qquad (8.41)$$

$$\dot{Q}' - N\dot{\kappa} + \dot{q} = \dot{Q}' - N\dot{\varphi}' + \dot{q} = 0, \qquad (8.42)$$

$$\dot{M}' - \dot{Q}(\varepsilon + 1) + N\dot{\gamma} + \dot{m} = 0. \qquad (8.43)$$

The corresponding incremental constitutive relations, Eqs. (8.35)–(8.37), take on the form

$$\dot{N} = C^{-1}\dot{\varepsilon} = C^{-1}\dot{u}', \qquad C^{-1} = \frac{1}{2}(2\mu + \lambda)\,A\left(1 + \frac{1}{(1 + \varepsilon)^2}\right) \qquad (8.44)$$

$$\dot{Q} = B^{-1}\dot{\gamma}, \qquad\qquad B^{-1} = \mu A, \qquad (8.45)$$

$$\dot{M} = D\dot{\varphi}' = D\dot{\kappa}, \qquad\qquad D = \frac{1}{2}(2\mu + \lambda)\,I\left(1 + \frac{1}{(1 + \varepsilon)^2}\right), \qquad (8.46)$$

with the cross-sectional moment of inertia about the y-axis:

$$I = \int_A z^2\, dA. \qquad (8.47)$$

The constitutive relations presented in Eqs. (8.44)–(8.46) are of the linear form that was stipulated by Reissner in [7], see Eqs. (8.17). However, since we started from the Ciarlet non-linear hyperelastic stress-strain relation stated in Eq. (8.20), our formulation reflects the influence of the deformation ε in the intermediate configuration upon stiffness and compliances.

Equations (8.40)–(8.46) form a set of eight linear relations for eight unknown entities, namely the three incremental stress resultants $\dot{N}$, $\dot{Q}$ and $\dot{M}$, the two incremental displacements $\dot{u}$ and $\dot{w}$, and the three generalized strains $\dot{\varepsilon}$, $\dot{\gamma}$ and $\dot{\varphi}$. This set can be considered as an exact linearization of the extended Reissner finite-strain theory that has been discussed in Sect. 8.3 above.

By proper elimination, this set of eight relations can be decoupled into a linear differential equation of second order for $\dot{u}$, and a linear differential equation of fourth order for $\dot{w}$. This demonstrates that prescribing the usual three static or kinematic boundary conditions at each beam end is sufficient to obtain a complete linear boundary value problem; e.g., at a clamped end, $\dot{u}$, $\dot{w}$, and $\dot{\varphi}$ must be prescribed, while at a free end, one has to prescribe the two components of the internal force $\dot{\mathbf{R}}$, as well

as the bending moment $\dot{M}$. Note that there is

$$\dot{R}_x = \dot{N} + Q\dot{\varphi}, \qquad\qquad \dot{R}_z = -N\dot{\varphi} + \dot{Q}. \qquad (8.48)$$

The linear boundary value problem under consideration conveniently can be solved in closed form using symbolic computer codes, given N, Λ, and ε in the intermediate configuration.

8.5 Beam Theory of Second Order with Shear

By inspection of the relations presented in Sect. 8.4, it becomes evident that two slight approximations only are necessary for approaching the fundamental relations of the beam theory of second order with shear as stated by Rubin and Vogel [9]. The first approximation is that the extensional strain ε in the intermediate configuration can be neglected

$$\varepsilon = 0 \rightarrow \Lambda = 1, \qquad \dot{\gamma} = \dot{\chi}, \qquad \dot{w}' = -\dot{\varphi} + \dot{\gamma}, \qquad (8.49)$$

see Eqs. (8.38) and (8.40). Using Eq. (8.49), the incremental moment equilibrium relation, Eq. (8.43), simplifies to

$$\dot{M}' - \dot{Q} + N(\dot{w}' + \dot{\varphi}) + \dot{m} = 0. \qquad (8.50)$$

The constitutive relations, Eqs. (8.44)–(8.50) become

$$\dot{N} = C^{-1}\dot{u}', \qquad\qquad C^{-1} = (2\mu + \lambda)A, \qquad (8.51)$$

$$\dot{Q} = B^{-1}(\dot{w}' + \dot{\varphi}), \qquad\qquad (8.52)$$

$$\dot{M} = D\dot{\varphi}', \qquad\qquad D = (2\mu + \lambda)I. \qquad (8.53)$$

Equations (8.50)–(8.53), together with the unchanged force equilibrium relations, Eqs. (8.41) and (8.42), form a set of six relations for the six unknowns $\dot{N}, \dot{Q}, \dot{M}, \dot{u}, \dot{w}$ and $\dot{\varphi}$. We note that, although the approximation of inextensibility in the intermediate configuration, Eq. (8.49), appears to be reasonable under many circumstances, it does not result in considerable mathematical simplifications, when compared to the formulation in Sect. 8.4.

In order to approach the particular formulas published in Rubin and Vogel [9], a skew decomposition must be utilized for the internal force $\mathbf{R}$. This decomposition is to be performed into a normal force $\bar{N}$ tangential to the deformed axis, i.e., in the direction of $\mathbf{r}'$, and into a shear force $\bar{Q}$ in the direction of the deformed cross section:

$$N = \bar{N} \cos \chi, \qquad\qquad Q = \bar{Q} + \bar{N} \sin \chi. \qquad (8.54)$$

The corresponding rate forms are

$$\dot{N} = \dot{\bar{N}} \cos \chi + \bar{N} \dot{\chi} \sin\chi, \qquad \dot{Q} = \dot{\bar{Q}} + \dot{\bar{N}} \sin \chi + \bar{N} \dot{\chi} \cos \chi. \qquad (8.55)$$

Since there is no shear in the intermediate configuration, $\chi = 0$, we obtain that

$$N = \bar{N}, \quad \dot{N} = \dot{\bar{N}}, \quad \dot{Q} = \dot{\bar{Q}} + \bar{N} \dot{\chi} = \dot{\bar{Q}} + N \dot{\gamma} = \dot{\bar{Q}} + N \left(\dot{w}' + \dot{\varphi} \right). \quad (8.56)$$

We thus may write, instead of Eqs. (8.41), (8.42) and (8.50):

$$\dot{\bar{N}}' + \dot{n} = 0, \qquad \dot{\bar{Q}}' + \bar{N} \dot{w}'' + \dot{q} = 0, \qquad \dot{M}' - \dot{\bar{Q}} + \dot{m} = 0. \qquad (8.57)$$

The constitutive force relations, Eqs. (8.51) and (8.52), become

$$\dot{\bar{N}} = C^{-1} \dot{u}', \qquad\qquad \dot{\bar{Q}} = (B^{-1} + \bar{N})(\dot{w}' + \dot{\varphi}). \qquad (8.58)$$

Moreover, we consider the sign conventions introduced by Rubin and Vogel [9], see Fig. 3.2-2 of [9]. Since rates were not introduced explicitly in [9], we subsequently avoid superimposed dots for the entities in the formulas of [9], but we indicate the latter by the index RV:

$$\dot{n} = -n_{RV}, \qquad \dot{q} = q_{RV}, \qquad \dot{m} = -m_{RV}, \qquad\qquad (8.59)$$
$$\bar{N} = -N_{RV}, \qquad \dot{\bar{N}}' = -N'_{RV}, \qquad \dot{\bar{Q}} = Q_{RV}, \qquad \dot{M} = M_{RV}, \qquad (8.60)$$
$$\dot{w} = w_{RV}, \qquad \dot{u} = u_{RV}, \qquad \dot{\varphi} = -\varphi_{RV}. \qquad\qquad (8.61)$$

Substituting Eqs. (8.59)–(8.61) into the above relation (8.57), we first obtain Eq. (3.2-14) of [9]

$$N'_{RV} + n_{RV} = 0. \qquad (8.62)$$

Using Eqs. (8.57) above, we get

$$Q'_{RV} - N_{RV} w''_{RV} + q_{RV} = 0, \qquad (8.63)$$

which coincides with the result of substituting Eq. (3.2.-12) of [9].

From Eq. (8.57), one obtains Eq. (3.2.-13) of [9]

$$M'_{RV} - Q_{RV} - m_{RV} = 0. \qquad (8.64)$$

Concerning the constitutive relations, replace C^{-1} by D_{RV} in Eq. (8.58) above. This gives Eq. (3.2-17) of [9]

$$N_{RV} = -D_{RV} u'_{RV}.$$ (8.65)

Similarly, replacing $(B^{-1} + \bar{N})$ in Eq. (8.58) by S_{RV} yields Eq. (3.2-16) of [9]:

$$Q_{RV} = S_{RV}(w'_{RV} - \varphi_{RV}).$$ (8.66)

This clarifies that, when using B^{-1} for S_{RV} directly, the influence of the normal force in the intermediate configuration is neglected. Since this influence often will be small, this second approximation appears to be reasonable, but again brings no computational advantage.

Finally, replacement of D in Eq. (8.53) above by B_{RV} finally results in Eq. (3.2-15) of [9]:

$$M_{RV} = -B_{RV} \varphi'_{RV}.$$ (8.67)

This closes our derivation of the fundamental relations of the beam theory of second order with shear, as stated in [9].

8.6   Conclusion

In Sects. 8.4 and 8.5 above, the fundamental relations of the beam theory of second order, see Rubin and Vogel [9], have been shown to represent a slight simplification of an exactly linearized version of the continuum mechanics-based extension of the Reissner finite-strain beam theory discussed before in Sect. 8.3. The more involved case of beams with shear and initial imperfections, which also was treated in [9], will be studied in a further contribution.

References

1. Ciarlet, P.G.: Mathematical Elasticity: Volume I: Three-dimensional Elasticity. North-Holland Publishing Company, Amsterdam (1988)
2. DaDeppo, D.A.: Note on Betti's theorem for infinitesimal deformations superimposed on finite deformation of a plane curved beam. Mech. Struct. Mach. **15**(2), 177–183 (1987)
3. Irschik, H.: Generalized reciprocity theorems for infinitesimal deformations superimposed upon finite deformations of rods: the plane problem. Acta Mech. **230**(11), 3909–3921 (2019)
4. Irschik, H., Gerstmayr, J.: A continuum mechanics based derivation of Reissner's large-displacement finite-strain beam theory: the case of plane deformations of originally straight Bernoulli-Euler beams. Acta Mech. **206**(1–2), 1–21 (2009)

5. Irschik, H., Gerstmayr, J.: A continuum-mechanics interpretation of Reissner's non-linear shear-deformable beam theory. Math. Comput. Model. Dyn. Syst. **17**(1), 19–29 (2011)
6. Petersen, C.: Stahlbau. Grundlagen der Berechnung und baulichen Ausbildung von Stahlbauten, 4th ed. edn. Springer Vieweg, Wiesbaden (2013)
7. Reissner, E.: On one-dimensional finite-strain beam theory: the plane problem. Zeitschrift für angewandte Mathematik und Physik (ZAMP) **23**(5), 795–804 (1972)
8. Rubin, H., Schneider, K.: Baustatik: Theorie I. und II. Ordnung. Werner Verlag GmbH & Co KG, Düsseldorf (2002)
9. Rubin, H., Vogel, U.: Baustatik ebener stabwerke. Stahlbau-Handbuch **1** (1982)
10. Simo, J.C., Hughes, T.J.: Computational Inelasticity. Springer, New York (1998)
11. Washizu, K.: Variational Methods in Elasticity and Plasticity, vol. 3. Pergamon Press, Oxford (1975)
12. Ziegler, F.: Mechanics of Solids and Fluids, 2nd edn. Springer, New York (1995)

Chapter 9
Surface Tension Revisited

Bernhard Jakoby

Abstract Inspired by a paper by Prandtl, a simple explanation for the occurrence and the character of the surface tension in liquids is devised, which connects a molecular view with a continuum model of the liquid. Doing so, the nature of the so-called surface tension can be understood as an imbalance between internal pressure and cohesive forces related to (virtual) cut surfaces orthogonal to the liquid's surface. By including these cohesive forces as part of the stress tensor, a non-isotropic stress tensor is obtained close to the surface.

9.1   Introduction

Surface tension is a cohesion-related phenomenon, which is best known for its effects on the surfaces of liquids. Examples are the formation of droplets, the contact angles of sessile droplets on substrates, and the ability of water striders to walk on water surfaces.

For individual molecules, the cohesive forces between liquid molecules can be modeled, e.g., using Lennard–Jones (LJ) potentials, which cover both, the repulsive forces acting between intimately neighboring molecules as well as the attractive forces acting when they are farther away.

On the macroscopic scale, continuum models are preferably used and thus it is desirable to devise a continuum-theoretic model that correctly represents the effects associated with surface tension. It turns out that surface tension can be represented by means of a thin elastic layer coating a liquid surface. This fictitious layer is under mechanical tension (stress), which conforms to the notion of surface tension. Such a fictitious elastic layer, however, apparently contradicts a fundamental assumption that is made in the continuum theory of ideal liquids, i.e., that an ideal liquid cannot support shear stresses and thus the stress tensor is isotropic:

B. Jakoby (✉)
Institute for Microelectronics and Microsensors, Johannes Kepler University Linz, Linz, Austria
e-mail: bernhard.jakoby@jku.at
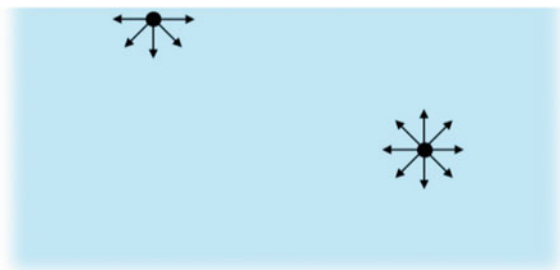
Fig. 9.1 Attraction forces of molecules close to the surface and within the bulk of a liquid (blue region) as commonly shown in textbooks. The picture suggests (and many textbooks claim) that there is a net force towards the bulk of the liquid for molecules close to the surface while there is none for molecules within the liquid. In reality (ignoring thermal motion), there is no force in equilibrium as the attraction forces are balanced by pressure forces representing the interaction with neighboring molecules

$$T_{ij} = -p\delta_{ij}. \tag{9.1}$$

Here, T_{ij} denotes the stress tensor (in component notation), p is the hydrostatic pressure, and δ_{ij} is the Kronecker delta symbol which equals 1 if $i = j$ and vanishes otherwise. The explanation for this behavior or, more accurately, the link between the microscopic and continuum-theoretical picture is scarcely discussed in the literature. Very often (particularly in textbooks) explanations of surface tension refer to "uncompensated" interaction forces experienced by molecules at the surface of a liquid, whereas molecules within the liquid (in the bulk of the liquid) feature balanced interaction forces in all directions. This is very often illustrated by figures such as Fig. 9.1. Here, the arrows indicate said attraction forces, which may indeed suggest that molecules at the surface experience a resulting force into the liquid, which is frequently also explicitly stated. In the author's opinion, this view is ill-conceived not only since this does not directly suggest the presence of a lateral tension in a surface layer but also as, according to Newton's third law, these seemingly non-vanishing forces are, in equilibrium, balanced by repulsive forces from intimately neighboring molecules,[1] which we will below relate to the so-called internal pressure. The internal pressure is, in turn, directly related to the distance of neighboring molecules, which thus changes (even if only slightly) when approaching the surface.

The author recently became aware of one of Ludwig Prandtl's papers dating from 1947 [1], which essentially deals with the relation between the macroscopic and the microscopic view, even though this was not Prandtl's main motivation. According to the Introduction in [1], Prandtl was rather disturbed by "physicists" refusing to accept that the phenomenon of surface tension is actually related to "real forces" and suspects that said physicists misinterpret or forgot the laws of balanced forces.

---

[1] In reality we, of course, are faced with superposed Brownian motion leading to the continuous movement of all individual molecules. For the sake of simplicity, we do not consider this motion and the related additional forces, which here are simply interpreted as superposed noise.

While these comments are clearly stimulated by specific discussions with several colleagues, I see a certain connection to the above-mentioned ill-conceived attempts to illustrate surface tension. Without explicitly saying so, Prandtl considers the balance of forces in a planar liquid surface using some simplified models to demonstrate what the character of the surface tension is and how it can be calculated, in principle, if the cohesive force between two liquid molecules is known thus achieving the aforementioned connection between the molecular level and continuum theory.

A key point in the approach is to distinguish between repelling forces essentially occurring between neighboring molecules and attractive forces between molecules that are farther away from each other. Using the concepts of continuum theory, the latter are considered as volume forces, while only the former are associated with a stress tensor, which is considered isotropic conforming to the previously mentioned fundamental properties of ideal liquids. However, as the ranges of these volume interaction forces are small, they could formally and approximately be considered by equivalent stresses, which would, in turn, yield a non-isotropic stress tensor close to the liquid surface as will be discussed below.

Prandtl does not characterize his approach in these terms and, at the same time, considers a specific interaction model to demonstrate the appearance of the surface tension. In this paper, we show that the same qualitative conclusions can be obtained without assuming a specific interaction model using some simple, partly geometric considerations. Also, the above interpretation with respect to stresses and volume forces will be outlined in more detail.

There are numerous other papers dealing with the phenomenon of surface tension and it is therefore impossible to provide a complete list of relevant references. In any case, [2–4] may serve as starting points to explore other accounts on the topic.

9.2 Interaction Between Molecules

Before moving to continuum theory, we consider how the interaction between molecules can be modeled. The Lennard–Jones potential V_{LJ} represents an established model describing repelling as well cohesive forces between molecules

$$V_{LJ} = E_0 \left(\left(\frac{r_0}{r} \right)^{12} - 2 \left(\frac{r_0}{r} \right)^{6} \right), \tag{9.2}$$

where E_0 represents the (negative) interaction energy at the minimum of the potential, which occurs at an equilibrium distance $r = r_0$ between the molecules. The first term represents a repulsive term, while the second accounts for the cohesive attractive forces between the molecules, which can be caused by van der Waals or dispersion forces. The exponent associated with the repulsive forces is much higher than that of the attractive forces and represents the quantum-mechanical forces appearing once the orbitals of the molecules start to overlap. There are other models representing

Fig. 9.2 Lennard–Jones
potential and attraction force
(each suitably scaled) versus
particle distance. At $r = r_0$
two interacting particles are
at equilibrium featuring a
minimum of the potential
and zero interaction force.
The dashed green line shows
the approximation of the
force characteristics
featuring arbitrary repulsion
forces as soon as $r = r_0$ is
approached
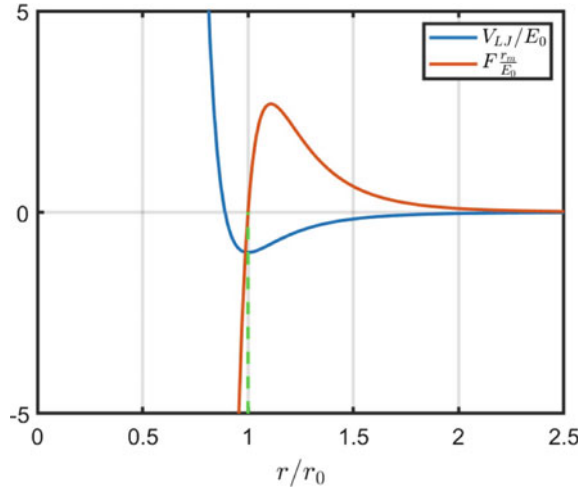
the repulsion and we will also see in this paper that the exact model is less important
as long as it is considered that the repulsion is much stronger than the attraction.

The forces acting between the molecules can be obtained by differentiation with
respect to r (i.e., taking the gradient). Figure 9.2 shows the obtained characteristics
for the potential and the associated force, where a positive force represents attraction.

Two particles in equilibrium assume the distance $r = r_0$. For many particles
(molecules) in a liquid featuring a surface, the equilibrium distances turn out to
be slightly closer (which is represented by an internal pressure as we shall discuss
below). In this case, additional attractive forces to molecules farther away are bal-
anced by the repulsive forces to intimately neighboring molecules. However, as the
repulsion is very strong, the associated changes in distance are minute. This can be
used to justify a simple approximation, i.e., that distances $r < r_0$ are prevented by
arbitrarily strong repulsion forces which occur as soon as $r = r_0$ is reached. This
corresponds to an infinitely steep slope in the force characteristics as illustrated by
the dashed line in Fig. 9.2. Using this approximation, the density in the macroscopic
description remains the same everywhere, which is one key assumption that was also
used in Prandtl's considerations.

We shall also note that in our considerations, we will ignore the effects of super-
posed thermal motion, which, of course, affects the average distances assumed by the
molecules. The basic mechanisms discussed here, however, remain intact and since
we are not aiming at a quantitative description of the phenomenon, this approach
appears justified.

In the following we will thus assume that the molecules are densely packed with an
equilibrium distance $r = r_0$ exerting repulsive forces on their closest neighbors while
attracting molecules farther away. Adopting a continuum view, these attraction forces
can thus be assumed to occur for distances $r > r_0$ obeying a dependence on r as, e.g.,
described by the LJ force. In his paper [1], Prandtl assumes a simple form for this

characteristic, i.e., a linearly increasing force which abruptly drops to zero at some distance $r = R > r_0$. Prandtl pointed out, that a more general relation can be modeled by superposing such characteristics. Since we are not going to calculate the surface tension quantitatively, we deal no further with specific interaction characteristics. Yet, it is useful to observe that the attraction force strongly decays with increasing distance such that it turns out to be beneficial to assume that the forces are negligible once r has exceeded a certain value. In the case of Prandtl's model, this distance is denoted by R and we will also use R to denote this distance (which is not strictly defined by the LJ potential).

9.3   Internal Pressure

The phenomenon of surface pressure can also be investigated theoretically for a plane liquid surface even though its effects are not directly visible such as in other cases as for liquids in a capillary, etc. Adopting the notions of continuum theory and considering the liquid at mechanical equilibrium, we require that the total forces acting on an arbitrary volume element of the liquid must vanish. According to the concepts of continuum theory, these total forces are represented by the surface stresses integrated over the surface of the volume plus a volume integral over body forces.

As discussed above, when considering individual molecules, we recognize that the repulsive forces with intimate neighbors can be associated with the internal pressure p of the liquid, whereas the mutual attraction forces with molecules farther away can be considered as body forces f (forces per volume) acting over longer, though in reality not very long, distances up to the order of $r = R$. In equilibrium, we have, according to Cauchy's first law of continuum mechanics,

$$\nabla p = f. \tag{9.3}$$

In our considerations, we assume zero gravity (which would merely represent an additional contribution to the body forces) and zero ambient pressure outside the liquid, which means that the internal pressure when approaching the surface must vanish. In Fig. 9.3, the effective interaction radius of a particular molecule close to the surface, is indicated by a circle (with radius R). It can be seen that in this case a net body force directed into the liquid results, as a part of the "interaction circle," i.e. the parts outside the liquid, is not filled with interaction partners. In contrast, a particle deeper within the liquid (depth larger than R) in total experiences zero attraction forces as, within the effective interaction range R, interaction partners in all directions are present and equally distributed. This consideration corresponds to the common observation illustrated in Fig. 9.1. Accordingly, we obtain a pressure gradient balancing these resulting body forces f and hence the pressure into the liquid increases up to a constant level p_i, yielding a vanishing gradient ∇p deeper within the liquid where $f = 0$ (see Fig. 9.3).
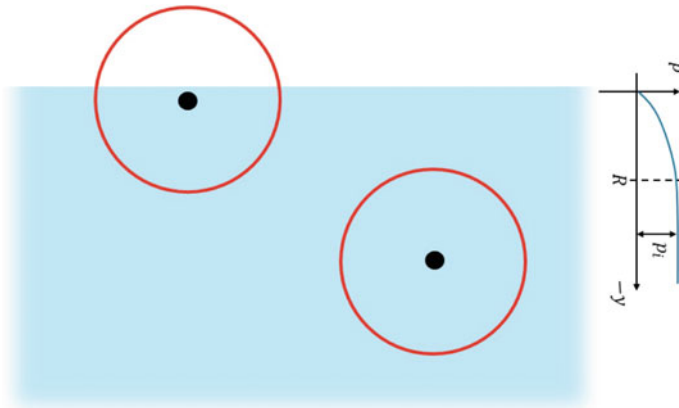
Fig. 9.3 Effective interaction ranges of particles with respect to attraction forces. Interactions with molecules outside this range (radius R)—if any—are considered to be negligible. It can be seen that for molecules close to the surface a net attraction force into the liquid (orthogonal to the surface) is obtained, which corresponds to the observation in Fig. 9.1. These forces, however, in the considered case of equilibrium, are balanced by repulsive forces from intimately neighboring molecules which represent the so-called internal pressure of the liquid
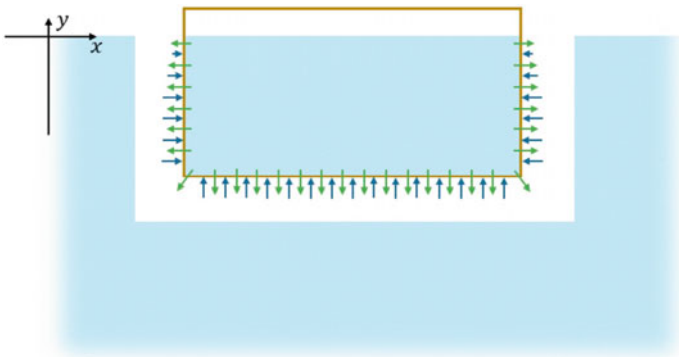
Fig. 9.4 Virtually cutout volume including the surface of the liquid. The attractive (volume) forces with particles outside the volume are represented by green arrows. The repulsive forces with intimately neighboring molecules are represented by blue arrows. Equilibrium in the vertical (y) direction is achieved by balancing the net attractive forces with the pressure forces acting on the lower boundary surface. Equilibrium in lateral (x) direction is warranted by the symmetry, i.e., the attractive forces traversing the vertical side walls need not be balanced by the pressures acting on the side walls. It turns out that close to the surface, this balance is indeed not fulfilled (illustrated by slightly longer green arrows in this region) which gives rise to the phenomenon referred to as surface tension

This conclusion can also be made in a similar manner by considering a finite volume V enclosed by a surface S as indicated in Fig. 9.4, where we obtain for the integral form of the previous equation (using the divergence theorem):

$$\int_V \mathbf{f} dV = - \oint_S p d\mathbf{S} \tag{9.4}$$

That means that the total (integrated) body forces within this volume are balanced by the integrated pressure at the circumference. Note that only interaction forces with molecules outside the volume contribute to the volume integral whereas the mutual interaction forces between molecules within V cancel each other.

9.4   Surface Tension

We can also extend the volume laterally into infinity yielding a slab of liquid. As we now have a laterally spatially invariant situation, the integrated pressure acting along a surface element ΔS must be balanced by all interaction forces (body forces) whose lines of action traverse ΔS (see Fig. 9.5 left). If we consider such a particular surface element ΔS for slabs of liquids with different thicknesses, we again find that the maximum pressure is asymptotically approached as soon as the thickness of the slab goes beyond those distances R where significant attraction forces between two molecules occur. We can illustrate this by drawing a circle (or sphere in 3D[2]), centered at ΔS, whose radius R represents such a distance[3] as shown in Fig. 9.5. For thin slabs, i.e., virtual cuts close to the surface, not the entire circle is filled with molecules such that the resulting interaction forces associated with ΔS are smaller than for the case, where the entire circle is submerged under the surface. As these attraction forces are balanced by the pressure force $p\Delta S$, the gradual increase of the pressure from the surface to an asymptotic value deep inside the liquid is demonstrated again. As gravitation was ruled out and no external pressure is applied, this pressure corresponds to the "internal pressure" of thermodynamics.

When considering virtual cuts in the vertical direction such as the side walls of the virtually cutout volume in Fig. 9.4, the equilibrium conditions do not require that pressure and attraction forces (with lines of action traversing the cut line) are balanced. This is because, concerning lateral forces, said volume is already in equilibrium by virtue of the symmetry with respect to the vertical axis, i.e., forces that are associated with the left cut surface (pressures and interaction forces with lines

---

[2] Note that here and, in the following, we restrict ourselves to 2D considerations; the generalization to the 3D case is straightforward.

[3] By doing so, we not only guarantee that we cover all interactions up to a distance R but also consider some (not all) interactions beyond that distance—for oppositely positioned molecules at the circumference of the circle even in a distance $2R$. But since we consider all interaction forces beyond R to be negligible, this partial contribution does not affect our approach.
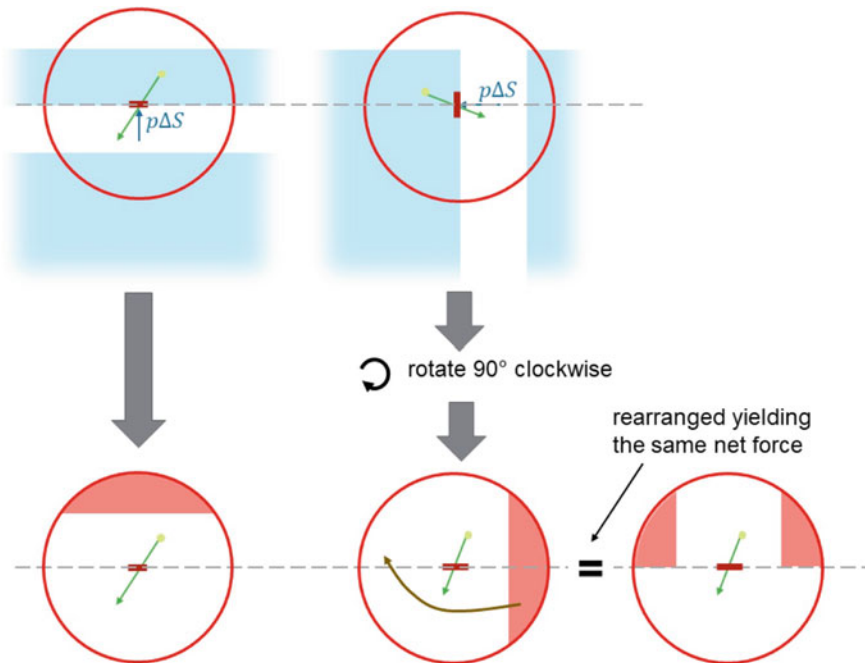
Fig. 9.5 Pressures and body forces associated with elements ΔS of a horizontal (left) and vertical (right) cut surface. In the case of horizontal cut surfaces, the pressures acting on ΔS are balanced by body forces between particles inside and outside the cutout volume whose lines of action traverse ΔS. In the case of the vertical cut surface, an element at the same depth level experiences the same pressures as in the horizontal case. However, the associated body forces, in general, do not balance these pressures. The scheme in the lower part of the figure is used to compare these forces

of action traversing the respective cut surface), are also present, equally strong but oppositely oriented, on the right side due to the symmetry of the arrangement.

It turns out that the forces associated with a particular portion of a vertical cut surface are indeed not balanced and this essentially represents the phenomenon that is commonly referred to as surface tension. The internal pressure in a particular depth beneath the liquid surface is given by the previous considerations and, due to the assumed isotropy of the stress tensor, this pressure also occurs as virtual tension at vertical cut surfaces. The attraction forces are again interpreted as body forces. As for the horizontal cut before, one may assign these body forces to a particular surface element ΔS of the vertical cut surface, if their lines of action traverse ΔS.

In the following, compare the magnitude of the pressure forces to that of the body forces associated with a vertical cut element ΔS. The upper drawings in Fig. 9.5 illustrate the situation for an element ΔS of a virtual horizontal (left) and vertical cut surface, where both elements are located at the same depth level. In equilibrium, as outlined above, the forces $p\Delta S$ are balanced by the body forces whose line of action traverses the element ΔS in case of the horizontal cut surface. As outlined above,

due to the limited interaction distance, which we consider only within the range indicated by a red circle (sphere in 3D), these forces decrease when approaching the surface as an increasing portion of the circle is not occupied by liquid molecules. In the corresponding lower scheme in Fig. 9.5, this portion is marked.

In case of the vertical cut surface, by virtue of the isotropy of the pressure, the same pressure forces apply. The body forces associated with the surface element ΔS (right upper illustration) are different, though. Again, the scheme in the lower part of Fig. 9.5 indicates, what portions of the considered interaction range are missing when approaching the liquid surface. To ease the comparison with the corresponding case for the horizontal cut line, the scheme is rotated 90° counterclockwise. The marked region in the lower half of the sphere can furthermore be moved as indicated into the lower right plot yielding the same interaction forces when integrating over all possible interaction partners in the lower and upper half of the circles drawn.

Thus, when comparing the schemes, we can also develop a notion about the degree of imbalance between attraction forces and pressure forces when considering horizontal cuts as the interaction forces corresponding to the scheme on the left (horizontal cut) exactly represent the pressure forces due to the balance in case of horizontal cuts.

First, it becomes obvious that the mentioned imbalance vanishes once the consideration is made in a depth, which is larger than the interaction distance, i.e., where the indicated circles are completely within the region filled with liquid such that the marked portions in the schemes vanish. This means that the pressure forces inside the liquid are in fact balanced by attraction forces in all directions (for vertical and horizontal cuts).

Closer to the surface the situation is different. In terms of area, the marked portions (representing missing interaction partners) are equally large in both cases. However, in the case associated with the horizontal cuts, these portions are located at the sides, while in the left case (vertical cut) the portion concerns the top of the circle. In the following, we consider the impact of this difference on the resulting normal force components.

Figure 9.6 shows the schemes for both cases again in an overlapping drawing. It turns out that, depending on the considered level, there can be a portion (marked B) that is missing in both cases, when the attraction forces are summed up. Portions A and C are not contributing in case of vertical and horizontal cuts, respectively. As A and C feature the same shape and the same distance to the center of the considered surface element ΔS, one might erroneously assume that the associated missing integrated attraction forces are equal in both cases. However, when comparing the lines of actions for particles at corresponding positions (for each point in A there is a corresponding point in region C; Fig. 9.6 shows a particular example) one can find out that the lines of action for all points associated with region A traverse ΔS at a smaller angle α than the line of action with the corresponding point in region C (angle β) thus yielding a smaller contribution to the normal force component (which is the one we are interested in). Furthermore, the integration of all interaction forces concerns all lines of action passing through the small, but finite, element. It can be seen that a point in region A interacts with a smaller part of the lower region (characterized
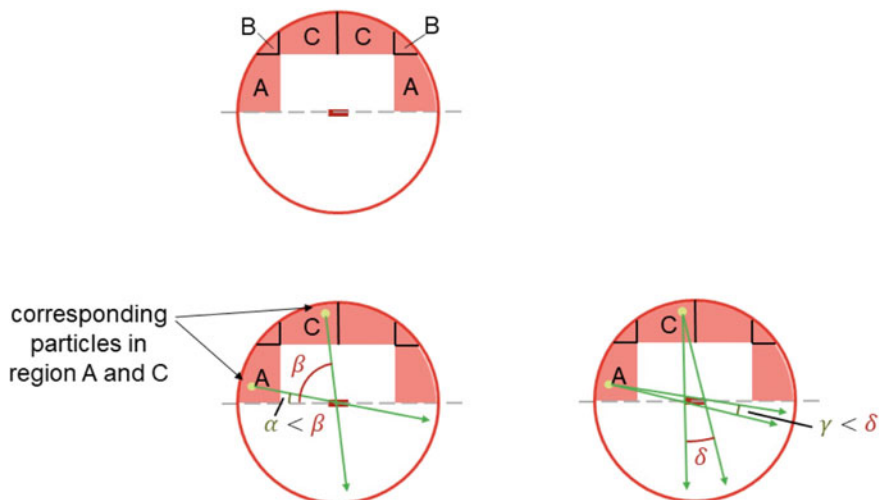
Fig. 9.6 Schematic drawing of portions not contributing to attraction forces in case of horizontal (B&C) and vertical cuts (A&B)

by the angle γ) than the corresponding point in region C (angle δ). So in summary, points in region A correspond to smaller force contributions than the corresponding ones in region C. Thus, in view of the fact that these forces are missing in the calculation of the attraction forces, the attraction forces corresponding to a vertical cut at a certain level are larger than the ones for a horizontal cut. As the pressure forces are the same in both cases, there remains a non-compensated attraction force for vertical cuts.

In our considerations, following Prandtl's idea, we took the attraction forces into account as body forces. Yet, in view of the strong decay of the LJ-potential significant contributions will only arise from particles very close (within a few molecule diameters) to the virtual cut. Hence, it could be argued that these forces could be included in the stress tensor. Doing so, the total pressure deep inside the liquid vanishes as the previously considered pressures ("internal pressure") are fully compensated by the attraction forces yielding zero pressures—just as one would expect as we did not consider the impact of gravity and did not assume any ambient pressure above the liquid surface. Approaching the surface, this compensation does not hold for components in the surface plane (tangential components) giving rise to a non-vanishing component of the so defined stress tensor—these are the stresses associated with surface tension. In this model, the stress tensor of the liquid is not isotropic close to the surface!

9.5 Conclusions

Inspired by a paper by Prandtl, we devised a simple explanation for the occurrence and the character of the surface tension in liquids, where we connected a molecular view (incorporating repulsive and attractive forces between molecules as described by the LJ potential) with a continuum model of the liquid. We assigned repulsive forces between neighboring molecules to the internal pressure of the liquid and considered attractive forces as body forces. By considering the balance of cut-out liquid volumes, we were able to establish that close to the surface, attractive forces traversing virtual vertical cuts in the liquid are not balanced by opposing pressures, which represents the phenomenon referred to as surface tension. By including these attraction forces in the stress tensor (which can be justified by the fact that they only occur close to the virtual cut surface), the so obtained stress tensor appears non-isotropic close to the surface corresponding to the continuum model of surface tension in terms of a stretched thin elastic sheet covering the surface.

References

1. Prandtl, L.: Zum Wesen der Oberflächenspannung. Annalen der Physik **463**(1–3), 59–64 (1947)
2. Jones, J.E.: On the determination of molecular fields.–II. From the equation of state of a gas. Proc. R. Soc. Lond. A **106**(738), 463–477 (1924)
3. Kirkwood, J.G., Buff, F.P.: The statistical mechanical theory of surface tension. J. Chem. Phys. **17**(3), 338–343 (1949)
4. Marchand, A., Weijs, J.H., Snoeijer, J.H., Andreotti, B.: Why is surface tension a force parallel to the interface? Am. J. Phys. **79**(10), 999–1008 (2011)

Chapter 10
Flatness-Based Control of a Closed-Circuit Hydraulic Press

Helmut Kogler, Karl Ladner, and Peter Ladner

Abstract Hydraulic drive technology is well known for its high force density and, hence, basically qualified for press applications. While systems with constant pressure supply suffer from a bad energy efficiency due to resistance control and, furthermore, an inferior controllability in particular at fast movement operation, the presented hydraulic press concept overcomes these drawbacks by using a synchronized cylinder in a closed circuit displacement control for rapid movement and in press mode. In this paper, a flatness-based control of the position of the main press actuator is presented. The derivation of the controller design is followed by simulation experiments and, furthermore, by a discussion of measurements on a two-axis prototype with a load capacity of 50 tons.

10.1 Introduction

Conventional hydraulic presses (see for instance [1, 5]) use hydraulic load sensing for the press mode and a controlled falling of the upper press tool for a fast movement downward. Since in the load-sensing mode and, furthermore, during the fast motion operation, the movement is controlled by resistance control a certain loss of energy occurs. The resulting heating of the oil must be reduced by additional coolers, at least in some cases. Another drawback of such systems is the permanent operation of the constant pressure supply, which results in additional energy losses and unnecessary noise (see, for instance, [6, 10]). The conventional concept has a single hydraulic supply for one machine, which needs besides pump, motor also transmission lines from a tank, and auxiliary components, which inhibit a strict modular and compact design of the machine, where each axis would be completely individual and realized in a compact manner. Furthermore, during the assembling process, numerous hydraulic connections must be installed, which constitute a potential danger of exter-

H. Kogler (✉) · K. Ladner · P. Ladner
Linz Center of Mechatronics GmbH, Altenberger Strasse 69, 4040 Linz, Austria
e-mail: helmut.kogler@lcm.at
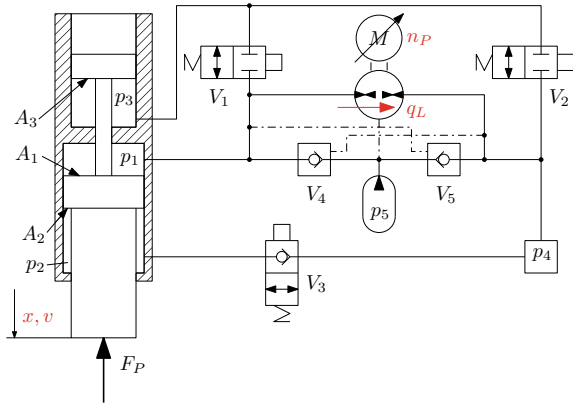
nal leakage, hose breaking, and replacement by spare parts which results in additional maintenance work.

In contrast to conventional hydraulic presses with the presented concept according to Fig. 10.1, the mentioned drawbacks can be prevented. The main actuator is a hydraulic cylinder, which is controlled by a pump, i.e., the rotational speed of the pump corresponds to the velocity of the piston. The cylinder has three hydraulic chambers, where the cross-sectional areas follow the relation

$$A_1 = A_2 + A_3, \tag{10.1}$$

which enables a different transmission ratio between the rotational speed of the pump and the velocity of the piston. In particular, if the valve V_1 is switched, then the effective cross-sectional area $A_2 = A_1 - A_3$ is active. Thus, a rapid motion at low forces can be achieved. If the valve V_2 is switched, then A_1 is the effective cross-sectional area and high forces can be produced at low velocities. The valve V_3 represents an emergency valve and, during a normal operation of the press, this valve is always open. In case of an emergency case, the valve V_3 must be shut quickly in order to prevent severe injuries of human operators. The accumulator keeps the whole configuration at a minimum pressure level. In combination with the unlockable check valves, V_4 and V_5, the compressibility of the fluid and certain leakage flows can be compensated.

In this paper, the application of a flatness-based controller according to the established literature (see, for instance, [2, 4, 8, 9]) for the position of the piston of the press is presented. In contrast to common PI controllers, which are only capable to stabilize a rest position, the flatness-based approach stabilizes the trajectory of the piston. Thus, with a properly designed flatness-based controller multiple press axes can be easily realized without an additional synchronizing controller.

10.2   Modeling

With regard to Fig. 10.1, the mechanical part of the press, respectively, the movement of the piston, follows the momentum equation

$$
\begin{bmatrix} \dot{x} \\ \dot{v} \end{bmatrix} = \begin{bmatrix} v \\ \frac{1}{m}\left(F_H - mg - F_P - \underbrace{\left(\mathrm{sign}\,(v)\left((F_S - d_c)\,e^{-\left|\frac{v}{v_0}\right|} + d_c \right) + d_v v \right)}_{\text{static friction model}} \right) \end{bmatrix},
$$
(10.2)

with the resulting hydraulic force $F_H = p_2 A_2 - p_1 A_1 + p_3 A_3$. This model consideres a static friction model including a stick-slip effect in the motion of the piston. The hydraulic model is represented by

$$
\begin{bmatrix} \dot{p}_1 \\ \dot{p}_2 \\ \dot{p}_3 \\ \dot{p}_4 \\ \dot{p}_5 \end{bmatrix} = \begin{bmatrix} \frac{E_{\text{oil}}}{V_{0_1} - A_1 x}\left(u_{V_1} K_{V_1} \sqrt[V]{p_3 - p_1} - V_S n_P + A_1 v - Q_L + Q_{V_4} \right) \\ \frac{E_{\text{oil}}}{V_{0_2} + A_2 x}\left(-A_2 v + u_{V_3} K_{V_3} \sqrt[V]{p_4 - p_2} \right) \\ \frac{E_{\text{oil}}}{V_{0_3} + A_3 x}\left(-A_3 v - u_{V_1} K_{V_1} \sqrt[V]{p_3 - p_1} + u_{V_2} K_{V_2} \sqrt[V]{p_4 - p_3} \right) \\ \frac{E_{\text{oil}}}{V_{0_4}}\left(-u_{V_3} K_{V_3} \sqrt[V]{p_4 - p_2} - u_{V_2} K_{V_2} \sqrt[V]{p_4 - p_3} + V_S n_P + Q_L + Q_{V_5} \right) \\ \frac{\kappa p_5 (-Q_{V_4} - Q_{V_5})}{V_{0_S}\left(\frac{p_0}{p_5}\right)^{\frac{1}{\kappa}}} \end{bmatrix},
$$
(10.3)

with the flow rates through the unlockable check valves

$$
Q_{V_4} = \begin{cases} K_{V_4} \sqrt[V]{p_5 - p_1} & 0.45 p_4 > p_1 \\ K_{V_4} \mathrm{cv}\,(p_5 - p_1) & \text{otherwise} \end{cases}
$$

$$
Q_{V_5} = \begin{cases} K_{V_5} \sqrt[V]{p_5 - p_4} & 0.45 p_1 > p_4 \\ K_{V_5} \mathrm{cv}\,(p_5 - p_4) & \text{otherwise} \end{cases}
$$
(10.4)

$$
\mathrm{cv}\,(\Delta p) = \begin{cases} \sqrt[V]{\Delta p} & \Delta p > 0 \\ 0 & \text{otherwise,} \end{cases}
$$

according to the orifice characteristics

$$
\sqrt[V]{\Delta p} = \mathrm{sign}(\Delta p)\sqrt{|\Delta p|},
$$
(10.5)

and the leakage flow through the pump

$$
Q_L = \frac{q_{\text{leak}}}{p_{\text{leak}}}\,(p_1 - p_4).
$$
(10.6)

The resulting complete model of the press consisting of Eqs. (10.2) and (10.3) is nonlinear and suffers from numerous square root characteristics due to the valve's flow equations and, furthermore, switching conditions of the check valves and the

friction model. Thus, the model is evaluated as too complicated for an efficient controller design but will be used for simulation experiments.

10.3 Synthesis

For an efficient controller design, a suitable dynamic model for the motion of the piston must be found. Therefore, in a first step the compressibility of the fluid is completely neglected. Then the continuity equation reduces to

$$0 = V_D n_P - A_E v - q_L, \tag{10.7}$$

with the displacement volume V_D of the pump, the effective cross-sectional area of the piston A_E and a certain leakage flow rate q_L depending on the pressure difference over the pump. Furthermore, the leakage flow q_L represents a certain correction term in Eq. (10.7) for the compressibility of the fluid, at least in a simplified manner. A re-arrangement of Eq. (10.7) leads to

$$\dot{x} = \underbrace{-\frac{q_L}{A_E}}_{f} + \underbrace{\frac{V_D}{A_E}}_{g} n_P, \tag{10.8}$$

which represents the basic model used for the following controller design. The model (10.8) is nonlinear and input-state linearizable according to literature (see, for instance, [3]). With the feedback of the input transformation

$$n_P = \frac{v_B - L_f x}{L_g x} \tag{10.9}$$

the model is linearized and now represented by the so-called Brunovsky canonical form

$$\dot{x} = -\frac{q_L}{A_E} + \frac{V_D}{A_E} \underbrace{\left(\frac{\left(v_B + \frac{q_L}{A_E} \right) A_E}{V_D} \right)}_{\text{Eq. (10.9)}} = v_B \tag{10.10}$$

with the new input v_B. From Eq. (10.10) it is clear that the actual velocity of the piston corresponds exactly to the new input v_B of the system. Thus, defining a control error $e = x - x_d$ with the desired piston position x_d a flatness-based controller is derived by

$$0 = \underbrace{(v_B - v_d)}_{\dot{e}} + \underbrace{(x - x_d)}_{e} \gamma_C, \tag{10.11}$$

which represents a linear differential equation for the trajectory error e. With the correct choice of the controller parameter γ_C for asymptotic stability, Eq. (10.11) can be solved for v_B and the trajectory error e is forced to decay with time. However, the controller only works properly, if the leakage flow rate q_L is known. Assuming that the dynamics of the process force F_P is low compared to the desired dynamics of the trajectory of the piston, then the leakage flow can be modeled like

$$\dot{q}_L = 0. \tag{10.12}$$

With the new state q_L the extended system calculates to

$$\begin{bmatrix} \dot{x} \\ \dot{q}_L \end{bmatrix} = \underbrace{\begin{bmatrix} 0 & -\frac{1}{A_E} \\ 0 & 0 \end{bmatrix}}_{\mathbf{A}} \begin{bmatrix} x \\ q_L \end{bmatrix} + \underbrace{\begin{bmatrix} \frac{V_D}{A_E} \\ 0 \end{bmatrix}}_{\mathbf{b}} n_P$$

$$y = \underbrace{\begin{bmatrix} 1 & 0 \end{bmatrix}}_{\mathbf{c}^\mathsf{T}} \begin{bmatrix} x \\ q_L \end{bmatrix}, \tag{10.13}$$

which is linear and even time-invariant. Thus, for the system (10.13), now a complete observer can be designed. For this purpose, the observability must be checked by the calculation of the observability matrix

$$\mathbf{Q} = \begin{bmatrix} \mathbf{c}^\mathsf{T} \\ \mathbf{c}^\mathsf{T}\mathbf{A} \end{bmatrix} = \begin{bmatrix} 1 & 0 \\ 0 & -\frac{1}{A_E} \end{bmatrix}, \tag{10.14}$$

which is regular for every point in time and, thus, the system (10.13) is observable. In order to simplify the observer design, the system is transformed into observer canonical coordinates by using

$$\mathbf{z} = \mathbf{\Theta}^{-1}\mathbf{x} \tag{10.15}$$

and the transformation matrix [7]

$$\mathbf{\Theta}^{-1} = \begin{bmatrix} \mathbf{Q}^{-1}\begin{bmatrix} 0 \\ 1 \end{bmatrix}, & \mathbf{A}\mathbf{Q}^{-1}\begin{bmatrix} 0 \\ 1 \end{bmatrix} \end{bmatrix} = \begin{bmatrix} 0 & -\frac{1}{A_E} \\ 1 & 0 \end{bmatrix}. \tag{10.16}$$

The system (10.13) in canonical coordinates calculates to

$$\mathbf{A}^\star = \mathbf{\Theta}\mathbf{A}\mathbf{\Theta}^{-1} = \begin{bmatrix} 0 & 0 \\ 1 & 0 \end{bmatrix}$$

$$\mathbf{c}^{\star\mathsf{T}} = \begin{bmatrix} 0 & 1 \end{bmatrix}, \tag{10.17}$$

where the dynamics of the observer can be easily designed

$$\mathbf{A}_{\mathcal{O}} = \mathbf{A}^\star + \begin{bmatrix} -\alpha_0 \\ -\alpha_1 \end{bmatrix} \mathbf{c}^{\star\mathsf{T}} = \begin{bmatrix} 0 & -\alpha_0 \\ 1 & -\alpha_1 \end{bmatrix}. \tag{10.18}$$

After a transformation back into original coordinates, the complete observer reads

$$\begin{bmatrix} \hat{\dot{x}} \\ \hat{\dot{q}}_L \end{bmatrix} = \begin{bmatrix} -\frac{\hat{q}_L}{A_E} + \frac{V_D}{A_E} n_P + \alpha_1 (x - \hat{x}) \\ A_E \alpha_0 (x - \hat{x}) \end{bmatrix}. \tag{10.19}$$

10.4   Simulations

The controller and the observer derived in the previous section were tested by simulation in *Matlab/Simulink*. The corresponding block diagram is depicted in Fig. 10.2. The blue-colored block on the right-hand side contains the dynamic model of the press according to Eqs. (10.2) and (10.3). In the orange block left to the press model, the flatness-based controller and the load observer are located. The block has five inputs, as two for the desired position and velocity of the piston, the actual rotational speed of the pump, the actual piston position, and, finally, the effective cross-sectional area of the piston according to the switching states of the valves V_1 and V_2 in Fig. 10.1. The decisions for the valve switching and, thus, the selection of fast or press mode are calculated in the state machine depicted at the bottom of the block diagram in Fig. 10.2. The remaining red blocks in the upper left corner of the simulation diagram represent the parameterization of the piston trajectory, which must be at least two times differentiable with respect to time according to the requirements for the flatness-based control.

The simulation experiments were carried out for a spring load according to Fig. 10.3, where the load was determined by the compressive force due to the displacement $x - x_{\text{contact}}$ of a linear spring. In Fig. 10.4, the simulation results for a full exemplary press cycle are depicted. In Fig. 10.4a, the position and the velocity of the piston are illustrated. The press cycle starts at an initial position of 200 mm
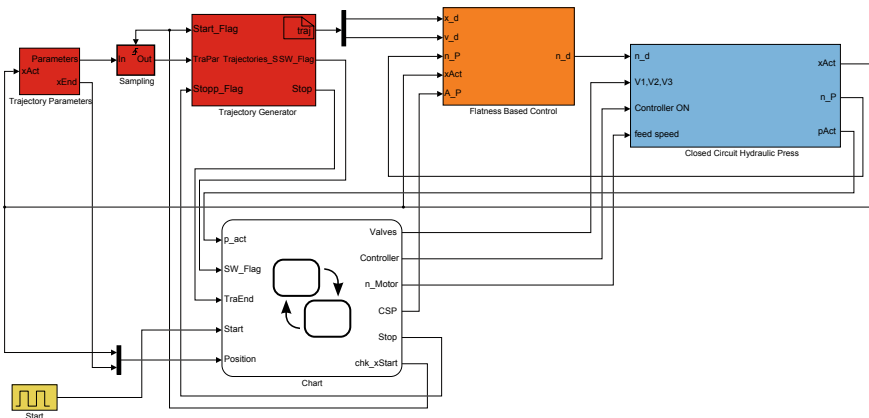
Fig. 10.2   Simulation model
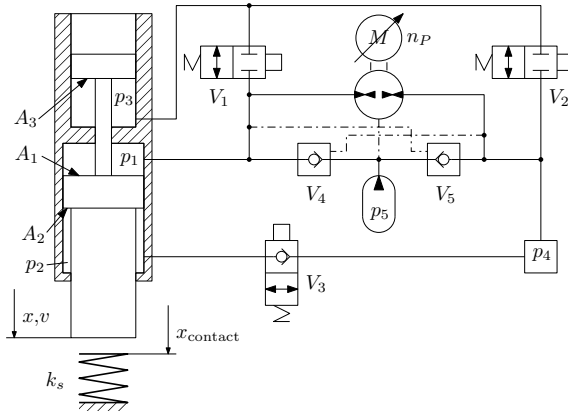
Fig. 10.3 Load model

with a rapid motion downward close to the position x_{contact} with a small effective cross-sectional area A_2. During this fast motion downward, some fluctuations in the velocity are present, which result from the switching of the unlockable check valves V_4 and V_5 according to the internal pressure states presented in the upper diagram of Fig. 10.4b. Then the configuration is switched to the large effective cross-sectional area A_1 for the press mode and the motion against the spring load is executed, which results in a pressure build up of p_1 in the main cylinder chamber. A certain holding phase in the desired target press position is followed by a decompression phase until the piston is losing contact with the load spring. Then the cross-sectional area is switched to fast mode again and a rapid motion to the initial position is performed. In the beginning of this phase, again fluctuations in the velocity can be observed, which

(a) Position and velocity   (b) Pressure and rotational speed
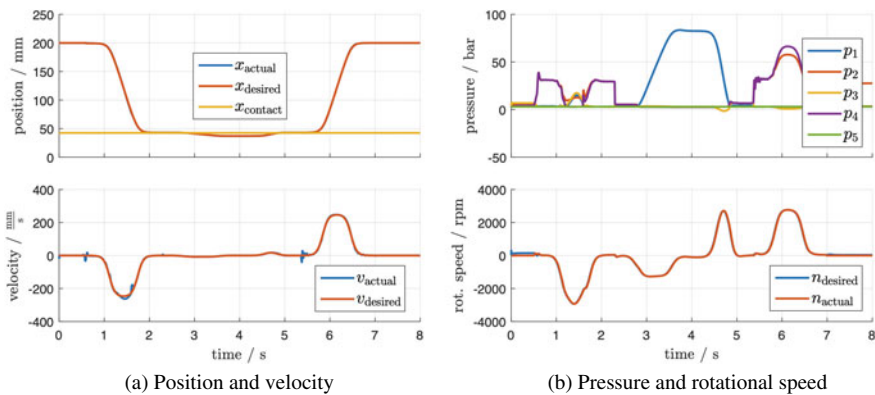
Fig. 10.4 Simulation of an exemplary press cycle
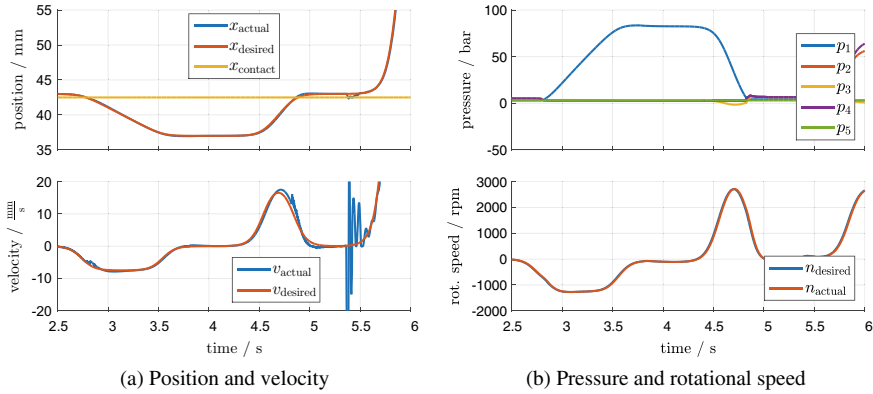
Fig. 10.5 Zoom into Press mode

results from switching to the small effective cross-sectional area A_2 and, furthermore, again from the switching of unlockable check valves V_4 and V_5.

Figure 10.5 presents a close-up of the press mode, which shows a satisfying control performance of the piston trajectory. Only in the decompression phase at higher velocity compared to the press motion and at switching to rapid motion configuration some fluctuations in the trajectory occur. However, the controller copes with such disturbances satisfyingly resulting in a nice decay of the trajectory error.

10.5 Measurements

In Fig. 10.6a, a picture of a single axis prototype with a force capacity of 25 tons is presented, and the major parts with regard to Fig. 10.1 are indicated. In Fig. 10.6b, a parallel arrangement of two single axes is depicted, which was considered for the measurements. By the use of a beam, the two individual press axes act simultaneously against the load, which is constituted by a distributed elastomer spring.

In Fig. 10.7, the measurements of an exemplary press cycle with the 50 tons two axes press are illustrated. In the diagram on the left-hand side (Fig. 10.7a), the position and the velocity of the piston are depicted. Like in the simulation results during the fast motion downward fluctuations occur in the measurements as well. Here, additionally to the effect of the switching of the unlockable check valves, a saturation effect in the rotational speed of the motor comes into play, which can be seen in the lower diagram of Fig. 10.7b.

In Fig. 10.8a, a zoom into the press mode phase is illustrated. The fluctuations in the actual velocity result from the numeric differentiation of the position signal. In Fig. 10.8b, a closer view to the target position of 37 mm shows 60 consecutive periods of one press cycle. In those measurements, an accuracy of approximately $40\,\mu$m at a repeatability in the range of $10\,\mu$m can be achieved. It must be remarked
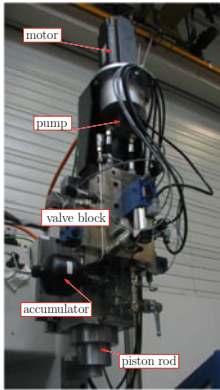
(a) Prototype with 25 tons capacity   (b) double axes press with 50 tons capacity
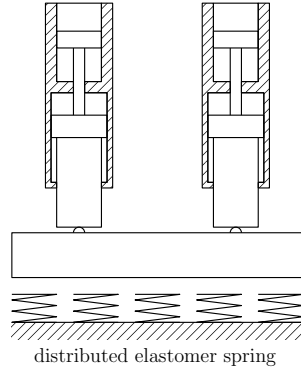
Fig. 10.6   Testrig for measurements

(a) Position and velocity   (b) Pressure and rotational speed
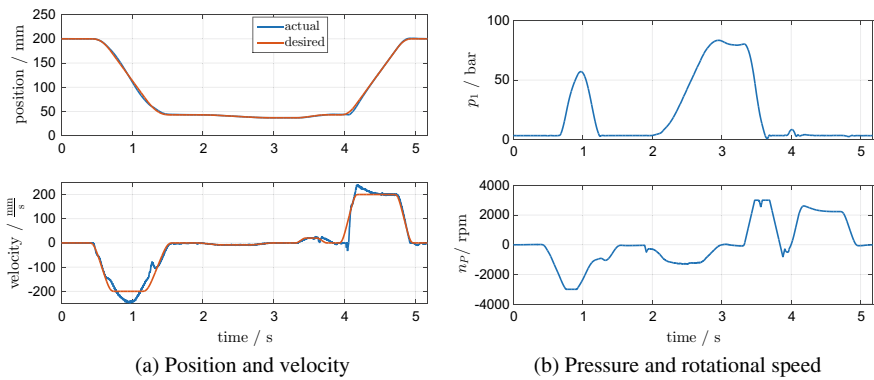
Fig. 10.7   Measurements of a full exemplary press cycle

that the results could be achieved without any parameter identification. Due to the simple structure of the dynamic model for the synthesis, only a few parameters from datasheets and the mechanical design were necessary. Furthermore, the measurements were carried out with a two axes prototype. Both axes respond a little bit differently due to their individual friction behavior and, thus, each axis represents a certain disturbance for the other press axis. Consequently, with a single axis press, even a better accuracy can be achieved.

(a) Position and velocity

(b) Accuracy and Repeatability
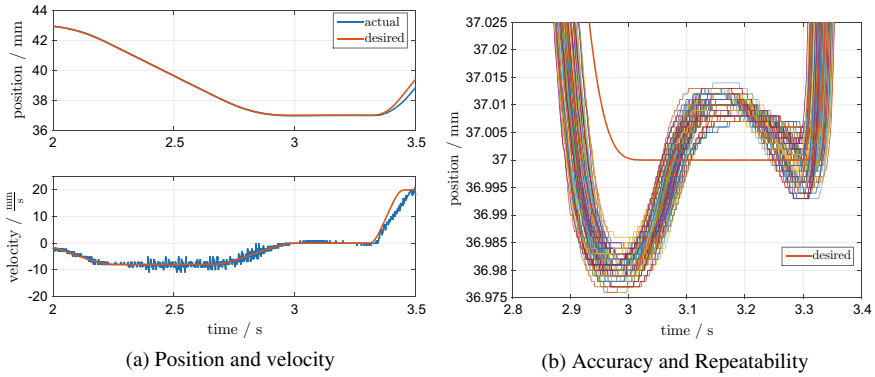
Fig. 10.8 Zoom into Press mode

10.6 Conclusions and Outlook

In this paper, the design and application of a flatness-based controller for a double-axis closed-circuit hydraulic press prototype was presented. The press concept is realized as displacement control, where the rotational speed of the pump corresponds to the velocity of the piston, thus, no resistance control is applied and no proportional valves are used. The transmission ratio between force and velocity of the piston with regard to the rotational speed of the pump is controlled by on/off switching valves. With regard to displacement control of the piston, an excellent energy efficiency can be achieved compared to conventional hydraulic press concepts; no additional cooler is needed. The closed-circuit system only needs a small amount of oil, thus, a compact design can be realized in order to completely hide the hydraulics from the operator; only electricity must be provided to the black-box system. For the controller design, a simple dynamic model could be found, which was used for the design of a flatness-based controller. This control strategy achieves a stabilization of the trajectory, which means that multiple individual press axes can be arranged and operated in parallel without any additional synchronizing controller. With the presented controller, satisfying control performance could be achieved on a two-axis press prototype. The next steps in development are focused on a more compact integration of the motor-pump section.

References

1. Costa, G., Sepehri, N.: Hydrostatic Transmissions and Actuators. Wiley (2015)
2. Fliess, M., Lévine, J., Martin, P., Rouchon, P.: Flatness and defect of nonlinear systems: introductory theory and examples. Int. J. Control **61**(6), 1327–1361 (1995). https://doi.org/10.1080/00207179508921959
3. Isidori, A.: Nonlinear Control Systems. Springer, London (1995). https://doi.org/10.1007/978-1-84628-615-5
4. Lévine, J.: Analysis and Control of Nonlinear Systems: A Flatness-based Approach. Springer, Berlin (2009)
5. Lovrec, D., Kastrevc, M., Ulaga, S.: Electro-hydraulic load sensing with a speed-controlled hydraulic supply system on forming-machines. Int. J. Adv. Manuf. Technol. **41**(11–12), 1066–1075 (2008). https://doi.org/10.1007/s00170-008-1553-y
6. Rahmfeld, R.: Development and control of energy saving hydraulic servo drives. In: Proceedings of the 1st FPNI-PhD Symposium (2000)
7. Rothfuß, R.: Anwendung der flachheitsbasierten Analyse und Regelung nichtlinearer Mehrgrößensysteme. Tech. rep., Fortschr.-Ber. VDI Reihe 8 Nr. 664, Düsseldorf: VDI Verlag, Germany (1997)
8. Rouchon, P.: Flatness based control of oscillators. ZAMM **85**(6), 411–421 (2005). https://doi.org/10.1002/zamm.200410194
9. Rudolph, J.: Rekursiver Entwurf stabiler Regelkreise durch sukzessive Berücksichtigung von Integratoren und quasi-statische Rückführungen. Automatisierungstechnik **53**, 389–399 (2005)
10. Rydberg, K.E.: Energy efficient hydraulic systems and regenerative capabilities. In: Proceedings of the 9th Scandinavian International Conference on Fluid Power, SICFP'05 (2005)

Chapter 11
On the Calculation of Differential Parametrizations for the Feedforward Control of an Euler–Bernoulli Beam

Bernd Kolar, Nicole Gehring, and Markus Schöberl

Abstract We are concerned with the motion planning for underactuated Euler–Bernoulli beams. The design of the feedforward control is based on a differential parametrization of the beam, where all system variables are expressed in terms of a free time function and its infinitely many derivatives. We derive an advantageous representation of the set of all formal differential parametrizations of the beam. Based on this representation, we identify a well-known parametrization, for the first time without the use of operational calculus. This parametrization is a flat one, as the corresponding series representations of the system variables converge. Furthermore, we discuss a formal differential parametrization where the free time function allows a physical interpretation as the bending moment at the unactuated boundary. Even though the corresponding series do not converge, a numerical simulation using the least term summation illustrates the usefulness of this formal differential parametrization for motion planning.

11.1 Introduction

The feedforward control of boundary actuated Euler–Bernoulli beams is usually concerned with the question of how an input has to be chosen in order to transition the beam from one steady state to another. The flatness-based approach, originally introduced for lumped-parameter systems, has proven very valuable for the motion planning in distributed-parameter systems (e.g., [1, 4, 8, 11]). It relies on a differential parametrization of the spatially dependent system solution in terms of a parametrizing

B. Kolar · N. Gehring · M. Schöberl (✉)
Institute of Automatic Control and Control Systems Technology, Johannes Kepler University Linz, Linz, Austria
e-mail: markus.schoeberl@jku.at

B. Kolar
e-mail: bernd_kolar@ifac-mail.org

N. Gehring
e-mail: nicole.gehring@jku.at

(boundary) output, and, in the case of the Euler–Bernoulli beam or parabolic systems like the heat equation involves infinite series. As these series comprise infinitely many time derivatives of the parametrizing output, in order to transition the system between two steady states and have the series converge, the desired trajectory of the parametrizing output has to be a non-analytic, smooth function of appropriate Gevrey class (e.g., [7]). If a Gevrey class ensuring convergence exists, the parametrizing output is called a flat output, and the differential parametrization is a flat one (e.g., [8]). On the other hand, if no such Gevrey class exists, the differential parametrization is specified by the prefix formal. However, even in this case, a flatness-based motion planning may still be possible (e.g. [7, 14]).

The main challenge of the flatness-based approach lies in finding a differential parametrization. For the heat conduction problem, this is either based on the ansatz of a power series in the spatial variable (e.g., [7]), the ansatz in [5] and [6] which generalizes the Brunovsky decomposition, or some kind of operational calculus (e.g., [9, 11]). All these ideas could be applied in a straightforward way to the fully actuated Euler–Bernoulli beam, i.e., configurations with two boundary inputs at one end. In contrast, in the more difficult case with only one input, considered here, all differential parametrizations found in the literature solely rely on operational calculus (e.g., [2, 10–12]), to the best of the authors' knowledge.

In this paper, we demonstrate that a time-domain approach similar to [5] and [6] is also applicable to an Euler–Bernoulli beam with one boundary input. One of our main results is an advantageous representation of the set of all formal differential parametrizations of the beam. Based on this representation, it is easy to identify a distinguished differential parametrization that is a flat one and well known from the literature (see e.g., [11]). As no physical interpretation is known for this flat output, we discuss an interesting formal differential parametrization with a parametrizing output that allows an interpretation as the bending moment at the unactuated boundary. Although the corresponding series do not converge (for any non-analytic function), inspired by the computations with divergent series in [7], simulation results based on the least term summation illustrate that this formal differential parametrization can still be useful for motion planning.

We use the convention that the set of natural numbers $\mathbb{N}$ includes 0. Thus, $(a_k)_{k \in \mathbb{N}}$ denotes the infinite sequence $(a_0, a_1, a_2, \ldots)$. By $(a_0, a_1, \ldots, a_k)$ we denote a finite sequence with the last element a_k for some fixed k.

11.2 A Series Ansatz for Solutions of the Euler–Bernoulli Beam

In this contribution, we consider an Euler–Bernoulli beam with a clamped end at $z = 0$ and a free end at $z = 1$, with the bending moment serving as the control input $u(t)$ at the latter. The deflection $w(z, t)$ satisfies the (normalized) beam equation

$$\partial_t^2 w(z, t) = -\partial_z^4 w(z, t), \quad 0 \le z \le 1, \ t \ge 0 \tag{11.1a}$$

and the boundary conditions

$$w(0, t) = 0, \quad \partial_z w(0, t) = 0, \quad \partial_z^2 w(1, t) = u(t), \quad \partial_z^3 w(1, t) = 0. \tag{11.1b}$$

This is a classical beam configuration that has been studied in the context of flatness-based feedforward control, e.g., in [11] and [3].[1]

The objective of the present paper is the construction of formal differential parametrizations for the Euler–Bernoulli beam (11.1). We call a representation

$$w(z, t) = \sum_{k=0}^{\infty} \alpha_k(z) y^{(k)}(t) \tag{11.2a}$$

$$u(t) = \sum_{k=0}^{\infty} \beta_k y^{(k)}(t) \tag{11.2b}$$

of the deflection $w(z, t)$ and the input $u(t)$ by a parametrizing output $y(t)$ and its time derivatives a formal differential parametrization of the system (11.1), if the series (11.2a) and (11.2b) formally satisfy the PDE (11.1a) and the boundary conditions (11.1b) for arbitrary smooth functions $y(t)$. It is important to emphasize the word formal since we are dealing with formal solutions[2] and discuss the problem of finding parametrizations (11.2) separately from the question of convergence, see also [14] or [7]. For a convergence analysis, $y(t)$ has to be restricted to so-called Gevrey functions with appropriately bounded derivatives, see e.g., [7].

Definition 1 A smooth function $y(t)$ defined on $\mathbb{R}^+$ is Gevrey of order γ if there exist constants $M, R > 0$ such that

$$\sup_{t \in \mathbb{R}^+} \left| y^{(m)}(t) \right| \le M \frac{(m!)^\gamma}{R^m}, \quad \forall m \in \mathbb{N}. \tag{11.3}$$

Gevrey functions of order $\gamma = 1$ are analytic. For planning transitions between equilibria of the system (11.1), which are characterized by constant values of $y(t)$, they cannot be used. The reason is that any analytic function that is constant on an open subset of $\mathbb{R}^+$ is constant everywhere. In contrast, this is no longer true for

---

[1] The general constant-coefficient case

$$\mu \partial_t^2 w(z, t) = -EI \partial_z^4 w(z, t), \quad 0 \le z \le L, \ t \ge 0$$

with linear mass density $\mu > 0$, flexural rigidity $EI > 0$, and a spatial domain $[0, L]$ can always be traced back to the normalized case (11.1) by transformations of the independent variables z and t.

[2] The series (11.2a) and (11.2b) are formal solutions if they satisfy (11.1a) and (11.1b) after formally interchanging differentiation and summation, even if they do not converge.

Gevrey functions $y(t)$ of order $\gamma > 1$. If the series (11.2a) and (11.2b) converge for a Gevrey class with $\gamma > 1$, the parametrizing output $y(t)$ is called a flat output.

Remark 1 In the context of motion planning, the question arises whether the span of the set $\{\alpha_k(z), \, k \in \mathbb{N}\}$ of functions of a parametrization (11.2a) is dense in the state space, see also [5]. However, this question is not within the scope of the paper.

In order to derive conditions for the functions $\alpha_k(z)$ and coefficients β_k, let us plug the ansatz (11.2) into the PDE (11.1a) and the boundary conditions (11.1b). Since the resulting equations must hold for arbitrary smooth functions $y(t)$, after formally interchanging differentiation and summation, the factors of all time derivatives of $y(t)$ have to vanish. Hence, we get

$$\alpha_0''''(z) = 0, \quad \alpha_1''''(z) = 0 \quad \text{and} \quad \alpha_k''''(z) = -\alpha_{k-2}(z), \quad k \geq 2 \qquad (11.4a)$$

as well as

$$\alpha_k(0) = 0, \quad \alpha_k'(0) = 0, \quad \alpha_k''(1) = \beta_k, \quad \alpha_k'''(1) = 0, \quad k \geq 0. \qquad (11.4b)$$

Therein, $'$ denotes the differentiation with respect to the spatial variable z. With (11.4) we have to solve a sequence of boundary value problems in the independent variable z. Obviously, for all $k \geq 2$, the function $\alpha_k(z)$ follows from a fourfold integration of $-\alpha_{k-2}(z)$. The integration constants are determined by the boundary values (11.4b). Consequently, the functions $\alpha_k(z)$ of the series representation (11.2a) of the deflection $w(z, t)$ are uniquely determined by the coefficients $(\beta_0, \beta_1, \ldots, \beta_k)$ of the series representation (11.2b) of the input $u(t)$. More precisely, the functions $\alpha_k(z)$ with even k are determined by the coefficients $(\beta_0, \beta_2, \ldots, \beta_k)$ with even indices, the functions $\alpha_k(z)$ with odd k by the coefficients $(\beta_1, \beta_3, \ldots, \beta_k)$ with odd indices. Hence, the functions $\alpha_k(z)$ with even and odd indices can be calculated independently. In particular, setting all β_k with odd k to zero yields a parametrization

$$w(z, t) = \sum_{k=0}^{\infty} \alpha_{2k}(z) y^{(2k)}(t) \qquad (11.5a)$$

$$u(t) = \sum_{k=0}^{\infty} \beta_{2k} y^{(2k)}(t), \qquad (11.5b)$$

where only time derivatives of even order occur. In the remainder of the paper, for simplicity, we restrict ourselves to this special case. The calculations for the case with odd indices could be performed in an analogous way.

Integrating $\alpha_0''''(z) = 0$ four times and using (11.4b) yields the first function

$$\alpha_0(z) = \tfrac{1}{2} \beta_0 z^2 \qquad (11.6)$$

of (11.5a). Note that $\alpha_0(z)$ corresponds to an equilibrium profile of the beam, since all time derivatives of $y(t)$ vanish in steady state. Continuing by solving

$\alpha_2''''(z) = -\alpha_0(z)$ and $\alpha_4''''(z) = -\alpha_2(z)$, it can be shown that the functions $\alpha_{2k}(z)$ are polynomials

$$\alpha_{2k}(z) = \sum_{i=0}^{k} \left(c_{k,i} z^{4i+2} + d_{k,i} z^{4i+3} \right) \tag{11.7}$$

with $d_{k,k} = 0$, where $c_{k,i}$ denotes the coefficients of the even powers z^{4i+2}, and $d_{k,i}$ denotes the coefficients of the odd powers z^{4i+3}. In principle, by successive integration we could calculate all functions $\alpha_{2k}(z)$—up to some arbitrary index k—in terms of the sequence $(\beta_0, \beta_2, \ldots, \beta_{2k})$. However, this is cumbersome and does not answer the important question how one has to choose the sequence $(\beta_{2k})_{k\in\mathbb{N}}$ in order for the series (11.5a) and (11.5b) to converge for a sufficiently large class of functions $y(t)$. Therefore, in the following section, we study the connections between the sequence $(\beta_{2k})_{k\in\mathbb{N}}$ and the coefficients of the polynomials (11.7) in more detail.

11.3 Derivation of Formal Differential Parametrizations

First, we determine how the coefficients of (11.7) depend on the coefficients of

$$\alpha_{2(k-1)}(z) = \sum_{i=0}^{k-1} \left(c_{k-1,i} z^{4i+2} + d_{k-1,i} z^{4i+3} \right) . \tag{11.8}$$

Integrating $-\alpha_{2(k-1)}(z)$ four times and using (11.4b), a comparison with (11.7) shows that the coefficients of (11.7) can be calculated from the coefficients of (11.8) according to

$$c_{k,0} = \tfrac{1}{2}\beta_{2k} - \tfrac{1}{2} \sum_{i=0}^{k-1} \left(c_{k-1,i} \tfrac{1}{4i+4} + d_{k-1,i} \tfrac{1}{4i+5} \right) \tag{11.9}$$

$$d_{k,0} = \tfrac{1}{6} \sum_{i=0}^{k-1} \left(c_{k-1,i} \tfrac{1}{4i+3} + d_{k-1,i} \tfrac{1}{4i+4} \right) \tag{11.10}$$

and

$$c_{k,i} = -c_{k-1,i-1} \tfrac{(4i-2)!}{(4i+2)!}, \quad d_{k,i} = -d_{k-1,i-1} \tfrac{(4i-1)!}{(4i+3)!}, \quad 1 \le i \le k . \tag{11.11}$$

It can be observed that, according to (11.9) and (11.10), the coefficients $c_{k,0}$ and $d_{k,0}$ of the powers z^2 and z^3 in (11.7) depend on all coefficients of (11.8) and on β_{2k}. In contrast, the coefficients of the higher powers of z in (11.7) depend only on one coefficient of (11.8) each (cf. (11.11)). Next, it is straightforward to show that the coefficients $c_{k,0}$ and $d_{k,0}$ of (11.7) can alternatively be expressed by the sequences $(c_{0,0}, c_{1,0}, \ldots, c_{k-1,0})$ and $(d_{0,0}, d_{1,0}, \ldots, d_{k-1,0})$, i.e., the coefficients of z^2 and z^3

of the polynomials $\alpha_0(z), \ldots, \alpha_{2(k-1)}(z)$, as well as β_{2k}: By a repeated application of (11.11) we get

$$c_{k,i} = (-1)^i \frac{2!}{(4i+2)!} c_{k-i,0}, \quad d_{k,i} = (-1)^i \frac{3!}{(4i+3)!} d_{k-i,0}, \quad 0 \le i \le k, \quad (11.12)$$

and plugging (11.12) into (11.9) and (11.10) results in

$$c_{k,0} = \frac{1}{2}\beta_{2k} - \frac{1}{2}\sum_{i=0}^{k-1}(-1)^i \left(c_{k-1-i,0}\frac{2(4i+3)}{(4i+4)!} + d_{k-1-i,0}\frac{6(4i+4)}{(4i+5)!} \right) \quad (11.13)$$

$$d_{k,0} = \frac{1}{6}\sum_{i=0}^{k-1}(-1)^i \left(c_{k-1-i,0}\frac{2}{(4i+3)!} + d_{k-1-i,0}\frac{6}{(4i+4)!} \right). \quad (11.14)$$

Based on (11.12), (11.13), and (11.14), we can now formulate one of our key results.

Theorem 1 *The functions $\alpha_{2k}(z)$ and coefficients β_{2k} of the formal differential parametrization (11.5) are uniquely determined by the sequence $(c_{k,0})_{k\in\mathbb{N}}$.*

Proof If we fix a sequence $(c_{k,0})_{k\in\mathbb{N}}$, (11.14) allows us to calculate step by step the corresponding sequence $(d_{k,0})_{k\in\mathbb{N}}$, starting with $d_{0,0} = 0$. Subsequently, by (11.12), the remaining coefficients of the functions $\alpha_{2k}(z)$ of (11.5a) can be determined from $(c_{k,0})_{k\in\mathbb{N}}$ and $(d_{k,0})_{k\in\mathbb{N}}$. Finally, solving (11.13) for β_{2k} yields the coefficients of (11.5b). □

Based on the fact that the sequence $(c_{k,0})_{k\in\mathbb{N}}$ can be chosen arbitrarily, the following corollary can be formulated.

Corollary 1 *There is a one-to-one correspondence between arbitrary sequences $(c_{k,0})_{k\in\mathbb{N}}$ and formal differential parametrizations (11.5) of the Euler–Bernoulli beam.*

Proof By Theorem 1, every sequence $(c_{k,0})_{k\in\mathbb{N}}$ determines a unique formal differential parametrization (11.5). Conversely, since the sequence $(c_{k,0})_{k\in\mathbb{N}}$ consists of the coefficients of z^2 in the functions $\alpha_{2k}(z)$ of (11.5a), every formal differential parametrization (11.5) determines a unique sequence $(c_{k,0})_{k\in\mathbb{N}}$. □

As already mentioned in Sect. 11.2, the functions $\alpha_{2k}(z)$ of (11.5a) are uniquely determined by the coefficients $(\beta_0, \beta_2, \ldots, \beta_{2k})$ of (11.5b). Hence, the formal differential parametrization (11.5) is also uniquely determined by the sequence $(\beta_{2k})_{k\in\mathbb{N}}$. However, a representation of all formal differential parametrizations of the Euler–Bernoulli beam using the sequence $(c_{k,0})_{k\in\mathbb{N}}$ as the free design parameter is advantageous. This becomes apparent when we want to find flat parametrizations, where the series (11.5a) and (11.5b) converge for functions $y(t)$ of appropriate Gevrey order: Since the input $u(t)$ is the bending moment at the free boundary, which follows from the deflection $w(z, t)$ as $u(t) = \partial_z^2 w(1, t)$, the convergence of the series (11.5a)

implies the convergence of the series (11.5b), under the assumption that $w(z, t)$ is twice differentiable with respect to z at $z = 1$. Thus, it is sufficient to check the convergence of the series representation (11.5a) of the deflection $w(z, t)$. In (11.5a), the elements of the sequence $(c_{k,0})_{k \in \mathbb{N}}$ appear as coefficients of the polynomials $\alpha_{2k}(z)$. This facilitates the construction of differential parametrizations, as will be illustrated by means of the examples in Sect. 11.4.

In the following, we derive explicit expressions for the sequences $(d_{k,0})_{k \in \mathbb{N}}$ and $(\beta_{2k})_{k \in \mathbb{N}}$ in terms of the sequence $(c_{k,0})_{k \in \mathbb{N}}$.

Lemma 1 *The sequence $(d_{k,0})_{k \in \mathbb{N}}$ is generated by the discrete convolution*

$$d_{k,0} = \sum_{i=0}^{k} \eta_{k-i} c_{i,0} \tag{11.15}$$

of the sequence $(c_{k,0})_{k \in \mathbb{N}}$ with the sequence $(\eta_k)_{k \in \mathbb{N}}$, which is defined recursively by

$$\eta_0 = 0 \quad and \quad \eta_k = -\frac{(-1)^k}{3(4k-1)!} - \sum_{i=1}^{k} \eta_{k-i} \frac{(-1)^i}{(4i)!} , \quad k \geq 1. \tag{11.16}$$

Proof First, it should be noted that $d_{k,0}$ could be calculated from (11.14) by eliminating successively $d_{k-1,0}, d_{k-2,0}, \ldots$ with shifted versions of (11.14). This shows that $d_{k,0}$ is a linear combination of the coefficients of the sequence $(c_{0,0}, c_{1,0}, \ldots, c_{k,0})$, justifying an ansatz of the form (11.15). Due to $d_{0,0} = 0$, from (11.15), we immediately get $\eta_0 = 0$. In order to determine $\eta_k, k \geq 1$, we plug the ansatz (11.15) into the relation (11.14). After some simplifications, this yields the equation

$$\sum_{i=0}^{k} \eta_{k-i} c_{i,0} = \frac{1}{3} \sum_{n=0}^{k-1} (-1)^{k-1-n} \frac{1}{(4(k-n)-1)!} c_{n,0}$$

$$+ \sum_{n=0}^{k-1} (-1)^{k-1-n} \sum_{j=0}^{n} \eta_{n-j} \frac{1}{(4(k-n))!} c_{j,0}, \tag{11.17}$$

which must hold for every choice of the sequence $(c_{0,0}, c_{1,0}, \ldots, c_{k,0})$. By the special choice $(1, 0, \ldots, 0)$, the relation (11.17) can be simplified to (11.16). $\qquad \square$

Similarly, the sequence $(\beta_{2k})_{k \in \mathbb{N}}$ can be calculated from the sequence $(c_{k,0})_{k \in \mathbb{N}}$.

Lemma 2 *The sequence $(\beta_{2k})_{k \in \mathbb{N}}$ is generated by the discrete convolution*

$$\beta_{2k} = \sum_{i=0}^{k} \mu_{k-i} c_{i,0} \tag{11.18}$$

of the sequence $(c_{k,0})_{k \in \mathbb{N}}$ with the sequence $(\mu_k)_{k \in \mathbb{N}}$, which is defined recursively by

$$\mu_0 = 2 \quad and \quad \mu_k = \frac{4^k}{(4k)!} - \sum_{i=1}^{k} \mu_{k-i} \frac{(-1)^i}{(4i)!}, \quad k \geq 1. \qquad (11.19)$$

Proof In principle, β_{2k} can be calculated by solving (11.13) for β_{2k} and replacing $d_{k-1,0}, d_{k-2,0}, \ldots$ successively with shifted versions of (11.14). This shows that β_{2k} is a linear combination of the coefficients of the sequence $(c_{0,0}, c_{1,0}, \ldots, c_{k,0})$, justifying an ansatz of the form (11.18). A comparison of (11.6) and (11.7) shows that $c_{0,0} = \frac{1}{2}\beta_0$, and from (11.18) with $k = 0$ we immediately get $\mu_0 = 2$. In order to determine μ_k, $k \geq 1$, we solve (11.13) for β_{2k} and insert the ansatz (11.18), which yields

$$\sum_{i=0}^{k} \mu_{k-i} c_{i,0} = 2c_{k,0} + \sum_{i=0}^{k-1} (-1)^i \left(c_{k-1-i,0} \frac{2(4i+3)}{(4i+4)!} + d_{k-1-i,0} \frac{6(4i+4)}{(4i+5)!} \right). \qquad (11.20)$$

To get rid of the coefficients $c_{i,0}$ and $d_{i,0}$ in (11.20), we can use the fact that the particular sequence $c_{k,0} = \frac{(-1)^k}{(4k)!}$ determines the sequence $d_{k,0} = -\frac{4k(-1)^k}{3(4k)!}$. This follows rather easily from (11.15) and (11.16) and will be shown in Sect. 11.4.1. After inserting these particular sequences, (11.20) can be simplified to (11.19). $\qquad \square$

A numerical evaluation of the recursively defined sequences (11.16) and (11.19) strongly suggests, that η_k and μ_k are defined by

$$\eta_k = \frac{4^{k+1}(1-16^k)}{6(4k)!} B_{4k} \quad and \quad \mu_k = \frac{2}{4^k (4k)!} \sum_{i=0}^{2k} (-1)^i E_{2i} \binom{4k}{2i}, \quad k \geq 0,$$

where B_i denotes the Bernoulli numbers and E_i the Euler numbers. This explicit representation may be advantageous for a convergence analysis of the parametrizations (11.5a) and (11.5b).

11.4 Two Notable Differential Parametrizations

In the previous section, we have shown that the sequence $(c_{k,0})_{k\in\mathbb{N}}$ can be used as a design parameter for the formal differential parametrizations (11.5) of the Euler–Bernoulli beam. Based on the representations (11.15), (11.16) and (11.18), (11.19) of the sequences $(d_{k,0})_{k\in\mathbb{N}}$ and $(\beta_{2k})_{k\in\mathbb{N}}$, we show that there is a natural choice for the sequence $(c_{k,0})_{k\in\mathbb{N}}$ that leads to a flat parametrization, which is well known from the literature (see e.g., [11]). Subsequently, we discuss a special formal differential parametrization where the parametrizing output $y(t)$ allows a physical interpretation.

11.4.1 A Natural Choice

Consider the sum (11.15). If we split off the term with $i = 0$ and substitute (11.16) for η_k, we get

$$d_{k,0} = -\frac{(-1)^k}{3(4k-1)!}c_{0,0} + \sum_{i=1}^{k} \eta_{k-i}\left(c_{i,0} - \frac{(-1)^i}{(4i)!}c_{0,0}\right).\qquad(11.21)$$

With the special choice

$$c_{k,0} = \frac{(-1)^k}{(4k)!}c_{0,0}, \quad k \geq 0 \qquad(11.22)$$

for the sequence $(c_{k,0})_{k\in\mathbb{N}}$, the sum in (11.21) vanishes, and therefore (11.21) simplifies to $d_{k,0} = -\frac{(-1)^k}{3(4k-1)!}c_{0,0}, k \geq 1$. Expanding with $4k$ finally yields the relation

$$d_{k,0} = -\frac{4k(-1)^k}{3(4k)!}c_{0,0}, \quad k \geq 0, \qquad(11.23)$$

which also includes the case $k = 0$ with $d_{0,0} = 0$.

Analogously, splitting off the term with $i = 0$ in the sum (11.18) and substituting (11.19) for μ_k yields

$$\beta_{2k} = \frac{4^k}{(4k)!}c_{0,0} + \sum_{i=1}^{k} \mu_{k-i}\left(c_{i,0} - \frac{(-1)^i}{(4i)!}c_{0,0}\right).\qquad(11.24)$$

By the choice (11.22) for the sequence $(c_{k,0})_{k\in\mathbb{N}}$, it is evident that the sum vanishes again, and (11.24) simplifies to $\beta_{2k} = \frac{4^k}{(4k)!}c_{0,0}, k \geq 1$. For $k = 0$, we have $\beta_0 = 2c_{0,0}$, and therefore, the complete sequence is given by

$$\beta_{2k} = \begin{cases} 2c_{0,0}, & k = 0 \\ \frac{4^k}{(4k)!}c_{0,0}, & k \geq 1. \end{cases} \qquad(11.25)$$

Finally, plugging (11.22) and (11.23) into (11.12) results in the complete set of coefficients

$$c_{k,i} = \frac{4(-1)^k}{(4i+2)!(4(k-i))!}c_{0,0}, \qquad 0 \leq i \leq k, \, k \geq 0 \qquad(11.26)$$

$$d_{k,i} = -\frac{16(-1)^k(k-i)}{(4i+3)!(4(k-i))!}c_{0,0}, \qquad 0 \leq i \leq k, \, k \geq 0 \qquad(11.27)$$

of the polynomials (11.7). If we set the scaling factor in (11.22) to $c_{0,0} = 2$, we get the same differential parametrization

$$w(z, t) = \sum_{k=0}^{\infty} 4(-1)^k \sum_{i=0}^{k} \left(\frac{1}{(4i+2)!(4(k-i))!} z^{4i+2} - \frac{4(k-i)}{(4i+3)!(4(k-i))!} z^{4i+3} \right) y^{(2k)}(t)$$

(11.28a)

$$u(t) = 4y(t) + \sum_{k=1}^{\infty} 2 \frac{4^k}{(4k)!} y^{(2k)}(t)$$

(11.28b)

that was derived, e.g., in [11] by means of operational calculus.[3] As shown in [11], the series (11.28a) and (11.28b) converge for all trajectories $y(t)$ of Gevrey class $\gamma < 2$. Hence, this parametrizing output $y(t)$ is a flat output.

11.4.2 Formal Differential Parametrization by the Bending Moment at the Clamped Boundary

In motion planning, one is often interested in a physical interpretation of the parametrizing output $y(t)$ in terms of a boundary value of the system. For the flat output $y(t)$ of the differential parametrization (11.28), no such physical interpretation is known. In contrast, for the fully actuated Euler–Bernoulli beam, with both the bending moment and the shear force at the free end as inputs, it is not difficult to show that the bending moment and the shear force at the clamped end form a flat output. For our underactuated configuration (11.1), we show that there exists at least one (useful) formal differential parametrization (11.5) where the parametrizing output $y(t)$ allows a physical interpretation.

First, let us restate the formal differential parametrization of the deflection $w(z, t)$ by plugging (11.7) into (11.5a):

$$w(z, t) = \sum_{k=0}^{\infty} \sum_{i=0}^{k} \left(c_{k,i} z^{4i+2} + d_{k,i} z^{4i+3} \right) y^{(2k)}(t).$$

Evaluating its second spatial derivative at $z = 0$ yields the parametrization of the bending moment

$$\partial_z^2 w(0, t) = \sum_{k=0}^{\infty} 2 c_{k,0} y^{(2k)}(t)$$

(11.29)

at the clamped boundary. If we choose the sequence $(c_{k,0})_{k \in \mathbb{N}}$ as

$$(c_{0,0}, c_{1,0}, c_{2,0}, \ldots) = (\tfrac{1}{2}, 0, 0, \ldots),$$

(11.30)

---

[3] In contrast to our double sum representation (11.28a), in [11], the parametrization of the deflection $w(z, t)$ is expressed by a single sum of real and imaginary parts of powers of complex numbers. Also, the input used in [11] has the opposite sign as compared to our input $u(t)$.

only the first term of the sum is left, and (11.29) simplifies to

$$y(t) = \partial_z^2 w(0, t). \tag{11.31}$$

Thus, in this case, the function $y(t)$ is simply the bending moment at the clamped boundary. By the choice (11.30) the discrete convolutions (11.15) and (11.18) simplify to $d_{k,0} = \frac{1}{2}\eta_k$, $k \geq 0$ and $\beta_{2k} = \frac{1}{2}\mu_k$, $k \geq 0$. Then with (11.12) we get the formal differential parametrization

$$w(z, t) = \sum_{k=0}^{\infty} \left((-1)^k \frac{1}{(4k+2)!} z^{4k+2} + \sum_{i=0}^{k-1} (-1)^i \frac{3}{(4i+3)!} \eta_{k-i} z^{4i+3} \right) y^{(2k)}(t) \tag{11.32a}$$

$$u(t) = \frac{1}{2} \sum_{k=0}^{\infty} \mu_k y^{(2k)}(t). \tag{11.32b}$$

However, since the sequence $(\mu_k)_{k \in \mathbb{N}}$ does not go to zero fast enough, (11.32b) cannot converge for any non-analytic function $y(t)$ of Gevrey order $\gamma > 1$. Hence, neither does (11.32a). A numerical evaluation of the elements μ_k reveals that $\frac{\mu_{k+1}}{\mu_k} \approx \frac{1}{24}$, for $k \geq 2$. Since $24^k < (2k)!$ for large k, the bound $\sup_{t \in \mathbb{R}^+} \left| y^{(2k)}(t) \right|$ guaranteed by (11.3) grows much faster than the coefficients μ_k converge to zero. Consequently, the product $\mu_k y^{(2k)}(t)$ diverges and the parametrizing output $y(t)$ is not a flat one.

However, a flatness-based transition between two equilibria is still possible using the divergent series (11.32b). In [7], simulation results for a heat conduction problem showed that the least term summation allows feedforward control even based on divergent series. More precisely, the divergent series discussed in [7] first converges very fast and then diverges very fast. A similar effect can be observed for our beam parametrization (11.32b), for suitable trajectories $y(t)$. Now, the idea of the least term summation in [7] is to take into account only the convergent part for each time t. Hence, instead of the series (11.32b), the feedforward control $u(t)$ is calculated by

$$u(t) = \frac{1}{2} \sum_{k=0}^{n_t} \mu_k y^{(2k)}(t), \tag{11.33}$$

with n_t defined for each t as the smallest integer greater than 1 that meets

$$\left| \mu_{n_t+1} y^{(2(n_t+1))}(t) \right| > \left| \mu_{n_t} y^{(2n_t)}(t) \right|.$$

Simulation studies were performed in order to illustrate the usefulness of this approach. Here, we defined the desired trajectory for $y(t)$ based on a function

$$\Phi_\sigma(t) = \begin{cases} 0 & t \leq 0 \\ \frac{\int_0^t \phi_\sigma(\tau)\,d\tau}{\int_0^1 \phi_\sigma(\tau)\,d\tau} & t \in (0, 1) \\ 1 & t \geq 1, \end{cases}$$

with $\phi_\sigma(t) = \exp\left(-1/((1-t)t)^\sigma\right)$, scaled for a transition in $1\,$s. This function is Gevrey of order $1 + \frac{1}{\sigma}$ for $\sigma > 0$. In order to transition the beam between the equilibria $w(z,0) = 0$ and $w(z,T) = \frac{1}{2}z^2$ in finite time T, based on the definition of the parametrizing output $y(t)$ in (11.31), the corresponding initial and final value of $y(t)$ are $y(0) = 0$ and $y(T) = 1$. By setting $T = 5\,$s and $\sigma = 1.1$, we use the same reference trajectory

$$y(t) = \Phi_\sigma\left(\tfrac{t}{T}\right) \tag{11.34}$$

that was used in [3] for the flat output in (11.28).

Remark 2 In [3], the transition time is $11.5\,$ms. As our normalized beam and the one with physical parameters in [3] are related by a scaling of the spatial variable and a time scaling with the factor $\frac{1}{2.3}10^3$, this corresponds to the transition time $T = 5\,$s used in our simulation.

Figures 11.1 and 11.2 give simulation results for the feedforward control (11.33) based on the reference trajectory (11.34). The distributed beam deflection in Fig. 11.1 shows that the desired transition is achieved. In Fig. 11.2, the (simulated) bending moment at the clamped boundary, i.e., the parametrizing output $y(t)$, matches the desired reference trajectory (11.34), apart from some small deviations. Thus, using only the formal differential parametrization (11.32), we managed to implement the same transition considered in [3] on the basis of the flat differential parametrization (11.28). However, in contrast to the flat output used in [3], our parametrizing output offers a physical interpretation. This is particularly interesting for applications where the bending moment must not exceed certain bounds since we can take account of these bounds in the design of the desired trajectory $y(t)$ directly. Nevertheless, it is important to mention that choosing the transition time T too small means that the series (11.32b) diverges too soon. Consequently, the least term summation would not make sense anymore. In contrast, increasing the transition time improves the results, in particular with respect to the small deviations visible in Fig. 11.2. For

Fig. 11.1 Deflection $w(z,t)$ of the beam
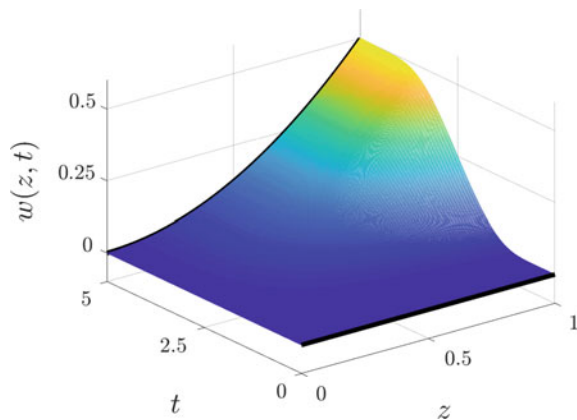
Fig. 11.2 Bending moment
$y(t)$ at $z = 0$
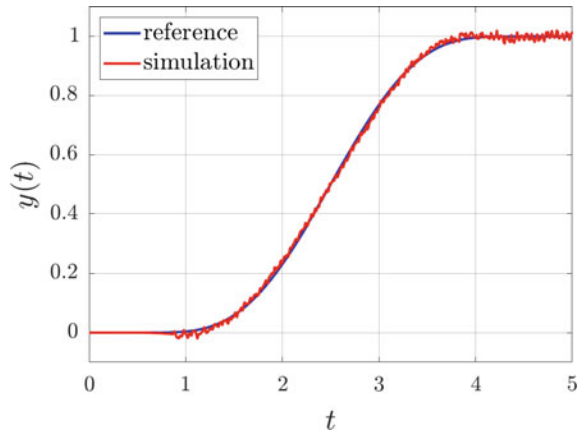
instance, with $T = 10\,\text{s}$ the simulated bending moment at the clamped boundary almost perfectly matches the reference (11.34). We also expect that evaluating the divergent series (11.32b) with the more sophisticated summation methods used in [13] and [14] should further improve the results.

11.5   Conclusion

We have derived an advantageous representation of the set of all formal differential parametrizations for an underactuated Euler–Bernoulli beam with one boundary input. Based on this result, it is straightforward to find the well-known classical differential parametrization for the considered configuration of the beam, which is usually derived by means of operational calculus. Since the parametrizing output $y(t)$ of this differential parametrization does not have a physical interpretation, we have also discussed a formal differential parametrization where the parametrizing output is the bending moment at the clamped boundary. This parametrization is particularly useful for motion planning problems where the bending moment should stay within certain limits.

The challenge with this formal differential parametrization is that for the trajectories of the parametrizing output $y(t)$ there does not exist a Gevrey class of order $\gamma > 1$ which ensures convergence of the corresponding infinite series. We conjecture that these non-convergent infinite series correspond to Taylor expansions of non-ananlytic solutions of the Euler–Bernoulli beam. To give meaning to these non-convergent infinite series, we have used the least term summation and presented the corresponding simulation results. Even though the results are already very promising, it is to be expected that they can still be improved by using more advanced summation methods.

References

1. Fliess, M., Mounier, H., Rouchon, P., Rudolph, J.: Controllability and motion planning for linear delay systems with an application to a flexible rod. In: Proceedings 34th IEEE Conference on Decision and Control (CDC), pp. 2046–2051 (1995)
2. Fliess, M., Mounier, H., Rouchon, P., Rudolph, J.: Systèmes linéaires sur les opérateurs de Mikusiński et commande d'une poutre flexible. ESAIM: Proc. **2**, 183–193 (1997)
3. Haas, W., Rudolph, J.: Steering the deflection of a piezoelectric bender. In: Proceedings 5th European Control Conference, pp. 3238–3243 (1999)
4. Knüppel, T., Woittennek, F.: Control design for quasi-linear hyperbolic systems with an application to the heavy rope. IEEE Trans. Autom. Control **60**(1), 5–18 (2015)
5. Laroche, B., Martin, P.: Motion planning for a 1-D diffusion equation using a Brunovsky-like decomposition. In: Proceedings 14th International Symposium on Mathematical Theory of Networks and Systems (MTNS) (2000)
6. Laroche, B., Martin, P.: Motion planning for a linearized Korteweg-de Vries equation with boundary control. In: Proceedings 15th IFAC World Congress, pp. 225–230 (2002)
7. Laroche, B., Martin, P., Rouchon, P.: Motion planning for the heat equation. Int. J. Robust Nonlinear Control **10**, 629–643 (2000)
8. Lynch, A., Rudolph, J.: Flatness-based boundary control of a class of quasilinear parabolic distributed parameter systems. Int. J. Control **75**(15), 1219–1230 (2002)
9. Martin, P., Murray, R., Rouchon, P.: Flat systems. In: Bastin, G., Gevers, M. (eds.) Plenary Lectures and Mini-Courses, Proceedings 4th European Control Conference (ECC), pp. 211–264 (1997)
10. Meurer, T., Schröck, J., Kugi, A.: Motion planning for a damped Euler-Bernoulli beam. In: Proceedings 49th IEEE Conference on Decision and Control (CDC), pp. 2566–2571 (2010)
11. Rudolph, J.: Flatness Based Control of Distributed Parameter Systems. Shaker Verlag, Aachen (2003)
12. Rudolph, J., Woittennek, F.: Motion planning for Euler-Bernoulli beams. In: Sira-Ramirez, H., Silva-Navarro, G. (eds.) Algebraic Methods in Flatness, Signal Processing and State Estimation, chap. 8, pp. 131–148. Innovacion Editorial Lagares Mexico (2003)
13. Wagner, M., Meurer, T., Kugi, A.: Feedforward control design for the inviscid burger equation using formal power series and summation methods. In: Proceedings 17th IFAC World Congress, pp. 8743–8748 (2008)
14. Wagner, M., Meurer, T., Zeitz, M.: K-summable power series as a design tool for feedforward control of diffusion-convection-reaction systems. In: Proceedings 6th IFAC Symposium on Nonlinear Control Systems (NOLCOS), pp. 147–152 (2004)

Chapter 12
An Application of Graphene Composites for Additional Damping of Vibrations of Smart Structures Based on Piezoelectric Elements

Valerii P. Matveenko, Dmitriy A. Oshmarin, and Nataliia A. Iurlova

Abstract In this paper, we consider a modified version of smart structures, which are the piecewise homogeneous bodies, incorporating elements made of elastic and viscoelastic materials and piezoelectric elements, whose electrodes can be connected to shunting circuits. One of the main intentions of such structures is the damping of vibrations. The focus of this study is to investigate the possibility of fitting smart structures with shunt circuits, in which the element made of a graphene composite behaves not only as a deformable solid but also as a resistor. A mathematical formulation of the problems of natural vibrations and forced steady-state vibrations is developed. The results of numerical experiments show that graphene-based composites can be used as an additional mechanism for damping vibrations in smart structures with attached piezoelectric elements.

12.1 Introduction

In general terms, a distinguishing feature of smart materials is their ability to maintain or change their characteristics in a predictable and controlled manner according to change of environmental conditions [6]. In this respect, they present considerable promise for various industrial applications. The feasibility of such applications is a challenging task. Its successful implementation involves the development of smart materials or, more precisely, smart structures incorporating elements, which operate as sensors, actuators, and processors, establishing the prescribed coupling between sensors and actuators. An abundance of smart structures is represented by various

V. P. Matveenko · D. A. Oshmarin · N. A. Iurlova (✉)
Institute of Continuous Media Mechanics Ural Branch of RAS, Acad. Korolev str., 1, Perm 614013, Russia
e-mail: yurlova@icmm.ru

V. P. Matveenko
e-mail: mvp@icmm.ru

D. A. Oshmarin
e-mail: oshmarin@icmm.ru

137

combinations of elements, which are able to partially or completely satisfy the above requirements [11].

It should be noted that in the last two to three decades, there has been almost an exponential increase in the number of publications devoted to various aspects of smart structures and their practical applications. Among the numerous smart structures, which basic parameters are associated with their mechanical behavior, the piezo-electric and optic fiber sensors are of considerable commercial importance, whereas the element showing the shape memory effect, as well as piezoelectric, magnetorhe-ological, electrorheological, and thermoelastic properties are used as actuators.

In this study, we consider smart structures, which are based on piezoelectric ele-ments. It is worth noting the fact that nowadays such smart structures have a rapidly developing resource base. Materials with a piezoelectric effect number more than one and a half thousand [4]. One of the advantages of smart structures incorporating based on the application of piezoelectric elements is the possibility of controlling their dynamic behavior with the aid of electric shunt circuits, which consist of resis-tive, capacitive, and inductive elements connected through to the electrodes to the surfaces of piezoelectric elements. In such systems, the electric potential from the piezoelectric elements is dissipated in the shunt circuits in the form of heat or electro-magnetic radiation, while the elements of shunt circuits are the mechanical analogues of the additional mass, elasticity, and viscosity. The possibility of using shunt elec-tric circuits in smart structures quickens the development of an appropriate base for producing elements with resistive, capacitive, and inductive properties.

The analysis of information on graphene composites [7, 8] available in the lit-erature allows us to conclude that the mechanical behavior of these composites can be described by a model of the elastic or viscoelastic body. Moreover, the elements made of these materials can act as resistors. Therefore, the objective of this study is to substantiate the idea of using graphene composites both as a structural material and resistive elements.

12.2   Mathematical Formulation of the Problem on Vibrations of a Deformable Body with the Elements Made of Piezoelectric Materials and Resistors

A mathematical formulation of the problem on vibrations of deformable bodies with piezoelectric elements is based on the variational equation of motion of a deformable body, whose elements exhibit a piezoelectric effect [5, 12]

$$\sum_{k=1}^{N} \left(\int_{V_1^k} \left(\sigma_{ij} \delta \varepsilon_{ij} + \rho_k \ddot{u}_i \delta u_i \right) dV \right) +$$

$$+ \int_{V_2} \left(\sigma_{ij} \delta \varepsilon_{ij} - D_i \delta E_i + \rho \ddot{u}_i \delta u_i \right) dV = \qquad (12.1)$$

$$= \int_{S_\sigma} p_i \delta u_i dS + \int_{S_p} q_e \delta \varphi dS.$$

Here, $V_1 = \sum_k^N V_1^k$ is a part of a piecewise homogeneous body of the volume $V = V_1 + V_2$, consisting of homogeneous elastic or viscoelastic elements, and V_2 is the volume of the element showing piezoelectric properties; D_i and E_i are the components of the vectors of electric induction and electric field strength flux density and electric field intensity, respectively; σ_{ij} are the components of the symmetric Cauchy stress tensor; ε_{ij} are the components of the linear strain tensor; u_i are the components of the displacement vector; ρ_k is the specific density of the material of the k-th component of a piecewise homogeneous body V_i^k; ρ is the specific density of piezoelectric material; S_σ is a part of the surface of the body of volume V with prescribed surface forces p_i; S_p is the surface of a piezoelectric body of volume V_2; q_e is the surface density of free charges; and φ is the electric potential.

For the electric field, the potentiality condition is fulfilled:

$$\varphi_{,i} = -E_i. \qquad (12.2)$$

For the examined body, the following physical relations hold true:

- For the elastic element of the volume V_1,

$$\sigma_{ij} - \sigma \delta_{ij} = 2G_k \left(\varepsilon_{ij} - \frac{1}{3} \vartheta \delta_{ij} \right), \qquad \sigma = B_k \vartheta. \qquad (12.3)$$

- For the viscoelastic elements of the volume V_1 [1],

$$s_{ij} = 2G_k^0 \left(e_{ij} - \int_0^t R_k(t - \tau) e_{ij}(\tau) d\tau \right),$$

$$\sigma = B_k^0 \left(\vartheta - \int_0^t U_k(t - \tau) \vartheta(\tau) d\tau \right). \qquad (12.4)$$

- For the piezoelectric element of the volume V_2,

$$\left.\begin{aligned}\sigma_{ij} &= C_{ijkl}\varepsilon_{kl} - \beta_{ijk}E_k \\ D_k &= \beta_{ijk}\varepsilon_{ij} + \ni_{ki}E_i\end{aligned}\right\}. \tag{12.5}$$

Here, G_k and B_k are the elastic shear and bulk modules, G_k^0 and B_k^0 are the instantaneous shear and bulk moduli, R_k and U_k are the relaxation kernels, σ is the mean stress, ϑ is the volumetric strain, s_{ij} and e_{ij} are the components of the deviators of the stress and strain tensors, C_{ijkl} are the tensor components of the elastic constants of the piezoelectric element, and β_{ijk} and $\ni_{kl}$ are the tensor components of the piezoelectric and dielectric coefficients.

In the problem under consideration, separate elements of the volume V_1 can be made of graphene composites, which, in addition to mechanical properties described by relations (12.3) or (12.4), exhibit high electrical conductivity and, therefore, can simultaneously play the role of a resistor. In the presence of electrode-covered surfaces $\left(S_э^i\right)$, the element made of the graphene composite (V_k) (Fig. 12.1a) will behave both as a deformable body and a resistor R_k. Furthermore, in the case when the electrodes of the piezoelectric element are connected via a conductor to the electrodes of the graphene element, the composite system will be considered as an electrode-formable body incorporating elastic and viscoelastic elements and a resistor.

Due to the presence of such a resistor, Eq. (12.1) should involve the term δA_R, which takes into account the work done by the electric field with the potential difference $\Delta\varphi$ to move the charge q on the resistance R:

$$\Delta\varphi_R = \varphi_1^R - \varphi_2^R, \qquad \delta A_R = \frac{1}{R}\int\left(\varphi_1^R - \varphi_2^R\right)\delta\varphi dt. \tag{12.6}$$

Here, φ_1^R and φ_2^R are the electric potentials on the electrode-covered surfaces of the piezoelectric element.
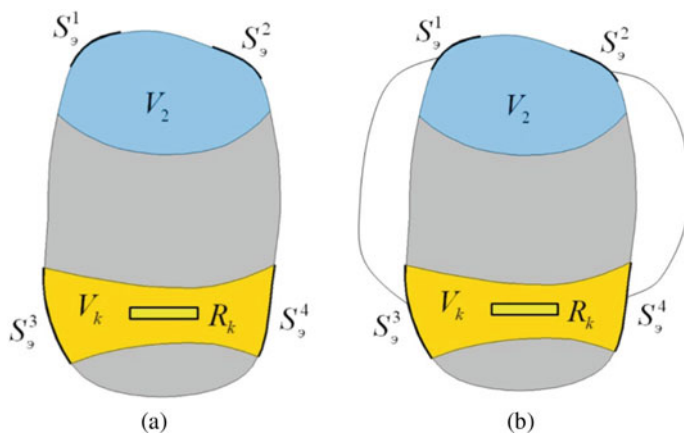
Fig. 12.1 Piecewise homogeneous body, exhibiting piezoelectrical properties (V_2) with electrode-covered surfaces $\left(S_э^1, S_э^2, S_э^3, S_э^4\right)$, containing element made of graphene composite (V_k)

Taking into account expression (12.6), the variational equation of motion for an electroviscoelastic body with a resistor can be written as follows [10]:

$$
\sum_{k=1}^{N} \left(\int_{V_1^k} \left(\sigma_{ij}\delta\varepsilon_{ij} + \rho_k\ddot{u}_i\,\delta u_i \right) dV \right) +
$$
$$
+ \int_{V_2} \left(\sigma_{ij}\delta\varepsilon_{ij} - D_i\delta E_i + \rho\ddot{u}_i\delta u_i \right) dV -
$$
$$
- \int_{S_\sigma} p_i\delta u_i\,dS - \int_{S_p} q_e\delta\varphi\,dS +
$$
$$
+ \sum_{q=1}^{n_R} \frac{1}{R_q} \int \left(\varphi_1^{R_q} - \varphi_2^{R_q} \right)\delta\varphi\,dt = 0.
$$
(12.7)

Here, n_R is the number of resistors in the system.

The dissipative properties of the systems under consideration are estimated using the values of displacement amplitudes in the resonance regimes in case of forced steady-state vibrations or the values of the decay rate of the corresponding vibration mode in case of natural vibrations.

A solution to the forced steady-state vibration problem is found in the following form [10]:

$$
u_i(\mathbf{x}, t) = \bar{U}_i(\mathbf{x})\,e^{ipt}, \qquad\qquad \varphi_i(\mathbf{x}, t) = \bar{\varphi}_i(\mathbf{x})\,e^{ipt}, \qquad (12.8)
$$

where p is the frequency of an external, periodical impact.

The vibration damping rate is characterized by the imaginary component of the complex natural vibration frequency [1, 9]. In the natural vibration problem with homogeneous boundary conditions, the solution is taken as [10]

$$
u_i(x, t) = \bar{u}_i(\mathbf{x})\,e^{i\omega t}, \qquad\qquad \varphi(x, t) = \bar{\varphi}(\mathbf{x})\,e^{i\omega t}. \qquad (12.9)
$$

Here, $\omega = \omega_R + i\omega_I$ is the complex eigenfrequency of vibrations, where ω_R corresponds to the eigenfrequency, whereas ω_I characterizes the damping rate of vibrations, $\bar{u}_i(\mathbf{x})$ and $\bar{\varphi}_i(\mathbf{x})$ are the natural vibration modes. In the natural vibration problems, physical equations (12.4) are replaced by their complex analogues (12.10) [9]:

$$
s_{ij} = 2\left(G_k^R + iG_k^I \right) e_{ij},
$$
$$
\sigma = \left(B_k^R + iB_k^I \right)\vartheta,
$$
(12.10)

where G_k^R, G_k^I, B_k^R, and B_k^I are the real and imaginary components of the shear and bulk complex dynamic moduli.

Taking into account the form of solution (12.9), the variational equation for the problem of natural vibrations of electroviscoelastic body with an external electric circuit can be written as

$$
\sum_{k=1}^{N} \left(\int_{V_1^k} \left(\sigma_{ij} \delta \varepsilon_{ij} + \rho_k \omega^2 u_i \delta u_i \right) dV \right) +
$$

$$
+ \int_{V_2} \left(\sigma_{ij} \delta \varepsilon_{ij} - D_i \delta E_i + \rho \omega^2 u_i \delta u_i \right) dV + \tag{12.11}
$$

$$
+ \sum_{q=1}^{n_R} \frac{1}{i \omega R_q} \int \left(\varphi_1^{R_q} - \varphi_2^{R_q} \right) \delta \varphi \, dt = 0.
$$

12.3 Numerical Implementation of Dissipative Properties of Deformable Solid Incorporating Elastic, Viscoelastic Elements, and a Resistive Element

For the numerical implementation of the problem of forced steady-state and natural vibrations of an electroviscoelastic body with external electric circuits consisting of resistors, capacitors, and inductors, we used the procedures of the finite element method [3, 10].

For the sake of illustration, we consider a plate ($500 \times 100 \times 1$ mm) shown in Fig. 12.2. The base plate was made of aluminum: $E = 6.85 \cdot 10^{10}$ Pa; $\nu = 0.3$; $\rho = 2750$ kg/m^3. The piezoelectric element ($60 \times 90 \times 1.3$ mm) was made of PKR7: $C_{11} = C_{22} = 12.5 \cdot 10^{10}$ Pa, $C_{12} = 8.40 \cdot 10^{10}$ Pa, $C_{13} = C_{23} = 8.10 \cdot 10^{10}$ Pa, $C_{33} = 12.1 \cdot 10^{10}$ Pa, $C_{44} = 2.05 \cdot 10^{10}$ Pa, $C_{55} = C_{66} = 2.36 \cdot 10^{10}$ Pa, $\beta_{31} = \beta_{32} = -9.0$ C/m^2, $\beta_{33} = 28.3$ C/m^2, $\beta_{52} = \beta_{61} = 17.9$ C/m^2, $\jmath_{11} = \jmath_{22} = 1.27 \cdot 10^{-8}$ F/m, $\jmath_{33} = 1.20 \cdot 10^{-8}$ F/m, $\rho = 7500$ kg/m^3.

The calculations were carried out for the variant of graphene composite, in which polymethylmethacrylate (PMMA) was used as a matrix, while graphene served as a filler [7]. For numerical modeling of this element within the framework of the elastic model, the following material properties were set: shear modulus $G = 2.29 \cdot 10^8$ Pa; bulk modulus $B = 5.96 \cdot 10^8$ Pa; specific density $\rho = 1190$ kg/m^3.

In the case when numerical modeling of the element was carried out in the framework of a viscoelastic model, the complex shear modulus $G = G^R + iG^I$ and elastic bulk modulus were specified as follows: $G^R = 2.29 \cdot 10^8$ Pa; $G^I = 5.73 \cdot 10^7$ Pa; $B = 5.96 \cdot 10^8$ Pa.

In the problem of forced, steady-state vibrations, it is assumed that the clamped end of the plate executes vibrations

$$
x = 0, \qquad u_x = u_y = 0, \qquad u_z = U_0 e^{ipt}. \tag{12.12}
$$
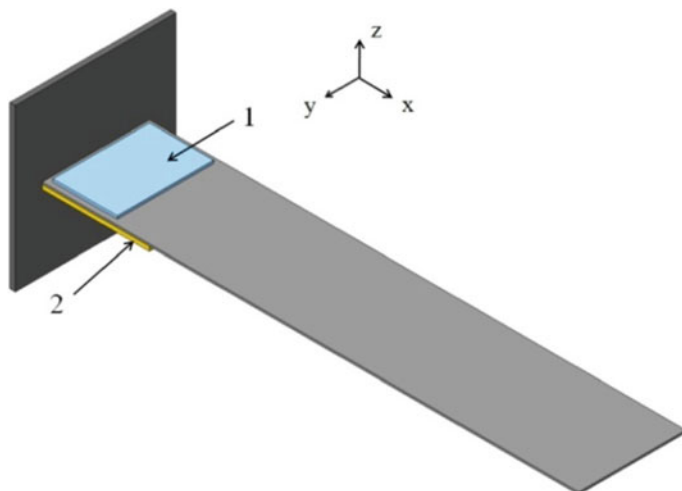
Fig. 12.2 A plate with piezoelectric element (1) and element made of graphene composite (2)

Figure 12.1 shows the amplitude–frequency characteristics frequency response plot of the component u_z of the displacement vector of the free plate end in the vicinity of the first and second resonances for three variants of modeling the examined system incorporating the element made of graphene composite:

1. only viscoelastic properties of the element made of graphene composite (dash-dotted line) are taken into account;
2. graphene composite is considered elastic and operates as a resistor (dashed line);
3. graphene composite is considered viscoelastic and operates as a resistor (solid line).

For the same variants, we calculated the values of complex natural frequencies. The complex eigenfrequencies for the first two modes of natural vibrations are summarized in Table 12.1. The imaginary parts of the eigenfrequencies characterize the damping rate of natural modes.

For the results presented above, the values of resistance for the first vibration mode (210 kΩ) and for the second mode (35 kΩ) were found by the numerical modeling under the condition of maximum vibration damping. The electric resistance (in Ω) of the element made of graphene material can be calculated with the use of the following formula:

$$R = \rho \frac{l}{S} = \frac{l}{\gamma \cdot S}, \tag{12.13}$$

where ρ is the specific resistance of the material of the conductor, γ is the specific conductivity of the conductor (the reciprocal of specific resistance), l is the length of the conductor, and S is the cross-sectional area of the conductor.

Table 12.1 The values of complex eigenfrequencies obtained for different scenarios of numerical simulations of graphene composite

Variant of numerical simulation	$\omega = \omega_R + i\omega_I$
First vibration mode	
1	$7.81597 - i\,0.04401$
2	$7.78116 - i\,0.03360$
3	$7.78344 - i\,0.07784$
Second vibration mode	
1	$46.33836 - i\,0.16603$
2	$46.10908 - i\,0.22177$
3	$46.11665 - i\,0.38729$

For the examined element made from the graphene composite, two variants of electrode covering can be realized: on the two opposite lateral surfaces; on the two large surfaces of the element. In the first case, $l = 100$ mm and $S = 100 \times 2$ mm^2, and in the second case, $l = 2$ mm and $S = 100 \times 100$ mm^2.

From this, it follows that for the evaluated optimal values of resistance, the values of the specific conductivity of graphene composite for the first and second variants of electrode plating, respectively, are as follows:

- for the first vibration mode,

$$\gamma_1 = 1/\rho \simeq 2.38 \cdot 10^{-3} \text{ S/m},$$
$$\gamma_2 = 1/\rho \simeq 9.52 \cdot 10^{-7} \text{ S/m};$$

- for the second vibration mode,

$$\gamma_1 = 1/\rho \simeq 1.42 \cdot 10^{-2} \text{ S/m},$$
$$\gamma_2 = 1/\rho \simeq 5.71 \cdot 10^{-6} \text{ S/m}.$$

It should be noted that the value of γ_1 is in the range of specific conductivity of graphene composites given in [2, 8].

The analysis of the results presented in Fig. 12.3 and the obtained values of the complex natural vibration frequencies have shown that the use of the electrical conductivity properties of graphene composites in smart structures incorporating piezoelectric elements provides an additional vibration damping mechanism.
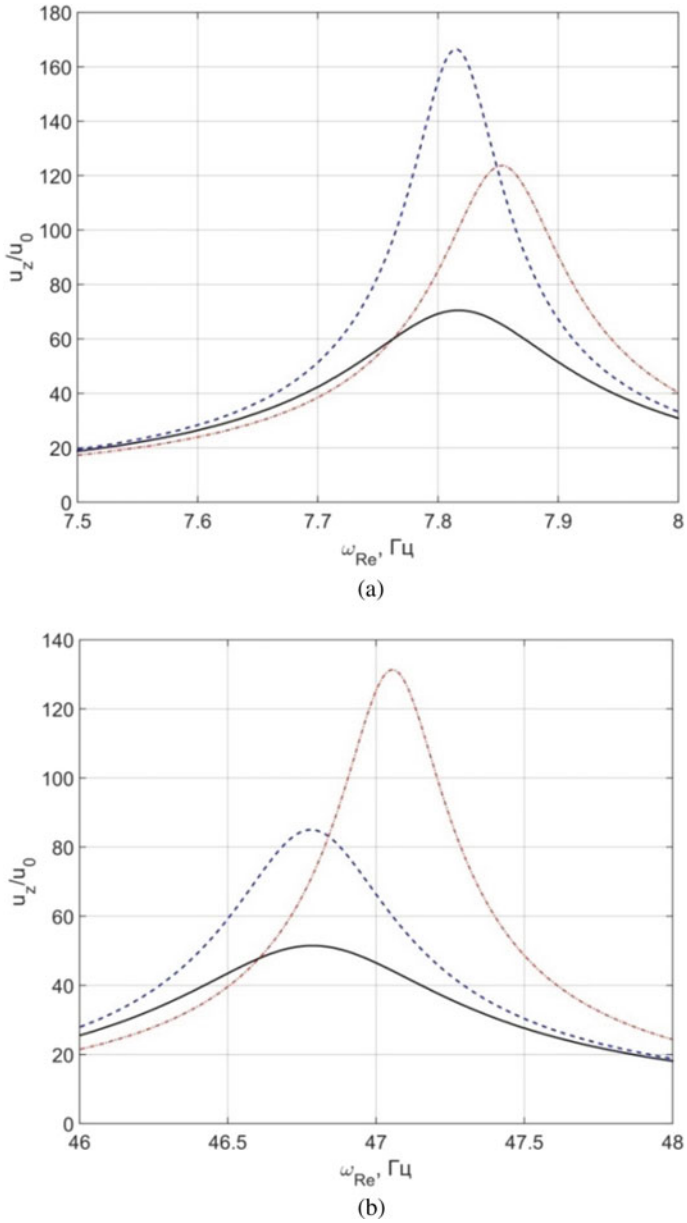
Fig. 12.3 Frequency response plot for u_z in the vicinity of the first (a) and second resonances (b)

12.4   Conclusions

We have considered a variant of smart structures containing piezoelectric elements and a shunt circuit, in which a deformable element made of a graphene composite operates as a resistor. A mathematical formulation of the problem of forced steady-state and natural vibrations has been developed for a smart structure, which is a piecewise homogeneous body consisting of the elastic, viscoelastic, and piezoelectric elements and the element made of graphene composite, which behaves not only as a mechanically deformable body, but also as a resistor. The numerical experiments have shown that in the smart structures of this kind, the electrical conductivity of the element made of graphene composite leads to the appearance of an additional damping mechanism.

References

1. Adamov, A., Matveenko, V., Trufanov, N., Shardakov, I.: Metody prikladnoy vyazkouprugosty. UrO RAN, Ekaterinburg (2003) (in Russian)
2. Alemour, B., Yaacob, M.H., Lim, H.N., Hassan, M.R.: Int. J. Nanoelectron. Mater. **11**, 4 (2018)
3. Iurlova, N., Sevodina, N., Oshmarin, D., Iurlov, M.: Int. J. Smart Nano Mater. **10**(2), 156 (2019)
4. Janos, B., Hagood, N.W.: Proceedings of the 6th International Conference on New Actuators, ACTUATOR 98. Bremen, Germany (1998)
5. Karnaukhov, V., Kirichok, I.: Electrothermal Viscoelasticity. Nauk, Dumka, Kiev 1 (1988) (in Russian)
6. Kelly, A.: Concise Encyclopedia of Composite Materials. Elsevier Science, England (1994)
7. Kumar, A., Sharma, K., Dixit, A.R.: J. Mater. Sci. **54**(8), 5992 (2019)
8. Marsden, A., Papageorgiou, D., Vallés, C., Liscio, A., Palermo, V., Bissett, M., Young, R., Kinloch, I.: 2D Mater. **5**(3), 032003 (2018)
9. Matveyenko, V.P., Kligman, E.P.: J. Vib. Control **3**(1), 87 (1997)
10. Matveenko, V., Oshmarin, D., Sevodina, N., Yurlova, N.: Comput. Cont. Mech. **9**(4), 476 (2016) (in Russian)
11. Moheimani, S.R., Fleming, A.J.: Piezoelectric Transducers for Vibration Control and Damping. Springer Science & Business Media (2006)
12. Washizu, K.: Variational Methods in Elasticity and Plasticity. Pergamon Press, Oxford, England (1982)

Chapter 13
Dynamics and Stability of Axially Loaded Elastic Rods

Nikita F. Morozov, Alexander K. Belyaev, Petr E. Tovstik, Tatyana P. Tovstik, and Chien-Ching Ma

Abstract The classical problem of buckling of a thin rod subjected to axial compressive force is studied. Two cases are studied in detail: (i) case of short loading and (ii) case of long-lasting loading. Dynamic buckling of a thin rod subjected to a continuously acting longitudinal load at the initial stage of the movement is studied. If the applied static load significantly exceeds the critical Euler force, one of the higher buckling modes has the maximum rate of amplitude growth at the initial stage of the motion. This result is obtained in the framework of a linear statement of the problem, and an explanation of the paradoxical result by Lavrentyev and Ishlinsky is provided. A possibility of the appearance of buckling due to a suddenly applied longitudinal load which is smaller than the Euler critical force is found out. This buckling can occur only for the rod length from a certain range and is caused by the parametric resonance. In the linear approximation, the amplitude increases unboundedly while a small resistance leads to a significant increase in the amplitude. Introduction of nonlinear terms into consideration results in beats with energy exchange between longitudinal and transverse vibrations. Axial impact on the rod by an impactor is considered as a way of reproduction of the jump force in the experiment. The contact force is determined analytically and by means of finite element analysis. The results of these two approaches are confirmed by test results on the example of the impact time.

N. F. Morozov · P. E. Tovstik
Petersburg State University, Universitetsky str., 22, 198504 St. Petersburg, Russia
e-mail: morozov@nm1016.spb.edu

A. K. Belyaev (✉) · T. P. Tovstik
Institute for Problems in Mechanical Engineering of RAS, V.O. Bolshoy pr., 61, 199178 St. Petersburg, Russia

C.-C. Ma
National Taiwan University, 4 Roosevelt Road, 106319 Taipei, Taiwan (R.O.C.)
e-mail: ccma@ntu.edu.tw

13.1 Introduction

The classical problem of buckling of a thin rod under axial compression is studied. A loading is said to be short provided that the impact time is comparable with the travel time of longitudinal wave along the rod length. It is typical for a short loading that the longitudinal wave runs along the rod and reflects many times from its ends. In the linear approximation, this wave process can cause parametric resonances with unlimited growth of the transverse vibration. Introducing damping results in bounded vibration amplitude which is nonetheless unrealistically high. To get a realistic picture, one applies a quasi-linear approach in which the longitudinal waves generate transverse vibrations and, in turn, the transverse vibrations affect the longitudinal ones. As a result, the vibrations look like beats with the energy exchange between longitudinal and transverse vibrations. The beats decay if damping is taken into account. The short impact is beyond the scope of the present paper, cf. [1, 2, 8, 9, 11].

The study of long-lasting compression refers to the works by Euler [3], Lavrentyev and Ishlinsky [6], Volmir [13], Ilgamov [5], and others. The transverse motion of the rod essentially depends on the way of loading, as well as the mechanical model. Euler solved two static problems: (i) in the linear approximation, he determined the critical load and possible buckling modes, and (ii) in nonlinear approach, he determined various equilibrium shapes of the rod loaded at its ends (Euler elastica). Further studies took into account the inertia forces in the rod. The paper by Lavrentyev and Ishlinsky [6] is concerned with the compressive load considerably exceeding the Euler critical load, and the highest growth rate of the amplitude of transverse deflection was shown to have a buckling mode with a greater number of waves in the axial direction. The nonlinear dynamic model used in the present paper shows that first the buckling mode predicted by Lavrentyev and Ishlinsky develops and later this mode transforms into a stable Euler elastica. Volmir [13] studied the transverse stability rod at the initial stage of loading under the assumption that the longitudinal compressive wave did not reach the opposite end of the rod. Instability begins if the increasing length of the compressed portion of the rod is sufficient for static buckling. Ilgamov [5] investigated the growth of the rod deflection at the initial time instants without propagation of longitudinal waves.

In what follows, we discuss the effect of the way of applying a constant longitudinal load on the dynamic buckling of a thin rod. In the case of linear statement and a static load that significantly exceeds the critical Euler load, the solution coincides with that obtained in [6], the greater rate of the buckling amplitude having one of the higher modes.

It is shown that the rod can buckle under the suddenly applied axial load which is smaller than the Euler force. This buckling can occur only under a constant force suddenly applied at the rod end and is associated with the parametric resonance. In the linear approximation, the amplitude grows beyond any bounds. Account for the nonlinear terms leads to the appearance of beats with the energy exchange between the longitudinal and transverse vibrations. The influence of the damping force and duration of the leading front of the pulse is studied.

The last part of the paper is concerned with the calculation of the contact force between two colliding elastic bodies. This statement is inspirited by understanding the fact that a jump force can be achieved in the field test and therefore another way of producing a short-time loading is needed. Two approaches are suggested which allow one to calculate the contact force. The results obtained are confirmed experimentally.

13.2 Axial Waves in Rod

In the linear approximation, the propagation of the longitudinal waves in the rod is governed by the equation

$$\frac{\partial^2 u}{\partial x^2} = \frac{1}{c^2} \frac{\partial^2 u}{\partial t^2}, \qquad 0 \le x \le L, \qquad u(L, t) = 0, \qquad (13.1)$$

where $u(x, t)$ denotes the axial displacement and stands for the speed of sound.

The right end of the rod is fixed and three types of the boundary condition for the left end of the rod $(x = 0)$ are shown in Fig. 13.1, where $w(x, t)$ denotes the transverse displacement of the rod.

The boundary conditions of the left end of the rod for three types of fixing are as follows:

$$\frac{\partial u}{\partial x}\bigg|_{x=0} = -\varepsilon_0, \qquad (13.2)$$

$$u(0, t) = \varepsilon_0 ct, \qquad (13.3)$$

$$u(0, t) = 0, \qquad (13.4)$$

where $\varepsilon_0 > 0$ denotes the axial strain. In the case (13.2), the rod is compressed by a constant force $P = E S \varepsilon_0$, where E is Young's modulus and S is the cross-sectional area. In the case (13.3) the rod's end moves with a constant velocity $v = \varepsilon_0 c$ and, e.g., this case can be realized by means of an axial impact of a heavy body. The last case (13.4) implies that both ends of the rod do not move at all. Ignoring for the time being condition (13.4), we obtain the solution for the first two boundary conditions under zero initial conditions $u(x, 0) = u_t(x, 0) = 0$.

Fig. 13.1 Three types of the rod under consideration

To investigate the transverse motion, we introduce the non-dimensional variables in Eq. (13.1)

$$x = rx^*, \qquad L = rL^*, \qquad u = ru^*, \qquad t = \frac{r}{c}t^*, \qquad r^2 = \frac{J}{S}, \qquad (13.5)$$

where J and r denote the geometrical moment of inertia and radius of inertia, respectively. In what follows, the asterisk $*$ is omitted. In terms of variables (13.5), the sound speed is equal to one and the equation of sound (13.1) takes the form

$$\frac{\partial^2 u}{\partial x^2} = \frac{\partial^2 u}{\partial t^2}. \qquad (13.6)$$

We are looking for the strain of axial compression $\varepsilon(x, t)$, and the solutions of boundary-value problems (13.6), (13.2) and (13.6), (13.3) are given by

$$\varepsilon^{(1)}(x, t) = -\frac{\partial u^{(1)}}{\partial x} = \varepsilon_0 - \frac{2\varepsilon_0}{L} \sum_{k=1}^{\infty} \frac{1}{\nu_k} \sin(\nu_k x) \, \cos(\nu_k t), \qquad \nu_k = \frac{(2k-1)\pi}{L}, \qquad (13.7)$$

$$\varepsilon^{(2)}(x, t) = -\frac{\partial u^{(2)}}{\partial x} = \varepsilon_0 t + \frac{2\varepsilon_0}{L} \sum_{k=1}^{\infty} \frac{1}{\hat{\nu}_k} \cos(\hat{\nu}_k x) \, \sin(\hat{\nu}_k t), \qquad \hat{\nu}_k = \frac{k\pi}{L}. \qquad (13.8)$$

Formulae (13.7) and (13.8) are actually the Fourier series in terms of the eigenfunctions of the corresponding boundary-value problems. Functions $\varepsilon^{(1)}(x, t)$ and $\varepsilon^{(2)}(x, t)$ are piecewise constant with respect to x for any fixed value of t. In addition to this, for any fixed value of x, function $\varepsilon^{(1)}(x, t)$ is periodical function of t having the period $T = 4L$, whereas function $\varepsilon^{(2)}(x, t)$ increases, cf. Fig. 13.2 showing functions $\varepsilon^{(1)}(x, t)$ and $\varepsilon^{(2)}(x, t)$ at $x = L/2$. For $0 \le t \le 2L$, we have $\varepsilon^{(1)}(x, t) = \varepsilon^{(2)}(x, t)$. To prove it, one can present the solution as a sum of two of traveling waves $u(x, t) = f(x - t) + g(x + t)$ and take into account the reflection conditions, namely, displacement $u(x, t)$ does not change sign under reflection at the fixed end and it changes sign at the free end.
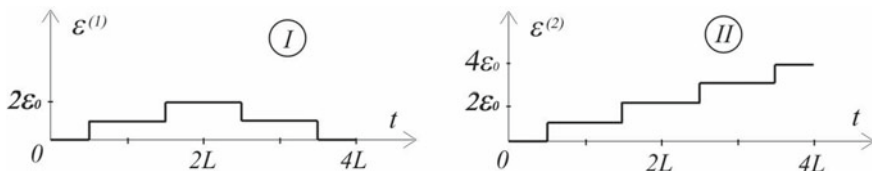
Fig. 13.2 Types of the wave reflection

13.3 Euler Solution and the Lavrentiev–Ishlinsky Solution

Using the Bernoulli–Euler model for the compressed pinned-pinned beam in terms of variables (13.5), we describe the small transverse vibration by the equation

$$\frac{\partial^4 w}{\partial x^4} + \frac{\partial}{\partial x}\left(\varepsilon(x,t)\frac{\partial(w+w^0)}{\partial x}\right) + \frac{\partial^2 w}{\partial t^2} = 0, \quad w = \frac{\partial^2 w}{\partial x^2} = 0 \quad (x = 0, L),$$

(13.9)

where $w^0(x,t)$ and $w(x,t)$ stand for the initial and actual deflections, respectively. The static problem of buckling of the pinned-pinned beam that was initially compressed by a constant force ($\varepsilon(x,t) = \varepsilon_0 = const$) under the conditions (13.4) and $w^0(x,t) = 0$ was first solved by Euler [3]. The buckling form with m half-waves $w(x) = w_0 \sin(m\pi x/L)$ corresponds to the compression strain

$$\varepsilon_m = m^2\pi^2/L^2.$$

(13.10)

In particular, for $m = 1$, one obtains the classical Euler critical (buckling) load $\varepsilon_{cr} = \pi^2/L^2$.

In the case of a considerably large value of the initial compression strain ε_0, the buckling can occur at several first modes, namely, at $m \leq m_0 = \left[\sqrt{\varepsilon_0 L^2/\pi^2}\right]$ where $[z]$ stands for the integer part of number z.

The authors of paper [6] paid attention to the fact that for $m_0 > 1$, the maximum rate of the buckling amplitude corresponds to a higher buckling mode, namely $m_* \simeq m_0/\sqrt{2}$. Indeed, the solution of Eq. (13.9) for $\varepsilon(x,t) = \varepsilon_0 = const$, $m \leq m_0$ is as follows:

$$w(x,t) = w_0 \sin\left(\frac{m\pi x}{L}\right) e^{\alpha_m t}, \qquad \alpha_m = \sqrt{\varepsilon_0 m^2\pi^2 - m^4\pi^4/L^2}.$$

(13.11)

Let us characterize the intensity of growth of the amplitude of m-th buckling mode by parameter α_m. Figure 13.3 displays the plots $\alpha_m(\varepsilon_0)$ for $m = 1, 2, \ldots, 8$ and $L = 500$.

Both the maximum intensity of the amplitude growth and the number of the corresponding modes increase with the growth of the compression amplitude ε_0.

The above-said is valid only for small deflections. In what follows, we discuss the further change in the rod shape.
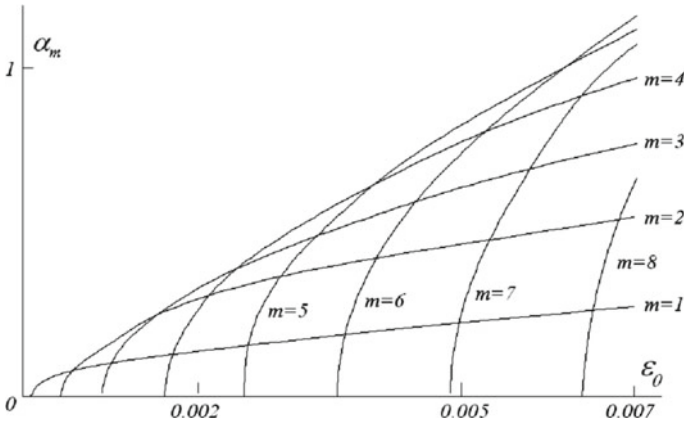
Fig. 13.3 Parameter of growth of the amplitude of m-th buckling mode $\alpha_m(\varepsilon_0)$

13.4 Buckling for Load Smaller Than the Euler Critical Force

Up to now, we considered the axial force that exceeded the Euler critical load. As proved in [10], the dynamic buckling is possible under the suddenly applied continuous longitudinal load which is smaller than the Euler critical load.

Consider a pinned-pinned rod, see the first graph in Fig. 13.1 and assume that a constant compressive force P is applied at the rod end at the initial time instant. Under these assumptions, the wave propagation in the rod has period $T = 4L$, cf. Fig. 13.2 (1). The periodic vibration in the rod is described by Eq. (13.9) where the axial strain is given by formula (13.7). Let us rewrite this equation in the following form:

$$\varepsilon(x, t) = \varepsilon_0 + \hat{\varepsilon}(x, t), \quad \hat{\varepsilon}(x, t) = -\varepsilon_0 \sum_{k=1}^{\infty} \frac{2}{v_k L} \sin(v_k x) e^{-v_k \delta t/2} \cos(v_k t),$$

$$v_k = \frac{(2k-1)\pi}{2L}. \tag{13.12}$$

Here δ denotes the factor of the viscous resistance and function $\hat{\varepsilon}(x, t)$ has a zero mean value at $\delta = 0$. Let us put the solution to Eq. (13.9) in the form

$$w(x, t) = \sum_{m=1}^{\infty} T_m(t) \sin(p_m x), \qquad p_m = m\pi/L, \tag{13.13}$$

where functions $T_m(t)$ satisfy the following system of equations:

$$\frac{d^2 T_m}{dt^2} + \omega_m^2 T_m - \varepsilon_0 p_m^2 w_m^0 + \varepsilon_0 \sum_{n=1}^{\infty} a_{nm}(t)(T_n + w_n^0) = 0,$$

$$w_m^0 = \frac{2}{L} \int_0^L w_0(x) \, \sin(p_m x) \, dx, \qquad \omega_m^2 = p_m^4 - \varepsilon_0 p_m^2, \quad m = 1, 2, \ldots, \quad (13.14)$$

$$a_{nm}(t) = \frac{8mn}{L^2} \sum_{k=1}^{\infty} \left(\frac{1}{(2k-1)^2 - 4(n-m)^2} + \frac{1}{(2k-1)^2 - 4(n+m)^2} \right) \cos v_k t.$$

Here ω_m is the eigenfrequency of the transverse vibration and depends on strain ε_0, whereas the constant values w_m^0 are the coefficients of the Fourier series of the initial imperfection $w^0(x)$. Here we consider the case $\varepsilon_0 < \varepsilon_{cr} = \pi^2/L^2$ in which the static buckling does not occur.

For $\delta = 0$ functions $a_{mn}(t)$ are periodic, that is, $a_{mn}(t + 4L) = a_{mn}(t)$, and system (13.14) generates a three-parameter set of resonances at $L = L_{mnk} = 2\pi(m^2 \pm n^2)/k$, $m, n, k = 1, 2, \ldots$. The overtone combination resonances are shown in [9] to be excited with much less intensity than the principle resonances. For this reason, we further restrict our consideration to the principle resonances, the latter having the critical length $L_m = 4\pi m^2$. We also neglect the interaction of the modes of transverse vibrations. As a result, for $w_m^0 = 0$, we obtain the following equation:

$$\frac{d^2 T_m}{dt^2} + \left(\omega_m^2 + \frac{8\varepsilon_0 p_m^2}{\pi^2} \sum_{k=1}^{\infty} C_{km} \cos v_k t \right) T_m = 0,$$

$$C_{km} = \frac{1}{(2k-1)^2 - 16m^2} + \frac{1}{(2k-1)^2}. \qquad (13.15)$$

The numerical integration of Eq. (13.15) yields the monodromy matrix, characteristic exponents [14] and the instability regions in the plane of parameters (L, ε_0) which are adjacent to the axis $\varepsilon_0 = 0$ at the points $L = L_m$.

The detailed analysis of the instability regions is given in [1, 9, 11]. Here we only touch upon a particular issue on existence of the instability regions for $\varepsilon_0 < \varepsilon_{cr} = (\pi/L)^2$. The sought-for values of length L for which the solution of Eq. (13.15) is unstable for $\varepsilon_0 < \varepsilon_{cr}$ and prescribed value of m lie in the interval $L_m^* < L < L_m$. Table 13.1 provides one with the numerical values of the above parameters for $1 \leq m \leq 10$.

One can see that the intervals $L_m^* < L < L_m$ where buckling is possible at $\varepsilon_0 < \varepsilon_{cr}$ occupy a relatively small part of axis L. The case $m = 1$ should be excluded from consideration since the Bernoulli–Euler model of the beam Eq. (13.9) is not valid for $L < 12.6$ (e.g., for a circular rod, the ratio of its length to diameter is less than 3.15). In the above table, α_m^{max} and L_m^{max} denote, respectively, the maximum rate of the amplitude growth and the corresponding length L. The rate α is determined from the formula $F(t) \simeq e^{\alpha t}$. One can see that the resonance intensity drops sharply with increasing resonance number m.

Table 13.1 Parameters of the instability regions

m	L_m^*	L_m	α_m^{max}	L_m^{max}	$\alpha_{m\delta}^{max}$
1	0	12.6	∞	0	∞
2	40.6	50.3	0.0523	43.3	0.0447
3	104.0	113.1	0.0198	106.5	0.0156
4	192.2	201.1	0.0106	194.6	0.0065
5	305.4	314.2	0.0066	307.9	0.0026
6	443.8	452.4	0.0045	446.1	0.0006
7	607.1	615.8	0.0033	609.6	–
8	795.4	804.2	0.0025	797.8	–
9	1009.1	1017.9	0.0020	1011.6	–
10	1247.8	1256.6	0.0010	1250.4	–
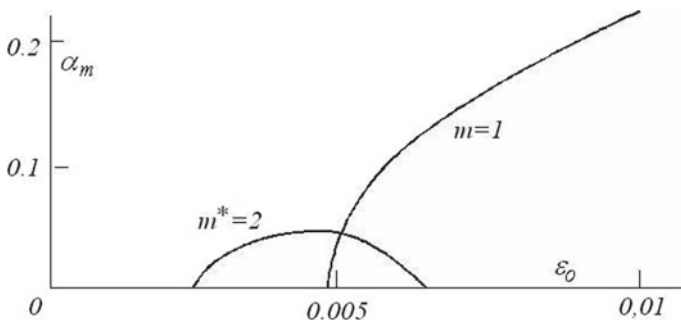
Fig. 13.4 The curves $\alpha_m(\varepsilon_0)$ for a rod of length $L = 45$

The table column $\alpha_{m\delta}^{max}$ demonstrates the influence of damping under the assumption that the damping affects only the transverse vibrations. The calculations were carried out for $\delta = 0.01$. It was found out that the maximum rate of the amplitude growth is smaller than that without damping, and the instability regions do not exist for $m \geq 7$ and $\varepsilon_0 \leq \varepsilon_{cr}$. The complete account of damping and the influence of nonlinearity are given below.

13.5 Example of Developing the Parametric Vibrations

Let us consider a rod of length $L = 45$. At $m = 2$, this length turns out within the interval (L_m^*, L_m) in which instability is possible for $\varepsilon_0 < \varepsilon_{cr} = 0.00487$. In Fig. 13.4, the curve $m^* = 2$ shows the dependence the rate of the amplitude growth $\alpha_m(\varepsilon_0)$ under the parametric resonance $m = 2$. The curve $m = 1$ displays the similar dependence under the Euler instability due to the first buckling mode.

Table 13.2 Increase in amplitude for some values of δ

δ	0.02	0.01	0.007	0.005	0.003	0.002	0.0015	0.001
$T_2^{\max}$	1.2	2.8	5.3	12.8	87.7	942.8	9823.0	1021345.0

Consider developing parametric vibration for $\varepsilon_0 = 0.0035 < \varepsilon_{cr} = 0.00487$. The amplitude first increases; however, with time, the longitudinal vibration (which is the source of parametric excitation) decays and the solution of Eq. (13.15) tends to zero. As a result of numerical integration for different coefficients of resistance, we find the maximum value of the amplitude. Table 13.2 shows the value that indicates how many times the increased amplitude is compared with the initial value.

Numerical simulation was used to determine the maximum values of amplitude for various damping factors δ. Table 13.2 displays values of $T_2^{\max}$ indicating increase in amplitude as compared with the initial value.

Small damping cannot prevent the development of large transverse vibrations so we proceed to nonlinear formulation of the problem. This solution is given in [11] and for this reason, we show here only some results.

Nonlinearity is taken into account only in the calculation of axial strain $\varepsilon = \partial u / \partial x + 1/2(\partial w / \partial x)^2$, which relates the longitudinal vibration to the transverse one. An approximate solution is sought in the form

$$u(x,t) = \sum_{k=1}^{K} a_k(t) \cos(v_k x), \qquad w(x,t) = \sum_{n=1}^{N} b_n(t) \sin p_n x. \qquad (13.16)$$

A nonlinear system of ordinary differential equations is obtained in [11] for unknown functions $a_k(t)$, $b_k(t)$. Five terms are taken for calculating sum (13.16). For numerical work, we take $L = 45$, $\varepsilon_0 = 0.0035$, and $b_2(0) = 0.0001$, assume trivial initial conditions, and perform integration in the interval $0 \le t \le 1000$. Two cases are considered: (i) no damping and (ii) the viscosity factor is $\delta = 0.002$.

Figure 13.5 shows the resonance amplitude $b_2(t)$ and a function $a_1(t)$ giving the main part of the longitudinal displacement. In the absence of viscosity, the motion is non-decaying beats manifesting an exchange of energy between axial and bending vibrations. Calculations have shown that the amplitude of beats is weakly dependent on the initial conditions. When $\delta = 0.002$, we observe damped beats, with the rate of decay being strongly dependent on the viscosity factor δ. The beat frequency also changed in comparison with the undamped case. In the linear approximation and for $\delta = 0.002$, the maximum amplitude increased by 942 times compared with the initial value, cf. Table 13.2, while in the nonlinear approach, the amplitude of beats is independent of the initial conditions.

It was assumed above that the applied force immediately takes a finite value. Suppose now that $\varepsilon_0(t) = \varepsilon_0 th(t/\tau)$ where τ denotes the duration of leading edge. We consider now the same problem as above for $\delta = 0$ and a number of values τ. Table 13.3 shows the maximum values of the beat amplitude $b_2^{\max} = \max_t b_2(t)$.
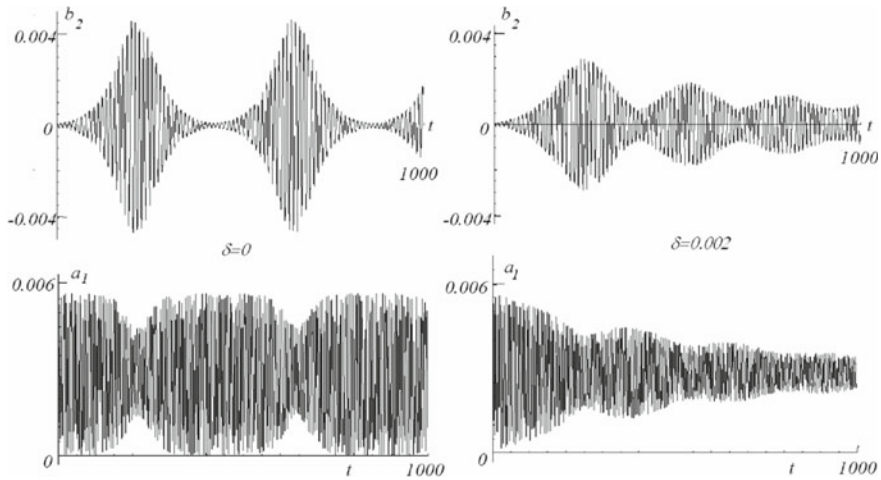
Fig. 13.5 Parametric resonance under nonlinear statement

Table 13.3 The amplitude of the beats versus the duration of leading edge of a shock pulse

τ	0	0.5	1	1.5	2	2.5
$b_2^{\max}$	0.0045	0.0034	0.0036	0.0025	0.0015	0.0005
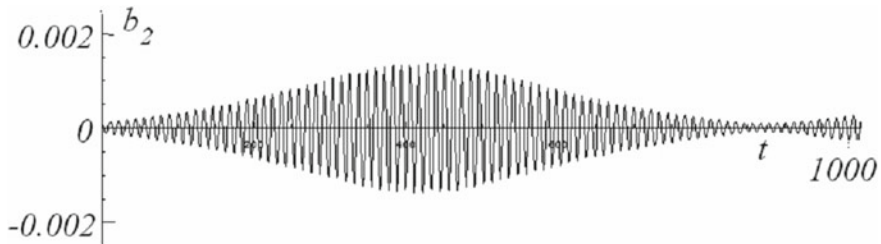
Fig. 13.6 Graph of function $b_2(t)$ at $\tau = 2$

We see that the beat amplitude decreases with increase in the duration of the leading edge. Figure 13.6 shows a graph in function $b_2(t)$ at $\tau = 2$ in the same scale as in Fig. 13.5.

13.6   Estimation of the Impact Force

Exact reproduction of the jump force in the experiment is not possible. A simple way of creating a short-time force is the axial impact on the rod by an impactor. Let us carry out a theoretical analysis of the impact.

Consider an elastic rod of length l with a fixed end. At the initial time instant, the free end is impacted by a rigid body (impactor) of mass m with velocity v_0.

We apply the Sears method [12] in the form

$$v_0 t - \alpha - y_1 - y_2 = 0, \tag{13.17}$$

implying the coincidence of the contact point of the rod and impactor. Here α denotes the contact deformation due to the collision and y_1 and y_2 are the dynamic displacements in the rod and impactor caused by the contact force $P(t)$ without contact deformation.

As the contact zone is small, we can neglect its mass and make use of Hertz's contact theory relating the contact force P and local displacement α, cf. [4]

$$P(\alpha) = k\alpha^{3/2}, \tag{13.18}$$

where k is a factor depending on mechanical and geometrical parameters of the colliding bodies. In the case under consideration [7],

$$k = \frac{2}{3(1 - \mu^2)} E\sqrt{R}, \tag{13.19}$$

where R is the curvature radius of the impact surface, E and μ are Young's modulus and Poisson's ratio, and the material of both bodies being assumed to be the same.

The displacements y_1 and y_2 can be expressed in terms of the contact force

$$y_1 = \int_0^t P(\theta) Y^{(1)}(t - \theta) d\theta, \qquad y_2 = \int_0^t P(\theta) Y^{(2)}(t - \theta) d\theta, \tag{13.20}$$

where $Y^{(1)}$ and $Y^{(2)}$ denote, respectively, the reaction of the rod and impactor on the applied unit pulse and

$$Y(t) = \frac{c}{ES} \begin{cases} +1, & 0 < t < 2L/c \\ -1, & 2L/c < t < 4L/c \end{cases}, \qquad Y(t + 4L/c) = Y(t). \tag{13.21}$$

13.7 Results of Mathematical Modeling

The time dependence of the contact force was calculated using the above method. The calculations show that the contact force is a smooth function of time which has from one to three maxima depending on the parameters of colliding bodies.

An example of calculation of the contact force with three maxima is shown in Fig. 13.7 (curve 1) for the parameters of the rod and impactor given in Table 13.4.

The results of the numerical simulation were verified by finite element analysis of the system with parameters of Table 13.4. The comparison of the results of finite
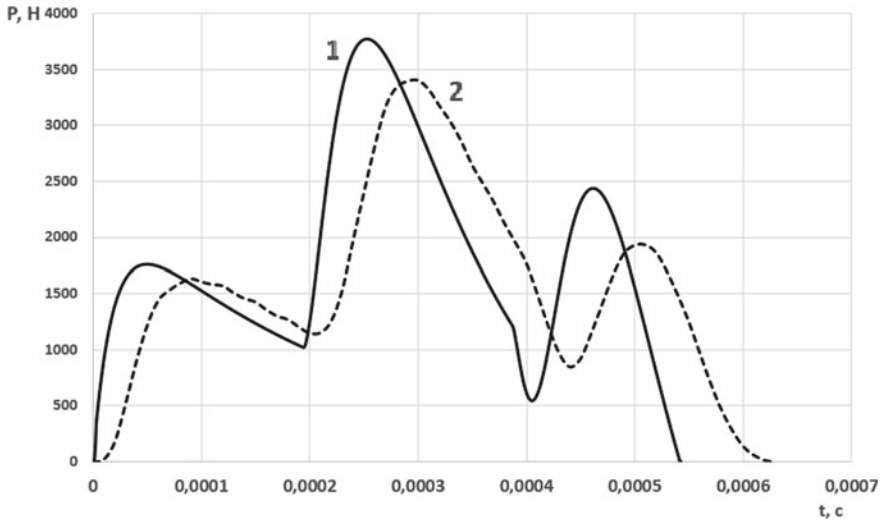
Fig. 13.7 The time dependence of the contact force obtained numerically (curve 1) and by finite element method (curve 2); the values of the parameters are given in Table 13.1

Table 13.4 Parameter of the system

Colliding body, material	Parameter	Denotation	Unit	Model value	Test value
Rod	Length	l	m	0.500	0.301
	Cross-sectional area	S	m^2	$5.0 \cdot 10^{-5}$	$3.14 \cdot 10^{-6}$
Impactor	Mass	M	kg	0.5	0.13–8.46
	Radius of impact surface	R	m	0.01	1.58–6.36
	Initial velocity	V_0	m/s	1.0	0.3225
Steel	Young's modulus	E	N/m^2	$2.1 \cdot 10^{11}$	$7.342 \cdot 10^{10}$
	Poisson's ratio	μ	–	0.30	0.34
	Mass density	ρ	kg/m^3	7800.0	2696.6

element modeling and numerical simulation with the data of field experiments is observed in Table 13.5.

Table 13.5 Comparison of test results with the data obtained by calculation

Parameters of impact		Time of contact interaction, μs			Error, %	
Diameter, m	Mass, g	Test	FEM	Simulation	FEM	Simulation
3.16	0.13	36.42	31.20	15.32	14.33	57.93
4.75	0.44	46.83	60.75	23.63	29.72	49.54
5.56	0.71	52.26	78.09	27.90	49.42	46.61
6.34	1.04	60.05	81.61	31.71	35.90	47.19
9.51	3.51	84.96	106.21	47.94	25.01	43.57
12.73	8.46	111.10	121.71	64.82	9.54	41.66

13.8 Conclusions

- The dynamic buckling of a thin rod subjected to a continuously acting longitudinal load at the initial stage of the movement is studied. If the applied static load significantly exceeds the critical Euler force, one of the higher buckling modes has the maximum rate of amplitude growth at the initial stage of the motion. This result is obtained in the framework of a linear statement of the problem.
- We established a possibility of the appearance of buckling due to a suddenly applied longitudinal load which is smaller than the Euler critical force. This buckling can occur only for the rod length from a certain range and is caused by the parametric resonance. In the linear approximation, the amplitude increases unboundedly while a small resistance leads to a significant increase in the amplitude. Introduction of nonlinear terms into consideration results in beats with an energy exchange between longitudinal and transverse vibrations. Account for damping leads to decaying beats.
- The behavior of the rod subjected to a suddenly applied constant longitudinal stress at the initial stage of motion which is limited to the time of run of the longitudinal wave along the rod is investigated. In the framework of the suggested formulation of the problem (elastic deformation and the left end is fixed in the transverse direction), the buckling results in bending deflection that does not exceed the initial perturbations at the beginning of motion, i.e., consideration of this particular stage of motion is not of practical importance.
- Axial impact on the rod by an impactor is considered since the accurate reproduction of the jump force in the experiment is not possible. Two approaches are applied for the determination of the contact force: (i) the Sears method and finite element analysis. They demonstrate that time histories of the contact force are close for these approaches. The numerical simulations were confirmed by test results in regard to the impact time.

References

1. Belyaev, A., Iliin, D., Morozov, N.: Dynamic approach to the Ishlinsky-Lavrentiev problem. Mech. Solids **48**(5), 504–508 (2013)
2. Bolotin, V.: Transverse Displacement and Critical Velocities. Publishers of Academy of USSR Sciences, vol. 1 1951, vol. 2 1953 (in Russian)
3. Euler, L.: Method of determining curved lines possessing the properties of maximum or minimum or solution to isoperimetric problem in the broadest sense. Gostekhizdat, Moscow (1934) (in Russian)
4. Hertz, H.: Ueber die Berührung fester elastischer Körper. J. für die reine und angewandte Mathematik **1882**(92), 156–171 (1882)
5. Ilgamov, M.: Dependence of dynamic buckling of rod on initial conditions. Doklady Phys. **457**(6), 456–459 (2014) (in Russian)
6. Lavrentiev, M., Ishlinsky, A.: Dynamic forms of loss of stability of elastic systems. Doklady Phys. **5**(6) (1949) (in Russian)
7. Lurie, A.: Theory of Elasticity. Springer, Berlin Heidelberg (2005)
8. Morozov, N., Tovstik, P.: Dynamics of rod under axial impact. Vestnik St. Peterzburg. Univ. Ser. I. Mat. Mekh. Astr **2**, 105–111 (2009) (in Russian)
9. Morozov, N., Tovstik, P.: Dynamics of a rod on short-time longitudinal impact. Vestnik St. Peterzburg. Univ. Ser. I. Mat. Mekh. Astr **3**, 131–141 (2013) (in Russian)
10. Morozov, N., Tovstik, P.: On dynamic loss of stability of rod under a load lower than euler force. Doklady Phys. **453**(3), 282–285 (2013) (in Russian)
11. Morozov, N., Tovstik, P.: Transverse vibrations of rod caused by axial impact. Doklady Phys. **452**(1), 37–41 (2013)
12. Sears, J.: On the longitudinal impact of metal rods with rounded ends. Proc. Cambridge Phil. Soc. (1908)
13. Volmir, A.: Nonlinear Dynamics of Plates and Shells. Nauka, Moscow (1972) (in Russian)
14. Yakubovich, V., Starzhinsky, V.: Linear differential equations with periodic coefficients and their applications. Nauka, Moscow (1972) (in Russian)

Chapter 14
A Numerical Study on the Response of the Oscillation Roller-Soil Interaction System

Ivan Paulmichl, Christoph Adam, and Dietmar Adam

Abstract In this contribution, the influence of the operating speed of a specific oscillation roller on the achieved soil compaction and the resulting response behavior of the roller is examined. The main objective is the further validation of an experimentally found Continuous Compaction Control (CCC) parameter for dynamic rollers with an oscillatory drum. The study is based on a recently developed two-dimensional numerical model of the oscillation roller-granular soil interaction system, in which the intergranular strain enhanced hypoplastic constitutive model is implemented to simulate the compaction process. The effect of one roller pass at standard excitation frequency on an initially very loose soil is investigated for six roller speeds in terms of the reduction of the void ratio. Moreover, the influence of the resulting predicted soil compaction on the drum response is analyzed in the time and frequency domain. A relationship between the computed compaction indicator and roller speed is established. It is shown that the roller speed has a significant effect on the achieved soil compaction both in terms of the compaction degree and the depth of influence. The results confirm that the CCC indicator under consideration qualitatively reflects the soil stiffness characterized by the predicted void ratio distribution.

14.1 Introduction

An *oscillation* roller, as shown in Fig. 14.1, is a heavy equipment for near-surface compaction of soil and asphalt. The main component is the oscillation drum, which is dynamically decoupled from the remaining unit by rubber buffers. The oscillation drum is equipped with two opposite offset eccentric masses, which rotate during

I. Paulmichl · C. Adam (✉)
University of Innsbruck, Unit of Applied Mechanics, Technikerstr. 13, Innsbruck 6020, Austria
e-mail: christoph.adam@uibk.ac.at

I. Paulmichl
e-mail: ivan.paulmichl@uibk.ac.at

D. Adam
TU Wien, Institute of Geotechnics, Karlsplatz 13/220/2, 1040 Vienna, Austria
e-mail: dietmar.adam@tuwien.ac.at
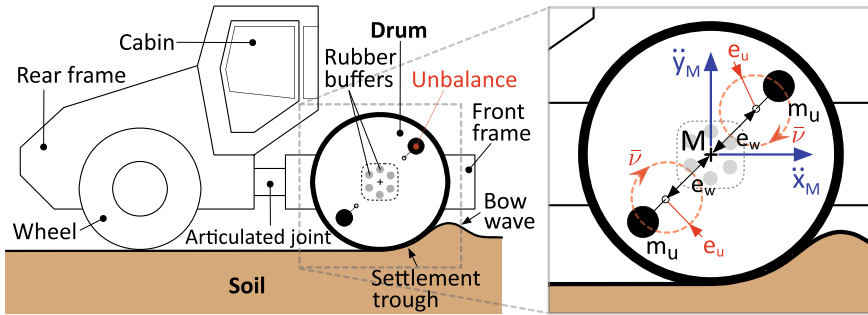
Fig. 14.1 Components of an oscillation roller compactor and detail of the unbalance configuration in the drum (schematic), modified from [17]

operation synchronously in the same direction (see Fig. 14.1) resulting in an alternating high-frequency forward-backward motion of the drum [17]. This oscillatory motion of the drum, superposed by the translational roller motion, leads to compaction due to the dynamic shear forces exerted on the subsoil. An oscillation roller can, therefore, also be referred to as "shear force roller". During compaction, a settlement trough forms below the drum and a bow wave in front of the drum in the direction of movement. In contrast to a *vibratory* roller, the triggered vibrations are smaller, but at the price of a lower compaction effect and compaction depth. The oscillation roller is therefore particularly suitable for use in densely built-up areas.

During roller compaction, an instant and continuous control of the actual degree of soil compaction is performed on the basis of the dynamic response of the roller-soil interaction system recorded during roller operation. This so-called *Continuous Compaction Control* (CCC) [1, 11] has become the standard technology for the work-integrated evaluation of soil compaction with vibratory rollers. However, until recently there was no mature CCC system available for the *oscillation* roller considered in this paper.

Dynamic soil compaction and its work-integrated control by means of vibratory rollers has been studied extensively; see, e.g., [3, 9, 21, 25] (compaction process), and [2, 4, 10] (CCC application). However, the detailed dynamic behavior of the oscillating roller-soil interaction system has so far been investigated relatively rarely. For example, Erdmann [3] used the *hypoplastic* constitutive law with intergranular strain to simulate soil compaction by means of vibratory and oscillation rollers equipped with different exciters. Pistrol [22] derived a CCC indicator for oscillation rollers from the drum response recorded in field tests by plotting the vertical against the horizontal drum center acceleration component as shown in Fig. 14.2. Based on this response representation, he found that the area enclosed in the resultant "curved, recumbent eight figure" becomes larger with increasing soil stiffness, and therefore, proposed it as a characteristic quantity for the compaction degree of non-cohesive, granular soils [22]. In the meantime, this empirically determined relationship has
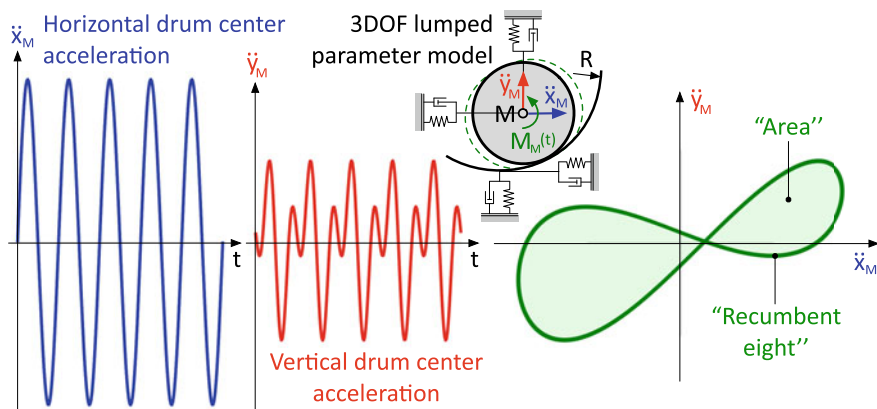
Fig. 14.2 Response of the drum center in form of a "recumbent eight" (schematic) representing the stiffness of a granular earth-moist soil, based on the lumped parameter model of [17], modified from [19]

also been proven theoretically based on a three degrees-of-freedom (3DOF) lumped parameter model (LPM) [17].

Recently, Paulmichl et al. [20] developed a plane-strain Finite Element model of the highly nonlinear oscillation roller-soil interaction system to predict for the first time simultaneously the compaction of granular, dry (or earth-moist) soils and the dynamic roller response based on the intergranular strain enhanced *hypoplastic* constitutive model as described in, e.g., [15]. The outcomes of the investigations based on a HD$^+$ 90 VO tandem roller [6] show all fundamental response characteristics observed in field tests [22] as well as in a recent parametric study based on a 3DOF LPM [19]. The sensitivity of the predicted soil compaction to various parameter variations, the parameter dependency of the drum response, and consequently of the CCC indicator proposed in [22] was recently evaluated by Paulmichl et al. [18]. In particular, the influence of soil properties such as the initial void ratio, the coefficient of friction between drum and soil surface, the static axle load, and the number of subsequent roller passes on both compaction effect and compaction control performance was examined. In addition, first studies were carried out into the influence of the operating speed of the roller. As these preliminary investigations mainly focused on the compaction effect achieved, the influence of the roller speed on both the compaction effect and especially in the compaction control performance will be analyzed in more detail in the present contribution.

14.2   Numerical Model

The present investigations are based on a two-dimensional (2D) Finite Element (FE) model recently developed by Paulmichl et al. [20], which allows both analyzing the dynamic response of the oscillation roller-soil interaction system (see Fig. 14.1)
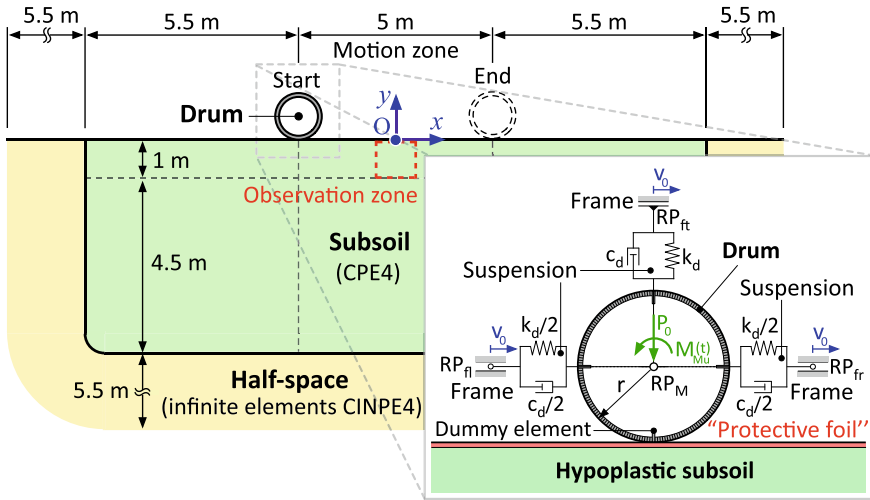
Fig. 14.3 Finite Element model (overview) and drum-suspension model (detail), schematic (without mesh), modified from [20]

during the compaction of granular, dry or earth-moist soils and predicting the compaction effect achieved. The "sufficient accuracy" of this numerical model created in ABAQUS/CAE was verified in [20] by comparing computed (predicted) results and corresponding recorded data (field tests, as described in [22]). It consists of three subsystems, i.e., the soil, the oscillation drum, and the spring-damper elements between drum and roller frame as shown in Fig. 14.3.

The finite soil domain of dimension $16\,\text{m} \times 5.5\,\text{m}$ (subsequently referred to as "subsoil") is discretized by four-node bilinear plane-strain quadrilateral elements (CPE4 [23]), which is embedded in infinite elements (CINPE4 [23]) with a length of $5.5\,\text{m}$ representing the semi-infinite soil domain ("halfspace" in Fig. 14.3). The dimension of the elements varies between $0.02\,\text{m} \times 0.02\,\text{m}$ (contact and compaction zone) and $0.1\,\text{m} \times 0.1\,\text{m}$ (transition zone finite to infinite soil domain). The mesh comprises 37569 elements including the infinite elements. To the "subsoil" domain, the *hypoplastic* constitutive law with the extension for intergranular strain, as proposed in [15], is assigned. This constitutive model allows a realistic description of the compaction of non-cohesive, granular, dry or earth-moist soils by introducing the void ratio e as a state variable with stress-dependent physical limits to model barotropy and pycnotropy. As in the study by Paulmichl et al. [20] and based on [7, 16], in the present simulations for the soil the so-called *Hochstetten sand* [24] is assumed. The respective values of the required thirteen constitutive parameters are as follows: $\varphi_c = 33°$, $h_s = 1.5 \times 10^9\,\text{Nm}^{-2}$, $n = 0.28$, $e_{d0} = 0.55$, $e_{c0} = 0.95$, $e_{i0} = 1.05$, $\alpha = 0.25$, $\beta = 1.50$, $R = 1 \times 10^{-4}$, $m_R = 5$, $m_T = 2$, $\beta_r = 0.5$, and $\chi = 6$ [8, 14, 15, 24]. Note, the initial value of the solution-dependent state variable e, i.e., the initial void ratio e_0, can be chosen between e_{d0} (void ratio for the densest packing for zero mean pressure) and e_{i0} (void ratio for the loosest packing for zero

mean pressure). In the present contribution, e_0 is set to 0.90 to simulate an initially very loose soil. The intergranular strain enhanced extended hypoplastic constitutive model was implemented in ABAQUS/Standard via a user-defined subroutine (UMAT), as described in [5, 13]; see also [15, 24].

To the "halfspace" domain, i.e., to the infinite elements, the following linear elastic isotropic constitutive parameters are assigned based on [16]: density $\rho = 2200\,\mathrm{kgm^{-3}}$, *Young*'s modulus $E = 250 \times 10^6\,\mathrm{Nm^{-2}}$, and *Poisson*'s ratio $\nu = 0.3$.

In accordance with [20], the parameters of a HD$^+$ 90 VO tandem roller [6] are employed. Since a deeply tuned suspension (i.e., the "rubber buffers" in Fig. 14.1) decouples dynamically the drum and the front frame, the entire roller can be reduced to the stiff oscillation drum, which is connected to the quasi-static frame via three lumped parameter spring-dashpot elements (*Kelvin-Voigt* bodies) as shown in Fig. 14.3. The frame moves horizontally at the constant speed v_0. To the spring-damper elements, which represent the viscoelastic properties of the rubber buffers, the following values are assigned: $k_d = 4 \times 10^6\,\mathrm{Nm^{-1}}$ (stiffness coefficient) and $c_d = 3 \times 10^2\,\mathrm{Nsm^{-1}}$ (damping coefficient) [20]. The drum modeled as an elastic circular steel ring with the outer radius equal to the drum radius $r = 0.60\,\mathrm{m}$ and the thickness of $0.02\,\mathrm{m}$ is discretized also by CPE4 elements, which are radially uniformly distributed and have a size of approximately $0.01\,\mathrm{m} \times 0.02\,\mathrm{m}$. To achieve the drum properties specified by the manufacturer, i.e., the mass $m = 1851\,\mathrm{kg}$ and the mass moment of inertia $I = 412\,\mathrm{kgm^2}$ [6], a lumped mass and rotary inertia is added to the reference point at the drum center "M" ("RP_M" in Fig. 14.3).

Inside the oscillation drum, two eccentric and (relative to the drum center) point-symmetrical unbalanced shafts rotate synchronously in the same direction at a constant angular velocity $\bar{\nu}$ (see Fig. 14.1). Since these unbalances are shifted relative to each other by 180°, the unbalance forces cancel each other out. The remaining spinning couple of forces leads to a torsional moment around the drum axis, which changes its sign during the rotation of the eccentric masses and moves the drum rapidly in an alternating forward-backward motion [17]. The resulting sinusoidal oscillation moment $M_{Mu}(t) = M_{Mu}^{(0)} \sin \bar{\nu} t$ (with $M_{Mu}^{(0)} = 2\,m_u e_u e_w \bar{\nu}^2$) [17] applied to the drum center captures this effect. $\bar{\nu}$ is 2π times the excitation frequency $\bar{f}$, m_u represents the eccentric lumped masses per shaft with distance e_u from the center of rotation, and e_w denotes the distance of the unbalanced shafts from the drum center as shown in Fig. 14.1. For the HD$^+$ 90 VO roller under consideration, operating at the standard oscillation frequency $\bar{f} = 39\,\mathrm{Hz}$, the resulting amplitude $M_{Mu}^{(0)}$ of the sinusoidal excitation moment is $54947\,\mathrm{Nm}$ [17]. In addition, the static axle load $P_0 = 44130\,\mathrm{N}$ [20] is applied in the center of the drum, which is made up of the dead weight of the front frame and the weight of the drum. The interaction between the outer surface of the drum and the subsoil surface in the "contact zone" (i.e., $-3\,\mathrm{m} \leq x \leq 3\,\mathrm{m}$) is modeled with the classical isotropic *Coulomb friction model* [23] assuming a constant coefficient of friction $\mu = 0.5$.

The "motion zone" of the drum bounded by $-2.5\,\mathrm{m} \leq x \leq 2.5\,\mathrm{m}$ represents the potential "compaction zone" for the soil below. The motion of the drum with constant velocity v_0 is modeled by defining boundary conditions in the form of velocity at the reference nodes RP_{fl}, RP_{fr}, RP_{ft}, which represent the quasi-static frame (see

Fig. 14.3) and the frictional contact between drum and soil mentioned above. Due to the alternating high-frequency forward-backward motion of the drum, which is super-imposed on the translational roller motion at constant speed v_0, the soil is exposed to about 35 oscillations per meter traveled (at standard speed $v_0 = 1.11\,\mathrm{ms}^{-1}$). The numerical analysis consisting of five steps was performed with the FE software ABAQUS/Standard (version R2016x) on the basis of a maximum time increment of 2×10^{-4}s. For details, see [20].

The hypoplastic constitutive model used can only process small tensile stresses depending on the "apparent cohesion" p_t, which is assigned to the subsoil [5]. Since granular, non-cohesive soils are considered in the present contribution, an "additional measure" must be applied to the stress-free surface to ensure better numerical stability. As proposed in Paulmichl et al. [20], the free soil surface is "sealed" by an elastic "protective foil" to prevent individual nodes from lifting so much that the analysis is aborted; as shown in Fig. 14.3. To model this "protective foil", a linear elastic isotropic constitutive law with a *Young*'s modulus E of $50 \times 10^6\,\mathrm{Nm}^{-2}$ is assigned to the elements of the first row of the subsoil mesh. An additionally applied apparent cohesion of $5\,\mathrm{kNm}^{-2}$ proved to be the lowest possible value of p_t to allow a stable numerical simulation for a wide range of input variables (e.g., initial void ratio e_0, roller speed v_0) [16, 20].

14.3 Results

To illustrate the influence of the roller speed v_0 on the effect of the oscillation drum, in addition to the default value $v_0 = 1.11\,\mathrm{ms}^{-1}$, five further speeds are considered, i.e., two below (0.55 and $0.75\,\mathrm{ms}^{-1}$) and three above (1.39, 2.22, and $3.33\,\mathrm{ms}^{-1}$) the default value. Considering the standard operating frequency $\bar{f} = 39\,\mathrm{Hz}$ the soil is thus exposed to about 12–70 oscillation cycles per meter driven, depending on v_0. In the following, the response of the described dynamic interaction model after one pass with the considered oscillation roller, which operates at different speeds v_0, is presented and evaluated under the assumption of an initially very loose soil, i.e., $e_0 = 0.90$.

14.3.1 Predicted Soil Compaction

First, the effect of the roller speed v_0 on the predicted soil compaction is investigated with regard to the reduction of the void ratio e. The soil section considered is the potential "compaction zone" up to 1 m depth and in the horizontal range $-0.5\,\mathrm{m} \leq x \leq 0.5\,\mathrm{m}$, also referred to as "observation zone" in Fig. 14.3.

Figures 14.4a to f show the predicted distribution of the normalized void ratio e/e_0 in the observation zone for six selected values of v_0. The areas highlighted in red correspond to non-compacted or weakly compacted areas, i.e., e is equal or
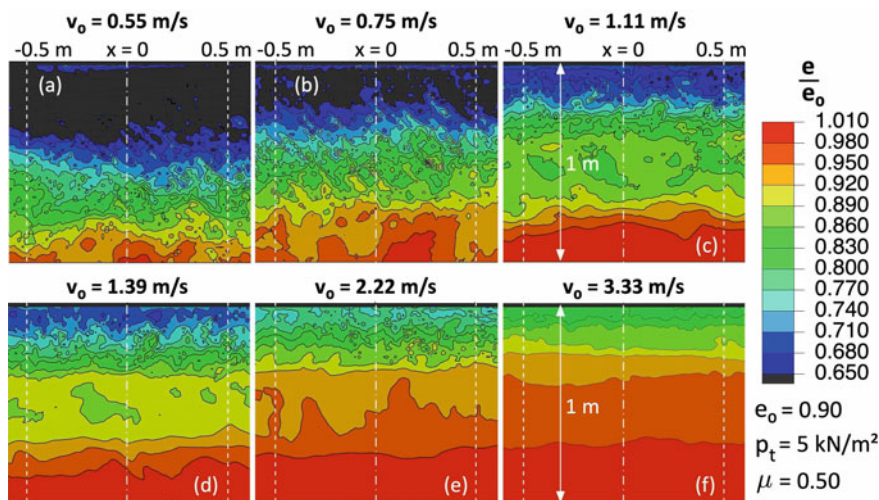
Fig. 14.4 Normalized void ratio after one pass with a HD$^+$ 90 VO roller ($\bar{f} = 39\,\text{Hz}$) for six selected roller speeds v_0, based on [16]

slightly smaller than its initial value e_0, while in blue areas a high reduction of e is achieved. Dark gray areas indicate most compacted soil zones. At a first glance, it can be seen that the roller speed has a considerable influence on the compaction effect of the oscillation drum. Both the maximum predicted void ratio reduction and the soil zone with uniformly high compaction become larger the lower the roller speed v_0 is. Moreover, the depth to which the soil is affected by the oscillation drum (i.e., $e < e_0$), represented by the depth at the transition from orange to red marked area ("depth effect"), increases with decreasing v_0 to more than one meter at the lowest speed.

For better readability, Fig. 14.5 shows the change $e_0 - e$ of the void ratio related to the maximum possible change $e_0 - e_d$ ("compaction effect") in relation to the soil depth for four selected speeds v_0. Each profile represents the mean of $(e_0 - e)/(e_0 - e_d)$ in the soil region $-0.5\,\text{m} \le x \le 0.5\,\text{m}$ (observation zone) analyzed in steps of $0.05\,\text{m}$. Note that the lower limit of the void ratio e_d is assumed to be 0.54 depending on the actual stress state [20]. In the case of the lowest value of v_0, about 90–95% of the maximum possible void ratio reduction is achieved after only one roller pass up to almost $0.35\,\text{m}$ depth. Since at this speed, due to about 70 oscillations per meter driven, the maximum possible compaction is almost reached after one pass close to the surface, compaction continuous further into depth. At a depth of about $1.3\,\text{m}$ the influence of the oscillation roller vanishes. In contrast to this, the predicted compaction effect is much smaller for a roller pass at the highest speed considered, both in terms of the degree of compaction (about 40–45%) and the corresponding depth (up to $0.1\,\text{m}$). The depth effect is $\approx 0.8\,\text{m}$ and thus also considerably smaller.

$$(e_0 - e)/(e_0 - e_d)$$

$e_0 = 0.90$

$v_0 = 0.55\ \text{m/s}$
$v_0 = 1.11\ \text{m/s}$
$v_0 = 2.22\ \text{m/s}$
$v_0 = 3.33\ \text{m/s}$
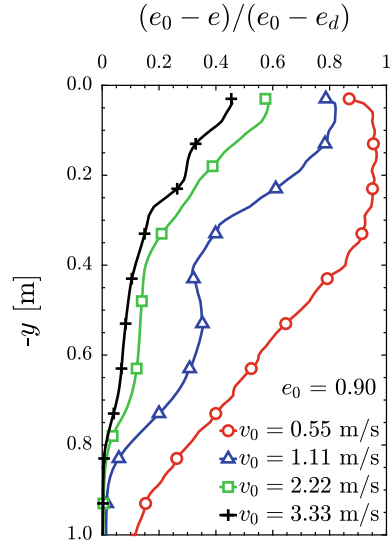
14.3.2 Predicted Drum Response

Next, the dynamic response of the drum during oscillation compaction is investigated
on the basis of the numerically predicted acceleration components $\ddot{x}_M$ (horizontal)
and $\ddot{y}_M$ (vertical) of the drum center M. Parameters based on the drum center response
are also evaluated because they form the basis of the CCC methodology for oscillation
rollers [22], as described in the introduction.

Figure 14.6 shows the (a) horizontal ($\ddot{x}_M$) and (c) vertical ($\ddot{y}_M$) acceleration com-
ponent for three selected roller speeds ($v_0 = 0.55,\ 1.11,\ 2.22\,\text{ms}^{-1}$) in a time frame
of one second during the first roller pass. It is readily seen that the roller speed
v_0 strongly affects both $\ddot{x}_M$ and $\ddot{y}_M$. The amplitudes of $\ddot{y}_M$ increase with decreas-
ing speed v_0 from about $-1 \div 1.5\,\text{ms}^{-2}$ ($v_0 = 2.22\,\text{ms}^{-1}$) to about $-4 \div 4\,\text{ms}^{-2}$
($v_0 = 0.55\,\text{ms}^{-1}$). The amplitudes of the horizontal response $\ddot{x}_M$ also become larger
with decreasing roller speed v_0. At the largest considered value of v_0, the predicted
amplitudes of $\ddot{x}_M$ are in the range of about $-8 \div 7\,\text{ms}^{-2}$, while the accelerations in
the drum center of a roller operating at the lowest considered speed vary between
-15 and $12\,\text{ms}^{-1}$. Thus, the amplitudes of $\ddot{y}_M$ are between three and eight times
smaller than the amplitudes of $\ddot{x}_M$, depending on the roller speed.

Figures 14.6b and d show the drum acceleration components ($\ddot{x}_M$ and $\ddot{y}_M$) of a
time frame of one second, as discussed above, in the frequency domain ($|\ddot{X}_M(f)|$ and
$|\ddot{Y}_M(f)|$). It can be observed that the excitation frequency $\bar{f}$ dominates $|\ddot{X}_M(f)|$ and
$|\ddot{Y}_M(f)|$ for all three roller speeds v_0. The amplitudes at the excitation frequency $\bar{f}$
of both the horizontal ($|\ddot{X}_M(\bar{f})|$) and the vertical ($|\ddot{Y}_M(\bar{f})|$) drum response become
larger with decreasing v_0. The additional harmonics in the spectra of the horizontal
response $|\ddot{X}_M|$ at $f/\bar{f} = 2, 3, 4, \ldots$, with amplitudes much smaller than those at
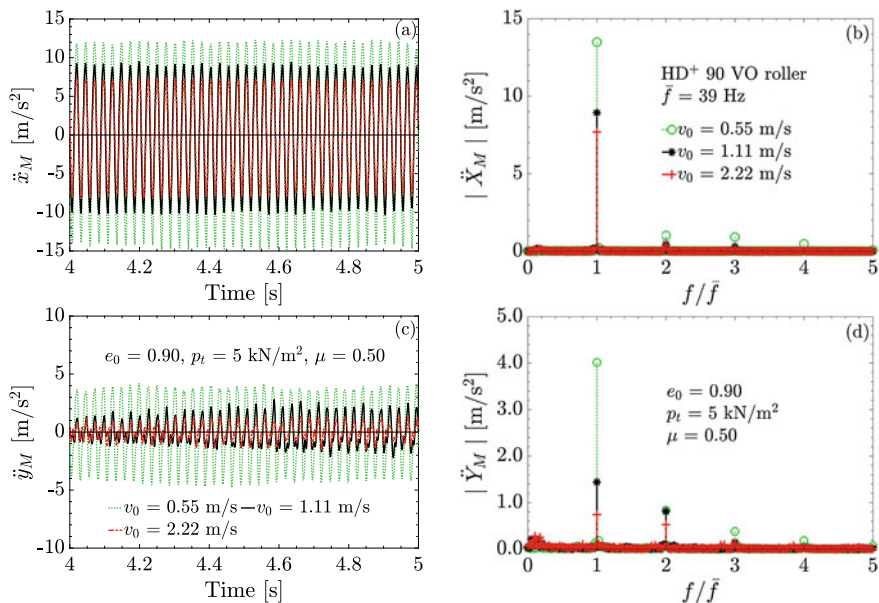
Fig. 14.6 **a**, **c** Time histories and **b**, **d** respective frequency spectra of the **a**, **b** horizontal and **c**, **d** vertical acceleration in the drum center after one oscillation roller pass on initially very loose soil for three selected roller speeds v_0 [16]

$f/\bar{f} = 1$, can be traced back to the "peak cut" due to slip phases of the drum motion resulting from a larger soil stiffness, as discussed in detail in [18]. For instance, the amplitude ratio $|\ddot{X}_M(3\bar{f})|/|\ddot{X}_M(\bar{f})|$ increases from about 0.03 ($v_0 = 1.11\,\mathrm{ms}^{-1}$) to almost 0.07 ($v_0 = 0.55\,\mathrm{ms}^{-1}$), i.e., the ratio more than doubles if the standard operating speed is halved and the oscillation cycles per meter traveled are doubled, respectively. Thus, the normalized amplitude at the third harmonic ($|\ddot{X}_M(3\bar{f})|/|\ddot{X}_M(\bar{f})|$) can be taken as a slip indicator, as proposed by Pistrol [22]. The second harmonic $|\ddot{Y}_M(2\bar{f})|$ in the vertical response spectra reflects the up and down motion of the drum in its "settlement trough", while the additional harmonics at $f/\bar{f} = 3, 4, 5, \ldots$, are a result of the slip phases of the drum [17]. The ratio $|\ddot{Y}_M(2\bar{f})|/|\ddot{Y}_M(\bar{f})|$ shows an increase from about 0.2 at the lowest speed to about 0.7 at the largest considered value of v_0. The amplitudes of the third ($|\ddot{Y}_M(3\bar{f})|$) and fourth ($|\ddot{Y}_M(4\bar{f})|$) harmonics start to vanish when the speed becomes larger than the default value of $1.11\,\mathrm{ms}^{-1}$.

Plotting the vertical component $\ddot{y}_M$ (Fig. 14.6c) against the horizontal counterpart $\ddot{x}_M$ (Fig. 14.6a) results in Fig. 14.7a. This response representation is fundamental to the CCC methodology described in [22]. For all considered values of v_0 a figure similar to a so-called *Lissajous curve* [12] is formed with one node and an asymmetric pattern. The larger v_0 is, the more the resulting shape resembles a "recumbent eight". In addition, the area in the $\ddot{y}_M$-$\ddot{x}_M$ plot becomes smaller as the roller speed increases, reflecting the lower soil compaction achieved by fewer oscillation cycles per meter
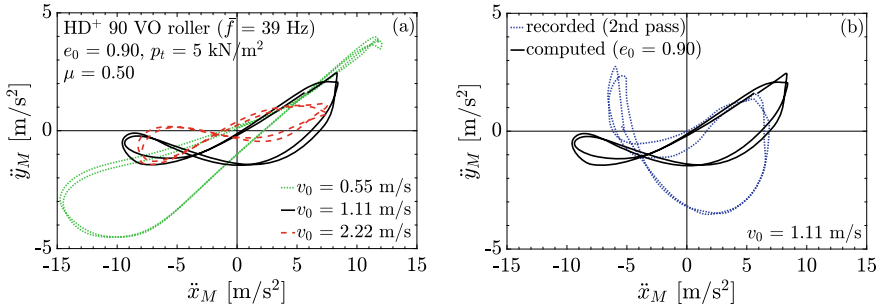
Fig. 14.7 Plot vertical against horizontal acceleration in the drum center for two representative oscillation cycles; **a** predicted "recumbent eight" figures based on Figs. 14.6a, c, and b computed versus recorded drum response

driven, as presented in Sect. 14.3.1. In Fig. 14.7b, the predicted response for the default value of v_0 (solid black line) is compared with the corresponding response representation based on drum accelerations recorded in a field test (dotted blue line based on [22]). It can be seen that the numerically derived drum response in terms of drum center accelerations qualitatively reproduces the drum response observed in the field. The computed amplitude of the horizontal acceleration component is about the same as that of the measured one. The vertical accelerations, however, are underestimated by the numerical analysis, which may be due to different soil parameters or boundary conditions in the field test [18]. The evaluation of the area in the $\ddot{y}_M$-$\ddot{x}_M$ figure successively (in time) for five subsequent excitation periods for each considered roller speed and plotting its mean value against v_0 results in Fig. 14.8. It can be observed that the aforementioned decrease of the "area", i.e., the compaction indicator, with increasing roller speed v_0 is almost linear, especially in the speed range $v_0 = 0.75 \div 1.67 \, \mathrm{ms}^{-1}$, as the red dotted line in Fig. 14.8 shows. These results essentially show that the CCC parameter proposed by Pistrol [22] decreases with decreasing number of oscillations per meter driven, as a lower resulting soil compaction is achieved.

14.4   Summary and Conclusions

The sensitivity of the soil compaction achieved by an oscillation roller, as well as of the drum response to the variation of the operating roller speed, was investigated on the basis of a recently developed plane-strain Finite Element model of the dynamic oscillation roller-soil interaction system. Soil compaction was simulated with the intergranular strain enhanced extended hypoplastic constitutive model and the void ratio reduction was evaluated. The presented results clearly show that the predicted compaction effect, both in terms of the compaction degree and depth of influence, increases with decreasing roller speed. In addition, the conducted sensitivity study

Fig. 14.8 Mean compaction indicator during the first roller pass as a function of the roller speed v_0, modified from [18]
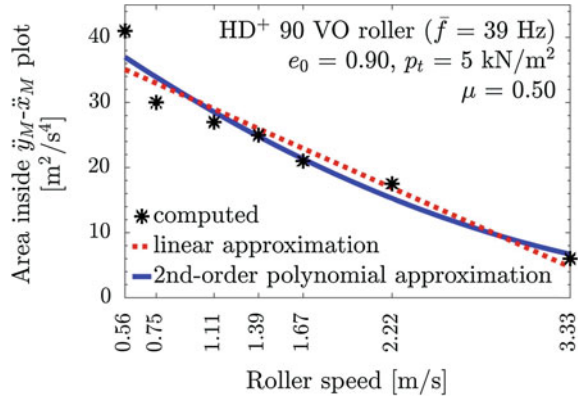
revealed that the shape of the plot vertical against horizontal drum center acceleration and its area depend on the subsoil stiffness, which is characterized by the predicted void ratio distribution. These outcomes confirm that the quantities derived from the presented drum response representation are appropriate indicators for work-integrated compaction control with oscillation rollers.

References

1. Adam, D.: Continuous Compaction Control (CCC) with vibrating rollers (in German) (Flächen-deckende Dynamische Verdichtungskontrolle (FDVK) mit Vibrationswalzen). Ph.D. thesis, TU Wien (1996)
2. Anderegg, R., Kaufmann, K.: Intelligent compaction with vibratory rollers: Feedback control systems in automatic compaction and compaction control. Transp. Res. Rec. **1868**, 124–134 (2004)
3. Erdmann, P., Adam, D.: Numerical simulation of dynamic soil compaction with vibratory compaction equipment. In: Brandl, H., Adam, D. (eds.) Proceeding XV Danube—European Conference on Geotechnical Engineering (DECGE 2014), pp. 243–248. Vienna, Austria (2014)
4. Grabe, J.: Continuous inverse calculation of soil stiffness from the dynamic behavior of a driving vibratory roller (in German) (Fortlaufend inverse Berechnung der Bodensteifigkeit aus dem Schwingungsverhalten einer fahrenden Vibrationswalze). Arch. Appl. Mech. **63**(7), 472–478 (1993)
5. Gudehus, G., Amorosi, A., Gens, A., Herle, I., Kolymbas, D., Mašín, D., Muir Wood, D., Niemunis, A., Nova, R., Pastor, M., Tamagnini, C., Viggiani, G.: The soilmodels.info project. Int. J. Numer. Anal. Methods Geomech. **32**(12) (2008)
6. Hamm A.G.: Data sheet HD+ 90 VO (2011)
7. Heiniger, R.: Contributions to the numerical simulation of the compaction of non-cohesive soils with oscillation rollers (in German) (Beiträge zur numerischen Simulation der Verdichtung von nichtbindigen Böden mit Oszillationswalzen). Master thesis, University of Innsbruck (2018)

8. Herle, I., Gudehus, G.: Determination of parameters of a hypoplastic constitutive model from properties of grain assemblies. Mech. Cohesive-Frict. Mater. **4**(5), 461–486 (1999)
9. Kelm, M.: Numerical simulation of the compaction of granular soils by vibratory rollers (in German) (Nummerische Simulation der Verdichtung rolliger Böden mittels Vibrationswalzen). Ph.D. thesis (2003). Publication of the Institute of Geotechnical and Construction Engineering, 6. Technische Universität Hamburg-Harburg (2004)
10. Kenneally, B., Musimbi, O.M., Wang, J., Mooney, M.A.: Finite element analysis of vibratory roller response on layered soil systems. Comput. Geotech. **67**, 73–82 (2015)
11. Kopf, F.: Continuous Compaction Control (CCC) during compaction of soil by means of dynamic rollers with different kinds of excitation (in German) (Flächendeckende Dynamische Verdichtungskontrolle (FDVK) bei der Verdichtung von Böden durch dynamische Walzen mit unterschiedlichen Anregungsarten). Ph.D. thesis, TU Wien (1999)
12. Lawrence, J.D.: A Catalog of Special Plane Curves. Dover Publications (1972)
13. Mašín, D.: Clay and sand hypoplasticity UMAT and Plaxis implementations, including UMAT-Plaxis interface. https://soilmodels.com
14. Mašín, D.: Modelling of Soil Behaviour with Hypoplasticity. Springer Series in Geomechanics and Geoengineering. Springer International Publishing (2019)
15. Niemunis, A., Herle, I.: Hypoplastic model for cohesionless soils with elastic strain range. Mech. Cohesive-Frict. Mater. **2**(4), 279–299 (1997)
16. Paulmichl, I.: Numerical modeling approaches to the oscillation roller-subsoil interaction problem. Ph.D. thesis, University of Innsbruck (2019)
17. Paulmichl, I., Adam, C., Adam, D.: Analytical modeling of the stick-slip motion of an oscillation drum. Acta Mech. **230**(9), 3103–3126 (2019)
18. Paulmichl, I., Adam, C., Adam, D.: Parametric study of the compaction effect and the response of an oscillation roller. In: Proceedings of the Institution of Civil Engineers—Geotechnical Engineering (2020). https://doi.org/10.1680/jgeen.19.00209
19. Paulmichl, I., Adam, C., Adam, D., Völkel, W.: Assessment of a compaction indicator for oscillation rollers with a lumped parameter model. In: Proceedings of the Institution of Civil Engineers—Geotechnical Engineering (2019). https://doi.org/10.1680/jgeen.19.00204
20. Paulmichl, I., Furtmüller, T., Adam, C., Adam, D.: Numerical simulation of the compaction effect and the dynamic response of an oscillation roller based on a hypoplastic soil model. Soil Dyn. Earthq. Eng. **132**, (2020)
21. Pietzsch, D., Poppy, W.: Simulation of soil compaction with vibratory rollers. J. Terramechanics **29**(6), 585–597 (1992)
22. Pistrol, J.: Compaction with oscillating rollers. Motion behaviour, roller integrated compaction control and assessment of wear (in German) (Verdichtung mit Oszillationswalzen - Bewegungsverhalten, walzenintegrierte Verdichtungskontrolle und Verschleißbeurteilung). Ph.D. thesis, TU Wien (2016)
23. Smith, M.: ABAQUS 2016 Documentation Collection. Simulia (2015)
24. von Wolffersdorff, P.A.: A hypoplastic relation for granular materials with a predefined limit state surface. Mech. Cohesive-Frict. Mater. **1**(3), 251–271 (1996)
25. Yoo, T.S., Selig, E.T.: Dynamics of vibratory-roller compaction. ASCE J. Geotech. Eng. Div. **105**, 1211–1231 (1979)

Chapter 15
Locking Free High-Order Mixed Elements for Ferroelectric Polarization

Astrid S. Pechstein, Martin Meindlhumer, Alexander Humer, and Michael Krommer

Abstract In this contribution, a finite element discretization for a thermodynamically consistent macroscopic model of the ferroelectric polarization process is introduced. Usually, finite elements are based on an incremental optimization problem for the electric enthalpy, and displacement and electric potential are the degrees of freedom of choice. Less common, energy-based models involving displacement and dielectric displacement have been proposed. In this work, the model is reformulated in terms of the mechanic enthalpy, leading to stress and dielectric displacement as independent unknowns. Choosing stable pairs of mixed finite elements for the mechanic and the electric quantities, a locking-free finite element method of arbitrary order is designed. Numerical results show the robustness of the method.

15.1 Introduction

The piezoelectric effect allows to convert electric loads into mechanical deformations and vice versa. Modern piezoceramics provide high precision actuation and sensing at moderate cost. In order to exhibit the piezoelectric effect, these ceramics have to be polarized initially by a high electric field. In most applications, it is assumed that the consequent remanent polarization state is unidirectional and constant, which leads essentially to Voigt's theory of linear piezoelasticity [22]. However, the remanent polarization state can change under different—sufficiently high—mechanical

A. S. Pechstein (✉) · M. Meindlhumer · A. Humer · M. Krommer
Institute of Technical Mechanics, Johannes Kepler University Linz, Altenberger Str. 69, 4040 Linz, Austria
e-mail: astrid.pechstein@jku.at

M. Meindlhumer
e-mail: martin.meindlhumer@jku.at

A. Humer
e-mail: alexander.humer@jku.at

M. Krommer
e-mail: michael.krommer@jku.at

173

or electrical loadings. On the other hand, for involved geometries as occurring in macro-fiber composites (MFCs), the applied poling electric field does not lead to a unidirectional polarization state. For these reasons, the numerical simulation of the polarization process and of mechanic and electric depolarization is an active field of research.

In this work, a phenomenological description of the macroscopic material behavior is adopted. The remanent polarization state is considered as an internal variable, similar to the plastic strain in elastoplasticity. The proposed model is thermodynamically consistent. The first to suggest such thermodynamically consistent models were the group around Maugin [1–4]. McMeeking and Landis [9], as well as Schröder and Romanowski [19] provided models including a remanent polarization strain depending directly on the remanent polarization. However, these models are still capable of mechanical depolarization. Independent polarization strains were considered, e.g., by Landis [7] or Klinkel [6].

An extensive introduction on variational frameworks for these models is provided by Miehe et al. [12]. In their work, energy and electric enthalpy-based models are considered. These different models require different sets of free unknowns. Most classical finite element methods are electric enthalpy based, where displacement (or strain) and electric potential (or electric field) are the primary unknowns. Few methods are energy-based with displacement and dielectric displacement as independent unknowns. We cite a vector potential model by Semenov et al. [20] and a one-dimensional model by Sands and Guz [18]. An energy-based method involving mixed finite elements was suggested by Pechstein et al. [16, 17].

The present work deals with a model based on the mechanic enthalpy. Stress and dielectric displacement are the primary unknowns of this model. For both the mechanical and the electrical quantities, stable pairs of mixed elements are employed. The major benefit of this approach is the fact that the mixed mechanic elements are locking free with respect to shear locking for flat elements. We choose *tangential displacement normal-normal stress* (TDNNS) elements, which were used in the context of simulation of linear piezoelectric materials by Pechstein et al. [15] and Meindl-humer et al. [10, 11]. Thus, these elements are well designed for the discretization of flat piezoelectric patches or thin integrated structures. The electric mixed elements were designed by Lehrenfeld and Schöberl [8] such that Gauss' law of zero charges is satisfied exactly.

15.2 Thermodynamic Model

Let $\Omega \subset \mathbb{R}^3$ denote the domain of interest. We introduce the quantities of interest in our electromechanically coupled model. First, $\mathbf{u} : \Omega \to \mathbb{R}^3$ shall denote the displacement field. We assume to stay in small-strain regime, where the linearized strain tensor $\mathbf{S} = \frac{1}{2}(\nabla \mathbf{u} + (\nabla \mathbf{u})^T)$ is used. Its work conjugate is the symmetric total stress tensor $\mathbf{T}$. For the electric quantities, we introduce the electric potential $\varphi : \Omega \to \mathbb{R}$ and the electric field as its negative derivative, $\mathbf{E} = -\nabla \varphi$. Its work conjugate is the

dielectric displacement vector denoted by $\mathbf{D}$. In the following, we will refer to displacement $\mathbf{u}$ and electric potential φ as well as strain $\mathbf{S}$ and electric field $\mathbf{E}$ as *primal* quantities, whereas the stress tensor $\mathbf{T}$ and dielectric displacement $\mathbf{D}$ are referred to as *dual* quantities. Ferroelectric polarization is described by a further macroscopic field, the remanent polarization $\mathbf{P}^i$. In this contribution, we assume that the remanent polarization $\mathbf{P}^i$ directly accounts for the polarization strain $\mathbf{S}^i = \mathbf{S}^i(\mathbf{P}^i)$ due to the smaller computational complexity of such a formulation.

The conjugate, dual quantities $\mathbf{T}$ and $\mathbf{D}$ both satisfy balance equations

$$- \operatorname{div} \mathbf{T} = \mathbf{f} \qquad \text{and} \qquad - \operatorname{div} \mathbf{D} = 0, \qquad (15.1)$$

where $\mathbf{f}$ denotes the given volume loads. Additionally, boundary conditions have to be satisfied. For the mechanic quantities, we assume the body is fixed on some part Γ_{fix} and free on the remaining part $\Gamma_{\text{free}} = \partial\Omega \backslash \Gamma_{\text{fix}}$. Moreover, we assume that the electric potential is prescribed on some part of the boundary Γ_{pot}, whereas the body is insulated elsewhere on $\Gamma_{\text{ins}} = \partial\Omega \backslash \Gamma_{\text{pot}}$,

$$\mathbf{u} = 0 \quad \text{on } \Gamma_{\text{fix}} \qquad \text{and} \qquad \mathbf{T} \cdot \mathbf{n} = 0 \quad \text{on } \Gamma_{\text{free}}, \qquad (15.2)$$

$$\varphi = V_0 \quad \text{on } \Gamma_{\text{pot}} \qquad \text{and} \qquad \mathbf{D} \cdot \mathbf{n} = 0 \quad \text{on } \Gamma_{\text{ins}}. \qquad (15.3)$$

Primal and dual quantities are related to each other via the material law. We assume a thermodynamically consistent material model, which is described by a thermodynamic potential. For a detailed introduction, we refer to Miehe et al. [12], in the following, we provide a short presentation of enthalpy-based material modeling.

Usually, a potential representing the electric enthalpy of the system is given, where the primal unknowns and the remanent polarization are the free variables,

$$\Psi_e = \int_\Omega \psi_e(\mathbf{S}, \mathbf{E}, \mathbf{P}^i) \, dx. \qquad (15.4)$$

Above, we used the convention that the lower-case expression ψ_e denotes the density of the upper-case potential Ψ_e. Then, stress and dielectric displacement are defined as (negative) derivatives of the potential density with respect to strain and electric field

$$\mathbf{T} = \frac{\partial \psi_e}{\partial \mathbf{S}}, \qquad\qquad \mathbf{D} = -\frac{\partial \psi_e}{\partial \mathbf{E}}. \qquad (15.5)$$

While Ψ_e corresponds to the energy stored in the system, the dissipated energy is represented by the dissipation function Φ. The dissipation function depends only on the rate of the irreversible polarization, and is again defined via a density function

$$\Phi(\dot{\mathbf{P}}^i) = \int_\Omega \phi(\dot{\mathbf{P}}^i) \, dx. \qquad (15.6)$$

We assume that the dissipation function is positively homogeneous, which corresponds to rate-independent behavior (see also [12])

$$\phi(\alpha\dot{\mathbf{P}}^i) = \alpha\phi(\dot{\mathbf{P}}^i) \qquad \text{for all } \alpha \geq 0. \qquad (15.7)$$

With the above ingredients, for any time interval $[t_0, t_1]$, the following incremental optimization problem has to be satisfied

$$\Psi(t_1) - \Psi(t_0) + \int_{t_0}^{t_1} \Phi(\dot{\mathbf{P}}^i)\,\mathrm{d}t + \int_{t_0}^{t_1} P_{\text{ext}}\,\mathrm{d}t \rightarrow \min_{\mathbf{S}(\mathbf{u})} \max_{\mathbf{E}=-\nabla\varphi} \min_{\mathbf{P}^i} \qquad (15.8)$$

Above, the work of external forces $\mathbf{f}$ is included in the external power by defining

$$P_{ext} = \int_{\Omega} \mathbf{f} \cdot \dot{\mathbf{u}}\,\mathrm{d}x. \qquad (15.9)$$

So far, only well-known contributions from the literature have been reviewed. In the following, we propose to use the mechanic enthalpy Ψ_m of the system instead of the electric enthalpy Ψ_e. Then, the dual quantites $\mathbf{T}$ and $\mathbf{D}$ are free variables. The mechanic enthalpy is related to the electric enthalpy via a Legendre transformation in the following way; see e.g. [21]

$$\Psi_m(\mathbf{T}, \mathbf{D}, \mathbf{P}^i) = \min_{\mathbf{S}(\mathbf{u})} \max_{\mathbf{E}=-\nabla\varphi} \Psi_e(\mathbf{S}, \mathbf{E}, \mathbf{P}^i) - \int_{\Omega} \mathbf{T} : \mathbf{S}\,\mathrm{d}x + \int_{\Omega} \mathbf{D} \cdot \mathbf{E}\,\mathrm{d}x. \quad (15.10)$$

In the simple case of potentials quadratic in strain and electric field, this transformation can be computed in the standard way: assume the electric enthalpy density ψ_e is of the standard form

$$\begin{aligned}
\psi_e = {} & \frac{1}{2}(\mathbf{S} - \mathbf{S}^i(\mathbf{P}^i)) : \mathbf{C}_E : (\mathbf{S} - \mathbf{S}^i(\mathbf{P}^i)) \\
& + (\mathbf{S} - \mathbf{S}^i(\mathbf{P}^i)) : \mathbf{e} \cdot \mathbf{E} \\
& - \frac{1}{2}\mathbf{E} \cdot \epsilon_S \cdot \mathbf{E} - \mathbf{P}^i \cdot \mathbf{E} + \psi_i(\mathbf{P}^i)
\end{aligned} \qquad (15.11)$$

where all material moduli $\mathbf{C}^E$, $\mathbf{e}$ and ϵ^S may depend on the remanent polarization state $\mathbf{P}^i$, and where $\psi_i(\mathbf{P}^i)$ denotes an additional hardening term. Then the mechanic enthalpy is given by the relation

$$\begin{aligned}
\psi_m = {} & -\frac{1}{2}\mathbf{T} : \mathbf{S}_D : \mathbf{T} - \mathbf{T} : \mathbf{g} \cdot (\mathbf{D} - \mathbf{P}^i) \\
& + \frac{1}{2}(\mathbf{D} - \mathbf{P}^i) \cdot \beta_T \cdot (\mathbf{D} - \mathbf{P}^i) \\
& - \mathbf{S}^i(\mathbf{P}^i) : \mathbf{T} + \psi_i(\mathbf{P}^i).
\end{aligned} \qquad (15.12)$$

The material moduli are connected to each other via

$$
\begin{aligned}
\mathbf{C}_E &= (\mathbf{S}_E)^{-1}, \\
\mathbf{S}_D &= \mathbf{S}_E - \mathbf{d}^T \cdot \beta_T \cdot \mathbf{d}, \\
\beta_T &= (\epsilon_T)^{-1}, \\
\epsilon_S &= \epsilon_T - \mathbf{d} : \mathbf{C}_E : \mathbf{d}^T, \\
\mathbf{e} &= \mathbf{d} : \mathbf{C}_E, \\
\mathbf{g} &= \beta_T \cdot \mathbf{d}.
\end{aligned}
\tag{15.13}
$$

An optimization problem equivalent to (15.8) can be posed

$$
\Psi_m(t_1) - \Psi_m(t_0) + \int_{t_0}^{t_1} \Phi(\dot{\mathbf{P}}^i)\, dt \ \rightarrow \ \max_{-\operatorname{div}\mathbf{T}=\mathbf{f}} \ \min_{-\operatorname{div}\mathbf{D}=0} \ \min_{\mathbf{P}^i}.
\tag{15.14}
$$

Note that, in comparison to (15.8), the work of external forces $\mathbf{f}$ is now not included in P_{ext}, but

$$
-\operatorname{div}\mathbf{T} = \mathbf{f}
\tag{15.15}
$$

is posed as constraint. Lagrangian multipliers may be introduced enforcing these constraints. We define the Lagrangian $\mathcal{L}$

$$
\mathcal{L}(\mathbf{T}, \mathbf{D}, \mathbf{P}^i, \mathbf{u}, \varphi) = \Psi_m(\mathbf{T}, \mathbf{D}, \mathbf{P}^i) - \int_{\Omega} \mathbf{u} \cdot (\operatorname{div}\mathbf{T} + \mathbf{f})\, dx - \int_{\Omega} \varphi \operatorname{div}\mathbf{D}\, dx.
\tag{15.16}
$$

The corresponding optimization problem for the Lagrangian $\mathcal{L}$ reads

$$
\mathcal{L}(t_1) - \mathcal{L}(t_0) + \int_{t_0}^{t_1} \Phi(\dot{\mathbf{P}}^i)\, dt \ \rightarrow \ \max_{\mathbf{T}} \ \min_{\mathbf{D}} \ \min_{\mathbf{u}} \ \max_{\varphi} \ \min_{\mathbf{P}^i}.
\tag{15.17}
$$

Above, $\mathbf{u}$ and φ have been introduced as Lagrangian multipliers. It shows that indeed they resemble the primal kinematic quantities displacement and electric potential.

15.3 Discretization

15.3.1 Semidiscretization in Time

We consider a discretization of the time interval $[0, T]$ into (not necessarily equal-sized) time steps $\{t_i\}_{i=0\ldots N}$, such that $t_0 = 0$ and $t_N = T$. We propose a time stepping scheme, where we assume at some time t_{n-1} all quantities known. We use

$\mathbf{u}_{n-1} = \mathbf{u}(t_{n-1})$ etc. as an abbreviation. Let $\Delta t = t_n - t_{n-1}$ denote the time step size. Approximating the remanent polarization rate by the quotient $\dot{\mathbf{P}}^i \simeq (\mathbf{P}_n^i - \mathbf{P}_{n-1}^i)/\Delta t$, we observe for positively homogeneous dissipation functions Φ that

$$\int_{t_{n-1}}^{t_n} \Phi(\dot{\mathbf{P}}^i)\, \mathrm{d}t = \Phi(\mathbf{P}_n^i - \mathbf{P}_{n-1}^i). \tag{15.18}$$

The optimization problem corresponding to (15.17) for this time step transforms into the problem of finding $\mathbf{T}_n$, $\mathbf{u}_n$ and $\mathbf{D}_n$, φ_n, $\mathbf{P}_n^i$ such that

$$\mathcal{L}(\mathbf{T}_n, \mathbf{D}_n, \mathbf{P}_n^i, \mathbf{u}_n, \varphi_n) - \mathcal{L}(\mathbf{T}_{n-1}, \mathbf{D}_{n-1}, \mathbf{P}_{n-1}^i, \mathbf{u}_{n-1}, \varphi_{n-1}) + \Phi(\mathbf{P}_n^i - \mathbf{P}_{n-1}^i)$$
$$\rightarrow \max_{\mathbf{T}_n} \min_{\mathbf{D}_n} \min_{\mathbf{u}_n} \max_{\varphi_n} \min_{\mathbf{P}_n^i}. \tag{15.19}$$

Together with a suitable choice of finite element bases, the variation of the above optimization problem leads to a system of nonlinear variational equations, that can be solved by a Newton-Raphson iteration.

15.3.2 Spatial Finite Element Discretization

The finite element discretization of the optimization problem for the Lagrangian (15.19) has to be done with care. Stable families of finite elements have to be chosen for the electric quantities $\mathbf{D}$ and φ as well as the mechanic quantities $\mathbf{T}$ and $\mathbf{u}$. Both pairs have to satisfy an inf-sup condition for the respective divergence operators, which will be discussed in the following.

Below, we assume that $\mathcal{T} = \{T\}$ is a regular finite element mesh of the domain Ω. The mesh $\mathcal{T}$ may contain tetrahedral, prismatic and hexahedral elements, but must be free from hanging nodes. Due to the choice of discretization, flat prismatic or hexahedral elements suitable for the discretization of plates or shells are admissible without additional mechanical locking effects.

15.3.2.1 Discretization of the Electrical Quantities

When analyzing the different terms of the optimization problem (15.19), one notes that different differentiabilities for $\mathbf{D}$ and φ are required as compared to standard problems. The divergence of the dielectric displacement, div $\mathbf{D}$, has to be computed, while no derivatives of the electric potential φ are evaluated. This is a standard feature of mixed methods. In choosing finite elements for $\mathbf{D}$ and φ, two requirements have to be met:

- the dielectric displacement $\mathbf{D}$ has to be divergence conforming, i.e., $D_n = \mathbf{D} \cdot \mathbf{n}$ has to be continuous across element boundaries, and

- dielectric displacement $\mathbf{D}$ and electric potential φ have to satisfy an inf-sup condition, i.e., there exists some constant c independent of the mesh size such that

$$\inf_{\varphi} \sup_{\mathbf{D}} \frac{\int_{\Omega} \varphi \, \mathrm{div} \, \mathbf{D} \, \mathrm{d}x}{\|\mathbf{D}\|_{H(\mathrm{div})} \|\varphi\|_{L^2}} \geq c. \tag{15.20}$$

We will not dwell any longer on these issues. The interested reader is referred to the exhaustive monograph by Boffi, Brezzi, and Fortin [5] for theoretical background on mixed problems. As a first choice, one could use standard mixed finite elements for the electrical quantities

$$\mathbf{D} \in \mathbf{V}_D := \{\mathbf{D} : \mathbf{D}|_T \in [P^k(T)]^3, \, D_n \text{ continuous}\}, \tag{15.21}$$

$$\varphi \in \mathbf{V}_{\varphi} := \{\varphi : \varphi|_T \in P^k(T)\}. \tag{15.22}$$

Using the notation of [5], this is the Brezzi-Douglas-Marini space $\mathcal{BDM}_k$ for the dielectric displacement, as well as a discontinuous polynomial space for the electric potential. In [17], we discussed that the number of degrees of freedom can be reduced significantly if one considers that $\mathrm{div} \, \mathbf{D} = 0$. Although this condition is non-local, Lehrenfeld and Schöberl [8] showed that it is possible to eliminate at least the high-order contributions locally on the element level. They designed a reduced set of basis functions, such that the $\mathrm{div} \, \mathbf{D}$ is at most constant per element. For this reduced set of basis functions, a smaller number of Lagrangian multipliers (i.e. electric potential φ basis functions) is necessary to enforce $\mathrm{div} \, \mathbf{D} = 0$. The finite element spaces are reduced to

$$\mathbf{D} \in \mathbf{V}_{D,red} := \{\mathbf{D} : \mathbf{D}|_T \in [P^k(T)]^3, \, \mathrm{div} \, \mathbf{D}|_T \in P^0(T), \, D_n \text{ continuous}\}, \tag{15.23}$$

$$\varphi \in \mathbf{V}_{\varphi,red} := \{\varphi : \varphi|_T \in P^0(T)\}. \tag{15.24}$$

15.3.2.2   Discretization of the Mechanical Quantities

In a mixed method comparable to Sect. 15.3.2.1, one would expect stress elements with continuous stress vector $\mathbf{T}_n = \mathbf{T} \cdot \mathbf{n}$ at element interfaces, whereas the displacement vector is allowed to be discontinuous. Such methods are difficult to design, but usually free from shear locking. For an overview on the mathematical properties of mixed methods in elasticity; see [5].

In the current contribution, we use the mixed finite element method introduced by Pechstein and Schöberl in [13]. There, only the normal component of the stress vector $T_{nn} = \mathbf{n} \cdot \mathbf{T} \cdot \mathbf{n}$ is continuous, which makes it easier to design conforming symmetric finite element basis functions. Complementarily, the tangential component of the displacement vector $\mathbf{u}_t = \mathbf{u} - (\mathbf{u} \cdot \mathbf{n})\mathbf{n}$ is continuous, and gaps between elements

may open up only in normal direction. For straight simplicial elements, the finite element spaces are

$$\mathbf{T} \in \mathbf{V}_T := \{\mathbf{T} : \mathbf{T}|_T \in [P^k(T)]_{sym}^{3\times 3}, T_{nn} \text{ continuous}\}, \tag{15.25}$$

$$\mathbf{u} \in \mathbf{V}_u := \{\mathbf{u} : \mathbf{u}|_T \in [P^k(T)]^3, \mathbf{u}_t \text{ continuous}\}. \tag{15.26}$$

For prismatic, hexahedral or curved elements, the definition of the spaces is more complex and addressed in [10, 14].

As such, the stress tensor is not divergence conforming. In other words, the work pair

$$\int_{\Omega} \operatorname{div} \mathbf{T} \cdot \mathbf{u} \, dx \tag{15.27}$$

cannot be evaluated as an integral, but has to be understood in distributional sense. It contains volume terms on each element, and additionally element boundary terms including the jumping tangential component of the stress vector $\mathbf{T}_{nt} = \mathbf{T} \cdot \mathbf{n} - (\mathbf{n} \cdot \mathbf{T} \cdot \mathbf{n})\mathbf{n}$. For a thorough discussion, we refer to the earlier works [13, 15]. For completeness, we provide the definition of the distributional divergence operator for the tangential continuous finite element function $\mathbf{u}$ and normal-normal continuous $\mathbf{T}$ by

$$\langle \operatorname{div} \mathbf{T}, \mathbf{u} \rangle_{\Omega} := \sum_{T \in \mathcal{T}} \left(\int_T \operatorname{div} \mathbf{T} \cdot \mathbf{u} \, dx - \int_{\partial T} \mathbf{T}_{nt} \cdot \mathbf{u}_t \, ds \right) \tag{15.28}$$

$$= -\sum_{T \in \mathcal{T}} \left(\int_T \mathbf{S}(\mathbf{u}) : \mathbf{T} \, dx - \int_{\partial T} T_{nn} u_n \, ds \right) = -\langle \mathbf{S}(\mathbf{u}), \mathbf{T} \rangle_{\Omega}. \tag{15.29}$$

Note that, also in this distributional sense, divergence and strain operator are dual. In both (15.28) and (15.29), on the element interfaces, the continuous finite element function ($\mathbf{u}_t$ or T_{nn}, respectively) acts as a Lagrangian multiplier enforcing continuity of their discontinuous counterpart ($\mathbf{T}_{nt}$ or u_n, respectively).

15.3.2.3   Discretization of the Remanent Polarization

The remanent polarization can be discretized in a completely independent way. It does not need to satisfy any continuity assumptions, as no derivatives of $\mathbf{P}^i$ occur in the variational equations. To be of consistent order, we propose to use piecewise polynomial elements for $\mathbf{P}^i$ that are of the same order as the dielectric elements,

$$\mathbf{P}^i \in \mathbf{V}_P := \{\mathbf{P}^i : \mathbf{P}^i|_T \in [P^k(T)]^3\}. \tag{15.30}$$

15.4   Numerical Results

We present a benchmark example taken from Semenov et al. [20]. A quadratic plate of size $l = 20\text{mm} \times 20\text{mm}$ and thickness $h = 6\text{mm}$ has a circular hole of diameter $d = 4\text{mm}$ through its center. Choosing the xy plane as the in-plane direction, it is electroded at $x = 0$ and $x = l$. By applying a potential of $\pm\varphi_0 = \pm15000\text{V}$ to the electrodes an electric field is induced in in-plane x direction. Singularities evolve around the circular hole. Due to symmetry, only one eigth of the plate is modeled by finite elements.

The plate is made from PZT-5H, which is modeled in the following way using the parameters from Table 15.1: the mechanic enthalpy is chosen as in (15.12). Electric permittivity at constant stress $\beta_T = 1/\epsilon_T \mathbf{I}$ is assumed isotropic constant. The piezo-electric tensor $\mathbf{d}$ depends on the remanent polarization as in [7], such that it reflects the d_{31} and d_{33} effect. The flexibility at constant dielectric displacement is chosen as

$$\mathbf{S}_D = \mathbf{S}(Y_E, \nu) - 0.6\,\mathbf{d}^T \cdot \beta_T \cdot \mathbf{d}, \tag{15.31}$$

as for this choice

$$\mathbf{S}_E = \mathbf{S}_D + \mathbf{d}^T \cdot \beta_T \cdot \mathbf{d} \tag{15.32}$$

is close to the anisotropic tensor found in material databases. There, $\mathbf{S}(Y_E, \nu)$ denotes the standard isotropic flexibility tensor for given Young's modulus Y_E and Poisson ratio ν. Concerning ferroelectric hardening and saturation, the additive energy ψ_i in (15.12) is chosen such that its derivative is

$$\psi_i'(\mathbf{P}^i) = \tilde{\psi}_i'(|\mathbf{P}^i|)\frac{\mathbf{P}^i}{|\mathbf{P}^i|}$$
$$\text{with} \quad \tilde{\psi}_i'(r) = \frac{h_0 P_0^m}{2(m-1)} \left((P_0 - r)^{1-m} - (P_0 + r)^{1-m}\right) \tag{15.33}$$

The remanent polarization strain, that depends fully on the remanent polarization, is given as proposed by McMeeking and Landis [9]

$$\mathbf{S}(\mathbf{P}^i) = \frac{3}{2}\frac{S_0}{P_0^2}\left(\mathbf{P}^i\mathbf{P}^i - \frac{1}{3}(\mathbf{P}^i \cdot \mathbf{P}^i)\mathbf{I}\right). \tag{15.34}$$

Finally, the dissipation function contains the coercive electric field, and describes the onset of switching. Its density is defined as

$$\phi(\dot{\mathbf{P}}^i) = E_0|\dot{\mathbf{P}}^i|. \tag{15.35}$$

This choice is motivated in detail in [16]. As discussed in [17], the additive energy ψ_i and the dissipation function are regularized by a small parameter $\varepsilon = 10^{-4}P_0$.

Table 15.1 Material parameters for PZT-5H, see also [20]

Young's modulus Y_E	$61 \times 10^9 \mathrm{Nm}^{-2}$
Poisson ratio ν	0.31
el. permittivity ϵ_T	$2.77 \times 10^{-8} \mathrm{Fm}^{-1}$
Piezoelectric d_{31}	$2.74 \times 10^{-10} \mathrm{mV}^{-1}$
Piezoelectric d_{33}	$5.93 \times 10^{-10} \mathrm{mV}^{-1}$
Coercive electric field E_0	$820 \times 10^3 \mathrm{Vm}^{-1}$
Hardening parameter h_0	$714 \times 10^3 \mathrm{mF}^{-1}$
Saturation polarization P_0	$0.24 \mathrm{Cm}^{-2}$
Saturation strain S_0	9.3×10^{-3}
Shape parameter m	1.4

The additive energy is modified such that its second derivative of ψ_i stays bounded as $|\mathbf{P}^i|$ approaches saturation, whereas the dissipation function is approximated by a differentiable function. We use

$$\psi'_{i,\varepsilon}(\mathbf{P}^i) = \begin{cases} \psi'_i(\mathbf{P}^i) & \text{if } |\mathbf{P}^i| \leq P_0 - \varepsilon, \\ (\tilde{\psi}'_i(P_0 - \varepsilon) + \tilde{\psi}''_i(P_0 - \varepsilon)(|\mathbf{P}^i| - \varepsilon + P_0))\frac{\mathbf{P}^i}{|\mathbf{P}^i|} & \text{if } |\mathbf{P}^i| > P_0 - \varepsilon \end{cases},$$
(15.36)

$$\phi_\varepsilon = E_0\sqrt{|\mathbf{P}^i|^2 + \varepsilon^2}.$$
(15.37)

In the original reference [20], the voltage was raised from zero to 15000V in several load steps. For our formulation, we found that we could use as little as four load steps and still observe convergence of a Newton iteration with linesearch. Note that such a low number of load steps may impede accuracy in case of non-proportional loading. However, in the present benchmark the focus lies on iteration numbers and maximum loadstep size. In Table 15.2, we present the iteration counts for different finite element orders, using prismatic meshes.

For the first three results, there was no refinement of the prismatic mesh in thickness z-direction, resulting in an overall count of 95 elements. For the latter three results, we used three elements over thickness, see e.g. Fig. 15.1 for the two different discretzations. We compare our values to the counts given by [20], where one layer of hexahedral elements was used.

To highlight the accuracy of the method, we compare the results for the lowest resolution (one layer of finite elements of order $k = 1$) to the highest resolution (three layers of order $k = 3$). In the former case, the mesh consisted of 95 elements, 10 184 overall degrees of freedom were obtained, of which 2 864 were coupling, while in the latter case we had 179 631 degrees of freedom of which 35 931 were coupling. Figure 15.1 shows the remanent polarization $|\mathbf{P}^i|$ at $\Delta V = 15000$V, and Fig. 15.2 shows the corresponding electric field.

Table 15.2 Iteration counts for the plate with hole

	5000 V	8000 V	10000 V	15000 V
Semenov [20]	5	6	27 (5 incr)	29 (6 incr)
One layer				
$k = 1$	8	11	29	27
$k = 2$	10	12	39	28
$k = 3$	14	14	48	31
Three layers				
$k = 1$	9	13	32	26
$k = 2$	10	16	34	29
$k = 3$	14	14	47	44 (2 incr)
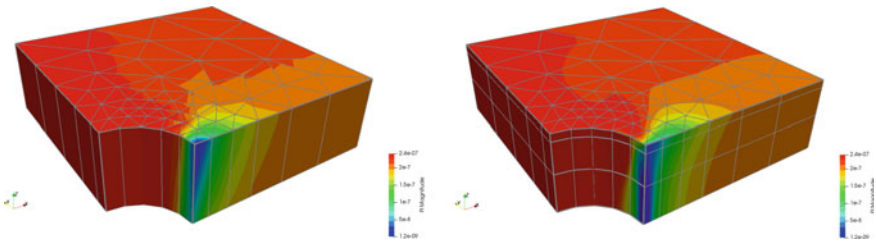
Fig. 15.1 Remanent polarization $|\mathbf{P}^i|$ (unit MC/m^2) for the coarsest discretization (one layer of prismatic elements of order $k = 1$) and the finest discretization (three layers of elements of order $k = 3$)
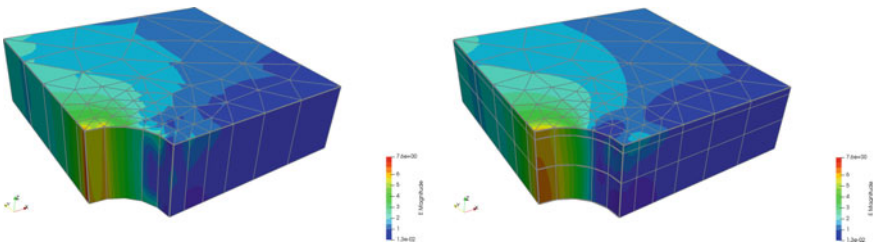
Fig. 15.2 Electric field $|\mathbf{E}|$ (unit MV/m) for the coarsest discretization (one layer of prismatic elements of order $k = 1$) and the finest discretization (three layers of elements of order $k = 3$)

In Figs. 15.3 and 15.4, the longitudinal stress component T_{xx} as well as the in-plane shear stress component T_{xy} are depicted. Note that in all plots, no stress reconstruction or smoothing was done, the fields are displayed directly as they were computed. The absolute value of the electric field over the central line $x = 0$, $y \in [2, 10 \, \text{mm}]$, $z = 0$ is displayed in Fig. 15.5.
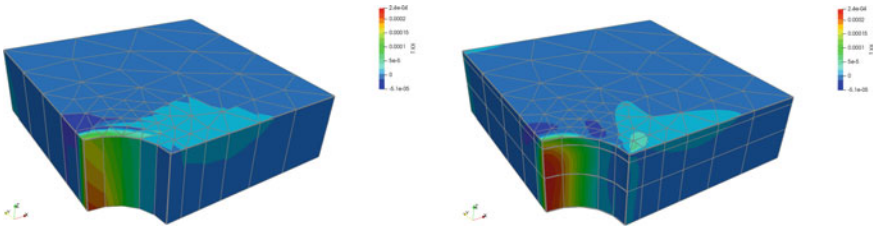
Fig. 15.3 Longitudinal stress component T_{xx} (unit N/(μm)^2) for the coarsest discretization (one layer of prismatic elements of order $k = 1$) and the finest discretization (three layers of elements of order $k = 3$)

Fig. 15.4 In-plane shear stress component T_{xy} (unit N/(μm)^2) for the coarsest discretization (one layer of prismatic elements of order $k = 1$) and the finest discretization (three layers of elements of order $k = 3$)
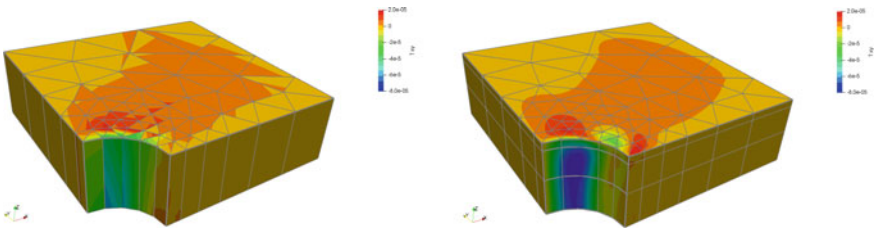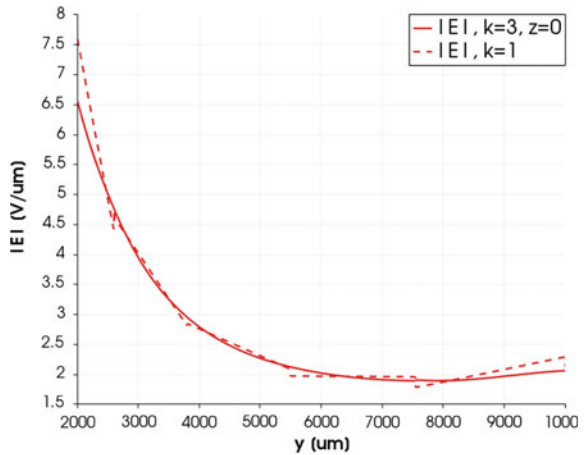
Fig. 15.5 Absolute value of the electric field $|\mathbf{E}|$ over the central line $x = 0$, $y \in [2, 10\,\text{mm}]$, $z = 0$ for the two different discretizations with $k = 1$ and $k = 3$

15.5 Conclusion

A finite element method for a mechanic enthalpy-based model of the ferroelectric polarization process has been presented. In such a model, dielectric displacement and stress are the primary unknowns. Two stable pairs of mixed finite elements were chosen to discretize the model. For the electric quantities, divergence-conforming dielectric elements are proposed, such that Gauss' law of zero charges is satisfied exactly. Taking this law into account, the total number of degrees of freedom could even be reduced, choosing only basis functions with at most constant divergence. For the mechanic quantities, mixed TDNNS elements are used, as they have been shown to be free from shear locking when using flat elements in thin layers of piezoelectric structures. By way of a numerical benchmark example, robustness of the method with respect to large load increments is shown.

References

1. Bassiouny, E., Ghaleb, A., Maugin, G.: Thermodynamical formulation for coupled electromechanical hysteresis effects–I: basic equations. Int. J. Eng. Sci. **26**(12), 1279–1295 (1988)
2. Bassiouny, E., Ghaleb, A., Maugin, G.: Thermodynamical formulation for coupled electromechanical hysteresis effects–II: poling of ceramics. Int. J. Eng. Sci. **26**(12), 1297–1306 (1988)
3. Bassiouny, E., Maugin, G.: Thermodynamical formulation for coupled electromechanical hysteresis effects–III: parameter identification. Int. J. Eng. Sci. **27**(8), 975–987 (1989)
4. Bassiouny, E., Maugin, G.: Thermodynamical formulation for coupled electromechanical hysteresis effects–IV: combined electromechanical loading. Int. J. Eng. Sci. **27**(8), 989–1000 (1989)
5. Boffi, D., Brezzi, F., Fortin, M.: Mixed finite element methods and applications. Springer Series in Computational Mathematics, vol. 44. Springer, Heidelberg (2013)
6. Klinkel, S.: A phenomenological constitutive model for ferroelastic and ferroelectric hysteresis effects in ferroelectric ceramics. International Journal of Solids and Structures **43**(22–23), 7197–7222 (2006)
7. Landis, C.: Fully coupled, multi-axial, symmetric constitutive laws for polycrystalline ferroelectric ceramics. Journal of the Mechanics and Physics of Solids **50**(1), 127–152 (2002)
8. Lehrenfeld, C., Schöberl, J.: High order exactly divergence-free hybrid discontinuous galerkin methods for unsteady incompressible flows. Computer Methods in Applied Mechanics and Engineering **307**, 339–361 (2016)
9. McMeeking, R., Landis, C.: A phenomenological multi-axial constitutive law for switching in polycrystalline ferroelectric ceramics. International Journal of Engineering Science **40**(14), 1553–1577 (2002)
10. Meindlhumer, M., Pechstein, A.: 3D mixed finite elements for curved, flat piezoelectric structures. Int. J. Smart Nano Mater. **10**(4), 249–267 (2019). https://doi.org/10.1080/19475411.2018.1556186
11. Meindlhumer, M., Pechstein, A., Humer, A.: Variational inequalities for ferroelectric constitutive modelling. J. Intell. Mater. Syst. Struct. **32**(3), 317–330 (2021). https://doi.org/10.1177/1045389X20951252

12. Miehe, C., Rosato, D., Kiefer, B.: Variational principles in dissipative electro-magneto-mechanics: A framework for the macro-modeling of functional materials. International Journal for Numerical Methods in Engineering **86**(10), 1225–1276 (2011)
13. Pechstein, A., Schöberl, J.: Tangential-displacement and normal-normal-stress continuous mixed finite elements for elasticity. Math. Models Methods Appl. Sci. 21(8), 1761–1782 (2011)
14. Pechstein, A., Schöberl, J.: Anisotropic mixed finite elements for elasticity. Int. J. Numer. Methods Engrg. 90(2), 196–217 (2012)
15. Pechstein, A.S., Meindlhumer, M., Humer, A.: New mixed finite elements for the discretization of piezoelectric structures or macro-fiber composites. J. Intell. Mater. Syst. Struct. **29**(16), 3266–3283 (2018). https://doi.org/10.1177/1045389X18781026
16. Pechstein, A.S., Meindlhumer, M., Humer, A.: The polarization process of ferroelectric materials in the framework of variational inequalities. ZAMM - J. Appl. Math. Mech. [Zeitschrift für Angewandte Mathematik und Mechanik] **100**(6), e201900329 (2020). https://doi.org/10.1002/zamm.201900329. https://onlinelibrary.wiley.com/doi/abs/10.1002/zamm.201900329
17. Pechstein, A.S., Meindlhumer, M., Humer, A.: High-order mixed finite elements for an energy-based model of the polarization process in ferroelectric materials. J. Intell. Mater. Syst. Struct. **32**(3), 355–368 (2021). https://doi.org/10.1177/1045389X20953895
18. Sands, C.M., Guz, I.A.: Unidimensional model of polarisation changes in piezoelectric ceramics based on the principle of maximum entropy production. Journal of Engineering Mathematics **78**(1), 249–259 (2013)
19. Schröder, J., Romanowski, H.: A thermodynamically consistent mesoscopic model for transversely isotropic ferroelectric ceramics in a coordinate-invariant setting. Archive of Applied Mechanics **74**(11–12), 863–877 (2005)
20. Semenov, A., Liskowsky, A., Balke, H.: Return mapping algorithms and consistent tangent operators in ferroelectroelasticity. International Journal for Numerical Methods in Engineering **81**(10), 1298–1340 (2010)
21. Tichỳ, J., Erhart, J., Kittinger, E., Privratska, J.: Fundamentals of piezoelectric sensorics: mechanical, dielectric, and thermodynamical properties of piezoelectric materials. Springer Science & Business Media (2010)
22. Voigt, W.: Lehrbuch der Kristallphysik (mit Ausschluß der Kristalloptik). Teubner Leipzig (1910)

Chapter 16
Theory of Critical Distances as a Method of Failure Prediction Under Dynamic Loading

Oleg A. Plekhov, Alena I. Vedernikova, and Anastasiia A. Kostina

Abstract The linear-elastic Theory of Critical Distances (TCD) is reformulated to make it suitable for estimating the strength of notched components subjected to dynamic loading. The theory modification in case of elasto-plastic stress–strain behavior to enhance accuracy of strength assessment is presented. The efficiency of the proposed methodologies is demonstrated for the experimental data on notched Grade 2 specimens that were subjected to uniaxial tensile loads within the rate range of 10^{-3}–$10^4\,s^{-1}$. The obtained results showed that the modification of the TCD based on elasto-plastic analysis gives estimates that fall within an error interval of ±5–10%, more accurate predictions than the linear-elastic solution. The physical meaning of the critical distance theory, in particular, the values of the critical distances L and inherent material strength σ_0, on the base of the original statistical thermo-dynamical model of evolution of an ensemble of defects in metals developed by Naimark (2003) in ICMM UB RAS is proposed. It has been observed that the critical distance value can be considered as a fundamental length scale of dissipative structure developing in a blow-up regime.

16.1 Introduction

The Theory of Critical Distances (TCD) is an effective tool developed by Taylor [12], allowing the strength of components with geometrical discontinuities (cracks, notches, holes) to be estimated accurately by directly post-processing the entire linear-elastic stress fields in the vicinity of the stress concentrators. According to the Theory of Critical Distances, failure occurs when an equivalent stress calculated either at a certain distance from the notch tip, either averaged at the some distance or area, becomes larger than the inherent material strength σ_0. These are the central ideas of TCD that are an extension of the approaches developed by Neuber [4], Novozhilov [5], Peterson [6], Whitney and Nuismer [14], and Pluvinage [7] to estimate the

O. A. Plekhov · A. I. Vedernikova (✉) · A. A. Kostina
Institute of Continuous Media Mechanics of the UB RAS, Perm, Russia
e-mail: terekhina.a@icmm.ru

strength of notched metallic materials. Recently, it was also proven that the TCD is successful in estimating the static [10, 11], fatigue [1, 9, 13], and dynamic strength [15, 16] of both ductile and brittle notched components.

The first part of this work is devoted to the verification TCD reformulation for notched Grade 2 specimens at the strain rates of 10^{-3}–$10^4 s^{-1}$ [16]. The dynamic TCD based on the simple power laws expression for the inherent strength and critical distance with regard to the strain rate and uses the post-process the linear-elastic stress fields near the assumed crack initiation locations.

The second part of work is aimed to modification of the Theory of Critical Distance in case of elasto-plastic material behavior to enhance the accuracy of the fracture assessment of notched components.

The second part of work is aimed to modification of the Theory of Critical Distance in case of elasto-plastic material behavior to enhance the accuracy of the fracture assessment of notched components.

The final part of the work is devoted to the physical interpretation of the effective length and inherent strength parameters, which is still an issue of fracture mechanics and generally found empirically.

16.2   Extending TCD to Dynamic Loading

16.2.1   Critical Distance Concept for the Dynamic Loading

The TCD postulates that the notched component under Mode I static loading being designed does not fail as long as the following condition is assured [12]

$$\sigma_{eff} \leq \sigma_0, \tag{16.1}$$

where σ_{eff} is the effective stress determined according to one of the methods of the theory of critical distances, σ_0 is the inherent material strength. If the TCD is used to perform the assessment of brittle notched materials, σ_0 can be taken equal to the material ultimate tensile strength σ_{UTS} [12], as far as for ductile materials, σ_0 is determined by testing of specimens with different notch sharpness [10].

Much experimental evidence [15] suggests that the dependence of the dynamic strength of metal alloys on the strain rate can be summarized by adopting simple power laws. The reformulation of the Theory of Critical Distances to dynamic loading is based on the following hypothesis: since both the dynamic failure stress σ_f and dynamic fracture toughness K_{Id} vary as applied strain rate $\dot{\varepsilon}$ increases, we assume that in the same way the also the inherent material stress σ_0 depends on the strain rate, and hence the value of the critical distance L. Mathematically, the hypothesis is formulated as follows:

$$\begin{cases} \sigma_f = f_{\sigma_f}(\dot{\varepsilon}) = a_f \dot{\varepsilon}^{b_f} \\ K_{Id} = f_{K_{Id}}(\dot{\varepsilon}) = \alpha \dot{\varepsilon}^{\beta} \end{cases} \Rightarrow \begin{cases} \sigma_0 = f_{\sigma_0}(\dot{\varepsilon}) = a_0 \dot{\varepsilon}^{b_0} \\ L = f_L(\dot{\varepsilon}) = \frac{1}{\pi}\left[\frac{K_{Id}}{\sigma_0}\right] = \frac{1}{\pi}\left[\frac{\alpha \dot{\varepsilon}^{\beta}}{a_0 \dot{\varepsilon}^{b_0}}\right] = M \dot{\varepsilon}^N \end{cases}, \quad (16.2)$$

where $\dot{\varepsilon}$ is strain rate, $a_f, b_f, \alpha, \beta, a_0, b_0, M, N$ are material constants to be determined by running appropriate experiments.

According to the Theory of Critical Distances, the dynamic effective stress σ_{eff} to perform the dynamic assessment has to be determined according to the Point method (PM), the Line method (LM) or the Area method (AM) [16]

$$\sigma_{eff} = \sigma_y\left(\theta = 0, r = \frac{L}{2}\right), \quad (16.3)$$

$$\sigma_{eff} = \frac{1}{2L}\int_0^{2L} \sigma_y(\theta = 0, r)\mathrm{d}r, \quad (16.4)$$

$$\sigma_{eff} = \frac{2}{\pi L^2}\int_{-\pi/2}^{\pi/2}\int_0^L \sigma_1(\theta, r)r\mathrm{d}r\mathrm{d}\theta, \quad (16.5)$$

where σ_y is stress parallel to axis y, σ_1 is maximum principal stress, L is critical distance, (θ, r) are polar coordinates.

16.2.1.1 Experimental Details

The accuracy and reliability of the proposed reformulation of the TCD was checked against a set of experimental results generated by testing, under different strain rates, specimens of titanium alloy Grade 2 containing notches of different sharpness. Quasi-static tensile tests were carried out with an electromechanical testing machine Shimadzu AG-X Plus (300 kN). A Hopkinson-Kolsky Split Bar was used to study the high strain-rate material properties. The tensile tests were carried out in the strain-rate range of 10^{-3}–$10^4 s^{-1}$. Measurement of strain during materials testing was carried out using video extensometer TRViewX240S f12.5. Three types of cylindrical specimens with different stress concentrators such as semi-circular edge notches with radius 1 and 2 mm, V-shaped notches (notch root radius 0.1 mm), and un-notched (plain) specimens were used.

16.2.1.2 Validation by Experimental Data

The linear-elastic stress fields in the vicinity of the notches being investigated were determined numerically by using commercial Finite Element (FE) software ABAQUS.
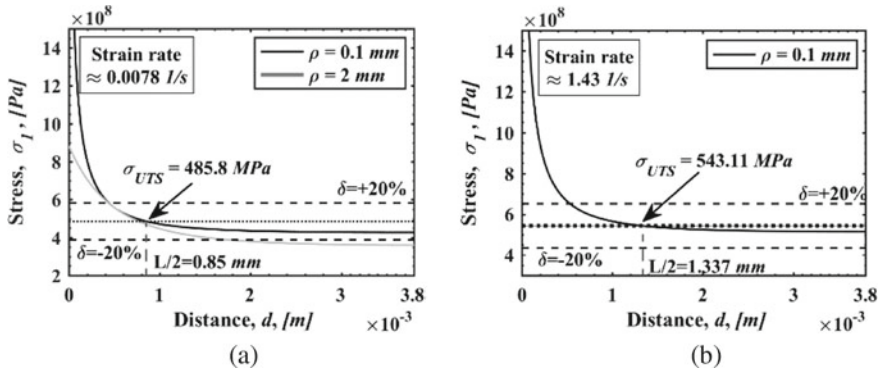
Fig. 16.1 Local linear-elastic stress fields under 0.0078/s (**a**) and 1.43/s (**b**) for notched Grade 2
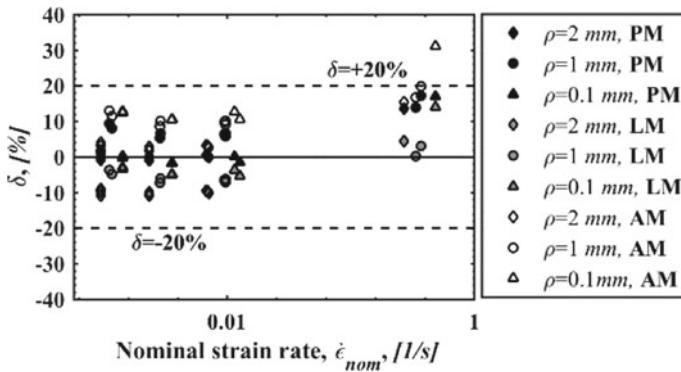
Fig. 16.2 Accuracy of the TCD reformulation in the strength predicting for notched Grade 2

Since the tested titanium alloy Grade 2 specimen were characterized by a mechanical behavior that was predominantly brittle, the hypothesis was formed that inherent material strength could be taken equal to the ultimate tensile stress. After that, the σ_0 versus $\dot{\varepsilon}_{nom}$ relationship was expressed by adopting a simple power law

$$\sigma_0 = 538.968 \dot{\varepsilon}_{nom}^{0.0214} [\text{MPa}], \tag{16.6}$$

Figure 16.1a shows the linear-elastic stress-distance curves plotted under quasi-static loading for Grade 2 specimens. This diagram fully confirms that, for this material, the inherent material strength σ_0 could be taken as equal to σ_{UTS} with little loss of accuracy. Figure 16.1b resulted a critical distance value for Grade 2 at a higher strain rate. The function $L = f_L(\dot{\varepsilon})$ was derived

$$L = 2.592 \dot{\varepsilon}_{nom}^{0.0869} [\text{mm}], \tag{16.7}$$

By making use of power laws (16.6), (16.7), the effective stress σ_{eff} was evaluated according to the Eqs. 16.3–16.5. The results are summarized in the Fig. 16.2, where error was calculated as

$$\delta = \frac{\sigma_{eff} - \sigma_0}{\sigma_0}[\%], \tag{16.8}$$

This validation exercise has demonstrated that the proposed reformulation of the TCD is capable of accurately assessing the static and dynamic strength of notched specimens from titanium alloy Grade 2, with the estimates falling within an error interval of $\pm 20\%$.

16.3   Theory of Critical Distances Based on Elasto-plastic Analysis

16.3.1   The Simplified Johnson-Cook Model

In this part of work, a simplified Johnson-Cook law in a form of (16.9) is used to model the material response, taking into consideration the changes in the strain rate. To determine the value of the critical distance, elasto-plastic stress fields will be used. The adoption of these measures is conditioned by the fact that the material behavior being, by nature, highly nonlinear and cannot be described in the framework of the linear theory of elasticity.

$$\sigma = (A + B\varepsilon^n)\left(1 + Cln\frac{\dot{\varepsilon}}{\dot{\varepsilon}_0}\right), \tag{16.9}$$

where A, B, n, and C are material constants, $\dot{\varepsilon}_0$ is reference strain rate. In the Johnson-Cook constitutive model, the combined two key material responses are strain hardening and strain-rate effects. The adiabatic heating effect is considered negligible for the tension tests, as the material necks down at relatively low strains before any significant adiabatic heating. All the materials constants could be obtained from the fitting equations (16.9) with experimental data obtained under different strain rates. The material parameters for titanium alloy Grade 2: A = 363.1 MPa, B = 389.89 MPa, n = 0.435, and C = 0.0176.

16.3.2   Using the TCD by Post-processing the Elasto-plastic Stress Fields

The strength estimation algorithm remained similar to the previous case. Mises stress field distributions at the cross section away from the notch tip at the time requiring to calculation of the value of the critical distance and the effective stress according to the TCD were determined. The cylindrical un-notched specimens and specimens with sharp stress concentrators under different strain rates were used for determining the values of the critical distance. The value of the critical distance for different strain rates is constant, which is equal to 0.24 mm (Fig. 16.3), while with linear-elastic analysis, the critical distance is a function of the strain rate.

Using value of critical distance equal to 0.24 mm, the effective stress for notched specimens under different strain rates according to the Point and Line Methods of the Theory of Critical Distances were calculated. The results of this analysis are summarized in Fig. 16.4.

The results showed that the use of modification of the TCD based on elasto-plastic analysis gives us estimates falling within an error band of ±5–10%, that more accurate predictions than the linear-elastic TCD solution. The use of an improved
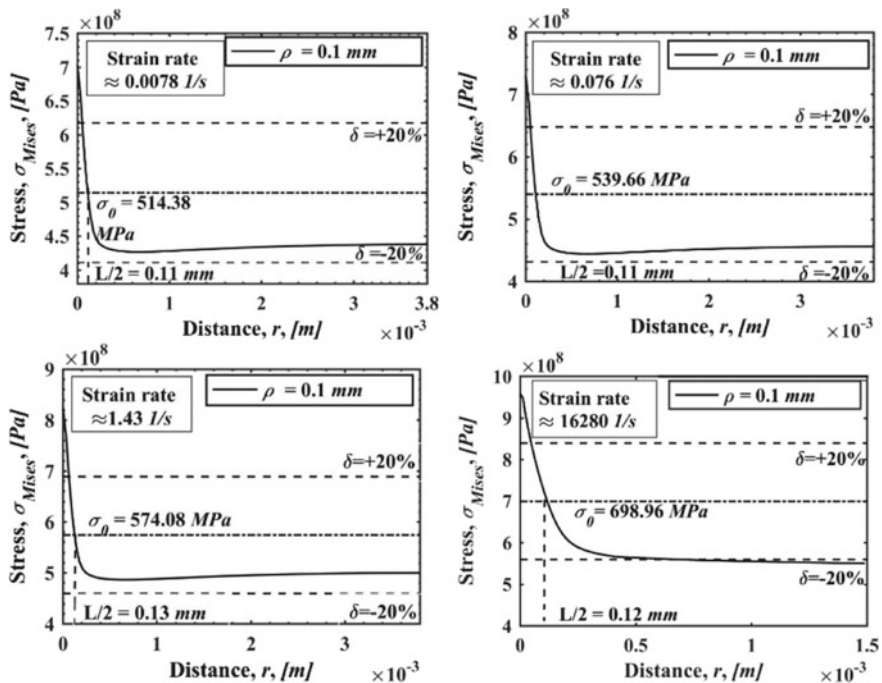
Fig. 16.3 Local elasto-plastic stress fields under different strain rates
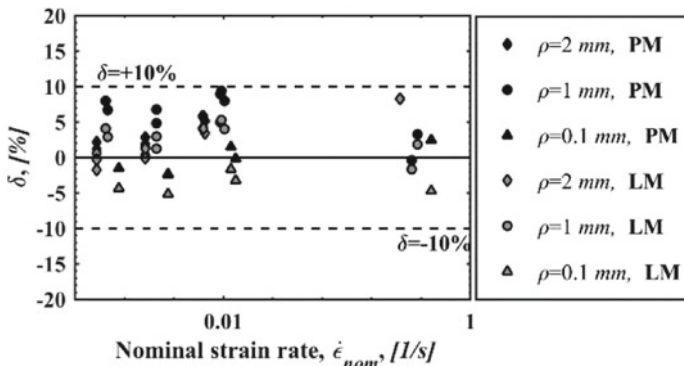
Fig. 16.4 Accuracy of the TCD based on elasto-plastic analysis in predicting the strength

description of the stress–strain state at the notch tip allows introducing the critical distances as a material parameter.

16.4 Physical Explanation of the Critical Distance Theory

16.4.1 Mathematical Model of Damage to Fracture Transition

Accounting of plastic deformation, which allows one to switch from the function of the critical distance of the strain rate to the material constant, makes it possible to introduce the hypothesis about critical distance as the fundamental length of the dissipative structure in the ensemble of defects, which develops in the blow-up regime. The description of the evolution of the ensemble of defects near the stress concentrator based on original statistical thermo-dynamical model of evolution of an ensemble of defects in metals, developed at ICMM UB RAS [3].

The constitutive equation for structural strain (deformation caused by the appearance of defects) has the form

$$\dot{\mathbf{p}} = \Gamma_p \left(\boldsymbol{\sigma} - \rho \frac{\delta F}{\delta \mathbf{p}} \right) + \Gamma_{p\sigma} \boldsymbol{\sigma}, \tag{16.10}$$

where $\Gamma_p, \Gamma_{p\sigma}$ are kinetic coefficients, F is specific Helmholtz free energy, $\mathbf{p}$ is defect density tensor (structural-sensitive parameter), $\boldsymbol{\sigma}$ is stress tensor, and ρ is volumetric mass.

The approximation of function $\boldsymbol{\sigma} - \rho \frac{\delta F}{\delta \mathbf{p}}$, which determines equilibrium state of material with defects in the one-dimensional case [2]

$$Z - \frac{\delta \Psi}{\delta p} = \frac{\sigma}{\sigma_{\max}} - ap + qp^\beta + \bar{\nabla} \cdot \left(kp^s \left(\bar{\nabla} p\right)\right), \qquad (16.11)$$

where $\sigma_{\max}$ is maximum value of the stress tensor component near the concentrator, β, s are degree of polynomials that determines the character of generation and the rate of diffusion of defects, q, k, a—material parameters, Z, Ψ—dimensionless stress and free energy corresponding.

The self-similar solution of Eq. (16.10) in the one-dimensional case with approximation (16.11) for constant stress values and parameters $\beta = s + 1$ can be written as [8]

$$p(x, t) = (q(t - t_c))^{-\frac{1}{s}} \left(\frac{2(s + 1)}{s(s + 2)} \sin^2 \left[\frac{\pi x}{L_c}\right]\right)^{\frac{1}{s}}, \qquad (16.12)$$

where t_c—the critical time of and L_c—the fundamental length scale.

The time of structure localization is estimated according to the relation

$$t_c = \frac{2(s + 1)}{s(s + 2)} \frac{1}{p^s q}, \qquad (16.13)$$

The fundamental length scale is defined by the following expression:

$$L_c = 2\frac{\pi}{s} \sqrt{s + 1} \sqrt{\frac{k}{q}}. \qquad (16.14)$$

Equations (16.10)–(16.14) used for the explanation of the fracture mechanisms near stress concentrators of the titanium alloy Grade 2 under tensile loading.

16.4.2 Application of the Proposed Model in One-Dimensional Case

For the explanation of the fracture mechanisms near stress concentrators, consider an analytical solution for stress at round-tip notch. In case of infinite plate with semi-circular notch (notch root radius r_n) under tensile, the stress components can be evaluated as [17]

$$\sigma_y(x, 0) = \frac{K_t \sigma_\infty}{3} \left(1 + \frac{1}{2} \left(\frac{x}{r_n} + 1\right)^{-2} + \frac{3}{2} \left(\frac{x}{r_n} + 1\right)^{-4}\right), \qquad (16.15)$$

where K_t—stress concentration factor, σ_∞—nominal stress.
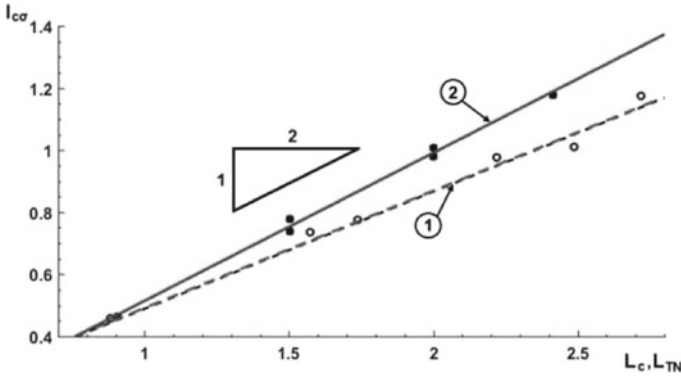
Fig. 16.5 Relations between analytically estimated fundamental length of dissipative structures L_c and spatial scale $l_{c\sigma}$ (line 1), numerically estimated fundamental length L_{TN} and spatial scale $l_{c\sigma}$

The Eqs. (16.11), (16.15) with initial condition $p_y(x, t) \mid_{t=0} = 0$ and boundary conditions $p_y(x, t) \mid_{x=0} = 0$, $\frac{\delta p_{yy}(x,t)}{\delta x} \mid_{x\to+\infty}$ were solved numerically for different value of nominal stress (model material).

The analysis of numerical simulation allows to conclude that the failure process (initiation of dissipative structure) requests a simultaneous fulfillment of two conditions: the stress should be bigger than critical value σ_0 (inherent material strength) in some area near the stress concentrator and the length of this area should be bigger than some critical spatial scale $l_{c\sigma}$ $((\exists l \geq l_{c\sigma})) : (\forall x \in [0, 1]), \sigma_y(x) > \sigma_0$.

Figure 16.5 presents a relations between the analytical estimation of spatial scale of dissipative structure by Eq. (16.14) (L_c) and scale $l_{c\sigma}$, numerically obtained value of fundamental length (L_{TN}) and scale $l_{c\sigma}$. The points represent simulation results for set of parameters β and s. Analysis of the data presented in Fig. 16.5 allow to conclude that the analytical assessment gives an overestimation of the localization scale. The estimation of the fundamental length scale by the results of numerical simulation gives the exact ratio corresponding to the result of the Theory of Critical Distances: the critical stress must be achieved at the half of the fundamental length of the dissipative structure

$$l_{c\sigma} = \frac{1}{2} L_{TN} \tag{16.16}$$

16.4.3 Application of the Proposed Model in Three-Dimensional Case

Consider the link between the critical distance and fundamental length scale of dissipative structure using quasi-static tension of the U-notched specimen of titanium alloy Grade 2 (notch root radius 1 mm) as an example.

Figures 16.6 and 16.7 show the values of the defect density tensor at the notch tip for two cases: $\sigma_y < \sigma_0$ and $\sigma_y > \sigma_0$, $1 < L_{TN/2}$, respectively. In both cases, there is a stable situation with an equilibrium concentration of defects in the notched area.

Figure 16.8 shows numerical results of the defect density along the line characterizing distance to the notch in the plane with the maximum normal stress. It can be seen that when $\sigma_y > \sigma_0$ and $1 = L_{TN/2}$ there is no equilibrium defect concentration and the dissipative structure is localized on the spatial scale that is equal to the half of the critical distance obtained for Grade 2 specimen under quasi-static loading.
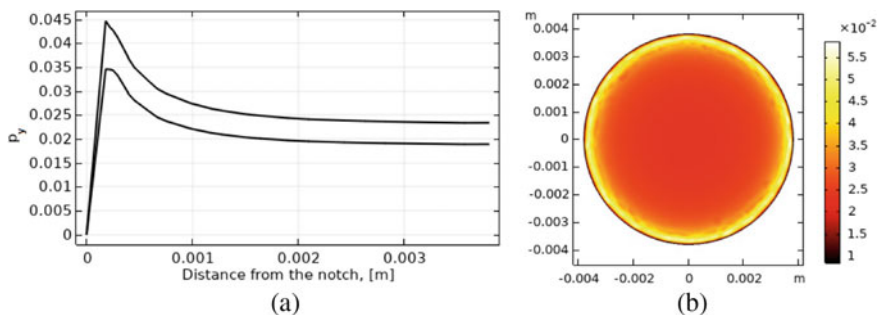
Fig. 16.6 **a** Values of p_y versus distance from the notch ($\sigma_y < \sigma_0$). **b** Spatial distribution of p_y component in the cross-sectional area perpendicular to the loading direction at the end-point to evolution
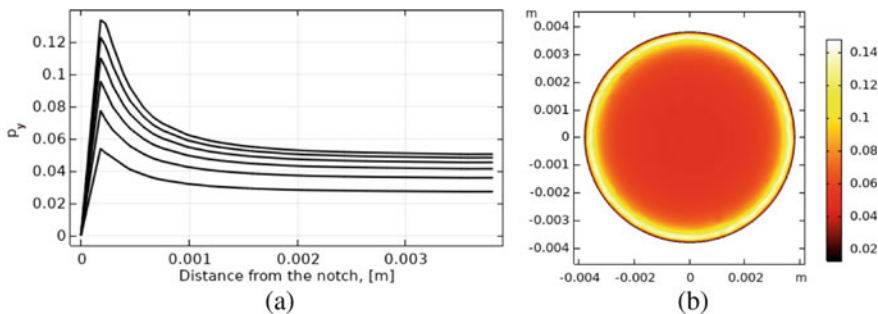
Fig. 16.7 **a** Values of p_y versus distance from the notch ($\sigma_y > \sigma_0$, $l_{c\sigma} < L_{TN}/2$). **b** Spatial distribution of p_y component in the cross-sectional area perpendicular to the loading direction at the end-point to evolution
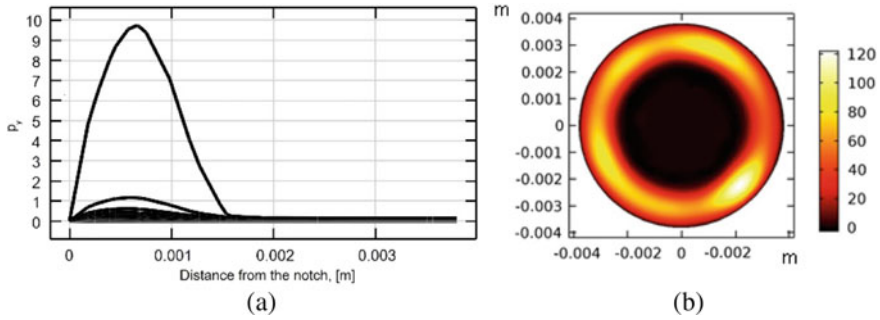
Fig. 16.8 a Values of p_y versus distance from the notch ($\sigma_y > \sigma_0$, $l_{c\sigma} = L_{TN}/2$). **b** Spatial distribution of component in the cross-sectional area perpendicular to the loading direction at the end-point to evolution

To get this scale equal to the 0.85 mm, we have used the material parameters included in Eq. (16.11): $q = 50.9$, $k = 2 \cdot 10^{-6}$, $a = 5.1$. Initial uniform distribution of p_{yy} is replaced by the heterogeneous p_{yy} with the localization zones where we can observe sharp increase in the defect density (Fig. 16.8b).

16.5 Conclusion

The aim of this work is to verify a reformulation of the linear-elastic TCD proposed in [15, 16] for notched specimens from titanium alloy Grade 2 under dynamic loading. It was shown that the TCD is capable of accurately assessing the static and dynamic strength of notched specimens within an error interval of ±20%.

The modification of the TCD in cases of elasto-plastic material behavior for dynamic loading was proposed. The use of an improved description of the stress–strain state at the notch tip allows estimating the fall within an error up to 10% and introducing the critical distances as a material parameter.

Last part of the work presents one of the possible physical explanation of the critical distance theory based on the statistical theory of defect evolution. As a result, it was shown that localization of the defect ensemble can be observed when two requirements are fulfilled: existence of the area where stresses are higher than inherent material strength and the spatial size of this area should be equal to the half of the critical distance. The critical distance mainly depends on the microstructural material morphology and can be considered as a fundamental length scale of dissipative structure developing in a blow-up regime.

References

1. Ibanez-Gutierrez, F.T., Cicero, S.: Fracture assessment of notched short glass fibre reinforced polyamide 6: an approach from failure assessment diagrams and the theory of critical distances. Compos. B Eng. **111**, 124–133 (2017)
2. Lifshitz, E.M., Pitaevskii, L.P., Sykes, J.B.: Physical Kinetics. Pergamon Press, Oxford (1981)
3. Naimark, O.B.: Collective properties of defect ensembles and some nonlinear problems of plasticity and fracture. Phys. Mesomech. **6**, 39–63 (2003)
4. Neuber, H.: Theory of Notch Stresses: Principles for Exact Calculation of Strength With Reference to Structural Form and Material, 2nd enl edn. Oak Ridge, Tenn (1961)
5. Novozhilov, V.V.: On a necessary and sufficient criterion for brittle strength. J. Appl. Math. Mech. **33**, 201–210 (1969)
6. Peterson, R.E.: Notch sensitivity. In: Sines, G., Waisman, J.L. (eds.) Metal Fatigue. McGraw Hill, New York (1959)
7. Pluvinage, G.: Fracture and Fatigue Emanating from Stress Concentrators. Kluwer Academic Publishers (2003)
8. Samarskii, A.A., Galaktionov, V.A., Kurdyumov, S.P., Mikhailov, A.P.: Blow-Up in Quasilinear Parabolic Equations. Walter de Gruyter, Berlin, New York (1995)
9. Susmel, L.: The theory of critical distances: a review of its applications in fatigue. Eng. Fract. Mech. **75**(7), 1706–1724 (2008)
10. Susmel, L., Taylor, D.: The theory of critical distances to estimate the static strength of notched samples of Al6082 loaded in combined tension and torsion. Part II: multiaxial static assessment. Eng. Fract. Mech. **77**(3), 470–478 (2010)
11. Taylor, D.: The theory of critical distances applied to the prediction of brittle fracture in metallic materials. Struct. Integrity Durability **1**, 145–154 (2006)
12. Taylor, D.: The Theory of Critical Distances: A New Perspective in Fracture Mechanics. Elsevier Science, Oxford (2007)
13. Wang, R., Li, D., Hu, D., Meng, F., Liu, H., Ma, Q.: A combined critical distance and highly-stressed-volume model to evaluate the statistical size effect of the stress concentrator on low cycle fatigue of TA19 plate. Int. J. Fatigue **95**, 8–17 (2017)
14. Whitney, J.M., Nuismer, R.J.: Stress fracture criteria for laminated composites containing stress concentrations. J. Compos. Mater. **8**, 253–265 (1974)
15. Yin, T., Tyas, A., Plekhov, O., Terekhina, A., Susmel, L.: On the use of the theory of critical distances to estimate the dynamic strength of notched 6063–T5 aluminium alloy. Frattura. Integr. Strutt. **30**, 220–225 (2014)
16. Yin, T., Tyas, A., Plekhov, O., Terekhina, A., Susmel, L.: A novel reformulation of the theory of critical distances to design notched metals against dynamic loading. Mater. Des. **69**, 197–212 (2015)

Chapter 17
Tuning Sliding Mode Controllers for String Stability

Markus Reichhartinger, Astrid Leitner, and Martin Horn

Abstract Due to their outstanding robustness properties, feedback loops based on the ideas of sliding mode control are well suited for the application in platooning scenarios. In this chapter, homogenous platoons without any communication between the vehicles in the platoon are investigated. It is demonstrated that neglecting actuator dynamics during the design phase of sliding mode controllers leads to chattering which becomes evident as stable self-sustained oscillations (limit cycles) within the control loop. In this contribution, the characteristics of these limit cycles are exploited to adjust the velocity-dependent inter-vehicle distances such that a string stable platoon can be achieved although the actuator dynamics are neglected in the design phase of the controllers. Two well-known sliding mode algorithms, a classical first-order concept and the super twisting algorithm, are investigated and simulation results are presented.

17.1 Introduction

Truck platooning on highways offers a number of advantages such as reduced fuel consumption and emissions, increased road capacity, improved road safety and comfort. Apart from these benefits the platooning scenario also is interesting from a system theoretic point of view. As it is addressed in a number of publications [5, 6, 12, 13, 21], it is not straightforward to ensure a satisfying dynamic behavior of a string of moving vehicles. Especially, the attenuation of disturbances along the platoon is

M. Reichhartinger (✉) · A. Leitner
Institute of Automation and Control, Graz University of Technology,
Inffeldgasse 21B/I, 8010 Graz, Austria
e-mail: markus.reichhartinger@tugraz.at

M. Horn
Christian Doppler Laboratory for Model Based Control of Complex Test Bed Systems,
Institute of Automation and Control, Graz University of Technology, 8010 Graz, Austria
e-mail: martin.horn@tugraz.at

of major interest. In this context, an established notion is the so-called string stability [7, 8, 15, 24]. A common strategy to achieve string stability is the introduction of speed-dependent inter-vehicle distances. In the present contribution, this is realized by a so-called constant time-headway spacing [10, 23]. It is assumed that the position of each vehicle within the platoon is controlled by means of a sliding mode controller. This control methodology which is known to render feedback loops immune with respect to certain classes of disturbances also proved to be a suitable approach in platooning applications [9, 18]. For the tuning of the controller parameters, the actuator dynamics is neglected. However, as it is shown in the present publication, the choice of an appropriate constant time-headway significantly depends on dynamic actuator properties.

   This chapter is organized as follows: In Sect. 17.2, a detailed problem statement is given. Sliding mode controllers and the tuning procedure for the time-headway are presented in Sect. 17.3. Section 17.4 illustrates the performance of the proposed concept via numerical simulation results and Sect. 17.5 concludes this chapter.

17.2   Problem Statement

We consider a platoon of consecutively driving vehicles (so-called agents) consisting of a leader (first vehicle, agent 0) and N followers (agnet $1, \ldots, N$). The desired formation of the platoon is characterized by prescribed inter-vehicle distances. We assume that each vehicle has access to its position and velocity and, furthermore, to the distance to its predecessor. Hence, by measuring the inter-vehicle distances, no communication along the platoon is required. The platoon is homogeneous, i.e., all vehicles have identical dynamics

$$\frac{\mathrm{d}x_i}{\mathrm{d}t} = v_i, \qquad \frac{\mathrm{d}v_i}{\mathrm{d}t} = a_i, \quad i = 0, \ldots, N. \tag{17.1}$$

Note that x_i, v_i and a_i denote position, velocity, and acceleration of vehicle i, where $i = 0$ corresponds to the leader. The acceleration a_i represents the input of this double integrator dynamics and is assumed to be the output of a BIBO-stable actuator with bounded input u_i and transfer function $W(s)$, i.e.,[1]

$$\bar{a}_i(s) = W(s)\bar{u}_i(s). \tag{17.2}$$

Position errors e_j between two consecutive agents are introduced as

$$e_j = x_{j-1} - x_j - \left(\Delta_j + t_\mathrm{h} v_j\right), \quad j = 1, \ldots, N, \tag{17.3}$$

---

[1] Laplace transforms are denoted by bars.

where $\Delta_j + t_h v_j$ represents the desired velocity dependent inter-vehicle distance. It consists of a constant component Δ_j and a velocity proportional component $t_h v_j$. Therein, the strictly positive constant t_h denotes the so-called time-headway.

The overall goal is to choose the actuating signals u_j such that the vehicles of the platoon form up as desired despite the leader's behavior due to u_0, which, as already mentioned above, is *not* communicated to the followers.

17.3 Controller Design and Tuning

Typically, in a first step (see Sect. 17.3.1), the agent controllers are designed for the idealized case characterized by $W(s) = 1$, i.e., the actuator dynamics are neglected. As the relative degree of the position errors e_j with respect to u_j is one, see equation (17.3), we propose a classical first-order sliding mode controller (see, e.g., [22]) or the super twisting controller which belongs to the family of second-order sliding mode algorithms [20]. The gains of these controllers are adjusted such that external disturbances due to the non-existent communication are dominated.

In the second step (see Sect. 17.3.2), the time-headway t_h is adjusted in order to eventually achieve the desired dynamics of the non-ideal platoon characterized by $W(s) \neq 1$. The proposed tuning procedure for t_h relies on a well-known string stability condition.

17.3.1 Agent Control

For $W(s) = 1$ Eqs. (17.1), (17.2) and (17.3) lead to the error dynamics

$$\frac{de_j}{dt} = v_{j-1} - v_j - t_h u_j, \quad j = 1, \dots, N, \tag{17.4}$$

where $v_{j-1} - v_j$ is regarded as an unknown external disturbance. This motivates the choice of the control signal

$$u_j = \frac{1}{t_h} w_j, \quad j = 1, \dots, N. \tag{17.5}$$

Therein, w_j is generated by nonlinear sliding mode control algorithms.

17.3.1.1   First-Order Sliding Mode Controller

Using the classical first-order sliding mode controller the algorithm reads as

$$w_j = k\,\text{sign}\left(e_j\right), \quad j = 1, \ldots, N, \tag{17.6}$$

where k is a positive tuning parameter. Obviously w_j and consequently the control signal u_j is discontinuous. It is well known that feedback loops based on sliding mode control suffer from the so-called chattering effect [2, 4]. This phenomenon produces undesired self-sustained oscillations in the resulting feedback loops and, for instance, is a result of neglected actuator dynamics.

17.3.1.2   Second-Order Sliding Mode Controller

In the case of the second-order sliding mode controller, the super twisting algorithm as discussed in [11, 19] is given by

$$\frac{\text{d}z_j}{\text{d}t} = 1.5\sqrt{k}\,\text{sign}\left(e_j\right), \tag{17.7}$$

$$w_j = 1.1k\sqrt{\left|e_j\right|}\,\text{sign}\left(e_j\right) + z_j \quad j = 1, \ldots, N, \tag{17.8}$$

with the constant positive parameter k. This algorithm can be regarded as a nonlinear version of the well-known PI control law [1]. Frequently this control law replaces the classical first-order controller in order to avoid discontinuities in the control signal. It should be noted that this does not imply an elimination of the above mentioned chattering phenomenon [16].

17.3.2   Time-Headway Tuning

According to [15] in a string stable platoon disturbances are attenuated as they propagate along the string. A necessary frequency domain condition for linear platoon dynamics reads as

$$\|T\left(j\omega\right)\|_\infty = \max_\omega |T\left(j\omega\right)| \leq 1, \tag{17.9}$$

where $T(s)$ is the transfer function relating the positions of two subsequent agents. In Fig. 17.1, the feedback loop structure for agent j is depicted. Note that the input to this feedback loop consists of the constant component Δ_j and the time-varying component x_{j-1}. However, we are only interested in the propagation of dynamic signal components along the string. Therefore, for the evaluation of condition (17.9), the transfer function $T(s)$ can be computed as
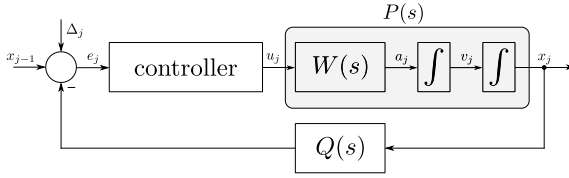
Fig. 17.1 Feedback loop of agent j. The input Δ_j represents the constant component of the desired spacing. The signals x_j and x_{j-1} denote the positions of the respective agents

$$T(s) = \left.\frac{\bar{x}_j(s)}{\bar{x}_{j-1}(s)}\right|_{\Delta_j=0}. \tag{17.10}$$

In the present case, the control laws are nonlinear and consequently this technique cannot be applied directly. As shown in [17], the describing function method permits to exploit condition (17.9) even in the nonlinear case. The basic idea of this approach is to replace the nonlinearity by its so-called describing function, a complex gain $N(A, \omega)$, which approximates the nonlinear behavior in the case of limit cycles $e_j \approx A \sin(\omega t)$. In the present platooning application, the nonlinearity is introduced by the above-mentioned control laws. Limit cycles occur due to the presence of the previously neglected actuator dynamics. Using the well-known equation of harmonic balance, i.e.,

$$N(A, \omega)P(j\omega)Q(j\omega) = -1 \tag{17.11}$$

amplitude A and frequency ω can be determined. According to Eqs. (17.1), (17.2), and (17.3), the transfer functions $P(s)$ and $Q(s)$ are given by

$$P(s) = W(s)\frac{1}{s^2} \qquad Q(s) = 1 + st_{\mathrm{h}}. \tag{17.12}$$

Once A and ω are known, the so-called equivalent gain k_{eq}, which replicates the mean value of the nonlinear system's response to slowly time-varying input signals, can be computed [2–4]. Finally, the nonlinear controller formally is substituted by the static gain k_{eq}. Hence, the nonlinear feedback loop is approximated by

$$T(s) = \frac{k_{\mathrm{eq}}P(s)}{1 + k_{\mathrm{eq}}P(s)Q(s)}. \tag{17.13}$$

Note that the equivalent gain is a function of the time-headway, i.e., $k_{\mathrm{eq}} = k_{\mathrm{eq}}(t_{\mathrm{h}})$. The idea of the proposed tuning procedure is to adjust t_{h} such that condition (17.9) holds. An algorithm which aims at minimizing inter-vehicle distances is presented in [17]. According to Eq. (17.3), this is equivalent to the minimization of the time-headway t_{h}.

17.4   Numerical Example

In this section, results of numerical simulations of a platoon consisting of $N = 6$ agents (one leader and five followers) are presented. All simulations are carried out with a fixed step solver using a step size of 0.001. The actuator dynamics is given by

$$W(s) = \frac{1}{(1 + s\tau)^2}. \tag{17.14}$$

As an excitation of the platoon dynamics the leader vehicle input signal

$$u_0 = \begin{cases} 2\sin(t + \pi) & \text{otherwise} \\ -4 & \text{for } t \in [29, 31] \end{cases} \tag{17.15}$$

is chosen. The resulting time-evolution of the leader's position $x_0(t)$ and velocity $v_0(t)$ are plotted in Fig. 17.2. Therein the initial position $x_0(0) = 130$ and the initial velocity $v_0(0) = 29$ of the leader as well as the considered braking scenario initiated at $t = 29$ become evident.
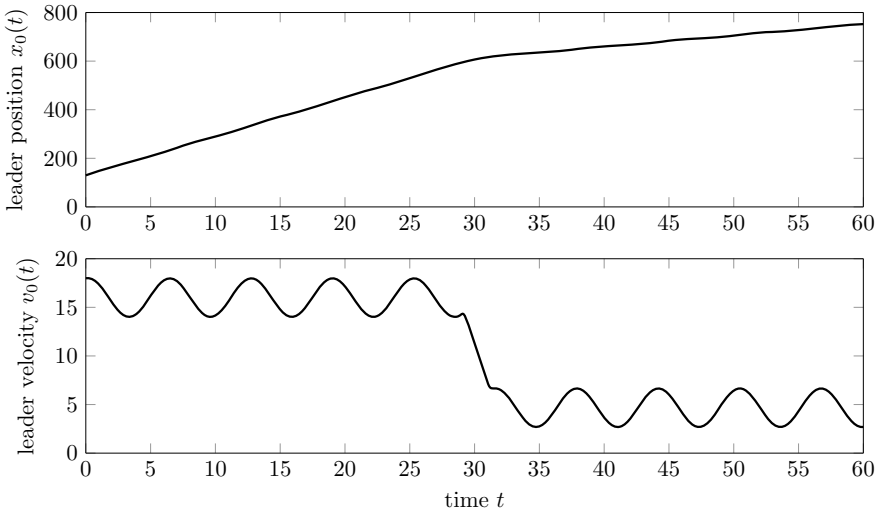
Fig. 17.2 Position x_0 and velocity v_0 of the leader vehicle due to a control signal u_0 given in Eq. (17.15)

17.4.1 First-Order Sliding Mode Controller

For the classical first-order sliding mode controller given in Eq. (17.6), the describing function

$$N(A) = \frac{4k}{\pi\,A} \tag{17.16}$$

can be found, e.g., in [2]. Solving the equation of harmonic balance (17.11) yields the amplitude

$$A = \frac{2kt_{\mathrm{h}}^2\tau}{\pi\,(t_{\mathrm{h}} - 2\tau)} \tag{17.17}$$

of the limit cycle which allows to compute the equivalent gain

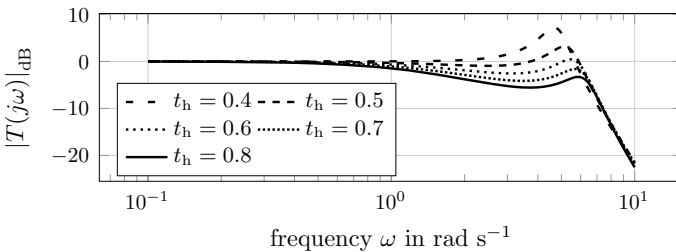$$k_{\mathrm{eq}} = \frac{2k}{\pi\,A} = 2\frac{t_{\mathrm{h}} - 2\tau}{t_{\mathrm{h}}^2\tau}, \tag{17.18}$$

see, e.g., [2]. In order to assess string stability of the platoon using the first-order sliding mode controller, the above determined equivalent gain is used to compute $T(s)$ as given in Eq. (17.10). For a controller gain $k = 2.5$ and an actuator time constant $\tau = 0.1$, the minimum value of t_{h} satisfying condition (17.9) can be computed via the algorithm presented in [17]. The obtained minimal time-headway is found to be $t_{\mathrm{h}} \approx 0.65$. This is confirmed by Fig. 17.3 where the magnitude plot of $T(j\omega)$ is depicted for different values of the time-headway t_{h}.

Figure 17.4 shows simulation results of the above-mentioned scenario using $\Delta_j = 5$. It is illustrated that the setting $t_{\mathrm{h}} = 0.9$ yields a string stable platoon behavior, whereas the setting $t_{\mathrm{h}} = 0.46$ results in a string unstable dynamic platoon behavior. In order to illustrate these characteristics, the inter-vehicle distances are plotted in Fig. 17.4. By comparing the amplitudes of the oscillations of these distances, it

Fig. 17.3 Magnitude plot of the transfer function $T(s)$ used to assess string stability. Choosing the time-headway such that $|T(j\omega)| < 0_{\mathrm{dB}}$ for all frequencies is necessary to generate a string stable platoon
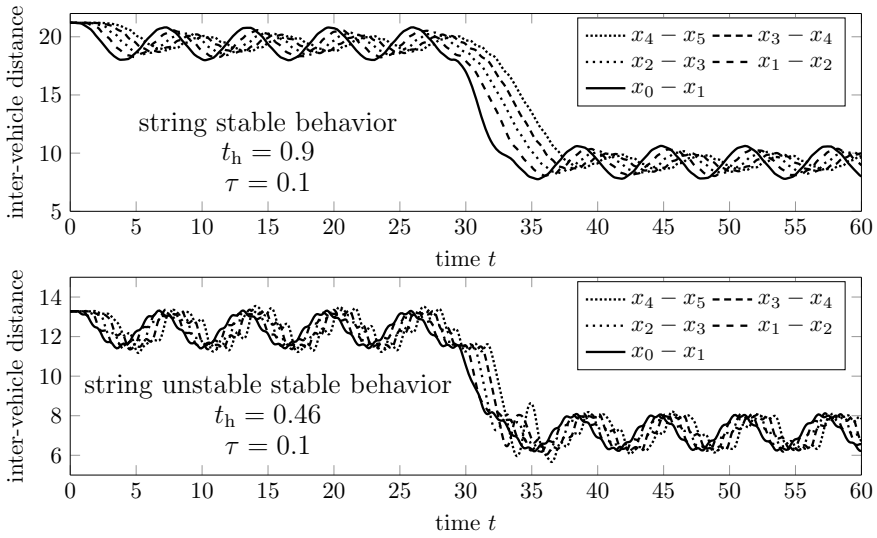
Fig. 17.4 Simulation results of the platoon using the discussed first-order sliding mode controller. String stability of the platoon is confirmed by this simulation with a time-headway of $t_h = 0.9$, whereas an unstable behavior can be observed for $t_h = 0.46$

becomes evident that they decrease along the string in the string stable case and that they increase in the string unstable case. Hence, the time-headway t_h introduces a kind of damping into the platoon dynamics, see, e.g., [14].

17.4.2 Second-Order Sliding Mode Controller

The first-order controller is replaced by the super twisting algorithm (17.7) and (17.8). As discussed in [16], the achievable control performance strongly depends on the actuator dynamics. This fact is confirmed by the results shown in Fig. 17.5 obtained by the same parameter settings as used in Sect. 17.4.1, i.e., $k = 2.5$, $\tau = 0.1$ and $\Delta_j = 5$. It can clearly be observed that the first-order controller achieves a smoother transition during the breaking scenario. Using the super twisting algorithm leads to large amplitudes of the inter-vehicle distances at the very end of the platoon especially at the end of the braking phase. However, the platoon is string stable, too. The second simulation experiment was carried out with a faster actuator ($\tau = 0.07$) which leads to similar results as achieved with the first-order controller.
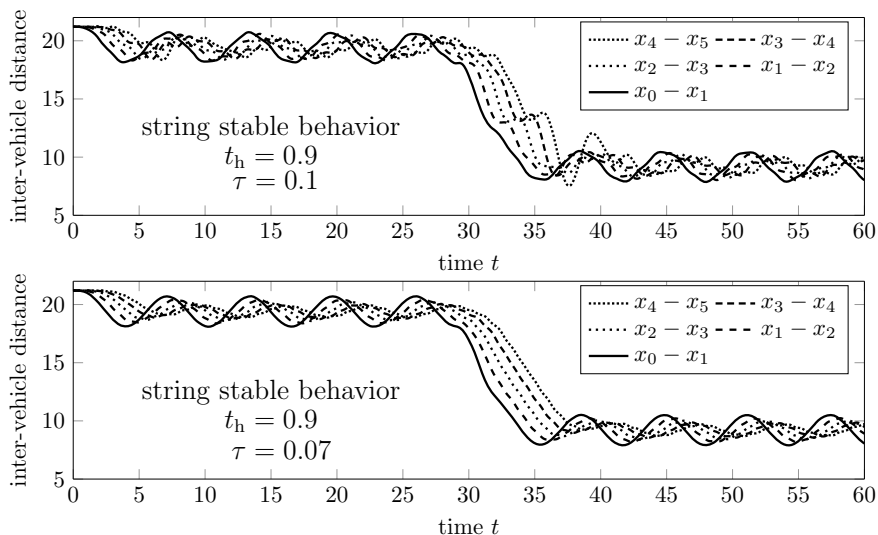
Fig. 17.5 This simulation results illustrate that the super twisting algorithm is also able to achieve a string stable platoon. However, the achieved performance heavily depends on the characteristics of the actuator. Here, results with an actuator with $\tau = 0.1$ (lower plot) and with $\tau = 0.07$ (upper plot) are shown

17.5 Conclusion

The presented approach, in principle, relies on the idea to approximate a nonlinear feedback loop by a linear one. Even though the resulting linear loop description is by far not exact, it proves to be a convenient tool for the string stability analysis of sliding mode controlled platoons. Apart from that, the present application confirms that replacing a first-order sliding mode controller by a super twisting algorithm does not necessarily lead to improved control performance.

References

1. Åström, K.J., Hägglund, T.: PID Controllers: Theory, Design, and Tuning, vol. 2. Instrument Society of America Research Triangle Park, NC (1995)
2. Boiko, I.: Discontinuous Control Systems: Frequency-Domain Analysis and Design. Springer Science & Business Media (2008)

3. Boiko, I., Castellanos, I., Fridman, L.: Analysis of response of second-order sliding mode controllers to external inputs in frequency domain. Int. J. Robust Nonlin. Control: IFAC-Affil. J. **18**(4–5), 502–514 (2008)
4. Boiko, I., Fridman, L., Pisano, A., Usai, E.: Analysis of chattering in systems with second-order sliding modes. IEEE Trans. Automat. Control **52**(11), 2085–2102 (2007)
5. Cook, P.: Conditions for string stability. Syst. Control Lett. **54**(10), 991–998 (2005)
6. De Wit, C.C., Brogliato, B.: Stability issues for vehicle platooning in automated highway systems. In: Proceedings of the 1999 IEEE International Conference on Control Applications (Cat. No. 99CH36328), vol. 2, pp. 1377–1382. IEEE (1999)
7. Eyre, J., Yanakiev, D., Kanellakopoulos, I.: A simplified framework for string stability analysis of automated vehicles. Vehicle Syst. Dyn. **30**(5), 375–405 (1998)
8. Feng, S., Zhang, Y., Li, S.E., Cao, Z., Liu, H.X., Li, L.: String stability for vehicular platoon control: definitions and analysis methods. Ann. Rev. Control (2019)
9. Ferrara, A., Vecchio, C.: Second order sliding mode control of vehicles with distributed collision avoidance capabilities. Mechatronics **19**(4), 471–477 (2009)
10. Klinge, S., Middleton, R.H.: Time headway requirements for string stability of homogeneous linear unidirectionally connected systems. In: Proceedings of the 48h IEEE Conference on Decision and Control (CDC) held jointly with 2009 28th Chinese Control Conference, pp. 1992–1997. IEEE (2009)
11. Levant, A.: Robust exact differentiation via sliding mode technique. Automatica **34**(3), 379–384 (1998)
12. Li, S.E., Zheng, Y., Li, K., Wang, J.: An overview of vehicular platoon control under the four-component framework. In: 2015 IEEE Intelligent Vehicles Symposium (IV), pp. 286–291. IEEE (2015)
13. Liang, K.Y., Mårtensson, J., Johansson, K.H.: Experiments on platoon formation of heavy trucks in traffic. In: 2016 IEEE 19th International Conference on Intelligent Transportation Systems (ITSC), pp. 1813–1819. IEEE (2016)
14. Lu, X.Y., Hedrick, J.K.: Practical string stability for longitudinal control of automated vehicles. Vehicle Syst. Dyn. **41**, 577–586 (2004)
15. Peppard, L.: String stability of relative-motion pid vehicle control systems. IEEE Trans. Automat. Control **19**(5), 579–581 (1974)
16. Pérez-Ventura, U., Fridman, L.: When is it reasonable to implement the discontinuous sliding-mode controllers instead of the continuous ones? Frequency domain criteria. Int. J. Robust Nonlin. Control **29**(3), 810–828 (2019)
17. Rupp, A., Reichhartinger, M., Horn, M.: String stability analysis for sliding mode controllers in platoons with unmodeled actuator dynamics: a frequency domain approach. In: 2019 18th European Control Conference (ECC), pp. 4067–4072. IEEE (2019)
18. Rupp, A., Steinberger, M., Horn, M.: Sliding mode based platooning with non-zero initial spacing errors. IEEE Control Syst. Lett. **1**(2), 274–279 (2017)
19. Seeber, R., Horn, M.: Stability proof for a well-established super-twisting parameter setting. Automatica **84**, 241–243 (2017)
20. Shtessel, Y., Edwards, C., Fridman, L., Levant, A.: Sliding Mode Control and Observation. Springer (2014)
21. Swaroop, D., Hedrick, J.K.: String stability of interconnected systems. IEEE Trans. Automat. Control **41**(3), 349–357 (1996)
22. Utkin, V.I.: Sliding Modes in Control and Optimization. Springer Science & Business Media (2013)
23. Yanakiev, D., Kanellakopoulos, I.: Variable time headway for string stability of automated heavy-duty vehicles. In: Proceedings of 1995 34th IEEE Conference on Decision and Control, vol. 4, pp. 4077–4081. IEEE (1995)
24. Zhou, J., Peng, H.: String stability conditions of adaptive cruise control algorithms. IFAC Proc. Vols. **37**(22), 649–654 (2004)

Chapter 18
Steady Motion of a Belt in Frictional Contact with a Rotating Pulley

Jakob Scheidl and Yury Vetyukov

Abstract The steady-state motion of belt drives is studied extensively in the literature. While traditional models rely on the theory of an extensible string, we aim to take bending effects into account. In this regard, it is well known that concentrated contact forces at the points of first and last contact with a pulley arise if shear deformations are restricted. To circumvent this issue, we utilise a shear deformable, Cosserat theory of rods. In particular, we study the contour motion of a belt that is transported over a single, rigid pulley with zones of stick, sliding friction and no contact. The Coulomb friction law governs the contact between the belt and the pulley. We present a novel finite element model that allows to obtain the steady-state solution directly. Furthermore, we deduce the corresponding closed boundary value problem and integrate it numerically. Results obtained for a particular parameter set demonstrate correspondence of the two approaches.

18.1 Problem Statement

We seek the steady-state motion of the belt segment depicted in Fig. 18.1. The domain of interest is enclosed by the two clamping positions, one on either side. The belt is transported from left to right, entering and leaving the interval $x \in [-L_x/2, \ L_x/2]$ with a constant mass transport rate $c = 1$.[1]

A circular, rigid pulley with radius $R = 0.7$ is placed symmetrically in between the borders and its centre is shifted by $H = -0.575$ in vertical direction j. The material length in the control volume L_s equals the distance between the clamping positions $L_x = L_s = 1$. The belt is made of linear elastic material with modulus $E = 5 \times 10^7$ and Poisson ratio $\nu = 0.45$. It has a rectangular cross section with thickness $h = 0.05$ and width $w = 0.1$. We assume Coulomb friction between belt

---

[1]The SI-system of units is used throughout the paper.

J. Scheidl (✉) · Y. Vetyukov
Institute of Mechanics and Mechatronics, TU Wien, Getreidemarkt 9/E325, 1060 Wien, Austria
e-mail: Jakob.Scheidl@tuwien.ac.at
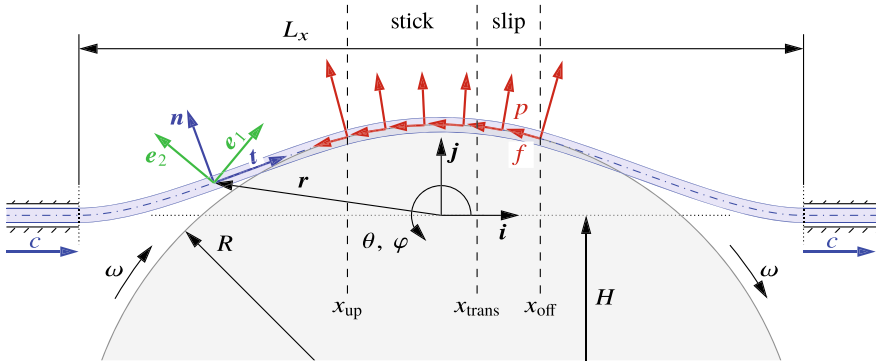
Fig. 18.1 One-pulley belt drive at contour motion; geometry and global coordinates

and pulley with the coefficient $\mu = 0.2$. In this respect, the belt's thickness is assumed to be small enough, such that we consider the contact reaction forces being applied at the middle line of the belt. Consequently, any distributed moments that would arise due to tractions acting on the lower fibre are disregarded. Inertia effects are ignored as well. Assuming that a solution with only one sticking and one sliding region exists, the latter succeeding the former in direction of travel, we explicitly set the position of the point where switching from stick to slip happens by means of x_{trans}. Admittedly, it would have been more natural to specify the angular velocity ω instead. However, in this academic example provision of x_{trans} is equally feasible and even proves beneficial with reasons to be given at the end of Sect. 18.4. The belt is modelled as a Cosserat elastic rod with bending stiffness a, extensional stiffness b_1 and shear stiffness b_2:

$$a = \frac{E h^3 w}{12}, \quad b_1 = E h w, \quad b_2 = \frac{E}{2 (1 + \nu)} h w. \tag{18.1}$$

Incorporating shear deformability is essential to avoid concentrated contact interactions at the run-up- and the run-off-point, which are marked with x_{up} and x_{off} in Fig. 18.1, see [4].

In the usual Lagrangian kinematic setting, the actual configuration is described by the position vector r as a function of the material arc coordinate $r = r(s)$. The tangential unit vector t and the corresponding normal vector n are parametrised with an angle φ, which is measured against i,

$$t = \partial_s r / |\partial_s r| = i \cos \varphi + j \sin \varphi, \quad n = -i \sin \varphi + j \cos \varphi, \tag{18.2}$$

where we have used the acronym $\partial_s(\ldots) = \partial(\ldots)/\partial s$ to denote the material derivative. It is natural to describe the contact forces in this vector basis. The second system

$$e_1 = i \cos \theta + j \sin \theta, \quad e_2 = -i \sin \theta + j \cos \theta, \tag{18.3}$$

grasps the rotation of a material point by an angle θ, again measured against i. In the sense of a Timoshenko like theory, the vector e_1 points in normal direction of the deformed cross section. Thus, the shear deformation angle follows as

$$\psi = \theta - \varphi . \tag{18.4}$$

The undeformed state is assumed to be a straight line ($r_0 = x\,i$) and we refer to [1] for an example of a looped belt with a circular reference configuration.

The generalised force resultants M and Q are related to the deformations through the constitutive law, again see [1],

$$M = a\,\kappa , \quad Q = Q_1\,e_1 + Q_2\,e_2 = b_1\,\varepsilon\,e_1 + b_2\,\Gamma\,e_2 , \tag{18.5}$$

where κ is the bending strain measure; ε and Γ are the conjugate strain measures of the force components Q_1 and Q_2. The strains are related to the deformations through

$$\kappa = \partial_s\theta , \quad \varepsilon = (D\cos\psi - 1) , \quad \Gamma = -(D\sin\psi) , \quad D = |\partial_s r| , \tag{18.6}$$

and in absence of shear deformation ($\psi = 0$) the axial strain ε corresponds to the stretch D.

We use a dot to designate time derivatives and utilise the stationary material transport rate c to introduce an appropriate coordinate transformation:

$$s = s\,(\sigma, t) = \sigma - c\,t , \quad \partial_s\sigma = 1 , \quad \dot\sigma = c , \tag{18.7}$$

where the last equation holds due to $\dot s = 0$. Rewriting the governing equations in the new coordinate σ by simply replacing ∂_s with ∂_σ effectively eliminates the time dependence of field variables.

18.2 Finite Element Formulation

One way to obtain the contour motion of the belt is to seek stationary points of the total potential energy Π:

$$\delta\Pi = \delta U + \delta V = 0 , \tag{18.8}$$

where we have introduced the elastic strain energy U and the potential of contact forces V. These energy contributions may be written as line integrals over σ:

$$U = \int_{L_s} \left(\frac{1}{2}\,a\,\kappa^2 + \frac{1}{2}\,b_1\,\varepsilon^2 + \frac{1}{2}\,b_2\,\Gamma^2 \right) d\sigma , \tag{18.9}$$

$$V = \int_{L_s} \left(\frac{1}{2}\,P_p\,\gamma^2 + \lambda_p\,\gamma \right) d\sigma + \int_{L_s} (-\lambda_f\,t \cdot r)\,d\sigma . \tag{18.10}$$

The strain energy is a simple quadratic form featuring couples of stiffness coefficients and squared strain components. The contact potential is more complicated and deserves an in-depth discussion: It is divided into two separate integrals, the first one dealing with the contributions attributed to the normal contact pressure p and the second one with those related to the frictional force f. The strategy to compute the contact forces in the finite element framework is known as augmented Lagrangian method [3]. It features a penalty regularisation with penalty factors such as P_p and combines it with an iterative update of Lagrangian multiplier estimates such as λ_p and λ_f. Upon convergence of the iteration process, the penalty contributions vanish and only the Lagrangian multipliers persist.

Concerning the normal contact, the main kinematic condition to enforce is that the belt must not penetrate the pulley surface. We release this rigidity constraint and aim to fulfil it approximately by penalising any penetration γ, defined as

$$\gamma = \max\left(0,\ R - |r - H\,j|\right) \geq 0\,. \tag{18.11}$$

The first quadratic term in (18.10) is further augmented with the actual Lagrangian multiplier estimate λ_p, which is updated iteratively:

$$\lambda_p \leftarrow \lambda_p + P_p\,\gamma\,. \tag{18.12}$$

Basically, the penalty contribution of the previous step is simply transferred to the Lagrange multiplier, improving the estimate and thereby reducing the penetration γ in the upcoming step.

The key condition for the frictional contact is that one must prevent any relative motion in the sticking part of the contact region. The velocity of a material point follows as the time derivative of the position vector:

$$v = \dot{r} = \partial_\sigma r\,\dot{\sigma} = c\,\partial_\sigma r = c\,D\,t\,. \tag{18.13}$$

The absolute value of a point's relative sliding velocity is

$$v_{\text{rel}} = c\,D - R\,\omega\,. \tag{18.14}$$

Since ω is considered unknown, we cannot fulfil $v_{\text{rel}} = 0$ directly, but have to demand $\partial_\sigma v_{\text{rel}} = 0$ instead, which translates to

$$\partial_\sigma D = 0 \quad \Rightarrow \quad D = \bar{D} = \text{const}\,. \tag{18.15}$$

The stretch in the sticking region $\bar{D}$ is constant. The original condition $v_{\text{rel}} = 0$ now serves as an equation to calculate the corresponding value of ω. As the transition position x_{trans} is provided explicitly, the zones of stick and slip are known in advance and the frictional tractions can be assigned directly:

$$x < x_{\text{trans}} : \lambda_f \leftarrow P_f\,\partial_\sigma D + \lambda_f\,, \quad x \geq x_{\text{trans}} : \lambda_f \leftarrow -\mu\,\lambda_p\,, \tag{18.16}$$

with P_f denoting the penalty factor for sticking contact. The negative sign in front of μ indicates forward sliding of the belt.

The finite element formulation itself is based on a discretisation of the position vector r as well as the angle of particle rotation θ. Cubic shape functions are used to approximate the fields and their first derivatives in the local coordinate $\xi \in [-1, 1]$ of a single, two-node element. The integrals (18.9)–(18.10) are transformed to a sum of finite element contributions in the usual manner and evaluated by means of Gaussian quadrature rules with three integration points.

A pure Newton–Raphson algorithm is used to solve the non-linear system of equations. In order to obtain results more reliably, the solution process is split into two phases: Firstly, a frictionless solution with relaxed penalty for normal contact is sought, which counteracts the ill-conditioning induced through the penalty terms and simply disregards the second integral of (18.10). Secondly, the full penalty is applied and frictional forces are taken into account. A number of steps is performed in order to reach convergence of the Lagrange multiplier estimates. We resolve the contact state discretely at individual integration points and call the update routines (18.12) and (18.16) once after each successful Newton step. The size of the contact zone is determined by the first and last integration point for which contact is recognised.

18.3   Analytic Model

Just like in the finite element model, we assume the solution to decompose into four sequential segments: the left free span, the sticking region, the sliding region and the right free span. In an effort to deduce the system of differential equations we will address a single free span and the two contact segments individually, each time being mindful of the particularities:

- No external forces act in any of the two free span regions.
- In the sticking region the belt adheres to the pulley surface.
- In the sliding region the friction forces must obey the friction law.

The model is an extension of the idealised one presented in [2]. We have already provided the constitutive relations (18.5) and also given the definition of strains in (18.6), but we have yet to present the balance equations of the non-linear theory:

$$\partial_s Q + q = 0\,, \quad \partial_s M + D\,(Q_1 \sin\psi + Q_2 \cos\psi) = 0\,. \tag{18.17}$$

The vector of external forces vanishes in the free spans and otherwise equals the contact forces, $q = f\,t + p\,n$.

Once again, we make use of the coordinate transformation (18.7) to get rid of the time dependence of field variables and replace every single instance of ∂_s with ∂_σ in the governing system. Beyond that, it is convenient to introduce spatial coordinates like x or φ for each solution region with the main consequence that σ becomes an additional unknown:

free span regions: $\sigma = \sigma(x)$, $\partial_\sigma = \partial_x/\partial_x\sigma$, $r = x\,i + y(x)\,j$,   (18.18)

contact regions: $\sigma = \sigma(\varphi)$, $\partial_\sigma = \partial_\varphi/\partial_\varphi\sigma$, $r = H\,j + R\,n(\varphi)$.   (18.19)

Owing to the absence of external forces, the derivation of a system of ODEs in the free span region is quite simple. We obtain equations for σ and y through evaluation of $\partial_\sigma r = D\,t$ with the above transformation rule (18.18) and projection onto the Cartesian basis vectors. The constitutive relation (18.5) for M serves as an equation for θ and the ones for the force components are used for substitution in the balance of moments, which yields an ODE for M. Lastly, based on the balance of linear momentum, we derive equations for the stretch D and the shear angle ψ:

$$\partial_x\sigma = (D\,\cos\varphi)^{-1}\,,\quad \partial_x y = \tan\varphi\,,\quad \partial_x\theta = \partial_x\sigma\,M/a\,,$$

$$\partial_x M = \partial_x\sigma\,\left(D^2\,\sin(2\,\psi)\,\frac{b_2 - b_1}{2} + D\,b_1\,\sin\psi\right)\,,$$

$$\partial_x D = \partial_x\theta\,\left(D\,\sin(2\,\psi)\,\frac{b_1^2 - b_2^2}{2\,b_1\,b_2} - \frac{b_1}{b_2}\,\sin\psi\right)\,,$$

$$\partial_x \psi = \partial_x\theta\,\left(\cos(2\,\psi)\,\frac{b_1^2 - b_2^2}{2\,b_1\,b_2} + \frac{b_1^2 + b_2^2}{2\,b_1\,b_2} - \frac{b_1}{b_2\,D}\,\cos\psi\right)\,.   \tag{18.20}$$

Treating the sticking region is more concise, because only three ODEs for $\{\sigma,\ \theta,\ M\}$ suffice. They resemble the ones given above, with the main differences that the unknown constant stretch $\bar{D}$ enters the equations and that φ is used for parametrisation instead of x:

$$\partial_\varphi\sigma = -R/\bar{D}\,,\quad \partial_\varphi\theta = \partial_\varphi\sigma\,M/a\,,$$

$$\partial_\varphi M = \partial_\varphi\sigma\,\left(\bar{D}^2\,\sin(2\,\psi)\,\frac{b_2 - b_1}{2} + \bar{D}\,b_1\,\sin\psi\right)\,.   \tag{18.21}$$

The above three equations also apply to the sliding region, once the constant $\bar{D}$ is replaced with the variable $D = D(\varphi)$. Consequently, another equation for the stretch is needed, whose deduction is more tedious as it requires substitution of the friction criterion $f = -\mu\,p$ in the balance of forces:

$$\partial_\varphi D = \frac{D\,(2\,\partial_\varphi\theta - 1)\,(b_1 - b_2)\,(\mu\,\cos(2\,\psi) + \sin(2\,\psi))}{(b_1 - b_2)\,(\cos(2\,\psi) - \mu\,\sin(2\,\psi)) + b_1 + b_2}$$
$$+ \frac{\mu\,D\,(b_1 + b_2) - 2\,\partial_\varphi\theta\,b_1\,(\mu\,\cos\psi + \sin\psi)}{(b_1 - b_2)\,(\cos(2\,\psi) - \mu\,\sin(2\,\psi)) + b_1 + b_2}\,.   \tag{18.22}$$

This concludes the system with a total of nineteen ODEs: two times six for the free spans, three for the sticking region and four for the sliding region. Boundary conditions at $x = \pm L_x/2$ demand continuity of σ, the vertical deflection and the particle rotation ($\sigma = \pm L_x/2$, $y = 0$, $\theta = 0$). In general, the shear deformation ψ will not vanish at these points and the beam axis will thus experience a slight kink.

Matching conditions have to be employed at the run-up- and the run-off-point (x_{up} and x_{off} in Fig. 18.1). There, we demand continuity of all six unknowns that appear in the system (18.20). Lastly, at the transition point x_{trans}, we require continuity of $\{\sigma, \theta, M, D\}$. These are a total of 22 boundary conditions for 19 first order ODEs and three unknown constants, namely: The points x_{up} and x_{off} as well as the constant stretch in the sticking region $\bar{D}$. Before passing the system to the Matlab collocation solver bvp4c, we further transform the equations to a normalised coordinate $\xi \in$ [0, 1], see [1, 4], and introduce dimensionless constants to reduce the number of parameters.

18.4   Results

Let us take a look at the contact forces in Fig. 18.2 and at the strains in Fig. 18.3. Plots are drawn for the results obtained through integration of the boundary value problem (BVP, dotted) as well as for a finite element simulation with 100 equally sized elements (FEM, dashed). Though both approaches converge rapidly, the FEM simulation requires a higher computational effort owing to the two-stage iterative solution strategy and the number of elements needed to reach accurate results. The transition point is set to $x_{\mathrm{trans}} = 0$ and the contact zone borders x_{up} and x_{off} are marked with additional vertical grid lines.

In Fig. 18.2, the normal contact pressure p shows distinct peaks at the points x_{up} and x_{off}. Contrary to unshearable rod theories though, the function does not tend to infinity. The frictional tractions experience corresponding peaks as well as a jump at the transition point $x_{\mathrm{trans}} = 0$ in obedience to the friction law. The coarse discretisation does not suffice to capture the high gradients at the two bordering positions, which is most evident at x_{up} in the right picture of Fig. 18.2. This issue can be easily resolved by using more elements or an appropriately refined mesh.

Figure 18.3 depicts the distribution of the two force strain measures. The results obtained with 100 elements conform very well to the semi-analytic reference solution. The axial strains ε are constant in the sticking region, as demanded by (18.15), and gradually increase in the sliding zone. The peaks of the shear strain distribution on
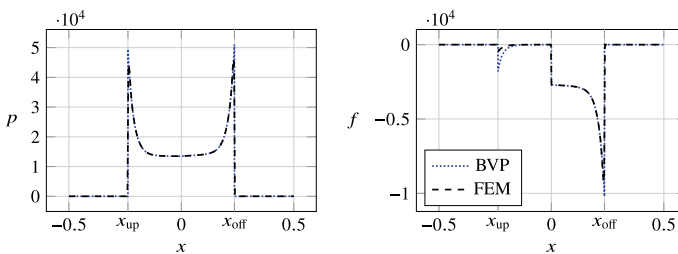
Fig. 18.2 Distributions of normal (left) and tangential contact forces (right)
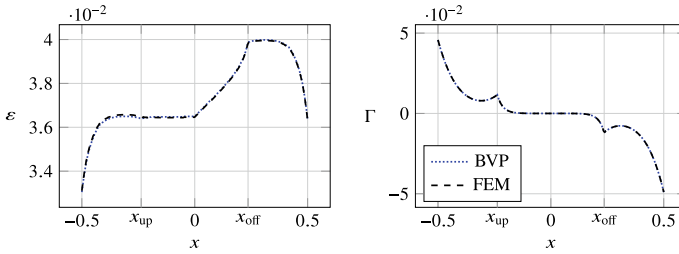
Fig. 18.3 Distributions of strain measures ε (left) and Γ (right)

the right are obviously related to the establishment and loss of contact and, aside from the bordering regions, no significant shear deformation arises in the contact domain. Different results are to be expected, once distributed contact moments come into play, which are absent here.

Demanding $v_{rel} = 0$ in (18.14) for $x_{trans} = 0$ yields an angular velocity of $\omega = 1.4807$ (the relative error between the models is less than 1×10^{-4}). Now, to estimate the range of meaningful values for ω, we can simply shift x_{trans} towards the bordering points x_{off} and x_{up} to find limiting solutions of a pure sticking and a pure sliding belt, respectively. The corresponding interval turns out to be extremely tight: $\omega \in [1.4779, 1.4825]$, which clearly demonstrates the advantage of providing x_{trans} as part of the system parameters instead of ω.

18.5   Conclusion

We have developed a finite element procedure to compute the stationary motion of the considered one-pulley belt drive example. The scheme relies on the theory of shear deformable rods, and the simulation results are compared to analytic results obtained through numerical integration of the corresponding boundary value problem.

To this end, only a single pulley has been considered and the closed loop, two-pulley belt drive problem is left for future research. Again, shear deformable rod theory should be used when tackling this more complex problem with the proposed solution strategies. For completeness, stationary dynamics should be considered as well. A difficulty that arises in the looped problem is that the constant material transport velocity c becomes an additional unknown.

References

1. Belyaev, A.K., Eliseev, V.V., Irschik, H., Oborin, E.A.: Dynamics of Contour Motion of Belt Drive by Means of Nonlinear Rod Approach, pp. 21–29. Springer International Publishing, Cham (2019). https://doi.org/10.1007/978-3-319-90884-7_3
2. Oborin, E., Vetyukov, Y.: Steady state motion of a shear deformable beam in contact with a traveling surface. Acta Mech. **230**(11), 4021–4033 (2019). https://doi.org/10.1007/s00707-019-02476-x
3. Simo, J., Laursen, T.: An augmented Lagrangian treatment of contact problems involving friction. Comput. Struct. **42**(1), 97–116 (1992). https://doi.org/10.1016/0045-7949(92)90540-G
4. Vetyukov, Y., Oborin, E., Scheidl, J., Krommer, M., Schmidrathner, C.: Flexible belt hanging on two pulleys: contact problem at non-material kinematic description. Int. J. Solids Struct. **168**, 183–193 (2019). https://doi.org/10.1016/j.ijsolstr.2019.03.034

Chapter 19
Modeling, Simulation, and Experimental Analysis of Liquid Sloshing Dynamics

Johannes Schröck, Johannes Wenninger, Erwin Karer, and Andreas Eitzlmayr

Abstract For the simulation of liquid sloshing, particle simulation methods allow a detailed investigation of the acting dynamics. Since these methods usually go along with considerable computational loads the application of alternative, simplified models is a usual proceeding. However, the parameters of the simplified model can not be directly computed from physical quantities in the general case, such that parameter identification based on measurements is required. In applications where experimental investigation is expensive, the use of particle simulation results for parameter identification can be a promising alternative. This contribution considers the identification of the parameters of a simplified model for different container geometries and filling levels based on smoothed particle hydrodynamics (SPH) simulation results. The comparison with experimental data verifies the accuracy and sensitivity of both the used particle model as well as the simplified model.

19.1 Introduction

New mechatronic conveyor concepts like the long stator linear motor (LLM) actuator give additional degrees of freedom for the transportation of objects compared to conventional conveyor systems. The conveyed objects get moved by separate shuttles individually controlled based on their position along the LLM actuator. This provides completely new options for object transportation, processing, and throughput optimization. The transport speed can be adapted to the radius of curvature along the transport track. The motion of the objects can be synchronized to each individual processing cell along the track. The flow of objects can be efficiently split to different tracks and several flows are easily brought together to a common track. Using individual controllable transportation shuttles instead of a common conveyor belt may be a key-enabler component for agile production.

J. Schröck (✉) · J. Wenninger · E. Karer · A. Eitzlmayr
Linz Center of Mechatronics GmbH, Altenberger Straße 69, 4040 Linz, Austria
e-mail: johannes.schroeck@lcm.at

A specific application is the fast transport of open containers filled with liquid. Depending on acceleration and track geometry, the dynamics can cause the liquid spilling over the container opening. Up to now, sloshing is prevented by a conservative setup of the transportation system. Using individually controlled transport shuttles instead of a common conveyor belt allows to accordingly adapt velocity profiles for the movement, which limit the sloshing angle to a predefined value. Hence, each segment of the track can be safely passed through by simultaneously maximizing the throughput. In order to determine the optimal shuttle trajectory along an arbitrary predefined track, a model-based approach is required. In this context, it is sufficient to consider the dominant sloshing characteristics.

The simplest model representing a sloshing liquid is a pendulum model with properly defined parameter values for the pendulum mass, pendulum length, and damping coefficient. For containers with circular or square cross sections at least mass and length parameters can be derived from analytical considerations of container geometry, filling level and liquid density, see, e.g., [1]. In the general case, where a more complex container geometry is used, the correct parameters have to be determined by parameter identification methods based on measurements from experimental investigations. Clearly, experimental investigations are often expensive and time-consuming. Therefore, this paper proposes to use SPH simulation results for identification of the parameters of the pendulum model. As a first step for a general approach, this procedure is validated by considering a simple container geometry. The comparison with measurements from experimental investigations illustrates the reliability of this approach.

The paper is structured as followed: Sect. 19.2 describes the experimental test-bed. Section 19.3 presents the mathematical model of the considered pendulum model. Identification and validation of the model parameters is reported in Sect. 19.4 based on measurement results. Section 19.5 shows the simulation results based on SPH, which are used for parameter identification of the pendulum model in Sect. 19.6.

19.2 Experimental Test-Bed

The test-bed consists of two linear axes with ball screw drives from *HIWIN* (HM060S and HM040S) which enable a range of motion of 0.5×0.3 m in the (x, y)-plane, see Fig. 19.1. Each linear axis is driven by a *B&R* synchronous motor of the 8LS series, that is controlled by an *ACOPOS* servo drive (8V1010). The control task is implemented on a *B&R Power Panel* C70 PLC with a cycle time of 2 ms using PID position control. The liquid container to be transported is mounted to the *y*-axis via a high accuracy 3-axis-force sensor (K3D60a) from *ME-Messsysteme GmbH* with nominal measuring force of ± 50 N and accuracy class 0.05%. *DEWETRON* DAQP-STG measurement amplifiers are used to connect the force signals to the PLC via an analog input X20 module. The measurement accuracy of the container position results from the motor encoder (10^4 increments per revolution) and the ball screw pitch of 10 mm. Data acquisition of force, position and velocity is realized by means of the PLC with a sample time of 2 ms.
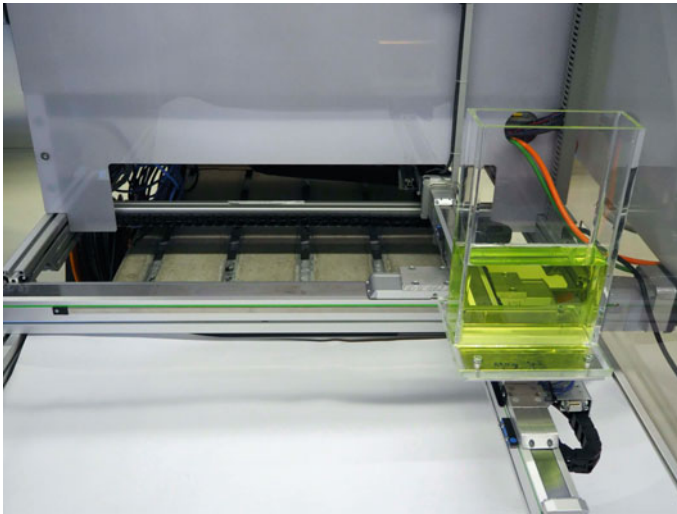
**Fig. 19.1**   Testbed with liquid filled container mounted on two linear axes

The test-bed is used to move containers filled with different amounts of water along certain trajectories in order to investigate the dynamics of the sloshing water by means of the force measurements. It will be shown, that the behavior of the liquid can be accurately reproduced by means of both proper defined particle simulations and a simplified model, suitable for real-time simulations and model-based control applications.

19.3   Simple Model for Sloshing

In this contribution, the focused application of transporting liquid-filled container results in a smooth sloshing behavior, i.e., there appears no splashing and no separation of the liquid volume in different entities. The container is considered to be open at the top, and a continuous free liquid surface is assumed. In this case, linear sloshing can be supposed, which means the sloshing can be represented by its natural frequencies [1]. Since the main contribution concerning sloshing forces and sloshing angle corresponds to the first sloshing mode, the pendulum model is a satisfactory choice.

In the following investigations, it turns out that only a certain amount of the liquid mass contributes to the sloshing dynamics. For this reason, the liquid mass M_{liq} is separated into two parts, $M_{liq} = M_{liq,r} + m$, with m responsible for the sloshing and $M_{liq,r}$ representing the remaining liquid mass. Hence, the pendulum model can be defined by the two masses M and m and the pendulum length l as shown in the scheme in Fig. 19.2a with $M = M_{liq,r} + M_t = M_{liq} - m + M_t$, where
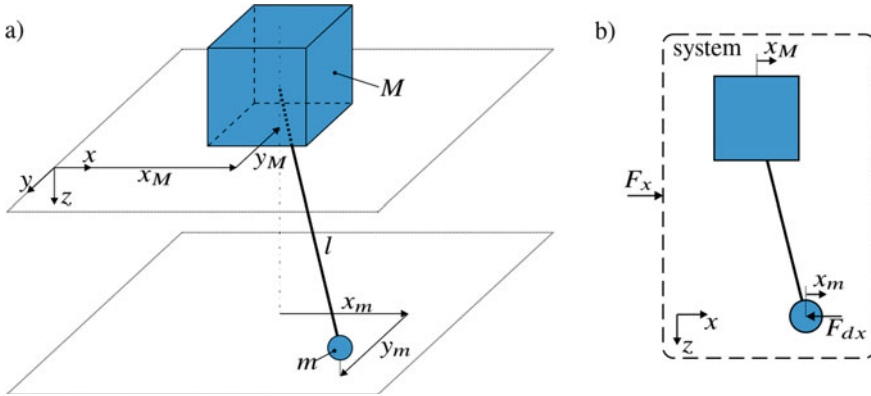
Fig. 19.2 Scheme of the pendulum model (**a**) and linear momentum in x-direction (**b**)

M_t represents the mass of the empty container. The masses have two degree of freedom $\{x_M(t), y_M(t)\}$ and $\{x_m(t), y_m(t)\}$. The governing equations of motion can be derived by means of the Euler-Lagrange approach, i.e.,

$$\frac{d}{dt}\left(\frac{\partial T}{\partial \dot{\mathbf{q}}}\right)^T - \left(\frac{\partial T}{\partial \mathbf{q}}\right)^T + \left(\frac{\partial V}{\partial \mathbf{q}}\right)^T = \mathbf{Q}, \tag{19.1}$$

where $\mathbf{q}(t) = [x_m(t), y_m(t)]^T$ represents the generalized coordinates $T = \frac{1}{2}m\mathbf{v}_m^T\mathbf{v}$ the kinetic, and $V = -m\mathbf{g}^T\mathbf{r}_m$ the potential energy with the displacement vector $\mathbf{r}_m(t)$ and the velocity vector $\mathbf{v}_m(t)$ of the point mass m given by

$$\mathbf{r}_m(t) = \begin{bmatrix} x_M(t) + x_m(t) \\ y_M(t) + y_m(t) \\ \sqrt{l^2 - x_m(t)^2 - y_m(t)^2} \end{bmatrix}, \quad \mathbf{v}_m(t) = \begin{bmatrix} \dot{x}_M(t) + \dot{x}_m(t) \\ \dot{y}_M(t) + \dot{y}_m(t) \\ \dfrac{-x_m(t)\dot{x}_m(t) - y_m(t)\dot{y}_m(t)}{\sqrt{l^2 - x_m(t)^2 - y_m(t)^2}} \end{bmatrix}. \tag{19.2}$$

The generalized forces $\mathbf{Q}(t)$ result from additionally introduced viscous damping

$$\mathbf{Q}(t) = \left(\frac{\partial \mathbf{r}_m(t)}{\partial \mathbf{q}}\right)^T \mathbf{F}_r(t), \quad \mathbf{F}_r(t) = \begin{bmatrix} -d_{px}\dot{x}_m(t) \\ -d_{py}\dot{y}_m(t) \\ 0 \end{bmatrix}, \tag{19.3}$$

with $\mathbf{F}_r(t)$ being the damping forces based on individual damping parameters d_{px} and d_{py} in x- and y-direction. Finally, the governing equations of motion can be given in the form

$$\mathbf{M}\,\ddot{\mathbf{q}}(t) + \mathbf{G}(\mathbf{q}, \mathbf{u}, t) = \mathbf{Q}(t), \tag{19.4}$$

with the mass matrix $\mathbf{M}$, the vector of non-linear terms $\mathbf{G}(\mathbf{q}, \mathbf{u}, t)$, and the acceleration of the mass M as the inputs $\mathbf{u}(t) = [\ddot{x}_M(t), \ddot{y}_M(t)]^T$. For the parameter identification and validation of the model, the forces experienced by the high accuracy 3-axis-force sensor have to be considered. These forces are given by

$$F_x = (m + M)\,\ddot{x}_M + m\,\ddot{x}_m + d_{px}\,\dot{x}_m, \tag{19.5}$$
$$F_y = (m + M)\,\ddot{y}_M + m\,\ddot{y}_m + d_{py}\,\dot{y}_m, \tag{19.6}$$

which can be derived based on the linear momentum in x- and y-direction also, see Fig. 19.2b.

19.4   Parameter Identification and Validation with Measurements

The test-bed described in Sect. 19.2 is used to execute experiments with two different container geometries (circular and square cross section) and each of them with two different filling levels of water (1 l and 0.33 l). Three different trajectories for the movements are used, two open trajectories similar to semicircles with different radii (Fig. 19.3a), and a closed eight-shaped trajectory (Fig. 19.3c). In the following, the trajectories are called semicircular-shaped and eight-shaped. The deviations from a precise semicircle as well as the initial variation of the eight-shaped trajectory result from the applied PID position controller. However, since we are focusing on the sloshing behavior and successive experiments with the same settings that provide precisely the same results, these deviations represent no restrictions for the following investigations.

The parameter identification for the pendulum model is done via minimization of the error between measured and simulated forces Eq. (19.5) by adopting the values of the parameter set $\{m, l, d_{px}, d_{py}\}$.[1] For that, measurements with an duration of $\Delta t = 10$ s from experiments based on the semicircular-shaped trajectory with radius 80 mm are used, see Fig. 19.3a solid lines. The resulting parameter values are given in Table 19.1, where they are compared to values from analytical models from the literature [1]. These analytical models consider the container geometry with circular and square cross section but do not include damping. The parameters m and l are in excellent correspondence for all four container configurations.

Figure 19.4 confirms that with these parameters a very accurate agreement between measurements and simulation results can be achieved for all configurations. In order to illustrate the effect of the sloshing, Fig. 19.5b compares the arising forces for the investigated configurations relative to a rigid mass movement along the same


[1] The corresponding optimization was performed by means of the open source software SyMSpace [2].
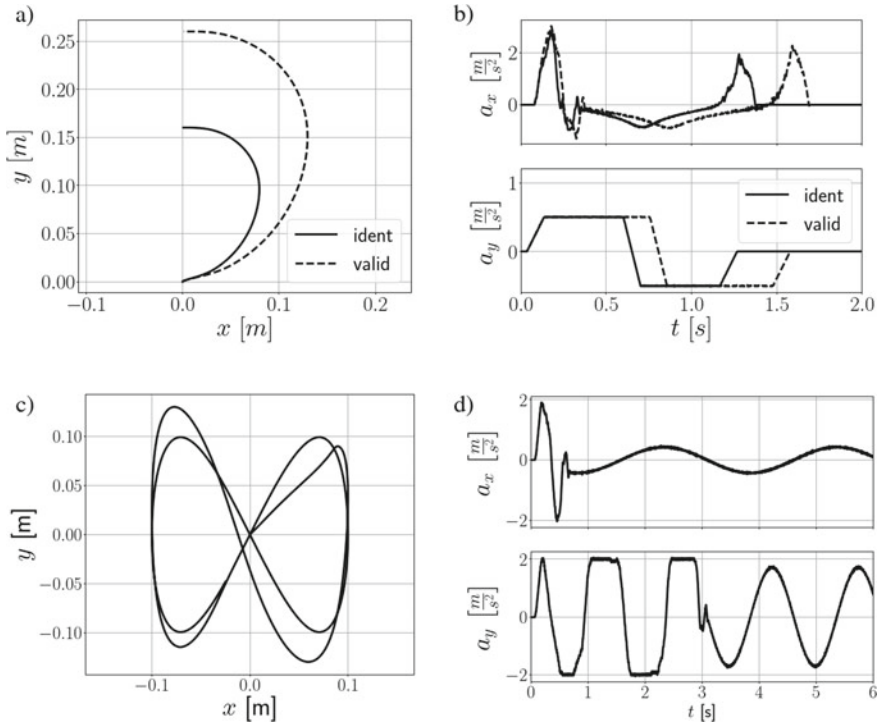
Fig. 19.3 Trajectories: **a** semicircular-shaped with radius $\in \{80, 130\}$mm and **c** eight-shaped; **b**, **d** corresponding acceleration signals $a_x(t)$ and $a_y(t)$ in x- and y-direction

trajectory, i.e., the sloshing forces are computed as the difference between measured forces and computed forces of a rigid mass. Obviously, there are minor differences in the evolution of the sloshing forces for square cross sections compared to circular cross sections. The amplitudes of the sloshing forces are not directly dependent on the filling level of the containers.

In order to validate the sensitivity of the identified parameter of the pendulum model, measurement and simulation results are compared for trajectories different from that used during the identification procedure. Figure 19.6a shows the evolution of the forces for a container with circular cross section and filling level 0.33 l moved along the semicircular-shaped trajectory with radius 130 mm, cf. Fig. 19.3a dashed lines. Obviously, this trajectory results in significantly lower sloshing compared the trajectory with radius 80 mm. Specifically, the sloshing represented by the force $F_y(t)$ is strongly reduced. While even for small amplitudes in $F_x(t)$ the agreement between measured and simulated results is highly accurate in Fig. 19.4, the deviations are higher with the trajectory of 130 mm. Nevertheless, the agreement between measured and simulated results is excellent, in particular during the motion of the liquid-filled container.
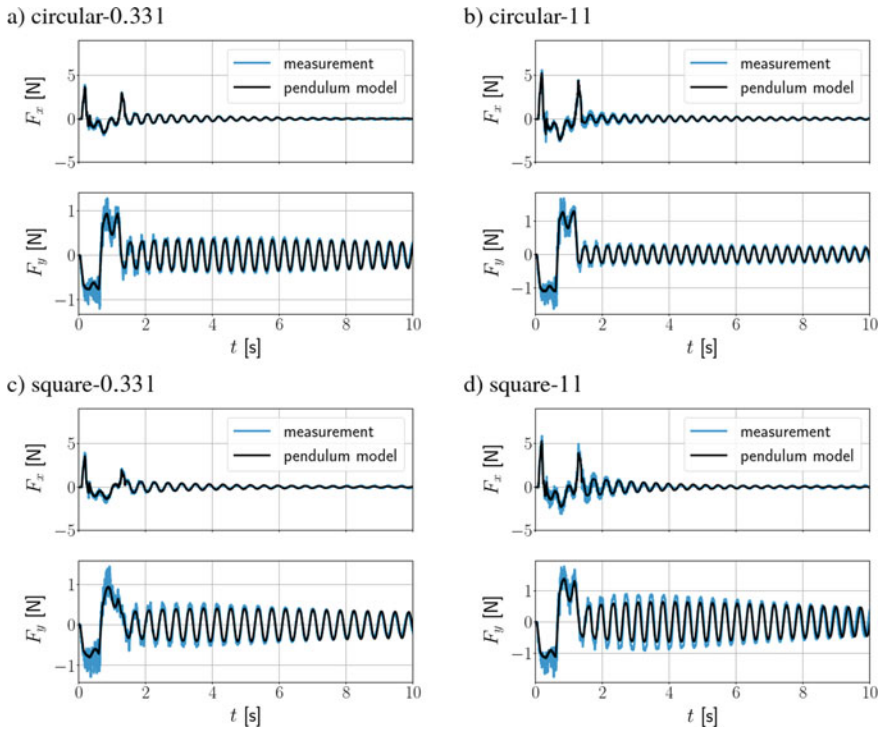
Fig. 19.4 Comparison of measurements and simulations results of the forces based on the semicircular-shaped trajectory with radius 80 mm for different container configurations
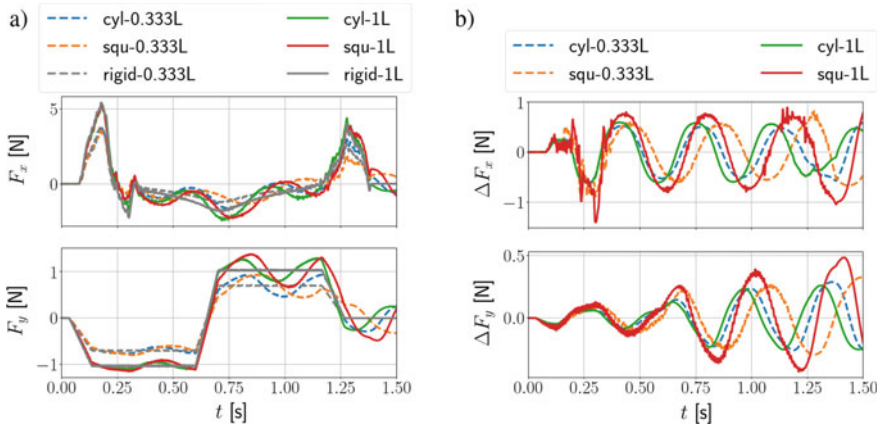
Fig. 19.5 Forces of the semicircular-shaped trajectory with radius 80 mm **a** absolute forces and **b** computed sloshing forces relative to a rigid mass movement
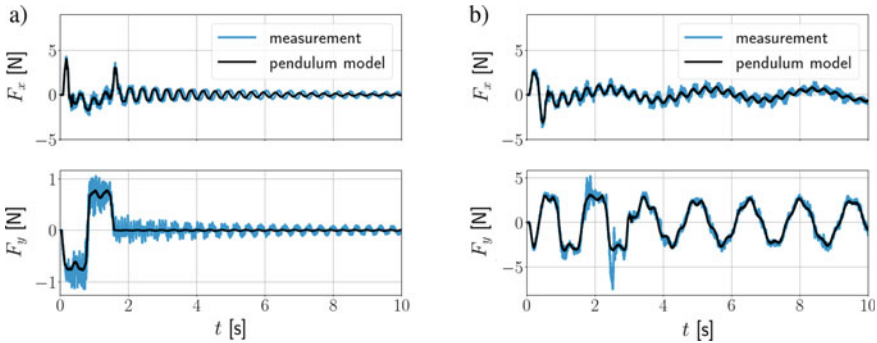
Fig. 19.6 Validation of the forces for the container with circular cross section and 0.33 l filling level for **a** the semicircular-shaped trajectory with radius 130 mm and **b** the eight-shaped trajectory

In addition, Fig. 19.6b shows the results for the same container configuration but for the eight-shaped trajectory. In contrast to all other experiments, here the liquid-filled container is in continuous motion. Also in this case, excellent agreement between measurement and simulation results can be observed. This leads to the conclusion that the pendulum model with identified parameters is sufficient accurate and robust for the representation of sloshing in moving liquid-filled containers.

19.5 Smoothed Particle Hydrodynamics Simulations

In addition to the experimental measurements, sloshing in moving containers is numerically investigated using the SPH method, which employs discrete Lagrangian mass elements (so-called fluid particles) instead of a mesh-based spatial discretization. For free-surface flow phenomena, this meshless nature is of specific advantage, since the Lagrangian fluid particles inherently allow the representation of the dynamic liquid surface, without any additional modeling complications, such as typically required for mesh-based methods.

The simulations are conducted using the particle simulation software LIGGGHTS [3], coupled to the mechatronic systems simulation package HOTINT [4, 5]. This coupling facilitates SPH simulations in the context of fluid structure interaction (FSI) problems [6]. The SPH model included in LIGGGHTS is based on the classical, weakly compressible formulation as originally introduced by Monaghan [7], and additionally the following specific variants or modifications are used:

- Morris model for viscous forces [8],
- discretized continuity equation for the density [7],
- first-order consistent density filtering by moving least squares (MLS) [9],
- equation of state for liquids according to [7],
- Wendland smoothing kernel [10] and

- explicit time integration by a 2nd order Verlet scheme, see, e.g., [11].

The solid wall boundary conditions are imposed by using the particle-wall interaction model according to [12]. Moreover, another correction is employed to the density field in order to avoid the accumulation of errors due to the numerical time integration of the continuity equation, which may lead to inconsistencies between mass, density, and volume. More details about this correction and the used SPH model are provided in previous work [13].

In the SPH simulations, the spatial resolution is varied by using values of 2 and 4 mm for the initial particle spacing, yielding a total particle number of 125000 and 15625 for 1 l of water, respectively. The smoothing length is set to the 1.25-fold of the initial particle spacing in each case, as previous studies [13] revealed to be reasonable. The speed of sound is chosen to be $10\frac{m}{s}$, which is sufficient to keep the numerical compressibility negligible under the investigated conditions. With that, a time step of $1e^{-5}$ s is sufficient for numerical stability in most cases, except for the cases with 125000 particles, here the time step is $5e^{-6}$ s. The MLS filter is periodically applied every 10 time steps.

Simulations are conducted for the same scenarios as in Sect. 19.4. The resulting forces in the x- and y-direction over time are shown in Fig. 19.7 compared to the corresponding measurement data. For the semicircular-shaped trajectory, excellent agreement of the forces is achieved during the movement (until approx. 1.4 s). In some cases the post-excitation sloshing agrees well too, specifically $F_x(t)$ for the cases with 0.33 l. Generally, $F_y(t)$ shows less agreement than the $F_x(t)$ and the cases with 0.33 l show better agreement than the cases with 1 l. However, the sloshing frequency agrees well in all cases, and the damping rate is similar between measurements and SPH results with 2 mm particle spacing. The 4 mm SPH results show significantly higher damping, therefore, the post-excitation sloshing is distinctly better reproduced by the 2 mm SPH resolution. Clearly, the computational expense is usually about the 10-fold with 2 mm compared to 4 mm SPH resolution, and if only the excitation period is of interest, the 4 mm resolution is sufficient (as often the case in automation and control applications).

For the eight-shaped trajectory, the comparison is similar, see Fig. 19.7e. In the first second of the movement, the agreement of the forces obtained from SPH simulations and measurements is excellent. In contrast to the semicircular-shaped trajectory, there is no post-excitation period, since the container is continuously moved along the closed eight-shaped trajectory. Instead of that, there are higher sloshing modes superposed, whose amplitudes decrease slowly over time. Interestingly, this is more pronounced in the x-direction, whereas for the semicircular-shaped cases discussed above the post-excitation sloshing amplitude is higher in the y-direction.

In summary, the comparison of the forces from SPH simulations and measurements shows excellent agreement, specifically during the movements. Some differences appear in the post-excitation sloshing. These could be related to the finite stiffness of the experimental setup, which introduces additional dynamics depending on direction and filling level, as well as numerical dissipation in the SPH simulations, which causes additional damping depending on the numerical resolution. Analogous

a) circular-0.33 l, semicircular traj. (80 mm)   b) circular-1 l, semicircular traj. (80 mm)

c) square-0.33 l, semicircular traj. (80 mm)   d) square-1 l, semicircular traj. (80 mm)

e) circular-0.33 l, eight-shaped trajectory
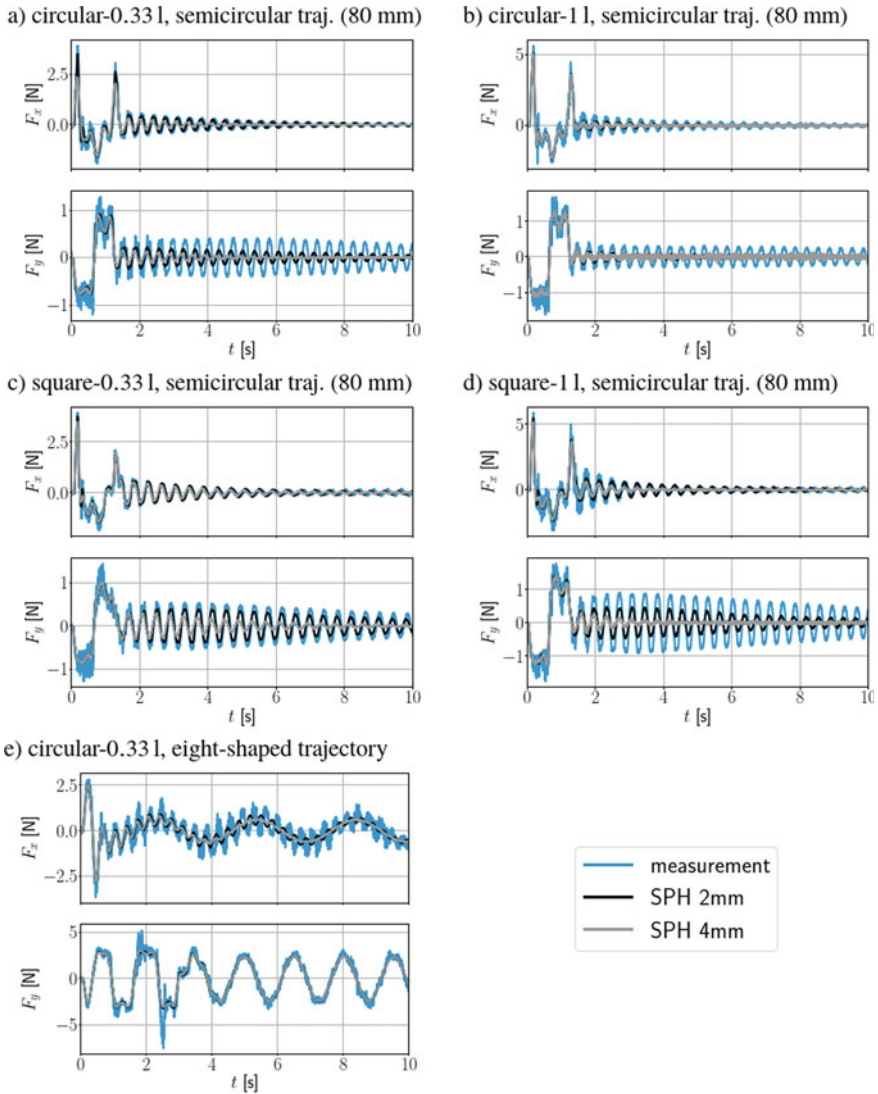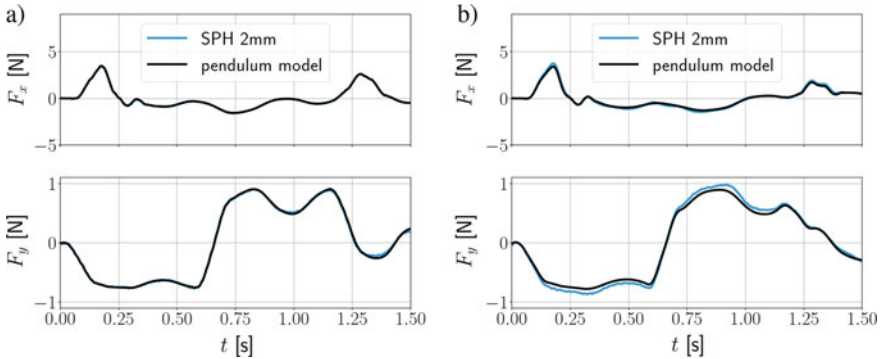
measurement
SPH 2mm
SPH 4mm

Fig. 19.7 Comparison of forces obtained from SPH simulations and measurements

to the measurements, the SPH results can be used for the parameter identification of the simplified model, which will be discussed in the following section.

Fig. 19.8 Comparison of SPH and pendulum model simulation results for the semicircular-shaped trajectory with radius 80 mm, filling level 0.33 l, and containers of **a** circular and **b** square cross section

19.6   Parameter Identification Based on the SPH Simulations

Similar to Sect. 19.4, the parameter identification for the pendulum model is repeated based on the SPH simulation results presented in the previous section. In contrast to Sect. 19.5, here only the moving phase of the container is considered for the identification, due to the above-discussed differences during the post-excitation evolution. However, this represents no restriction here, since the focus of this contribution is on the sloshing behavior during the movement in order to address, e.g., optimal trajectory planning of a transportation shuttle, where the evolution of post-excitation effects are of minor interest.

As shown in Fig. 19.8, simulation results of the identified pendulum model for containers with circular and square cross sections and filling level 0.33 l are in excellent agreement with the SPH simulations. Table 19.1 shows a comparison of the parameters identified from SPH results, with the parameters identified from measurement data. Obviously, the pendulum length l agrees well in all cases, while the sloshing mass m shows some deviations, specifically for the container with the square-shaped cross section (18.2%). The damping parameters identified from SPH results differ strongly, which results from the exclusion of the post-excitation phase in that case.

Table 19.1 Comparison of the values for the identified pendulum parameters with values from the literature [1]

	Circular			Circular			Square			Square		
	0.331			11			0.331			11		
	lit	meas	SPH	lit	meas	SPH	lit	meas	SPH	lit	meas	SPH
m	0.163	0.1630	0.1490	0.178	0.1730	0.1580	0.201	0.1980	0.1630	0.256	0.2480	0.2030
l	0.030	0.0309	0.0305	0.027	0.0280	0.0279	0.041	0.0415	0.0407	0.032	0.0338	0.0342
d_{px}		0.097	0.110		0.062	0.200		0.088	0.019		0.156	0.091
d_{py}		0.016	0.000		0.020	0.000		0.025	0.000		0.037	0.000

19.7 Conclusion

Liquid sloshing in containers of different geometries that are transported along different trajectories is investigated by considering the forces acting on the container. Comparisons with measurements show that the system dynamics can be accurately reproduced by a pendulum model. Simulations based on smoothed particle hydrodynamics (SPH) provide results in excellent agreement to the measurements too. However, special attention must be paid to the damping behavior. These investigations justify the approach of identifying the pendulum model parameters based on SPH simulation results.

As a final result, it can be shown that this approach yields reliable values for the main model parameters, such that it is reasonable to replace experiments with simulations in this context in order to reduce costs and time. Future activities will take advantage of the simple pendulum model for trajectory planning and optimization for fast container transport to prevent the liquid from spilling over the container opening by assuring limits of the maximum sloshing angle.

References

1. Dodge, F.T.: The new "dynamic behavior of liquids in moving containers". Southwest Research Institute, San Antonio (2000)
2. SyMSpace, Linz Center of Mechatronics GmbH (2020). http://www.lcm.at
3. LIGGGHTS(R): Open source particle simulation code (2020). https://www.cfdem.com
4. Gerstmayr, J., et al.: Hotint: a script language based framework for the simulation of multibody dynamics systems. In: Proceedings of the ASME 2013 IDETC-CIE Conference (2013)
5. HOTINT: A flexible multibody system dyn. freeware code (2020). https://hotint.lcm.at
6. Schörgenhumer, M.: Smoothed particle hydrodynamics with consistent boundaries for fluid-structure interaction, No. 33 in Schriftenreihe Advances in Mechatronics. Trauner Verlag, Linz, Austria (2016)
7. Monaghan, J.J.: Simulating free surface flows with SPH. J. Comput. Phys. **110**(2), 399–406 (1994)

8. Morris, J.P., et al.: Modeling low Reynolds number incompressible flows using SPH. J. Comput. Phys. **136**(1), 214–226 (1997)
9. Gomez-Gesteira, M., et al.: State-of-the-art of classical SPH for free-surface flows. J. Hydraul. Res. **48**(S1), 6–27 (2010)
10. Wendland, H.: Piecewise polynomial, positive definite and compactly supported radial functions of minimal degree. Adv. Comput. Math. **4**, 389–396 (1995)
11. Monaghan, J.J.: Smoothed particle hydrodynamics. Rep. Prog. Phys. **68**(8), 1703–1759 (2005)
12. Eitzlmayr, A., et al.: A novel method for modeling of complex wall geometries in smoothed particle hydrodynamics. Comput. Phys. Commun. **185**(10), 2436–2448 (2014)
13. Schörgenhumer, M., Eitzlmayr, A.: Modeling of liquid sloshing with application in robotics and automation. IFAC-PapersOnLine **52**(15), 253–258 (2019)

Chapter 20
Test and Verification of Applying Neutral Equilibrium Mechanisms as Multiple Virtual Piers

Ming-Hsiang Shih and Wen-Pei Sung

Abstract The control logic of Neutral Equilibrium Mechanism, NEM, enables all the functions and advantages of the active control method, with little additional energy supply required, and provides reliable and effective control effects. In this study, a reduced-scale bridge with two virtual piers is constructed and the mathematical model of active control for this proposed NEM is proposed. Then, the control stability is discussed with dynamic test verification. Test results show that vertical displacement control at the installation position of NEM is more than 95% and closes to zero displacement; Arduino can accurately detect the displacement of the bridge and create a control signal; the PID controller precisely controls the cantilever rotation to the appropriate angle and provides the appropriate lift-balanced force based on bridge displacement changes. This experiment verifies that the NEM adjusts the rotation position of each control mechanism during the dynamic process so that it is synchronized with the structural deformation of the bridge, and achieves the research purpose of controlling the deformation of the bridge. The feasibility and practicality of this technology can be verified by this research and deserves continuous research and development.

20.1 Introduction

Taiwan has many rivers and steep mountains, and all districts rely on bridge systems. Presently, reinforced concrete construction, including pre-stressed construction, is mainly used for bridge construction in various countries.

M.-H. Shih (✉)
Department of Civil Engineering, National Chi Nan University, Nan-Tou, Taiwan
e-mail: wps@ncut.edu.tw

W.-P. Sung
Department of Landscape Architecture, Integrated Research Center for Green Living Technologies, National Chin-Yi University of Technology, Taichung, Taiwan
e-mail: wps@ncut.edu.tw

Especially, Taiwan is in the earthquake zone; frequent earthquakes and typhoons frequently threaten this area to cause various natural disasters and destruct bridges. After the natural disaster, the construction of these bridges takes time, and it is difficult to repair the traffic in a short time. Otherwise, the bridge is one of the vital living pipelines for disaster relief to shipping goods and materials. Therefore, how to build temporary bridges quickly to facilitate access and transport supplies is the most important issue for disaster relief units.

Presently, most of the military units are requested to set up a "Bailey Bridge" in response to the need for passage in the event of a related disaster in Taiwan. Sometimes, riverbed footpaths, culvert slings, steel bridges, and container-type steel bridges are built in different topographical conditions. But, the length of the net span of the installation of a disaster relief bridge must vary depending on the location according to the long section of the river or the water impact section. If the bridge length is increased, it will inevitably cause the following disadvantages: (1) structural components become larger in size, increase construction costs; (2) The relevant assembly material parts cannot be standardized. If the span is too long, it is necessary to install multi-bridge piers to meet the design requirement of the bridge. Therefore, the purpose of this study is to expect that the Neutral Equilibrium Mechanism can be developed for multi-virtual piers of the bridge. The research achievements [10–12, 14] show that this NEM can be developed into a single virtual pier of bridge, especially, the dynamic experimental verification that this NEM can provide the upper lift balance force to balance the moving load. The cantilever arm can rotate to the appropriate angle according to the measured displacement of the bridge. Therefore, to achieve the rapid construction of bridges and emergency relief, Neutral Equilibrium Mechanism, NEM, is expanded to form as multiple virtual piers of the bridge in this study. The operating mechanism of multi-virtual piers of the bridge must simultaneously detect the displacement of the bridge, and the cantilever mechanisms of NEMs need to consider the mutual behavior in this bridge with multiple NEMs to achieve the control purpose of this study.

The control logic concept and control mechanism of Neutral Equilibrium Mechanism enable this mechanism with all the functions and advantages of the active control method, and provide reliable and effective control effect with little additional energy supply. This NEM is mainly the application of the Newtonian motion theorem and is based on the principle of conservation of energy. This technology properly applied the principles of machinery to generate useful active control force; it can be designed as a force-saving tool. This study is related to the development of new technology-structural control theory of structural shock absorption, and structural control [4, 13, 16] can be generally divided into passive control (isolation, shock absorption, and energy dissipation [2, 5, 7, 9], active control [1, 6, 17], and semi-active control [3, 8, 15]. This study briefly explains the concept and control theory of NEM used in the virtual pier of the bridge. Then, the reduced-scale bridge with two virtual piers is constructed with experimental design parameters and control parameters of this study is introduced. The dynamic test is to verify the control stability of the bridge with this NEM. This test also demonstrates that the rotation position
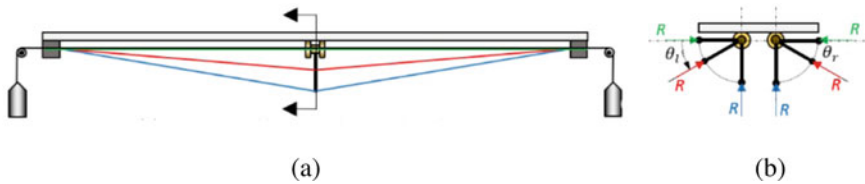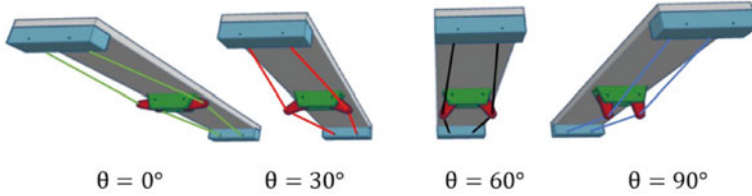
Fig. 20.1 The change of the cantilever arm and pre-stressed anchor of steel tendon

of each NEM is adjusted in the dynamic process by the experimental method, so as to synchronize with the deformation of the bridge structure and achieve the research purpose of controlling the deformation of the bridge.

20.2 Methodology

20.2.1 The Concept of Virtual Pier

The reduced-scale bridge with dynamic test [11] verified that this NEM can be applied to form a single virtual pier of the bridge. This NEM can perform the desired effect of precisely controlling the vertical deformation of the bridge. This NEM must detect the static and dynamic load of the bridge in the course of operation. The cantilever arm of NEM must timely operate to the appropriate angle to produce the control force to balance the dead and dynamic load of the bridge and achieve the purpose of precision deformation control and practical application. Two high-tension steel tendons of NEM are anchored at the two ends of the bridge, supported at the midpoint of the bridge with a pair of cantilever arms with adjustable angle rotating to form a three-force balance state with an angled angle, as shown in Fig. 20.1a. The hinge of the rotary cantilever arm is parallel to the vertical axis of the bridge and coincides online with the anchor point of the steel tendon at both ends of the bridge. When the rotary cantilever arm changes the corner of the arm, it can change the combined vertical force of the steel tendons at the midpoint of the bridge on the left and right sides—control force, as shown in Fig. 20.1b. Thus, the deformation of the bridge can be changed to offset the dead and moving load on the bridge and reduce displacement. Figure 20.2 shows the rotation of the cantilever arm changing the position of the corner of the spin arm. The change of this rotation angle must be based on the static and moving load caused by the displacement change timely to produce the control force of NEM, to avoid the deformation of the bridge. However, the strength of pre-stressed tendon and the rotation of the cantilever arm to change the turn of the rotating arm must reach the required. It cannot exceed the expected value to achieve the control requirements and avoid the upper arch force causing upward deformation.

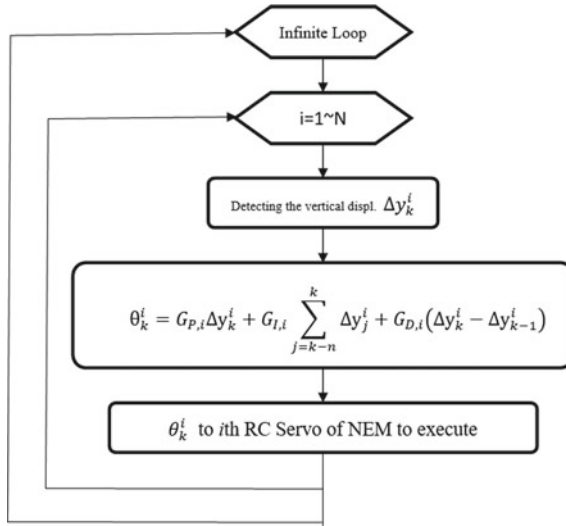Fig. 20.2 The change of the rotation angle of the cantilever arm of NEM

However, if NEMs are applied to form as multi-virtual piers of the bridge, the displacement changes of each unit position with NEM must be considered. To achieve the purpose of automatic control of the displacement at each installation position of NEM to be zero, the controller must continuously monitor the changes of the displacement of the bridge at each installation position of the NEM. Then, PID controllers are applied to calculate the target value of the control force in the next step. The target value is then sent to the servo controller to complete the control adjustment action. This control process is executed cycle by cycle, with the working steps for each cycle as follows:

1. Detection of the dynamic responses at each installation location of NEM. The displacement responses of the bridge due to the moving load is Δx_k^i, where i represents the number of the i-th NEM (same as below); k represents the k-th step (same as below).
2. The PID controller determines the rotation angle change of the cantilever arm for each NEM to the target position of the next step θ_k^i, as follows:

$$\theta_k^i = G_{P,i}\Delta x_k^i + G_{I,i} \sum_{j=k-n}^{k} \Delta x_j^i + G_{D,i}(\Delta x_k^i - \Delta x_{k-1}^i) \qquad (20.1)$$

where the Δx_k^i represents the displacement of k step at the position of i-th NEM. $G_{P,i}$, $G_{I,i}$, and $G_{D,i}$ are proportional, integral, and differential gain factors, respectively. n is the number of integral steps; take at least 2 steps.
3. Transfer the target position of each NEM to the micro-actuator at each positioned mechanism, so that it completes the corresponding rotary cantilever arm to change the rotation angle of NEM. Control flowchart is shown in Fig. 20.3. Each NEM detects the deformation of the bridge at the position of the device to change the rotation angle of the cantilever arm of NEM. The control technology is similar to the concept of active control method; Feedforward and Feedback control diagram of active control is shown in Fig. 20.4.

Fig. 20.3 The flowchart of the rotation angle changes of multiple virtual piers of bridge at each NEM
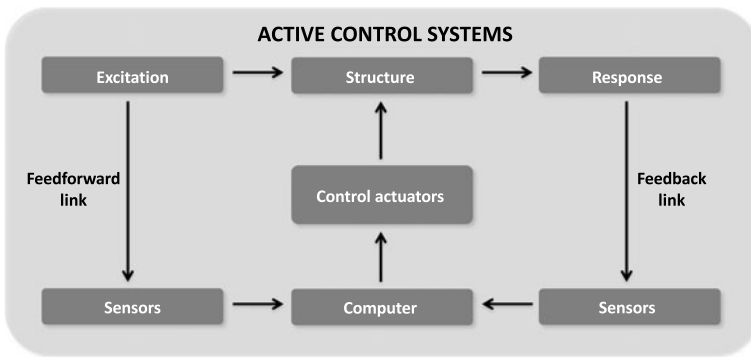
Fig. 20.4 The control diagram of active control for multiple virtual piers of bridge

20.2.2 Test Set-Up

In order to judge the control benefits of this NEM to form as multi-virtual piers of the bridge, dynamic experiments are conducted, as shown in Fig. 20.5, to obtain relevant data. This data contains the gain coefficients in the operation of PID controllers and the setting of the high-tension values of steel tendons as well as the rotation angle change of cantilever arm of NEMs. Then, the change of the vertical displacements at each NEM installed position is detected by the digital image correlation method. Figure 20.5 is the setup of experimental device for multi-virtual piers of bridge, and Table 20.1 is the relevant parameter set for this dynamic test.
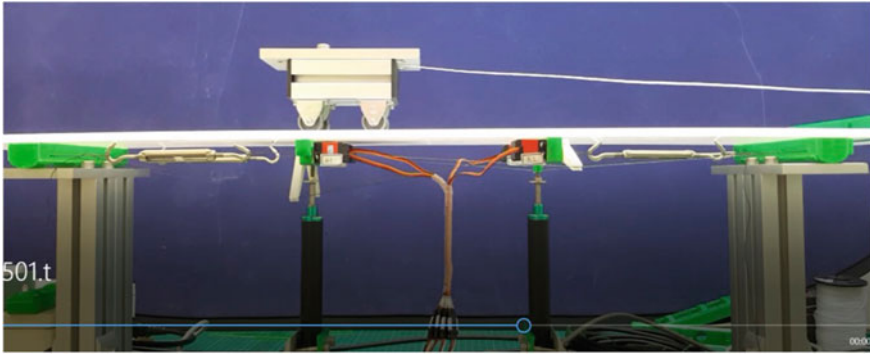
Fig. 20.5 The test setup for multiple virtual piers of bridge

The sensor part of this experiment: (1) displacement meter is set up at the one-third and two-thirds of the bridge model to measure the displacement responses of the bridge; (2) microcontroller units, MCUs, are applied to measure the displacement and speed responses of the bridge, calculated by the detected displacements and time interval of the sensor data of MCU. The operating principle is to receive the displacement change of the one-third and two-thirds of the bridge from the displacement meters and calculate their instantaneous velocity, respectively. Then, the required control forces are separately calculated to predict the rotation angles of these two positions by Eq. (20.1) of RC servos to turn the RC servo to their suitable angles to provide the appropriate control forces. The main power of RC servo, used in the remote-control model with very little output power, is applied to explore the displacement response of the bridge with two NEMs. In this study, a PID controller with one control gain under the action of moving load is used to compare the control effect with the bridge without control. The test parameters of this experiment are listed in Table 20.1.

This test is equipped with a single-chip microcomputer controller (Arduino) and modified digital image correlation method, DIC, to detect vertical displacement responses and the rotation angle change of the rotating cantilever arm of the NEMs to explore the change of control forces, moving load, and displacement variations of the bridge with and without control. The displacement responses, caused by the moving load at the installation position of NEMs of the bridge, are discussed according to the relevant response of the cantilever mechanism, servo machine, and steel tendon. Then, the control signal is provided to the RC servo. The RC servo controls the rotation angle of the cantilever arm, which in turn controls the change of angle between the combined force and the horizontal plane supplied by the steel tendon on the lever arm to verify the suitability and correctness of this control mechanism.

Table 20.1 The materials and specification of reduced-scale and test parameters of this test

| Category	Material	Specification	Q'ty
Control mechanism	RC Servo	Size of torque : 250N · cm; Angle control accuracy of RC Servo : 1.2 degree	4
	Cantilever arm	Length between the connection of fixed steel tendon and anchor point : 50mm; Material: Polylactic Acid (PLA), manufactured by 3D printing.	4
	Polyethylene Line (PE)	Tensile strength: 250N	2
Model of Bridge	Bridge deck	Size : Length=1100mm, width= 120mm, thickness=15mm, moment of inertia of area= $2 \times 10^5 (mm^4)$; Material: Polypropylene plastic sheet, polypropylene (PP);Young's modulus is between $1300{\sim}1800(N/mm^2)$ 。	1
	Anchor seat	Size: Length=120mm, width=30mm, thickness=20mm; Material: Aluminum alloy metal block; Support type: Simple support.	2
Sensor	Displacement meter	Resistive type	2
Controller	Microcontroller unit (MCU)	Arduino DUE	1
Test parameter	**Parameter range**		
Dynamic test	Self-weight: 18.97N; Speed of Vehicle: 6.38 cm/sec, Speed of test vehicle is equivalent to 4.5km/hr. when the length of the bridge is 20m.		
	1. Without NEM control		
	2. Control gain of PID controller of these two NEMs: G_P=2, G_D=0.0 G_I = 0.02		

20.3   Test Results and Discussions

The time history of vertical displacements for the bridge with and without NEM control is shown in Fig. 20.6, where the blue and red circles are located at the position of the NEMs, at 1/3 and 2/3 net span of the bridge. When the moving load moves from right to left, the blue and red dotted lines are uncontrolled for the bridge, with the displacement time running at 1/3 and 2/3 net span of the bridge. The blue and red solid lines are at 1/3 and 2/3 net span of the bridge when under NEM control. At the right of the figure is the image during the experiment and the rotation response of the
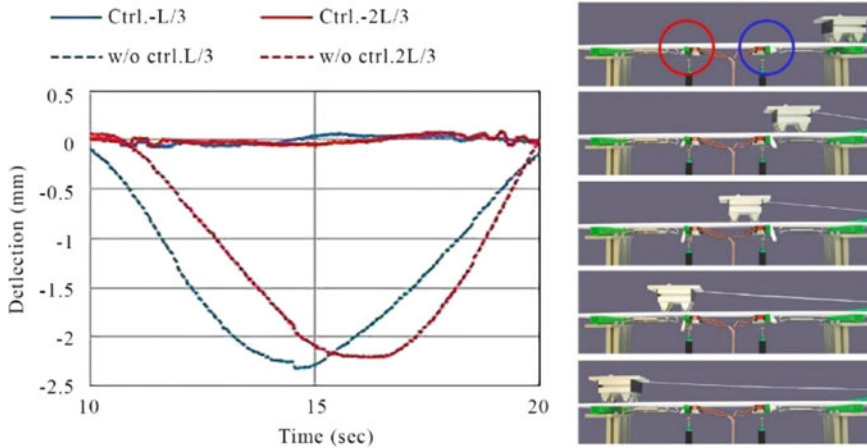
Fig. 20.6 Test results of bridge under control of multiple NEMs and without control

NEM cantilever when it is controlled by the PID controller. The following five stages describe the control status and effect of the NEM controller in this experiment.

1. Stage One: When the vehicle moves from the right-hand side to left-hand side, the NEMs just bear the dead load of the bridge. Therefore, the cantilever arms of the control mechanism at the location of 1/3 and 2/3 of the bridge maintain a horizontal orientation, as shown in Fig. 20.7a. These NEMs do not provide the control force to balance the moving load, and the vertical displacements of 1/3 and 2/3 of the bridge are zero.
2. Stage Two: When the moving load is located between the right end and 1/3 point of the bridge, the vertical displacements without the NEMs at the 1/3 and 2/3 of the bridge are 1.5 mm and 0.8 mm, respectively. However, the rotation angle of the RC servo at 1/3 position of bridge turns bigger degrees than that at 2/3 position of the bridge under NEMs control, as shown in Fig. 20.7b. The vertical displacements are only 0.02 and 0.03 mm at 1/3 and 2/3 of the bridge, respectively.
3. Stage Three: When the moving load is located at the midpoint of the bridge, the vertical displacements without the NEMs are 2.3 mm and 2.1 mm at 1/3 and 2/3 of the bridge, respectively. Moreover, both rotation angles of the servos increase and almost turn at the same degree, as shown in Fig. 20.7c. Otherwise, the vertical displacements under NEMs controlled are only 0.03 and 0.02 mm at 1/3 and 2/3 of the bridge, respectively.
4. Stage Four: When the moving load is located at the 2/3 point and the right end of the bridge, the vertical displacements without the NEM are 1.0 mm and 1.5 mm at 1/3 and 2/3 of the bridge, respectively. However, the rotation angle of the RC servo at 1/3 position turns less degrees than that at the 2/3 position of the bridge under NEMs controlled, as shown in Fig. 20.7d. Moreover, the vertical displacements are only 0.03 and 0.02 mm at 1/3 and 2/3 of the bridge, respectively.

(a) Stage one   (b) Stage two

(c) Stage three   (d) Stage four
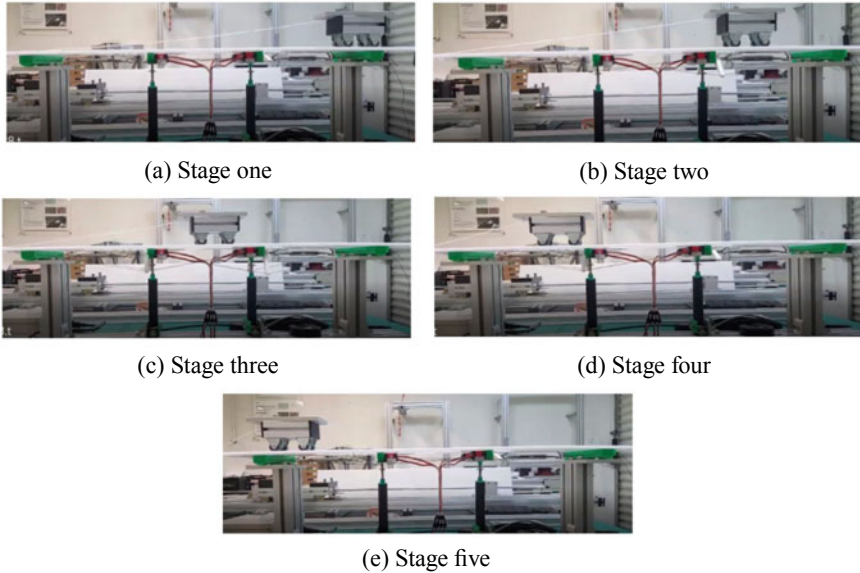
(e) Stage five

Fig. 20.7 Five stages of photos for the dynamic test of bridge with two virtual piers

5. Stage Five: The bridge bears only the dead load of the bridge. The rotation angles of the cantilever arms return to the horizontal direction, as shown in Fig. 20.7e, and the vertical displacement is zero.

20.4 Conclusions

In this study, the concept of the bridge with two NEMS to form as two virtual piers and the active control method to control the dynamic deformation, and then a reduced-scale bridge with two virtual piers and Arduino devices to detect the dynamic deformation of the bridge are proposed. The angle change of the cantilever arm of NEM is calculated and predicted by the proposed mathematical model, and transmitted to the PID controller to control the cantilever rotation to the appropriate angle to provide the lifting force in order to balance the moving load. After the dynamic experiment, some conclusions are obtained as follows:

1. The vertical displacement control of the bridge under control of NEM at the position with NEM is more than 95%, and it closes at zero;
2. From the test photos displayed, the PID controller can precisely control the cantilever rotation to the appropriate angle and provide the appropriate lift-balancing load based on the vertical displacement change.

3. This experiment confirms that NEM can be expanded to multi-virtual piers of a bridge, and the interaction behavior between multiple NEMs can be controlled for precise control purposes. The feasibility and practicality of this technology can be certified by this research and deserves continuous research and development.

References

1. Chung, L.L., Lin, R.C., Soong, T.T., Reinhorn, A.M.: Experiments on active control for MDOF seismic structures. J. Eng. Mech. ASCE **115**(8), 1609–1627 (1989)
2. Cunningham, B.B.: Using lead rubber bearings in base isolation systems. https://www.comsol.com/blogs/using-lead-rubber-bearings-in-base-isolation-systems/ (2015)
3. Hiemenz, G.J., Choi, Y.T., Wereley, N.M.: Seismic control of civil structures utilizing semi-active MR braces. Comput.-Aided Civil Infrastruct. Eng. **18**(1), 31–44 (2003)
4. Housner, G.W., Bergman, L.A., Caughey, T.K., Chassiakos, A.G.: Structural control: past present and future. J. Eng. Mech. **123**(9), 897–971 (1997)
5. Jangid, R.S.: Optimum lead-rubber isolation bearings for near-fault motions. Eng. Struct. **29**(10), 2503–2513 (2007)
6. Liu, K., Chen, L.X., Cai, G.P.: Active control of a nonlinear and hysteretic building structure with time delay. Struct. Eng. Mech. **40**(3), 431–451 (2011)
7. Nakajima, K., Iemura, H., Takahashi, Y., Ogawa, K.: Pseudo dynamic tests and implementation of sliding bridge isolators with vertical motion. In: 12thWCEE (2000)
8. Palacios-Quiñonero, F., Rubió-Massegú, J., Rossell, J.M., Karimi, H.R.: Semi-active-passive structural vibration control strategy for adjacent structures under seismic excitation. J. Franklin Inst. **349**(10), 3003–3026 (2012)
9. Salic, R.B., Garevski, M.A., Milutinovic, Z.V.: Response of lead-rubber bearing isolated structure. In: 14th World Conference on Earthquake Engineering (2008)
10. Shih, M.H., Sung, W.P., Wang, Y.C.: Developing a neutral equilibrium device as dynamic virtual piers for an emergency relief bridge. J. Measure. Eng. **6**(4), 289–296 (2018)
11. Shih, M.H., Sung, W.P.: Experimental verification of applying active control method as virtual support for relief bridge. Adv. Civil Eng. 12. Article ID 8505091. https://doi.org/10.1155/2019/8505091 (2019)
12. Shih, M.H., Sung, W.P.: Development of virtual-pier-control for eliminating moving load induced deflection of disaster relief bridge. In: 4th International Workshop on Advanced Dynamics and Model Based Control of Structures and Machines, Linz, Austria, September 22–25, 2019
13. Spencer Jr., B.F.: State of the art of structural control. J. Struct. Eng. **129**(7), 845–856 (2003)
14. Sung, W.P., Shih, M.H.: Applying neutral equilibrium control mechanism to develop new simple relief bridge. In: Global Engineering & Applied Science Conference (GEASC 2019), Tokyo, Japan, Aug. 27–29, 2019
15. Symans, M.D., Constantinou, M.C.: Seismic testing of a building structure with a semi-active fluid damper control system. Earthquake Eng. Struct. Dyn. **26**(7), 759–777 (1997)
16. Yao, J.T.P.: Concept of structural control. J. Struct. Div. **1972**, 1567–1574 (1972)
17. Zeng, X., Peng, Z., Mo, L., Su, G.Y.: Active control based on prediction of structural vibration feedback. In: 2014 Fifth International Conference on Intelligent Systems Design and Engineering Applications (2014). https://doi.org/10.1109/ISDEA.2014.35

Chapter 21
Optimal Control for a Space Rendezvous

Alois Steindl, Alexander Schirrer, and Stefan Jakubek

Abstract We consider the transfer of a chaser vehicle to a space station using impulsive control with minimal fuel consumption. It is assumed that the space station moves on a circular Keplerian orbit in a rotational symmetric gravitational field and that the chaser vehicle has already reached the station's orbital plane. The vehicle is steered by impulsive burns of the rockets. The problem is solved numerically using Pontryagin's maximum principle for impulsive controls by a multiple shooting method and a continuation procedure to study the variation of the optimal control strategy for varying time constraints. The problem is studied using a local linearized system and the fully nonlinear system using local Cartesian and polar coordinates.

21.1 Introduction

We investigate the energy-optimal impulsive control of a chaser vehicle (C) to a space station (S), which moves on a circular Keplerian orbit (Fig. 21.1). The chaser is steered by impulsive burns of its rockets. Finding the control strategy, which uses the least amount of propellant, is one of the most important tasks in manoeuvre planning.

The transfer problem between different Keplerian orbits has already been solved by Hohmann [1]. He suggested applying two thrusts in a tangential direction, which yields the optimal solution, as long as the orbits are not too far apart.

In this article we investigate the control problem using Pontryagin's Maximum principle, which is discussed in depth in [2]. In this reference also the problem with
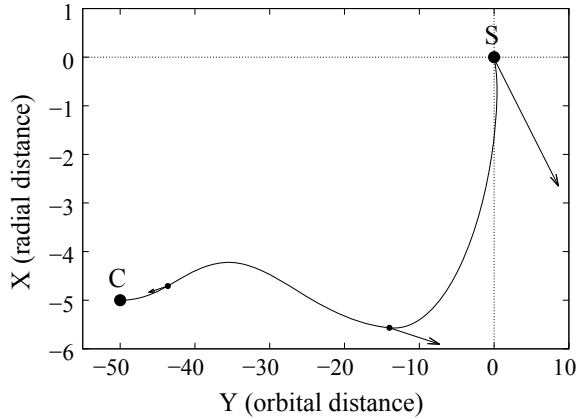
A. Steindl (✉) · A. Schirrer · S. Jakubek
TU Wien, Institute for Mechanics and Mechatronics, Getreidemarkt 9, 1060 Vienna, Austria
e-mail: Alois.Steindl@tuwien.ac.at

A. Schirrer
e-mail: Alexander.Schirrer@tuwien.ac.at

S. Jakubek
e-mail: Stefan.Jakubek@tuwien.ac.at

Fig. 21.1 A chaser vehicle (C) should be transferred to the vicinity of the space station by impulsive thrusts

impulsive control thrusts is considered and the proof relies on a previous article by Blaquiere [3].

While most applications of Optimal Control Theory assume quadratic control costs, we are interested in the more relevant L_1-norm of the cost, the actually burned fuel. This choice leads to a complication, because from the Maximum Principle we cannot directly derive the optimal control depending on the state and costate variables, as is the case for quadratic control costs.

A further topic in this article is the comparison between different sets of coordinate systems: While localized coordinates around the space station lead to the frequently used linear Clohessy-Wiltshire equations, we are also interested in the results for the full nonlinear equations using either a local co-rotating Cartesian frame or localized polar coordinates. While the Cartesian coordinates reflect the view from the space station, the polar coordinates better reflect the orbital dynamics of the system. The computed results demonstrate that one has to be careful in stating the initial conditions, otherwise one obtains significant differences in the solutions. Although the considered distances are very small compared to the orbital radius, the small differences in the different coordinate descriptions cause quite large effects in the optimal solution.

The article is organized as follows: First, we introduce the used coordinate systems and the equations of motion for the chaser vehicle in these coordinates. Then we derive the difference equations for the considered impulsive control and state the necessary optimality conditions following from Pontryagin's Maximum Principle for systems with impulsive controls, as given in [2]. Finally, we apply the method to the chasing problem in the different coordinate systems.

21.2 Equations of Motion

During free flight, the chaser vehicle's motion is governed by the equations of a body in the earth's gravitational field. In planar Cartesian coordinates, the equations of motion read

$$\ddot{\boldsymbol{x}} = -\frac{k\boldsymbol{x}}{|\boldsymbol{x}|^3}, \tag{21.1}$$

with $k = Gm_E$, where G is the gravitational constant and m_E is the mass of the earth. The space station rotates on a circular part of radius r_S with angular velocity ω, where $k = r_S^3\omega^2$.

$$\boldsymbol{x}_S = \mathbf{B}(t)\begin{pmatrix} r_S \\ 0 \end{pmatrix}, \quad \text{where } \mathbf{B}(t) = \begin{pmatrix} \cos\omega t & -\sin\omega t \\ \sin\omega t & \cos\omega t \end{pmatrix}. \tag{21.2}$$

Introducing a relative rotating reference frame (see Fig. 21.2), in which the space station S rests at the origin,

$$\boldsymbol{x} = \boldsymbol{x}_S + \mathbf{B}(t)X \tag{21.3}$$

and rescaling the time by $\tau = \omega t$, we obtain the near-field dynamics

$$\ddot{X} = 2\dot{Y} + r_S + X - \frac{r_S^3(r_S + X)}{\left((r_S + X)^2 + Y^2\right)^{3/2}}, \tag{21.4a}$$

$$\ddot{Y} = -2\dot{X} + Y - \frac{r_S^3 Y}{\left((r_S + X)^2 + Y^2\right)^{3/2}}, \tag{21.4b}$$

where the dots now denote derivatives with respect to orbital time τ. For $|X| \ll r_S$, Eq. (21.4) can be approximated by the linear system, well known as *Clohessy-Wiltshire equations* [4],

$$\ddot{X} = 2\dot{Y} + 3X, \tag{21.5a}$$

$$\ddot{Y} = -2\dot{X}. \tag{21.5b}$$

A second possible choice of coordinates are polar coordinates: $\boldsymbol{x} = r(\cos\varphi, \sin\varphi)^T$. In these coordinates, the equations of motion are given by

Fig. 21.2 Local Cartesian (X, Y) and polar coordinate (X_P, Y_P) systems
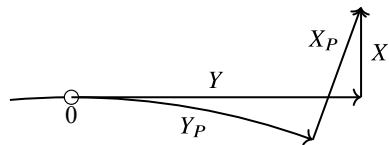
$$\ddot{r} - r\dot{\varphi}^2 = -\frac{k}{r^2}, \tag{21.6a}$$

$$\frac{d}{dt}r^2\dot{\varphi} = r^2\ddot{\varphi} + 2r\dot{r}\dot{\varphi} = 0. \tag{21.6b}$$

Now we again introduce local variables $X_P = r - r_S$ and $Y_P = r_S(\varphi - \omega t)$ (see Fig. 21.2), which agree with the Cartesian coordinates at first order. The positions in the polar and Cartesian coordinate systems are related by

$$X = (r_S + X_P)\cos(Y_P/r_S) - r_S, \tag{21.7a}$$
$$Y = (r_S + X_P)\sin(Y_P/r_S). \tag{21.7b}$$

We obtain the rescaled equations

$$\ddot{X}_P - (r_S + X_P)\left(1 + \frac{\dot{Y}_P}{r_S}\right)^2 = -\frac{r_S^3}{(r_S + X_P)^2}, \tag{21.8a}$$

$$2\dot{X}_P\left(1 + \frac{\dot{Y}_P}{r_S}\right) + (r_S + X_P)\frac{\ddot{Y}_P}{r_S} = 0. \tag{21.8b}$$

As expected, at leading order we again obtain the linear system (21.5).

21.2.1 Impulsive Control Actions

In order to steer the chaser to its target position, a series of impulsive controls is applied by firing the engine for infinitely short intervals. We assume, that the direction and magnitude of these impulses can be chosen arbitrarily. During firing, the position of the vehicle remains unaltered, but the velocity changes instantaneously. If the scaled impulsive control at time τ_i is denoted by v_i, the change in the velocities is given by

$$\Delta\dot{X}(\tau_i) = \dot{X}(\tau_i^+) - \dot{X}(\tau_i^-) = v_{i,1}, \tag{21.9a}$$
$$\Delta\dot{Y}(\tau_i) = \dot{Y}(\tau_i^+) - \dot{Y}(\tau_i^-) = v_{i,2}, \tag{21.9b}$$

where $\dot{X}(\tau_i^+)$ and $\dot{X}(\tau_i^-)$ denote the values of $\dot{X}$ immediately before and after the impulsive control action, respectively.

In polar coordinates, the impulse control leads to

$$\Delta\dot{r}(\tau_i) = v_{i,r}, \qquad \text{with } v_{i,r} = v_{i,1}\cos\varphi + v_{i,2}\sin\varphi, \tag{21.10a}$$
$$\Delta(r^2\dot{\varphi})(\tau_i) = rv_{i,\varphi}, \qquad v_{i,\varphi} = -v_{i,1}\sin\varphi + v_{i,2}\cos\varphi, . \tag{21.10b}$$

Since r is unaffected by the impulse, (21.10b) becomes

$$\Delta\dot{\varphi}(\tau_i) = v_{i,\varphi}/r. \tag{21.10c}$$

In local variables, (21.10) becomes

$$\Delta\dot{X}_P(\tau_i) = v_{i,r}, \tag{21.11a}$$

$$\Delta\dot{Y}_P(\tau_i) = r_S v_{i,\varphi}/(r_S + X_P). \tag{21.11b}$$

In these coordinates, the jump in $\dot{Y}_P$ also depends on the state variable X_P; since $|X_P| \ll r_S$, this dependency vanishes in the linearized equations, but has to be taken into consideration in the treatment of the nonlinear system. We further note that $|(v_{i,r}, v_{i,\varphi})| = |(v_{i,1}, v_{i,2})|$ holds.

21.2.2 Optimal Control Problem

In space missions, the propellant consumption is one of the most important topics, therefore we search for a control strategy, which steers the chaser vehicle to its target position and uses the least amount of fuel. Under some circumstances, it might be necessary to reach the target in a shorter time at the cost of higher energy expenditure. In this case, we prescribe the time interval for the manoeuvre, otherwise the final time is left to be determined by optimizing fuel consumption alone.

We search for an optimal sequence of impulsive controls, which minimizes the cost

$$C = \sum_{i=1}^{k} |\boldsymbol{v}_i|, \tag{21.12}$$

where the number k of impulses, the time instances τ_i, the impulse vectors $\boldsymbol{v}_i$, and possibly the time interval T have to be chosen optimally.

Let us stress here that we search the minimum propellant usage in the L_1-norm, which corresponds to the real costs. Quadratic cost functions are usually easier to handle, but do not properly describe the minimal cost.

The necessary conditions for optimal control problems with impulsive controls were already stated in [2, 3] and apply to the general optimal control problem with continuous controls $u_i(t)$, impulsive controls $\boldsymbol{v}_i$, utility functions $F(\boldsymbol{q}(t), \boldsymbol{u}(t), t)$, and $G(\boldsymbol{q}(\tau_i^-), \boldsymbol{v}_i, \tau_i)$ for the continuous and discrete controls, respectively, and a terminal value $S(\boldsymbol{q}(T^+))$:

$$\max_{\boldsymbol{u}, k, \tau_i, \boldsymbol{v}_i} \left\{ J = \int_0^T F(\boldsymbol{q}(t), \boldsymbol{u}(t), t) dt + \sum_{i=1}^{k} G(\boldsymbol{q}(\tau_i^-), \boldsymbol{v}_i, \tau_i) + S(\boldsymbol{q}(T^+)) \right\}, \tag{21.13}$$

such that

$$\dot{q}(t) = f(q(t), u(t), t), \quad q(0^-) = q_0, \tag{21.14}$$

$$q(\tau_i^+) - q(\tau_i^-) = g(q(\tau_i^-), v_i, \tau_i). \tag{21.15}$$

Similarly to the Maximum Principle by Pontryagin, one defines two Hamilton functions, one for the continuous part, and one for the discontinuities

$$H(q, p, u, t) = F(q(t), u(t), t) + p^T f(q(t), u(t), t), \tag{21.16}$$

$$\mathcal{H}(q, p, v, t) = G(q(t), v, t) + p^T g(q(t), v, t). \tag{21.17}$$

As usual, the (piecewise) optimal continuous control $u^\star$ is obtained from the Maximum Principle for the Hamiltonian H, and the differential equations for the costate variables are also determined by H. The optimal impulse controls $v_i^\star$ are given by maximizing $\mathcal{H}$:

$$u^\star = \arg\max_u H(q^\star(t), p(t), u, t), \tag{21.18}$$

$$\dot{p} = -\partial H(q^\star(t), p(t), u^\star, t)/\partial q, \tag{21.19}$$

$$v_i^\star = \arg\max_{v_i} \mathcal{H}(q^\star(\tau_i^{*-}), p(\tau_i^{*+}), v_i, \tau_i^\star), \tag{21.20}$$

$$p(\tau_i^{*+}) - p(\tau_i^{*-}) = -\partial \mathcal{H}(q^\star(\tau_i^{*-}), p(\tau_i^{*+}), v_i^\star, \tau_i^\star)/\partial q, \tag{21.21}$$

$$H(q^\star(\tau_i^{*+}), p(\tau_i^{*+}), u^\star(\tau_i^{*+}), \tau_i^\star) - H(q^\star(\tau_i^{*-}), p(\tau_i^{*-}), u^\star(\tau_i^{*-}), \tau_i^\star)$$

$$\begin{Bmatrix} > \\ = \\ < \end{Bmatrix} \frac{\partial \mathcal{H}(q^\star(\tau_i^{*-}), p(\tau_i^{*+}), v_i^\star, \tau_i^\star)}{\partial \tau} \quad \text{for } \tau_i^\star \begin{cases} = 0 \\ \in (0, T), \\ = T. \end{cases} \tag{21.22}$$

Here starred quantities denote optimal values for the controls, states, and firing times.

From (21.21), it follows that the adjoint variables become discontinuous, if the jump conditions depend on the state variables, which is the case in our system for the polar coordinates.

Finally, we see from (21.22), which ensures the optimality of the impulse instances τ_i, that the Hamiltonian H is continuous at interior impulse times τ_i, if $\mathcal{H}$ doesn't depend on τ explicitly.

Since our model is autonomous, the optimal final time $T^\star$ is obtained by the boundary condition

$$H(q^\star(T^\star), p^\star(T^\star), u^\star) = 0. \tag{21.23}$$

No continuous controls u_i are present and the considered cost depends on the impulsive controls v_i, therefore the utility function F doesn't show up in the Hamiltonian, and the Maximum condition (21.18) doesn't apply.

21.3 Optimal Control Problem for the Linearized System

Since during the considered phase of the chasing manoeuvre the chaser is already quite close to the space station, the approximation (21.5) together with the jump conditions (21.9) provides a good approximation for the dynamics. Rewriting (21.5) as a first- order system, one obtains the Hamiltonian H and the adjoint differential equations

$$\dot{q}_1 = q_2, \tag{21.24a}$$
$$\dot{q}_2 = -q_1 + 2q_4, \tag{21.24b}$$
$$\dot{q}_3 = -2q_1 + q_4, \tag{21.24c}$$
$$\dot{q}_4 = 0, \tag{21.24d}$$
$$H(\boldsymbol{q}, \boldsymbol{p}) = p_1 q_2 + p_2(-q_1 + 2q_4) + p_3(-2q_1 + q_4), \tag{21.24e}$$
$$\dot{p}_1 = p_2 + 2p_3, \tag{21.24f}$$
$$\dot{p}_2 = -p_1, \tag{21.24g}$$
$$\dot{p}_3 = 0, \tag{21.24h}$$
$$\dot{p}_4 = -2p_2 - p_3, \tag{21.24i}$$

where the state variables q_i are given by $q_1 = X, q_2 = \dot{X}, q_3 = Y$, and $q_4 = \dot{Y} + 2X$. The choice of these variables is motivated by the rotational symmetry of the system, by which the angular momentum $d = r^2 \dot{\varphi}$ is a first integral. In the linearized system, the variable $q_4 = \dot{Y} + 2X$ is constant, as can be seen from (21.5b).

In these state variables, the jump conditions (21.9) read

$$\boldsymbol{q}(\tau_i^+) - \boldsymbol{q}(\tau_i^-) = \boldsymbol{g}(\boldsymbol{q}(\tau_i^-), \boldsymbol{v}_i) = (0, v_{i,1}, 0, v_{i,2})^{\mathrm{T}}. \tag{21.25}$$

With $G = -C$ the Hamiltonian for the impulsive controls is therefore given by

$$\mathcal{H}(\boldsymbol{q}(\tau_i), \boldsymbol{p}(\tau_i), \boldsymbol{v}_i, \tau_i) = -\sqrt{v_{i,1}^2 + v_{i,2}^2} + p_2 v_{i,1} + p_4 v_{i,2}. \tag{21.26}$$

Now we find from (21.20)

$$\frac{v_{i,1}}{\sqrt{v_{i,1}^2 + v_{i,2}^2}} = p_2, \quad \frac{v_{i,2}}{\sqrt{v_{i,1}^2 + v_{i,2}^2}} = p_4, \tag{21.27}$$

from which it follows that

$$\boldsymbol{v}_i \parallel (p_2, p_4) \quad \text{and} \quad \sqrt{p_2^2 + p_4^2} = 1. \tag{21.28}$$

So we know only the direction of the impulsive controls; their magnitude has to be obtained by solving the boundary value problem. We also know that at the instances τ_i, the adjoint variables must satisfy $|(p_2, p_4)| = 1$.

Since $\mathcal{H}$ doesn't depend on the state variables q_i and on τ_i, the costate variables $\boldsymbol{p}$ are continuous at τ_i by (21.21), and also the Hamilton function H is continuous by (21.22). By (21.25), the continuity condition for H becomes

$$\Delta H = p_1 v_{i,1} + (2p_2 + p_3)v_{i,2} = 0, \tag{21.29}$$

which is equivalent to the condition $d(p_2^2 + p_4^2)/d\tau = 0$ by (21.28).

The boundary conditions state that the chaser should be steered from a starting position to a target point at the station's orbit:

$$
\begin{align}
q_1(0) &= X_0, & q_1(T) &= 0, \tag{21.30a}\\
q_2(0) &= \dot{X}_0, & q_2(T) &= 0, \tag{21.30b}\\
q_3(0) &= Y_0, & q_3(T) &= 0, \tag{21.30c}\\
q_4(0) &= \dot{Y}_0 + 2X_0, & q_4(T) &= 0. \tag{21.30d}
\end{align}
$$

Since the final position is an equilibrium, the Hamiltonian $H(\boldsymbol{q}(T), \boldsymbol{p}(T))$ vanishes for all choices of T. Therefore, the condition (21.23) for the optimal planning period T has to be stated immediately before the last impulse.

We note that since q_4 can only reach its final value by impulses in the horizontal direction, the difference $|q_4(T) - q_4(0)|$ provides a lower bound for fuel consumption. The Hohmann transfer [1] with two horizontal burns provides an energy-optimal solution.

The boundary value problem (BVP) (21.24) and (21.30) is solved numerically by the Multiple Shooting Method Boundsco [5], which is especially designed for Optimal control problems with discontinuous state variables.

The following results are calculated for the initial conditions:

$$
\begin{align}
X(0) &= -5\,\text{km}, & \dot{X}(0) &= 0, \tag{21.31a}\\
Y(0) &= -50\,\text{km}, & \dot{Y}(0) &= 50\,\text{km/rev} \stackrel{\wedge}{\approx} 9\,\text{m/s}, . \tag{21.31b}
\end{align}
$$

and orbit radius $r_S = 6778\,\text{km}$.

In the first step, a Hohmann transfer for the energy-optimal trajectory with two horizontal burns is calculated. The first impulse occurs when the chaser reaches the proper elliptical orbit, the second one occurs when it reaches its target position at $t = T \approx 1.492T_0$.

Starting with this solution, a continuation method [6] is employed to decrease the time interval from the value needed for an energetically optimal manoeuvre. By monitoring the switching function $S(\tau) = \sqrt{p_2^2 + p_4^2}$ (see Fig. 21.3), we observe that close to $T = 1.465\,T_0$, where $T_0 = 2\pi/\omega$ denotes the revolution period, it crosses

Fig. 21.3 Variation of the switching function $S = \sqrt{p_2^2 + p_4^2}$ for different time intervals
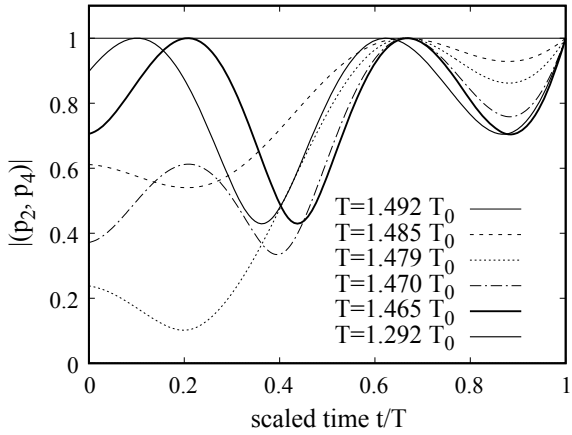
Fig. 21.4 Trajectories and directions of impulsive thrusts for different planning intervals
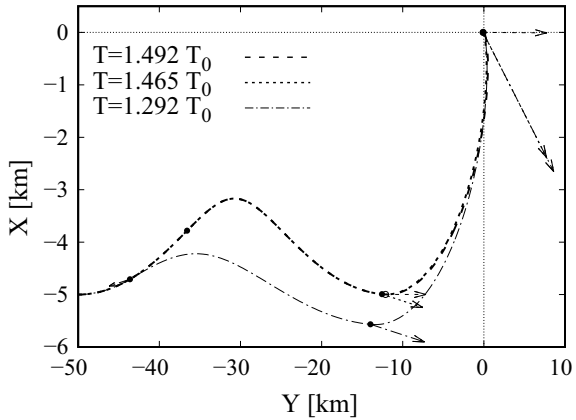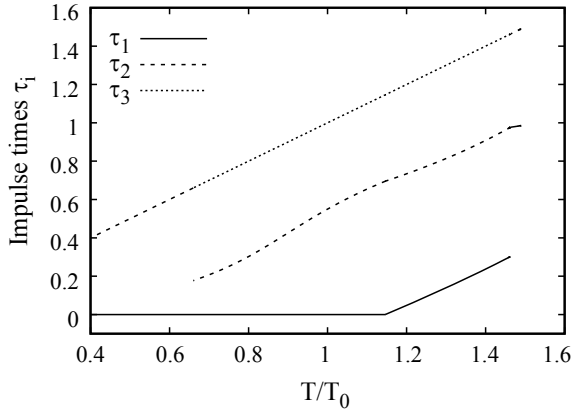

the line $S = 1$ at $t \approx 0.2T$, where a new firing event should occur. The trajectories for $T = 1.492\, T_0$, and $T = 1.465\, T_0$ are displayed in Fig. 21.4. Although the thrusts have different directions, the trajectories are almost the same.
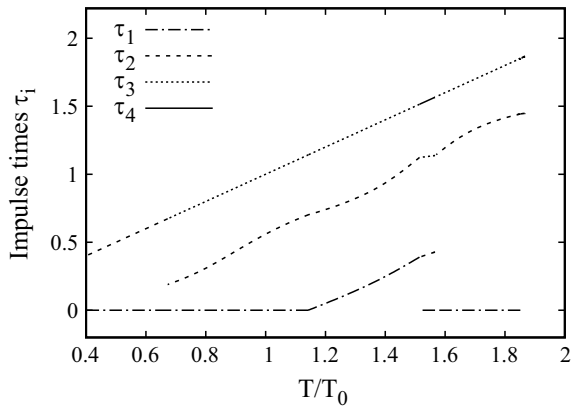
Reducing T further, the new firing time decreases down to $t = 0$, as can be seen in Fig. 21.5. The firing time τ_2 also decreases and vanishes at $T \approx 0.65\, T_0$: The impulse magnitude $|v_2|$ shrinks to zero and the switching function $S(\tau)$ separates from the line $S = 1$. For shorter time horizons, only firings at the start and at the end of the manoeuvre are executed.

The cost C depending on the permitted manoeuvre duration T is displayed in Fig. 21.7; for quick transfers the fuel consumption increases strongly. The labels in Fig. 21.7 denote the firing instances: "S" at the start, "I" in the interior, and "E" at the end of the transfer.

21.4 Optimal Control Problem for the Nonlinear System

For validation of the linear approximation (21.5) also, the optimal control for the
nonlinear systems (21.4) and (21.8) was computed.

21.4.1 Optimal Control Problem for the Local Cartesian Frame

Using the local Cartesian system (21.4), the equations of motion become nonlinear,
but the cost function C and the equations for the impulsive control (21.9) remain
the same as in the linear system (21.5). Since the jumps in (21.9) do not depend on
the state variables and time τ, the costate variables p_i and the Hamiltonian remain
continuous at the firing instances τ_i.

Fig. 21.7 Dependence of fuel cost on the permitted manoeuvre duration T for systems (21.5) and (21.8)
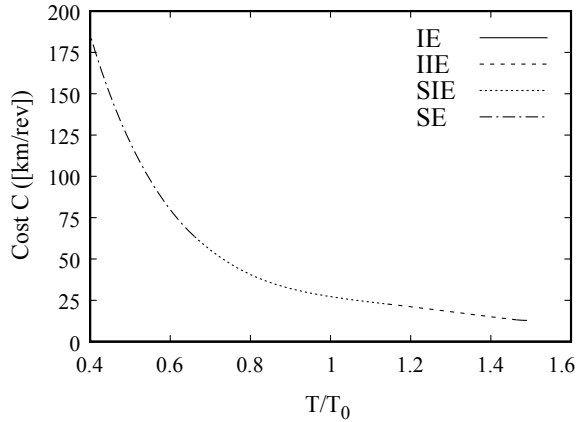
Fig. 21.8 Dependence of fuel cost on the permitted transfer duration T for systems (21.4)
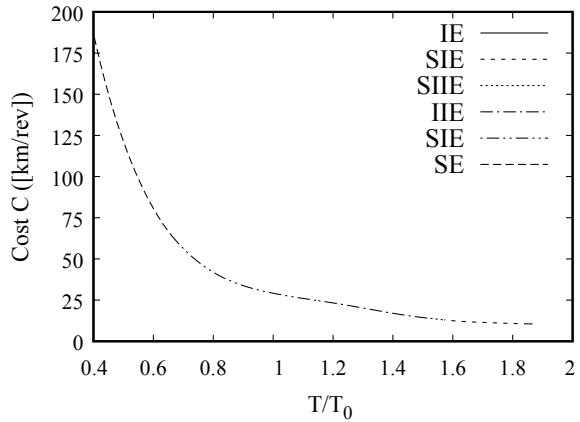

As initial values, we choose the same ones as in the linear system and obtain the results shown in Fig. 21.8, which differ significantly from the results obtained with the linear system (21.5) and for the polar coordinates (21.8). Also the sequence of impulse instances τ_i differs between these calculations, as can be seen from Figs. 21.5 and 21.6. The optimal time $T^\star$ for the least propellant consuming solution increases from approximately 1.5 revolutions to 1.85 revolutions.

21.4.2 Optimal Control Problem for the Polar Coordinate Frame

When using the local polar coordinate system (21.8), the jump conditions (21.11) lead to the maximum condition

Fig. 21.9 Comparison of the
energy-optimal trajectories
for the different choices of
coordinate systems. The
arrows indicate the direction
and magnitude of the
impulsive controls
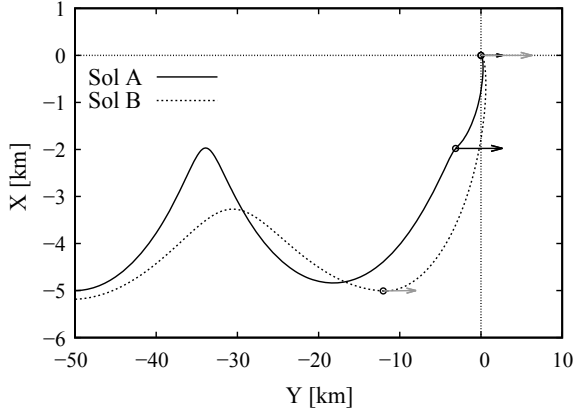
$$v_i^\star = \arg\max_{v_i} \left(-\sqrt{v_{i,r}^2 + v_{i,\varphi}^2} + p_2 v_{i,r} + p_4 \frac{r_S v_{i,\varphi}}{r_S + X_P} \right), \tag{21.32}$$

giving

$$\frac{v_{i,r}}{\sqrt{v_{i,r}^2 + v_{i,\varphi}^2}} = p_2, \quad \frac{v_{i,\varphi}}{\sqrt{v_{i,r}^2 + v_{i,\varphi}^2}} = \frac{r_S p_4}{r_S + X_P}.$$

The switching function $S(\tau)$ which governs the impulse time instances becomes

$$S = \sqrt{p_2^2 + \frac{r_S^2 p_4^2}{(r_S + X_P)^2}}.$$

Since (21.11) is time-independent, due to (21.22) the Hamiltonian H is continuous at the firing times. The occurrence of the state variable $q_1 = X_P$ in the jump condition (21.11) leads to the jump

$$p_1(\tau_i^{*+}) - p_1(\tau_i^{*-}) = \left. \frac{r_S p_4}{(r_S + X_P)^2} \right|_{\tau = \tau_i^\star} \tag{21.33}$$

in the costate variable p_1, according to (21.21).
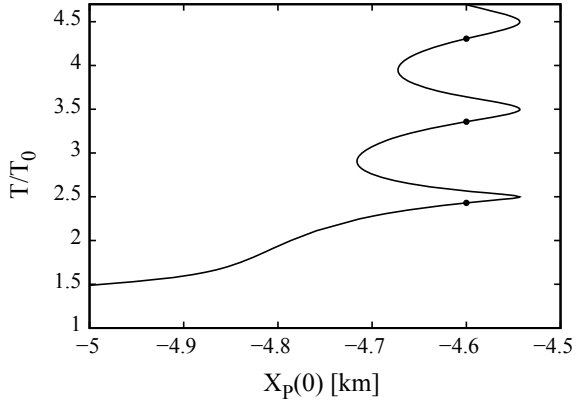
As initial values, we choose

$$X_P(0) = -5\,\text{km}, \qquad\qquad \dot{X}_P(0) = 0, \tag{21.34a}$$

$$Y_P(0) = -50\,\text{km}, \qquad\qquad \dot{Y}_P(0) = 50\,\text{km/rev} \tag{21.34b}$$
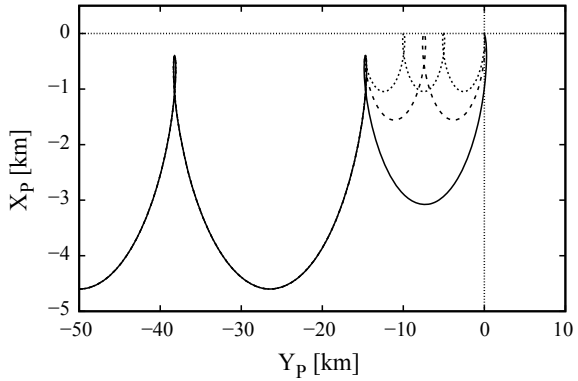
and obtain the results shown in Figs. 21.5 and 21.7, which agree very well with the results for the linear system.

Fig. 21.10 Dependence of the required time T for the energy-optimal solution on the initial height $X_P(0)$

Fig. 21.11 Different trajectories starting at the initial height $X_P(0) = -4.6\,\text{km}$

Now it remains to explain the significant difference between the results for the two nonlinear variants: One might think that the difference between the initial positions is negligible, since 50 km is much smaller than the earth circumference. Indeed the positions given by $(X, Y) = (-5\,\text{km}, -50\,\text{km})$ and $(X_P, Y_P) = (-5\,\text{km}, -50\,\text{km})$ differ only by approximately 200 m. In Fig. 21.9, the energy-optimal trajectories for the different initial conditions are displayed. The initial values for solution A are again given by (21.31), and those for solution B in (21.34), corresponding to

$$X(0) \approx -5.184\,\text{km}, \qquad\qquad \dot{X}(0) \approx 0.369\,\text{km/rev},$$
$$Y(0) \approx -49.962\,\text{km}, \qquad\qquad \dot{Y}(0) \approx 49.962\,\text{km/rev}.$$

Using the same initial conditions in both systems gives of course the same solutions.

In order to study the dependence of the required time T of the energy-optimal solution on the initial height, a continuation with varying values of $X_P(0)$ was carried out, with the remaining initial conditions kept fixed. The obtained curve is displayed

in Fig. 21.10: It shows an increase of T/T_0 from 1.488 to 1.936, when $X_P(0)$ varies from -5 km to -4.8 km. Close to $X_P(0) = -4.55$ km, a series of turning points can be seen along the curve, leading to a series of different energy-optimal solutions for the same initial conditions. In Fig. 21.11, three different trajectories are displayed starting at the same initial position $X_P(0) = -4.6$ km, corresponding to the points in Fig. 21.10. After reaching the final orbit height, the system performs an increasing number of oscillations, until it ends up in its target position.

21.5 Conclusions

The energy-optimal chasing strategy for a space rendezvous using the L_1-norm for the fuel consumption has been investigated for different sets of coordinate systems. Using a homotopy strategy to reduce the time duration of the manoeuvre shows a quite complicated variation of the applied impulsive control. In the considered range of initial conditions, the control strategy and the optimal path depend sensitively on the initial height $X(0)$. When comparing the results calculated in different coordinate systems, the seemingly small differences must therefore not be neglected. The linear system governing the near-field dynamics, which approximates the equations in the polar and the Cartesian frame, agrees better with the nonlinear system in polar coordinates.

References

1. Hohmann, W.: Die Erreichbarkeit der Himmelskörper - Untersuchungen über das Raumfahrt-problem. Oldenbourg, München (1925)
2. Feichtinger, G., Hartl, R.: Optimale Kontrolle ökonomischer Prozesse: Anwendungen des Max-imumprinzips in den Wirtschaftswiss. De Gruyter, New York (1986)
3. Blaquière, A.: Impulsive control with finite or infinite time horizon. JOTA **46**, 431–439 (1985)
4. Lovell, T.A., Spencer, D.A.: Relative orbital elements formulation based upon the Clohessy-Wiltshire equations. J. Astronaut. Sci. **61**, 341–366 (2014)
5. Oberle, H.J., Grimm, W., Berger, E.: BNDSCO, Rechenprogramm zur Lösung beschränkter optimaler Steuerungsprobleme. Benutzeranleitung M 8509, Techn. Univ. München (1985)
6. Seydel, R.: A continuation algorithm with step control. In: Numerical Methods for Bifurcation Problems, vol. 70. ISNM. Birkhäuser (1984)

Chapter 22
Scanning Bridge Frequencies by Wheel Size Embedded Two-Mass Vehicle Model

Check for updates

Judy P. Yang and Cheng-Yi Cao

Abstract This work proposes a novel vehicle model for effectively scanning bridge frequencies, in which wheel size and unsprung mass are incorporated. With the advanced two-mass vehicle model, it is recognized that the moving path of the wheel is the envelope of road surface roughness. Furthermore, it is shown that the proposed vehicle model is able to scan bridge frequencies up to the fifth frequency with the desired accuracy even under high class of road surface roughness in the presence of vehicle damping, whereas the traditional two-mass vehicle model can identify no more than the first two bridge frequencies in the absence of vehicle damping.

22.1 Introduction

The terminology vehicle-bridge interaction (VBI) came out in the 1990s when people were trying to figure out the dynamic responses of bridges and high-speed trains [12, 16]. The interaction between the bridge and vehicle occurs naturally as the moving vehicle excites the vibration to the bridge, and the bridge turns back the vibration to the vehicle at the same time. Such an interaction loop makes the VBI system possible for practical applications, including health monitoring of structures, damage detection of bridges, design of bridges and mobile sensors, etc. Nowadays, VBI has become one prosperous research direction in the world. For readers interested in a detailed review of VBI topics, recent publications are referred to the state-of-the-art review [14] and the book [15], Vehicle Scanning Method, by Yang and his co-workers.

In a VBI system, it is known that the key components are the bridge and vehicle although there are factors affecting the interaction between the bridge and vehicle [3, 8, 9, 11]. In the literature [7, 10, 13], the vehicle is mostly treated as a moving load. Particularly, a single-degree-of-freedom (SDOF) sprung mass is adopted due to its simplicity. Nevertheless, by carefully examining the SDOF vehicle model, there

J. P. Yang (✉) · C.-Y. Cao
Department of Civil Engineering, National Yang Ming Chiao Tung University, Hsinchu 30010, Taiwan
e-mail: jpyang@nycu.edu.tw

is room for improvement of the vehicle model in order to effectively obtain bridge frequencies. For instance, a two-mass vehicle model was proposed to consider both sprung mass and unsprung mass [6]. As the test vehicle is assumed to be in contact with the road via its wheels, the dynamic responses of both vehicle and bridge can be better reflected when the unsprung mass is included. Nevertheless, the assumption of direct contact of the wheel at a particular point in the presence of road surface roughness is still not realistic since the wheels are of finite size in general. Therefore, a massless disk model was proposed by including the influence of wheel size [4]. In this work, a comparison of the disk model and the SDOF vehicle model was made. It was shown that the moving paths obtained by these two models are different under road surface roughness, and the moving path of the disk model is the envelope of that of the point model. In view of the aforementioned models, the present work further proposes a wheel size embedded two-mass vehicle model. By combining the wheel size and unsprung mass, a wider application is easily seen in the future. The interested readers are referred to the authors' recent publication [5] for complete description of the VBI model.

The structure of this work is arranged in the following: the VBI formulation for the proposed vehicle model is briefly introduced in Sect. 22.2. In Sect. 22.3, the proposed vehicle model is first verified by comparing it with an analytical solution. Then, a numerical investigation is given. Section 22.4 concludes this work.

22.2 VBI Formulation

The schematic diagram of the proposed VBI system, wheel size embedded two-mass vehicle model, is depicted in Fig. 22.1. The symbols are introduced as follows: m_v is the sprung mass representing the vehicle body; m_u is the unsprung mass representing the axle mass; R is the wheel radius; the two masses are connected by a spring of stiffness k_v and a dashpot of damping coefficient c_v. For the VBI system in consideration, the vehicle is assumed to move with a constant velocity v on the road with surface roughness denoted by $r(x)$. A simply supported beam of length L is adopted for the bridge.

The corresponding equations of motion for the vehicle and beam element are given as follows:

$$\begin{bmatrix} m_v & 0 \\ 0 & m_u \end{bmatrix} \begin{Bmatrix} \ddot{q}_v \\ \ddot{q}_u \end{Bmatrix} + \begin{bmatrix} c_v & -c_v \\ -c_v & c_v \end{bmatrix} \begin{Bmatrix} \dot{q}_v \\ \dot{q}_u \end{Bmatrix} + \begin{bmatrix} k_v & -k_v \\ -k_v & k_v \end{bmatrix} \begin{Bmatrix} q_v \\ q_u \end{Bmatrix} = \begin{Bmatrix} 0 \\ m_v \ddot{q}_v + m_u \ddot{q}_u \end{Bmatrix}$$

(22.1)

$$[m_b] \{\ddot{q}_b\} + [c_b] \{\dot{q}_b\} + [k_b] \{q_b\} = -f_c \{N(\bar{x}_c)\} - M_c \{N'(\bar{x}_c)\} \qquad (22.2)$$

Fig. 22.1 Schematic
diagram of the VBI system
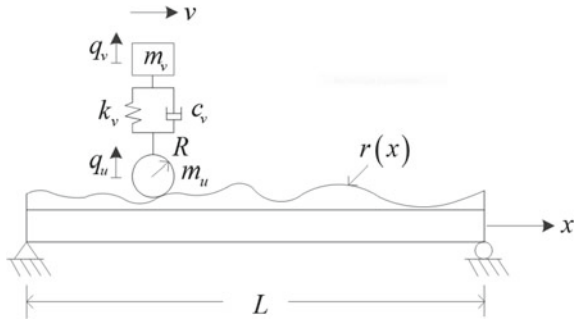
In Eq. (22.1), q_v and q_u represent the displacements of the vehicle body and unsprung
mass, respectively; g is the gravitational constant. In Eq. (22.2), $[m_b]$, $[c_b]$, and $[k_b]$
are the mass, damping, and stiffness matrices of the beam element, with $\{q_b\}$ the
corresponding displacement vector. $\{N\}$ and $\{N'\}$ denote the vector composed of the
cubic Hermitian interpolation functions and the first-order derivative of the vector.
$\bar{x}_c$ is the location of contact point. The expressions for f_c and M_c are

$$f_c = (m_v + m_u)g + m_v \ddot{q}_v + m_u \ddot{q}_u \tag{22.3}$$

and

$$M_c = f_c \, \Delta x \tag{22.4}$$

The following displacement relation is adopted:

$$q_u = \{N(\bar{x}_c)\}^{\mathrm{T}} \{q_b\} + \bar{r}(x_c) \tag{22.5}$$

where $\bar{r}(x_c)$ represents the lift of the entire wheel, and x_c represents the location of
wheel center.

Substituting Eqs. (22.3)–(22.5) into Eqs. (22.1) and (22.2) leads to the following
matrix form of the equations of VBI system:

$$\mathbf{M} \begin{Bmatrix} \ddot{q}_v \\ \{\ddot{q}_b\} \end{Bmatrix} + \mathbf{C} \begin{Bmatrix} \dot{q}_v \\ \{\dot{q}_b\} \end{Bmatrix} + \mathbf{K} \begin{Bmatrix} q_v \\ \{q_b\} \end{Bmatrix} = \mathbf{F} \tag{22.6}$$

To reach the above equation, the detailed derivation is given in the authors' recent
publication [5]. In Eq. (22.6), the boldface denotes the matrix form, and the corre-
sponding components in the matrices are given as follows:

$$\mathbf{M} = \begin{bmatrix} m_v & \mathbf{0} \\ \mathbf{M}_{vu} & \mathbf{M}_{uu} \end{bmatrix},$$

$$\mathbf{M}_{vu} = m_v \left(\{N \, (\bar{x}_c)\} + \{N' \, (\bar{x}_c)\} \, \Delta x \right),$$

$$\mathbf{M}_{uu} = [m_b] + \{N \, (\bar{x}_c)\} \{N \, (\bar{x}_c)\}^{\mathrm{T}} m_u + \{N' \, (\bar{x}_c)\} \{N \, (\bar{x}_c)\}^{\mathrm{T}} m_u \Delta x \qquad (22.7)$$

$$\mathbf{C} = \begin{bmatrix} c_v & -c_v \{N \, (\bar{x}_c)\}^{\mathrm{T}} \\ \mathbf{0} & [c_b] + 2v m_u \left(\{N \, (\bar{x}_c)\} \{N' \, (\bar{x}_c)\}^{\mathrm{T}} + \{N' \, (\bar{x}_c)\} \{N' \, (\bar{x}_c)\}^{\mathrm{T}} \Delta x \right) \end{bmatrix} \tag{22.8}$$

$$\mathbf{K} = \begin{bmatrix} k_v & -c_v v \{N' \, (\bar{x}_c)\}^{\mathrm{T}} - k_v \{N \, (\bar{x}_c)\}^{\mathrm{T}} \\ \mathbf{0} & [k_b] + v^2 m_u \left(\{N \, (\bar{x}_c)\} \{N'' \, (\bar{x}_c)\}^{\mathrm{T}} + \{N' \, (\bar{x}_c)\} \{N'' \, (\bar{x}_c)\}^{\mathrm{T}} \Delta x \right) \end{bmatrix} \tag{22.9}$$

$$\mathbf{F} = \left\{ \begin{array}{c} f_v \\ \{f_b\} \end{array} \right\}$$

$$= \left\{ \begin{array}{c} c_v v \bar{r}' \, (x_c) + k_v \bar{r} \, (x_c) \\ -\left[(m_v + m_u) \, g + m_u v^2 \bar{r}'' \, (x_c) \right] \left(\{N \, (\bar{x}_c)\} + \{N' \, (\bar{x}_c)\} \, \Delta x \right) \end{array} \right\} \tag{22.10}$$

In Eqs. (22.7)–(22.10), the parameters including $\bar{x}_c$, x_c, and $\bar{r}(x_c)$ are unknowns to be determined numerically. Therefore, the procedure for finding these parameters is crucial in this work. Due to limited space, it is referred to the work given in [5].

22.3 Numerical Results

22.3.1 Verification

The following parameters and material properties are adopted for verifying the proposed vehicle model [5]. For the bridge, $\bar{m} = 1000$ kg/m, $L = 30$ m, $E = 27.5$ GPa, and $I = 0.175$ m^4; for the vehicle, $m_v = 1500$ kg, $m_u = 150$ kg, $k_v = 170$ kN/m, $R = 0.3$ m, and $v = 5$ m/s. In the finite element simulation, 40 beam elements are adopted. The dynamic equations are solved by using a time interval $\Delta t = 0.001$ s. The damping effect is ignored for both bridge and vehicle.

As depicted in Figs. 22.2 and 22.3, the dynamic responses including deflection and acceleration of both bridge and vehicle obtained by the present vehicle model agree well with the analytical solutions derived by Biggs [2].

22.3.2 Identification of Bridge Frequencies

In this study, the same information about bridge and vehicle given in Sect. 22.3.1 is adopted again while the damping ratio 0.2 is considered in the test vehicle. In
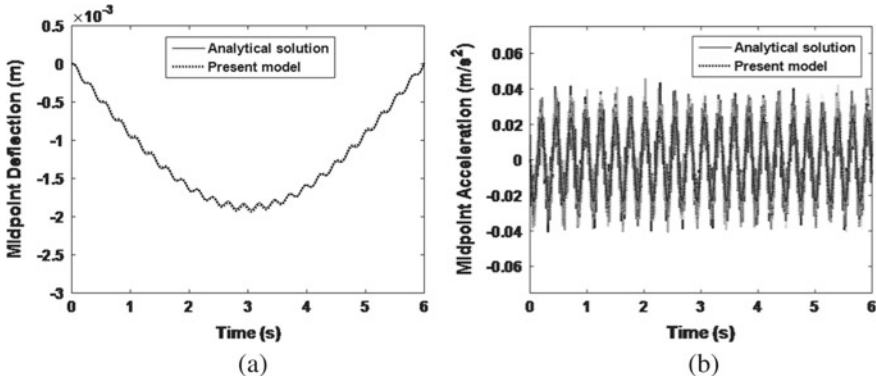
Fig. 22.2 Dynamic responses of the bridge: **a** deflection; **b** acceleration
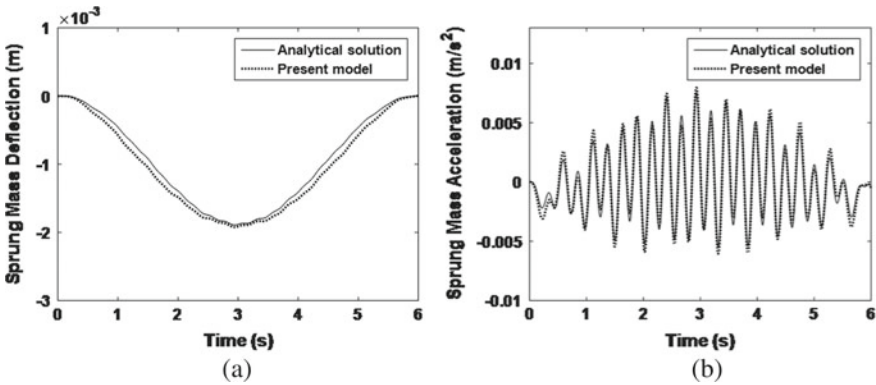

Fig. 22.3 Dynamic responses of the vehicle: **a** deflection; **b** acceleration

addition, a high level of road irregularity is adopted. The numerical generation of road irregularity is referred to ISO 8608 [1]. Figure 22.4 shows the moving path of the wheel together with the road irregularity. Obviously, the moving path of the wheel encloses the periphery of the profile of road irregularity, which indicates the effect of wheel size.

Next, the ability of the proposed vehicle model to identify bridge frequencies is investigated. As shown in Fig. 22.5a, the overview of vehicle's spectrum is presented. By zooming in this figure, as shown in Fig. 22.5b, the marked high peaks in the spectrum are corresponding to bridge frequencies. In particular, it is observed that the first four bridge frequencies can be identified clearly even under a high level of road irregularity. By examining the maximal relative error of the identified bridge frequencies, it is found that the proposed vehicle model can extract at least the first five bridge frequencies with maximal relative error less than 5%.
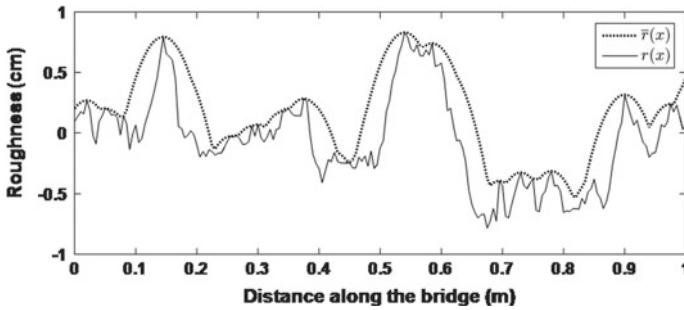
Fig. 22.4 Moving path of the wheel corresponding to road irregularity
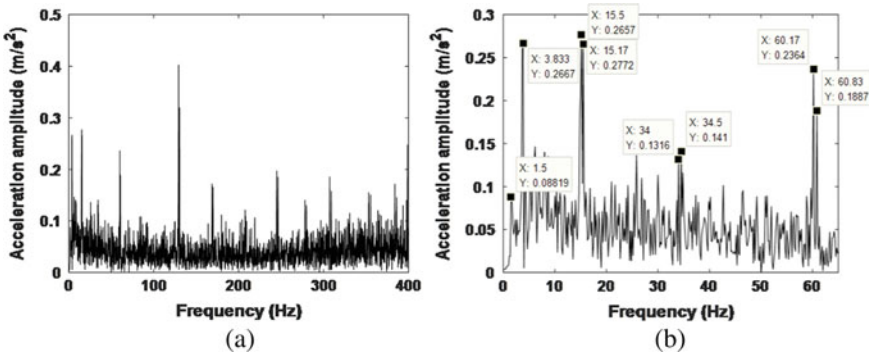

Fig. 22.5 Vehicle's spectra: **a** overview of the spectrum; **b** enlargement of the spectrum

22.4 Conclusion

In this work, an advanced vehicle model is proposed for the identification of bridge frequencies. Aiming at effectively and efficiently scanning bridge frequencies, the wheel size is embedded in the two-mass vehicle model. From numerical investigation, it is easily seen that the major contribution of this work is the ability to scan high bridge frequencies even under a high level of road irregularity. In particular, no additional technique such as empirical mode decomposition (EMD) is involved to process the vehicle's spectra, thereby making the proposed VBI model practical. Through the spectral analysis of dynamic responses recorded by the vehicle, both the vehicle and bridge frequencies can be identified directly. The efficacy of the proposed VBI model is therefore demonstrated.

References

1. ISO 8608:1995(en): Mechanical vibration—road surface profiles—reporting of measured data. Standard. International Organization for Standardization (1995)
2. Biggs, J.M.: Introduction to Structural Dynamics. McGraw-Hill, New York (1964)
3. Chang, K., Wu, F., Yang, Y.: Effect of road surface roughness on indirect approach for measuring bridge frequencies from a passing vehicle. Interact. Multiscale Mech. **3**(4), 299–308 (2010)
4. Chang, K., Wu, F., Yang, Y.B.: Disk model for wheels moving over highway bridges with rough surfaces. J. Sound Vib. **330**(20), 4930–4944 (2011)
5. Yang, J.P., Cao, C.-Y.: Wheel size embedded two-mass vehicle model for scanning bridge frequencies. Acta Mech. **231**(4), 1461–1475 (2020). https://doi.org/10.1007/s00707-019-02595-5
6. Yang, J.P., Chen, B.H.: Two-mass vehicle model for extracting bridge frequencies. Int. J. Struct. Stab. Dyn. **18**(04), 1850056 (2018)
7. Yang, J.P., Chen, B.L.: Rigid-mass vehicle model for identification of bridge frequencies concerning pitching effect. Int. J. Struct. Stab. Dyn. **19**(02), 1950008 (2019)
8. Yang, J.P., Lee, W.C.: Damping effect of a passing vehicle for indirectly measuring bridge frequencies by EMD technique. Int. J. Struct. Stab. Dyn. **18**(01), 1850008 (2018)
9. Yang, Y.B., Chang, K.: Extracting the bridge frequencies indirectly from a passing vehicle: parametric study. Eng. Struct. **31**(10), 2448–2459 (2009)
10. Yang, Y.B., Chang, K.: Extraction of bridge frequencies from the dynamic response of a passing vehicle enhanced by the EMD technique. J. Sound Vib. **322**(4–5), 718–739 (2009)
11. Yang, Y.B., Li, Y., Chang, K.: Effect of road surface roughness on the response of a moving vehicle for identification of bridge frequencies. Interact. Multiscale Mech. **5**(4), 347–368 (2012)
12. Yang, Y.B., Lin, B.H.: Vehicle-bridge interaction analysis by dynamic condensation method. J. Struct. Eng. **121**(11), 1636–1643 (1995)
13. Yang, Y.B., Lin, C., Yau, J.: Extracting bridge frequencies from the dynamic response of a passing vehicle. J. Sound Vib. **272**(3–5), 471–493 (2004)
14. Yang, Y.B., Yang, J.P.: State-of-the-art review on modal identification and damage detection of bridges by moving test vehicles. Int. J. Struct. Stab. Dyn. **18**(02), 1850025 (2018)
15. Yang, Y.B., Yang, J.P., Wu, Y., Zhang, B.: Vehicle Scanning Method for Bridges. Wiley Online Library (2019)
16. Yang, Y.B., Yau, J.D.: Vehicle-bridge interaction element for dynamic analysis. J. Struct. Eng. **123**(11), 1512–1518 (1997)

Chapter 23
Wave Attenuation in a Pre-tensioned String with Periodic Spring Supports

Y.-B. Yang, J. D. Yau, and S. Urushadze

Abstract The overhead catenary system is a crucial conductor for delivering steady electric power to the trains running on modern electrified railways. The propagation of vibration waves in the catenary system is of interest to railway engineers due to the pantograph-catenary interaction. To explore the wave transmission via the contact wires of a catenary system supported by hanging devices offered by the bracket structures, a simplified model composed of a pre-tensioned string periodically suspended by hanging springs is adopted. For a periodic structure with wider band gaps, also known as stop bands, a wider cluster of frequencies of waves propagating in the periodic structure can be attenuated (or filtered out). This will be beneficial to the maintenance of the catenary system. To take advantage of such a feature, a resonator is usually equipped on each of the hanging spring supports so as to widen band gaps for better attenuation of the waves transmitted in the pre-tensioned string. In this study, a unit cell conceived as a spring-resonator-string unit is adopted to formulate the closed-form dispersion equation, from which the key condition for widening the band gaps is derived. From the exemplar study, it was shown that the installation of adjustable resonators on a catenary system can increase the band gap width, serving as a wave filter for attenuating the pantograph-induced wave transmission in the contact wires of the pantograph-catenary system.

Y.-B. Yang (✉)
School of Civil Engineering, Chongqing University, Chongqing 400044, China
e-mail: ybyang@ntu.edu.tw

Department of Construction Engineering, National Yunlin University of Science and Technology, Yunlin 64002, Taiwan

J. D. Yau
Department of Architecture, Tamkang University, New Taipei City 25137, Taiwan
e-mail: jdyau@mail.tku.edu.tw

S. Urushadze
Institute of Applied and Theoretical Mechanics, Czech Academy of Sciences, Prague, Czech Republic
e-mail: urushadze@itam.cas.cz

23.1   Introduction

High-speed railways have become one of the most efficient ground transportation tools for passengers traveling between major cities in many countries. For high-speed or traditional railways, the overhead catenary system contains contact wires for transmitting the electrical current to the pantographs equipped on each train, thereby supplying the power to the electrical engines of the locomotives of the train. In the past decades, many studies were conducted on the dynamic behaviors of the pantograph and catenary, considering their interaction. Sophisticated models have been developed to carry out the response analysis of the pantograph-catenary system, by which the effect of the locomotive motion was taken into account [6]. However, few research has been conducted to explore the problem of wave attenuation via the contact wires of a catenary system.

For the theoretical formulation aimed at obtaining a closed-form solution, the overhead catenary system is simplified as a pre-tensioned string supported period- ically by hanging springs in this study. Using the Floquet-Bloch theory [1, 5] to account for the periodicity of a periodic structure, the dispersion relation between the wavenumber and frequency of the pre-tensioned string will be derived. Moreover, a resonator is installed on each of the hanging spring supports to widen the band gaps (stop bands) of the pre-tensioned string for better attenuation of the wave compo- nents transmitted via the string. Then, the key condition for determining the critical resonator is identified from the closed-form dispersion equation of the pre-tensioned string with resonators.

23.2   Problem Formulation of Overhead Catenary System

For the present purposes, the catenary system is simplified as a pre-tensioned string supported by periodic hanging springs with identical interval L, as shown in Fig. 23.1.

To derive the closed-form solution for the dispersion equation of the pre-tensioned string, the following assumptions are adopted:

1. The main contact wire of the catenary system is modeled as a horizontal pre- tensioned string supported by periodic hanging springs of uniform interval L [6];
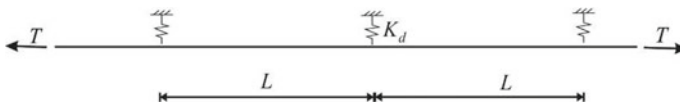2. The tensioned force T in the string is assumed to be constant during vibration.

Fig. 23.1 Schematic of a pre-tensioned string suspended by equal-distance hanging springs

With the above tensioned string model, the dispersion relation between the wavenumber and frequency of the periodically supported tensile string will be derived and presented in closed form.

23.2.1 Dynamic Stiffness Matrix of a Tensioned String

As shown in Fig. 23.1, the governing equation for the transverse motion of a tensioned string can be written as follows [3]:

$$m_s \frac{\partial^2 u(x, t)}{\partial t^2} - T \frac{\partial^2 u(x, t)}{\partial x^2} = 0 \tag{23.1}$$

where m_s is the mass of the string per unit length and $u(x, t)$ the vertical displacement of the string. By letting $a^2 = m_s \omega^2 / T$, with ω denoting the frequency, and solving Eq. (23.1), one can obtain the following solution:

$$u(x, t) = [C_1 \sin(ax) + C_2 \sin(a(L - x))] e^{i\omega t}. \tag{23.2}$$

By introducing the dynamic equilibrium conditions at the two ends of a string of length L, the well-known dynamic stiffness matrix of the pre-tensioned string element with length L can be written as [4]

$$\mathbf{D}(aL)_{string} = \frac{aT}{\sin(aL)} \begin{bmatrix} \cos(aL) & -1 \\ -1/\cos(aL) & \end{bmatrix}. \tag{23.3}$$

With the dynamic stiffness matrix given in Eq. (23.3), one can conceive a unit cell of the periodic spring-supported string as in Fig. 23.2, and derive from this the closed-form expression for the dispersion relation of the wavenumber and the frequency, as in the section to follow.

23.2.2 Dispersion Equation of a Tensioned String with Periodical Spring Supports

With the dynamic stiffness matrix given in Eq. (23.3), the dynamic stiffness equation of the unit cell in Fig. 23.2 for the pre-tensioned string with periodic spring supports can be expressed as

$$\begin{bmatrix} d_{LL} & d_{LR} \\ d_{LR} & d_{RR} \end{bmatrix} \begin{Bmatrix} u_L \\ u_R \end{Bmatrix} = \begin{Bmatrix} f_L \\ f_R \end{Bmatrix} \tag{23.4}$$

Fig. 23.2 A spring-string
unit cell

(u_L, f_L) ●————————●(u_R, f_R)

K_d

$L/2$ $L/2$
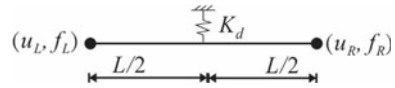
where $\{f\}$ and $\{u\}$ are the element forces and displacements, respectively, and

$$d_{LR} = d_{RL} = \frac{-aT \csc(aL/2)}{2\left(\cos(aL/2) + \frac{K_d}{2aT}\sin(aL/2)\right)}, \tag{23.5}$$

$$d_{LL} = d_{RR} = aT \cot(aL/2) + d_{LR}. \tag{23.6}$$

By adopting the periodic boundary conditions of $(u_R = e^{-i\kappa L}u_L, f_R + e^{-i\kappa L} f_L = 0)$ of the Floquet-Bloch theory [2] for the string element, the following dispersion equation can be obtained [1, 5]:

$$\cos(\kappa L) = \cos(aL) + \frac{K_d L}{2aL \times T}\sin(aL). \tag{23.7}$$

For the pass-band condition of $|\cos(\kappa L)| \leq 1$ in Eq. (23.7), the bounding frequencies are defined by $|\cos(\kappa L)| = \pm 1$. Clearly, the condition of bounding frequencies listed in Table 23.1 depends on the stiffness parameter $(K_d L/T)$, which is related to the tensile force T in the string, spring stiffness K_d, and uniform interval L of the hanging supports offered by the bracket structures. In real electrified railways, the span interval L of the bracket structures and the pre-tensioned force T in a catenary system are determined by the regulations or provisions suggested by railway codes. Consequently, a change in the hanging spring stiffness K_d may lead to a spectral band gap that allows certain frequency components to be attenuated (or filtered out) during the wave transmission in the periodically spring-supported string. To further this consideration, a resonator will be equipped in the hanging spring support for the purpose of widening the band gaps for attenuating certain frequency components in the pre-tensioned string.

Table 23.1 Bounding frequencies of the unit cell

Modes	Bounding frequencies (aL)
Symmetrical Mode $(u_R = u_L, \cos(\kappa L) = 1)$ $u(x, t) = \sin\left(\frac{aL}{2}\right)\cos\left(\frac{aL}{2}\left(1 - \frac{2x}{L}\right)\right)$	$\frac{aL}{2}\tan\left(\frac{aL}{2}\right) = \frac{1}{2}\frac{K_d L}{2T}$
Anti-symmetrical Mode $(u_R = -u_L, \cos(\kappa L) = -1)$ $u(x, t) = \cos\left(\frac{aL}{2}\right)\sin\left(\frac{aL}{2}\left(1 - \frac{2x}{L}\right)\right)$	$\frac{aL}{2}\cot\left(\frac{aL}{2}\right) + \frac{1}{2}\frac{K_d L}{2T} = 0$

23.3 Dispersion Equation of the Unit Cell with Resonator

For a periodic structure with wider band gaps, more frequencies of waves propagating in the periodic structure can be attenuated (or filtered out). To make use of this feature, a resonator is equipped on each of the hanging spring supports (Fig. 23.3) so that a widened band gap (stop band) can be achieved, so as to attenuate a wider range of frequencies of waves transmitted via the pre-tensioned string. By using the element assemblage procedure, the spectral equation of the unit cell with two string elements each of length $L/2$ and an intermediate resonator at the mid-node (see Fig. 23.3) can be expressed as follows:

$$
\begin{bmatrix}
aT \cot(aL/2) & -aT \csc(aL/2) & 0 & 0 \\
-aT \csc(aL/2) & 2aT \cot(aL/2) + K_d + k_r & -k_r & -aT \csc(aL/2) \\
0 & -k_r & k_r - m_r \omega^2 & 0 \\
0 & -aT \csc(aL/2) & 0 & aT \cot(aL/2)
\end{bmatrix}
\begin{Bmatrix}
u_L \\ u_m \\ u_r \\ u_R
\end{Bmatrix}
=
\begin{Bmatrix}
f_L \\ 0 \\ 0 \\ f_R
\end{Bmatrix}.
$$

(23.8)

Here, m_r is the lumped mass and k_r the spring constant of the resonator, and (u_m, u_r) denote the vertical displacements of the mid-node of the string and the lumped mass. By the matrix condensation method, one can condense the slaved displacements (u_m, u_r) into the corresponding master displacements (u_L, u_R) of the unit cell, as shown in Fig. 23.3. Then the condensed stiffness equation becomes

$$
\begin{bmatrix}
\bar{d}_{LL} & \bar{d}_{LR} \\
\bar{d}_{LR} & \bar{d}_{RR}
\end{bmatrix}
\begin{Bmatrix}
u_L \\ u_R
\end{Bmatrix}
=
\begin{Bmatrix}
f_L \\ f_R
\end{Bmatrix}
$$

(23.9)

where

$$
\bar{d}_{LR} = \bar{d}_{RL} = \frac{-aT \csc(aL/2)}{2 \left(\cos(aL/2) + \frac{\bar{K}_d L}{2aL \times T} \sin(aL/2) \right)},
$$

(23.10)

$$
\bar{d}_{LL} = \bar{d}_{RR} = aT \cot(aL/2) + \bar{d}_{LR},
$$

(23.11)

$$
\bar{K}_d = K_d \left(1 + \frac{k_r}{K_d} \frac{(\omega/\omega_r)^2}{(\omega/\omega_r)^2 - 1} \right)
$$

(23.12)

with $\omega_r = \sqrt{k_r/m_r}$ denoting the frequency of the resonator. Clearly, the effect of the resonator was taken into account in the expression for the condensed spring stiffness
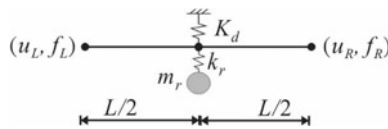

Fig. 23.3 A spring-resonator-string unit cell

in Eq. (23.12). For the special case when the spring constant k_r of the resonator is zero, the condensed stiffness equation of Eq. (23.9) reduces to Eq. (23.4) as expected. By introducing the periodic boundary conditions mentioned above to Eq. (23.9), the following dispersion equation can be derived

$$\cos(\kappa L) = \cos(aL) + \frac{\bar{K}_d L}{2aL \times T} \sin(aL). \tag{23.13}$$

The second term on the right side of the preceding characteristic equation describes the dispersive feature of a resonator to attenuate the wave components transmitting from one span to the next one of the periodic pre-tensioned string. For the calculation to follow, the frequency ratio ω/ω_r is introduced:

$$\left(\frac{\omega}{\omega_r}\right)^2 = \frac{\mu T}{k_r L}(aL)^2 \tag{23.14}$$

where μ is the mass ratio defined as $\mu = m_r/m_s L$. Then the second term in Eq. (23.13) can be rewritten as

$$\frac{\bar{K}_d L}{2aL \times T} \sin(aL) = \frac{K_d L}{2aL \times T} \sin(aL) + \frac{\mu}{2} \frac{aL \times \sin(aL)}{(aL)^2 \mu T/k_r L - 1}. \tag{23.15}$$

Let us consider the critical condition by letting $aL \rightarrow N\pi|_{N=1,2,3...}$ and $\omega \rightarrow \omega_r$ (or $(aL)^2 \mu T/k_r L \rightarrow 1$) in Eq. (23.15), that is,

$$\lim_{aL \rightarrow N\pi, \omega \rightarrow \omega_r} \frac{\bar{K}_d L}{2aL \times T} \sin(aL) = (-1)^N \frac{\mu}{2} N\pi. \tag{23.16}$$

With this, the dispersion relation in Eq. (23.13) reduces to

$$\cos(\kappa L) = (-1)^N \left(1 + \mu \left(\frac{N\pi}{2}\right)^2\right) \tag{23.17}$$

or

$$|\cos(\kappa L)| = 1 + \mu \left(\frac{N\pi}{2}\right)^2 > 1. \tag{23.18}$$

As can be seen from Eq. (23.18), the resonator provides a widening mechanism to increase the band gap of wave transmission in a pre-tensioned string supported by the hanging springs. Concerning the band gap for attenuating the wave transmission with specific frequencies in the string, some numerical analyses will be carried out in the following section.

23.4   Illustrative Example

Let us consider the simplified catenary system shown in Fig. 23.1. Using the empirical data given by Ref. [6], the pre-tensioned force in the contact wire is set to be $T = 15$ kN, the mass per unit length of the contact wire is $m_s = 0.925$ kg/m, the suspension stiffness of the registration arm assembly is $K_d = 130$ N/m, and the span length of bracket structures is $L = 65$ m. See Table 23.2 for a list of the properties

Table 23.2 Properties of the pre-tensioned string

L (m)	m_s (kg/m)	T (N)	K_d (N/m)	$v_c = \sqrt{T/m_s}$ (m/s)
65	0.925	15 000	130	127[a]

[a]Critical velocity of the pre-tensioned string
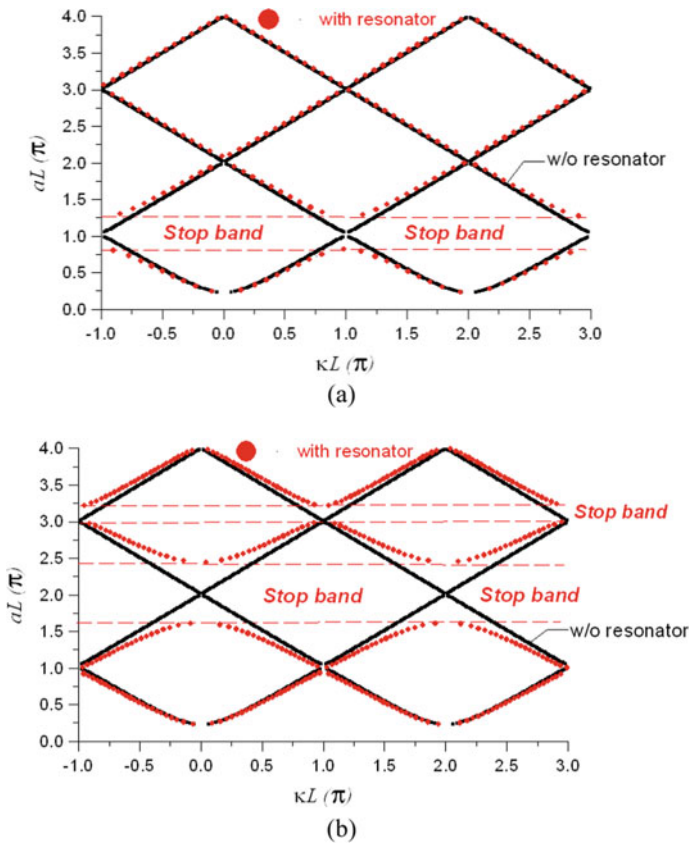
Fig. 23.4 Dispersion curves of the string with critical resonators with **a** $k_{r,cr} = \pi^2 \mu T/L$; **b** $k_{r,cr} = 4\pi^2 \mu T/L$

adopted in the analysis. Correspondingly, the stiffness parameter $(K_d L/T)$ is equal to 0.564. Let us adopt a resonator with the mass of $m_r = 0.1$ kg, $m_s L = 6$ kg. If the nondimensional frequency aL is selected as $aL = \pi$ for attenuating the frequencies, then the critical spring stiffness $(k_{r,cr} = \pi^2 \mu T/L)$ of the resonator can be designed as 228 N/m.

With these data, the dispersion curves of the pre-tensioned string derived have been plotted in Fig. 23.4a, in which the black lines represent the dispersion curve of the string without resonator and the lines with red dots the curve with resonators.

As indicated, the band gap (stop band) at $aL = \pi$ is significantly widened once the critical resonator is taken into account. Similarly, if the nondimensional frequency is set at $aL = 2\pi$, the critical spring stiffness is $k_{r,cr} = 911$ N/m. Figure 23.4b shows the corresponding dispersion curves of the pre-tensioned string, in which the band gaps (stop bands) at $aL = 2\pi$ and $aL = 3\pi$ have been significantly widened.

23.5 Concluding Remarks

In this study, a simplified model composed of pre-tensioned string suspended periodically by equal-distance springs is used to simulate the pantograph-catenary interaction encountered in railway engineering. With this, the dispersion relation between the wavenumber and frequency of the pre-tensioned string hung by periodical spring supports is derived in closed form. For wave attenuation, a resonator was attached to each hanging spring support, for which the closed-form solution was also derived from the corresponding dispersion relation. The numerical results indicate that the installation of resonators can widen the band gaps (or stop bands) of the dispersion curves of the pre-tensioned string. With this conclusion, a further pantograph/catenary interaction model will be carried out to study the overall pantograph-catenary interaction dynamics.

References

1. Brillouin, L.: Wave propagation in periodic structures: electric filters and crystal lattices (1953)
2. Floquet, G.: Sur les équations différentielles linéaires à coefficients périodiques. Annales scientifiques de l'École normale supérieure **12**, 47–88 (1883)
3. Frýba, L.: Vibration of Solids and Structures Under Moving Loads. Thomas Telford Publishing, London (1999)

4. Lee, U.: Vibration analysis of one-dimensional structures using the spectral transfer matrix method. Eng. Struct. **22**(6), 681–690 (2000)
5. Yang, Y.B., Yau, J., Urushadze, S.: Wave transmission of linked railcars moving over multi simple beams under dual resonance. J. Sound Vib. **452**, 51–57 (2019)
6. Zhai, W., Cai, C.: Effect of locomotive vibrations on pantograph-catenary system dynamics. Veh. Syst. Dyn. **29**(S1), 47–58 (1998)